POLYTECHNIC UNIVERSITY OF MARCHE - ANCONA

SCIENZE BIOMOLECOLARI

P H D T H E S I S

Defended by

Caterina RICCI

Study of amyloid proteins aggregation processes in presence of active biomolecules

Thesis Advisor: Paolo MARIANI

Thesis Co-Advisor: Maria Grazia ORTORE

Contents

Introduction

Alzheimer's disease (AD) is, together with Parkinson's disease (PD), the most common form of senile dementia, characterized by progressive impairment in cognitive function and behavior. With the size of the elderly population rising dramatically, the development of new methodologies for diagnosis and treatment of these pathologies represents a fundamental challenge for public health in the 21st century. The onset of the diseases is identified by the incorrect folding and reorganization in beta sheets structures of peptides (Aβ peptide or α-synuclein respectively for AD and PD) that are normally present in cerebral tissues. These misfolded proteins accumulate and generate insoluble bundle of fibrils and plaques that are considered the hallmark of the pathologies. It is well established, however, that the very onset of the disease is linked to intermediate oligomeric populations, more than mature fibrils. In this framework, my PhD project concerns the study of the molecular basis of neurodegenerative disorders, to better characterize pattern and interconnections in the amyloid fibrillation process.

The intervention in amyloid diseases, towards a therapeutic approach for their treatment, can include different strategies interfering with the route of amyloid formation: from blocking the production of the amyloidogenic proteins, to inhibiting or reverse their misaggregation with exogenous or endogenous compounds, to modulate an auxiliary cellular pathway that affects beneficially one or more of the foregoing approaches. In this thesis, the effect of molecules suspected to interfere with amyloid formation has been investigated, to identify their interrelationship mechanisms with the target proteins. Furthermore, the structures of the selected compounds have been analyzed, to gain a deepen view on their physiological configuration. The chosen molecules belong to different classes: a biomolecular class, the one of molecular chaperones, that are already present in the cellular environments and yet play a role in maintaining cellular homeostasis, and a chemical and exogenous one, the class of curcumin derivatives. After this, the effect of Aβ peptide on model membranes has been analyzed to better understand the mechanisms underlying the toxic action of the peptide.

Molecular chaperones play essential roles in many cellular processes, including protein folding, targeting, transport, degradation and disruption of toxic aggregates by clearance mechanisms. Moreover, they regulate protein functions in order to protect against oxidative stress due to toxicity resulting from amyloid aggregates. Current studies have attributed to the human chaperones Hsp60 and Hsp70 an important role in amyloid neurodegenerative diseases, even if with often controversial mechanisms that need to be clarified. Nevertheless, the oligomeric stability of Hsp70 has been studied only recently while little is known about Hsp60 in the two forms in which it is present in the cellular environment: the naïve and mitochondrial form. Even for the extensively studied GroEL, the bacterial homologue of Hsp60, some concerns

remain about its structure and function in solution and, more importantly, under physiological conditions. Since these molecules are readily emerging as therapeutic and diagnostic targets, their comprehensive structural knowledge is an important field for molecular biology, useful for the development of new drugs and therapies. For this reason, a characterization of these proteins' structures in solution was due and has been firstly obtained. Subsequently a study of chaperones-amyloidogenic proteins direct interactions has been carried out for the validation of possible defense pathways based on preferential binding effects.
The chemical agents considered to interfere with amyloid β peptide are new curcumin derivatives. In fact, in the past years, curcumin seemed to be among the most powerful candidates for the inhibition of the Aβ *in vitro* aggregation and fibrillization, being a natural compound and being already used as a natural drug for different targets, including primarily as an antioxidant. The idea of exploiting curcumin for therapeutic purposes, however, presents considerable limitations inherent to its poor solubility, stability and ability to permeate the blood-brain barrier. Hence it is necessary to synthesize compounds with the same ability of curcumin to bind Aβ peptide, but that do not present stability and bio-availability problems, allowing a real applicability in the treatment of the pathologies. The leading characters of this part of the study, i.e. curcumin derivatives, have been designed to specifically maintain the merits of curcumin, avoiding its defects, and have been characterized with different techniques until the biological evaluation on a cellular model system.
My research project is focused on the study of the interactions between amyloidogenic proteins and different chemical and biological agents mainly by means of Small Angle X-Ray Scattering (SAXS), but presents a multidisciplinary experimental approach.
In this work the main technique used for the analysis, i.e. SAXS, is presented firstly in Chapter 1, where the approaches exploited in the experimental data analysis are introduced.
In Chapter 2, the two principal protein studied, α-synuclein and β amyloid, are presented and characterized even in comparison with model proteins, with the purpose of investigating the interactions in their pathogenic pattern.
In Chapter 3 and 4 the molecular chaperones Hsp60 and Hsp70 have been at first characterized in solution and compared with their crystallographic structures. After this, the interaction with amyloid peptides has been inspected, showing their potential role in a therapeutical approach to neurodegenerative diseases.
Subsequently, chemical compounds specifically designed to interact with Aβ peptide are illustrated in Chapter 5. In this study two compounds have been proposed, with different effects on the fibrillation kinetics, suggesting different possible therapeutic strategy.
Finally, the effect of Aβ peptide on a model membrane have been investigated in Chapter 6. The result has been repeated in presence of Hsp60, revealing its protective function in the protein-membrane interaction.
In the appendix A, the formation of a nanocarrier system has been characterized, in the perspective of a potential use in the therapy of different pathologies like can-

cer and Alzheimer's disease. In appendix B, the theory of SAS technique has been reported.

Candidate's bibliography

- Angelo Spinello, Maria Grazia Ortore, Francesco Spinozzi, Caterina Ricci, Giampaolo Barone, Antonella Marino Gammazza, and Antonio Palumbo Piccionello. *Quaternary structures of GroEL and naïve Hsp60 chaperonins in solution: a combined SAXS-MD study.* RSC Advances, 5:49871-49879, 2015.

- Caterina Ricci, Maria Grazia Ortore, Silvia Vilasi, Rita Carrotta, Maria Rosalia Mangione, Donatella Bulone, Fabio Librizzi, Francesco Spinozzi, Giosalba Burgio, Heinz Amenitsch, and Pier Luigi San Biagio. *Stability and disassembly properties of human naïve Hsp60 and bacterial GroEL chaperonins.* Biophysical Chemistry, 208:68-75, 2016.

- Caterina Ricci, Francesco Spinozzi, Paolo Mariani, and Maria Grazia Ortore. *Protein amyloidogenesis investigated by small angle scattering.* Current pharmaceutical design, 22(26):3937-3949, 2016.

- Antonella Battisti, Antonio Palumbo Piccionello, Antonella Sgarbossa, Silvia Vilasi, Caterina Ricci, Francesco Ghetti, Francesco Spinozzi, Antonella Marino Gammazza, Valentina Giacalone, Annamaria Martorana, Antonino Lauria, Claudio Ferrero, Donatella Bulone, Maria Rosalia Mangione, Pier Luigi San Biagio and Maria Grazia Ortore. *Curcumin-like compounds designed to modify amyloid beta peptide aggregation patterns.* RSC Advances, 7(50):31714-31724, 2017.

- Caterina Ricci, Rita Carrotta, Giacoma Cinzia Rappa, Maria Rosalia Mangione, Fabio Librizzi, Pier Luigi San Biagio, Heinz Amenitsch, Maria Grazia Ortore, and Silvia Vilasi. *Investigation on different chemical stability of mitochondrial Hsp60 and its precursor.* Biophysical chemistry, 229:31-38, 2017.

Chapter 1

Small Angle Scattering: theory and applications

Contents

1.1 Introduction

Small Angle Scattering (SAS) is a fundamental tool in the study of biological macromolecules. The major advantage of the method lies in its ability to provide structural information about partially or completely disordered systems with a resolution from about one up to hundreds of nanometers. SAS allows one to study the structure of native particles in near physiological environments and to analyze structural changes in response to variations in external conditions. Given its sensitivity, it is an appropriate technique in the structural study of polymers, in solution or not, of colloids in general, of nanocomposites and porous materials for biological purposes.
Scattering techniques can be used regardless of any manipulation of the sample under examination: this possibility avoids procedures such as solvent removal, freezing or the production of thin sections that often alter the sample leading to the formation of artifacts. Unlike an image in direct space, the result of a scattering experiment contains a statistically significant overall mean of the structure present in the investigated sample: with a single measure it is possible to access to an information with a statistical relevance that is difficult to reach by any means with direct microscopy.
In general, in a scattering experiment, a suitable probe (photons or neutrons) of wavelength λ is collimated on the sample (see Fig. 1.1). The interaction is dependent on the chosen probe, that can be visible light (Small Angle Light Scattering, SALS), X-rays (Small Angle X-ray Scattering, SAXS) or neutrons (Small Angle Neutron Scattering, SANS). However, regardless of the kind of probe, the incident

radiation will be transmitted, absorbed and diffused: while the transmitted radiation is blocked by an absorber (beam stop) before reaching the detector the diffused radiation is revealed through a detector that is usually mono- or two-dimensional (see Fig. 1.1, right).

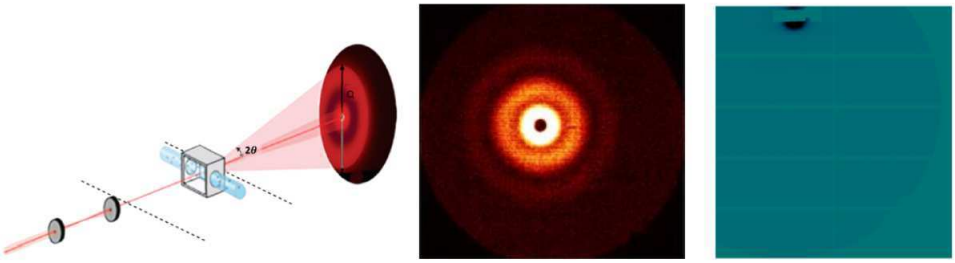

Figure 1.1: Left: Schematic representation of SAS experiment: the sample is illuminated by X-rays and the scattered radiation is registered by the detector. Right: Example of SAXS scattering pattern, from [1] and of BSA as recorded by the two dimensional detector Pilatus 1M at Elettra synchrotron, Trieste.

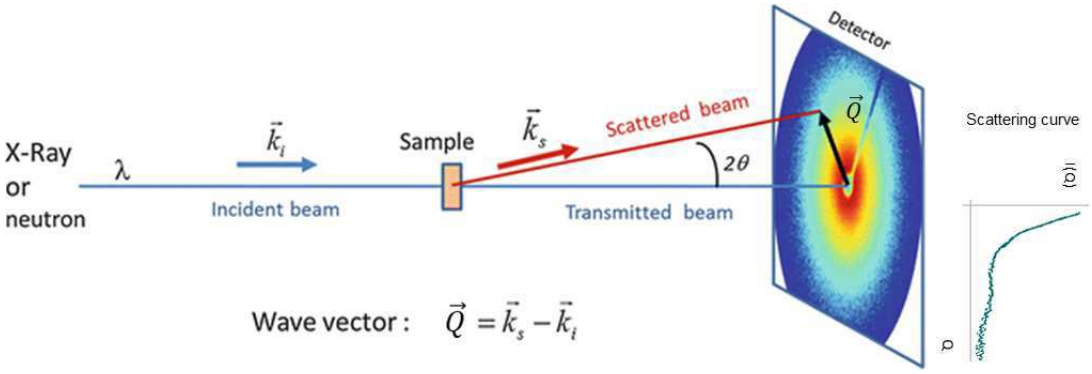

Figure 1.2: Schematic representation of SAXS experiment: the incident wave characterized by a wave vector k_i impacts on the sample, and is scattered with k_f. The detector records the bi-dimensional scattered pattern. The radial average of this pattern gives the signal in function of 2θ and hence Q. Adapted from [2].

If the scattering is isotropic, the two-dimensional image can be reduced, through a radial average, to a one-dimensional curve called a scattering curve or scattering intensity, $I(Q)$ reported as a function of the scattering vector, Q (see Figure 1.2), defined as the difference between the wave vector of scattered radiation, $\mathbf{k_s}$ and that of the incident wave, $\mathbf{k_i}$. In the case of the interaction between X-rays and matter, each atom illuminated in the sample by the incident plane wave will become a

scattering center that generates a spherical wave. The intensity that reaches the detector is given by the constructive and destructive interference resulting from the coherently emitted waves from the atoms present in the sample and contains structural informations. $I(Q)$ is the dependent variable of the scattering experiment: it contains information on the size, shape and the interaction between the scattering centers present in the sample. In fact the measured scattering intensity is linked to the spherically averaged Fourier transform of the autocorrelation of the electron density of the particle and to a factor depending on the distribution of the particle in solution, namely the form factor.
A complete discussion of the Small Angle Scattering theory, with focus on SANS and SAXS, is reported in appendix B. In the following, instead, the experimental procedures and approximations that will be exploited in this thesis are summarized.

1.2 SAXS experimental analysis

1.2.1 Experimental procedure

The experimental scattered intensity from a determinate sample can be written as:

$$I(Q) = KN_P V_P^2 (\Delta\rho)^2 P(Q) S(Q) + B \tag{1.1}$$

where K depends on the specific variables of the instrument (incident flow, efficiency of the detector), N_P is the numerical density of the particles that scatter the probe, V_P the volume of the single particle, $\Delta\rho$ (contrast of the experiment) quantifies the difference between probe and particle interaction with respect to probe-to-medium interaction continuous, $P(Q)$ is the form factor, $S(Q)$ is the structure factor, Q is the scattering vector and B is a linear background dependent on different contributions such as instrumental noise.
Through simple geometric considerations it can be shown that:

$$Q = |k_s - k_i| = \frac{4\pi n}{\lambda} sin(\theta) \tag{1.2}$$

where n is the index of refraction of the sample (approximate to the unit in the case of neutrons e X-ray) and λ is the wavelength of the probe used. The Bragg equation ($\lambda = 2dsin\theta$), together with Equation 1.2 yields $Q = 2\pi/d$, where d is the characteristic distance sampled by the chosen scattering vector, allowing to obtain informations on the dimensions accessible to the experiment once the probe wavelength and the angles sampled by the detector are fixed. At the same time, it defines the maximum and minimum dimensions detectable from scattering experiment. For example, in the case of a laboratory SAXS instrument which uses the X emission of copper (Cu Kα = 1.542 Å), if the sample-detector distance is about 30 cm, the range of Q is 0.01-0.5 Å^{-1} corresponding to size in real space from 1 to 60 nm approximately. In the case of a SANS instrument present in research infrastructures using neutrons from 1 to 10 Å, for sample detector distances from 1 to 20 m, the interval of Q varies from 0.001 to 0.5 Å^{-1} corresponding to size sampled from 1 to

600 nm approximately.
In a scattering experiment, the resolution is defined as $\Delta R = \pi/Q_{max}$, the minimum discriminable dimension, where Q_{max} is nothing but the maximum value of Q accessible. If $Q_{max} = 0.5$ Å^{-1} it is easy to calculate that ΔR is about 6 Å. In other words, small angle scattering techniques can be considered as experimental methods where no interatomic distances are sampled, as in the case of high-angle diffraction.

The experimental curve obtained on a pratical session is connected to the scattering cross section by:

$$\frac{d\Sigma}{d\Omega}(Q) = \frac{I(Q)}{\Phi S \varepsilon(\lambda) t D T(\frac{2\pi R \Delta R}{d^2})} \tag{1.3}$$

where $I(Q)$ in the number of photons detected, Φ is the incident flux, A is the incident surface, $\varepsilon(\lambda)$ is the efficiency of the detector, that depends on λ incident, t is the time of the measurement, D the thickness of the sample and T is the transmission:

$$T = \frac{I_1}{I_0} \tag{1.4}$$

where I_1 is the transmitted intensity while I_0 the incident intensity. Since samples absorb different fractions of radiation and this fraction does not contribute to the scattering effect, the degree of absorption of a particular energy of radiation needs to be determined for each sample, and this needs to be corrected for [3]. The measure of the transmission factor of a sample can be obtained analyzing the beam flux of the x-ray beam before and after the sample has been inserted. This can be realized by some detectors after attenuation of the primary beam (to avoid damaging the detector), by means of a beamstop-mounted photodiode, or by insertion of a strongly scattering material behind the sample position. An alternative way is to determine the transmission factor using a ionization chamber before (upstream) and behind (downstream of) the sample through the ratio of the two ion chambers before and after insertion of the sample. A large number of detector- and geometry-specific variables can be corrected for by performing an absolute intensity calibration. To obtain an absolute datum, i.e. a $d\Sigma/d\Omega$ expressed in units of cm^{-1}, the number of sample counts can be compared with an effective measure set on a standard material, which provides the I_{std} intensity, whose section of impact for $Q = 0$ is known.The expression of the scattering cross section in absolute units ($d\Sigma/d\Omega(Q)|_{abs}$) can be thus obtained, considering Equation 1.3:

$$\left.\frac{d\Sigma}{d\Omega}(Q)\right|_{abs} = \frac{I(Q)_{samp}}{I(Q=0)_{std}} \frac{D_{std}}{D_{samp}} \frac{T_{std}}{T_{tot}} \left.\frac{d\Sigma}{d\Omega}(Q=0)\right|_{std} \tag{1.5}$$

Furthermore, the scattering intensity has to be corrected for the spurious contribution of solvent, capillary, air for to prevent misanalysis of the data. In the expected experiments the concentration of sample is less than 1% by weight of the solution, therefore if the concentration of solvent is approximated as unitary ($C_b \simeq 1$). In this approximation, taking into account the contributions of the empty cell, of the

buffer, of the particles in solution and of the background B, I_p, i.e. the scattered intensity from the sample can be written as:

$$I_p = (I_p^m - B) - \frac{T_{tot}}{T_{b+c}}(I_b^m - B) \tag{1.6}$$

where I_p^m is the measured scattering intensity of the particles in solution, I_b^m the measured scattering intensity of the buffer, $T_{b+c} = T_b T_c$ the transmission of buffer and empty cell and T_{tot} the overall transmission. Therefore, to obtain the intensity diffused exclusively by the suspended sample in solution, only the additional measures of background B and of the cell holder filled with solvent in which the sample will be suspended must be performed. The procedure described here, which allows to arrive at the determination of the contribution of the sample only to the scattering spectrum, is usually defined as data reduction. Considering the relative transmission as unitary, $T_{tot} \simeq T_{b+c}$:

$$I_p = (I_p^m - B) - (I_b^m - B) = I_p^m - I_b^m \tag{1.7}$$

1.2.2 Data treatment

In this section, an overview of the principal approximation and methods used in the thesis will be presented. The theoretical basis of this section refers to appendix B.

1.2.2.1 Guinier approximation

The Guinier approximation starts from the expression of the form factor in terms of Taylor expansion with isotropy conditions:

$$\begin{aligned} <F^2(\mathbf{Q})>_{\omega_Q} &= \frac{1}{4\pi}\int d\omega_Q \,\frac{1}{f^2}\int_{V_P}\int_{V_P} d\mathbf{r}_1 d\mathbf{r}_2 \,\delta\rho(\mathbf{r}_1)\delta\rho(\mathbf{r}_2)\, e^{i\mathbf{Q}\cdot(\mathbf{r}_2-\mathbf{r}_1)} \\ &= \frac{1}{f^2}\int_{V_P}\int_{V_P} d\mathbf{r}_1 d\mathbf{r}_2 \,\delta\rho(\mathbf{r}_1)\delta\rho(\mathbf{r}_2)\frac{1}{4\pi}\int d\omega_Q \; e^{i\mathbf{Q}\cdot(\mathbf{r}_2-\mathbf{r}_1)} \\ &= \frac{1}{f^2}\int_{V_P}\int_{V_P} d\mathbf{r}_1 d\mathbf{r}_2 \,\delta\rho(\mathbf{r}_1)\delta\rho(\mathbf{r}_2)\frac{\sin\left(Q|\mathbf{r}_2-\mathbf{r}_1|\right)}{Q|\mathbf{r}_2-\mathbf{r}_1|}. \end{aligned} \tag{1.8}$$

Considering the Taylor series of $\frac{\sin x}{x}$ truncated at the second order, and the origin of the axis in the center of mass of the particle so that $\int_{V_P} d\mathbf{r}\,\delta\rho(\mathbf{r})\,r_\alpha = 0$ with $\alpha = x, y, z$, we obtain:

$$<F^2(\mathbf{Q})>_{\omega_Q} \;=\; 1 - \frac{Q^2}{3f}\int_{V_P} d\mathbf{r}\, r^2\,\delta\rho(\mathbf{r}) + \ldots \tag{1.9}$$

And define the gyration radius R_g in respect to the electronic center of mass and to the electronic density fluctuations $\delta\rho(r)$:

$$R_g^2 \;=\; \frac{\int_{V_P} d\mathbf{r}\, r^2\,\delta\rho(\mathbf{r})}{\int_{V_P} d\mathbf{r}\,\delta\rho(\mathbf{r})} \tag{1.10}$$

$$< F^2(\mathbf{Q}) >_{\omega Q} = 1 - \frac{Q^2 R_g^2}{3} + \dots \quad (1.11)$$

$$\approx \exp\left(-\frac{Q^2 R_g^2}{3}\right) \quad (1.12)$$

The radius of gyration represents the effective size of the scattering "particle" whether it is a polymer chain, part of a protein, a micelle, or a domain in a multiphase system. The usefulness of this plot stems from the fact that the obtained particle "size" R_g is independent of the absolute intensity I_0 and of any model. Instrumental smearing as well as polydispersity and multiple scattering appear to decrease the effective Rg. Inter-particle effects also contribute to R_g except at the infinite dilution limit (case of an isolated particle). This relationship loses validity at increasing Q values. It can be shown that Guinier's law is valid if we are in a range of exchanged wave vectors such that $QR_g < 1.3$. The gyration radius of the particle can be directly associated with the geometrical characteristics of the particle. For example, for a sphere of radius R, $R = R_g\sqrt{\frac{5}{3}}$, for an ellipsoid of semi-axes A, B and C instead ${R_g}^2 = 1/5(A^2 + B^2 + C^2)$ and for other regular geometric shapes it is possible to determine a relation between the turning radius and their characteristic parameters.

1.2.2.2 The Guinier plot for elongated objects

The Guinier plot is modified when the scattering objects are elongated [4, 5]. The two dimensional analogous of the gyration radius is the cross-section radius

$$R_c^2 = \frac{\int_0^\infty P_c(r) r^2 dr}{2\int_0^\infty P_c(r) dr} \quad (1.13)$$

where $P(r)$ is the distance distribution function and for the intermediate Q cross section

$$I(Q) = \frac{I(0)}{Q} e^{-\frac{Q^2 R_c^2}{2}} \quad (1.14)$$

For a cylinder, the radius R can be obtained by $R = R_c\sqrt{(2)}$. Similarly for a lamella (flat object) of thickness T, the gyration radius of the lamella is

$$R_t^2 = \frac{\int_0^\infty P_t(r) r^2 dr}{2\int_0^\infty P_t(r) dr} \quad (1.15)$$

and the intermediate-Q Guinier approximation becomes:

$$I(Q) = \frac{I(0)}{Q^2} e^{-Q^2 R_t^2} \quad (1.16)$$

where $R_t^2 = \frac{T^2}{12}$.

1.2.2.3 Porod approximation and P(r) distribution function

Consider the expression for the form factor relative to a scattering particle:

$$< F^2(\mathbf{Q}) >_{\omega_Q} = P(\mathbf{Q}) = \int_0^\infty dr\, P(r)\, \frac{\sin Qr}{Qr}, \tag{1.17}$$

where the pair distribution function $P(r)$ is:

$$P(r) = \frac{2r}{\pi} \int_0^\infty dQ\, P(Q)\, Q\, \sin Qr \tag{1.18}$$

and is normalized to unit $\int_0^\infty dr\, P(r) = 1$. In order to determine the physical significance of $P(r)$, let us start from the Eq. (1.8) by making the substitution $\mathbf{r} = \mathbf{r}_2 - \mathbf{r}_1$

$$\begin{aligned} P(Q) &= \frac{1}{f^2} \int_{V_P} \int_{V_P} d\mathbf{r}_1 d\mathbf{r}\, \delta\rho(\mathbf{r}_1)\delta\rho(\mathbf{r}_1+\mathbf{r}) \frac{\sin(Qr)}{Qr} \\ &= \int_0^\infty dr \frac{\sin(Qr)}{Qr} r^2 \frac{1}{f^2} \int_{V_P} d\mathbf{r}_1 d\omega_r\, \delta\rho(\mathbf{r}_1)\delta\rho(\mathbf{r}_1+\mathbf{r}) \\ &= \int_0^\infty dr \frac{\sin(Qr)}{Qr} \left\{ 4\pi r^2 \frac{1}{f^2} \left\langle \int_{V_P} d\mathbf{r}_1\, \delta\rho(\mathbf{r}_1)\delta\rho(\mathbf{r}_1+\mathbf{r}) \right\rangle_{\omega_r} \right\}. \end{aligned} \tag{1.19}$$

By comparing this result with the Eq. (1.17), the term $\{\dots\}$ results to be the $P(r)$,

$$P(r) = 4\pi r^2 \frac{1}{f^2} \left\langle \int_{V_P} d\mathbf{r}_1\, \delta\rho(\mathbf{r}_1)\delta\rho(\mathbf{r}_1+\mathbf{r}) \right\rangle_{\omega_r}. \tag{1.20}$$

Thus, the $P(r)$ is connected with the orientational average of the autocorrelation function of the particle contrast $\delta\rho(\mathbf{r})$. The $P(r)$ function can be used to calculate the radius of gyration. By entering in the Eq. (1.17) the expansion

$$\frac{\sin x}{x} = 1 - \frac{x^2}{6} + \frac{x^4}{120} + \dots \tag{1.21}$$

it can be written:

$$\begin{aligned} P(Q) &= \int_0^\infty dr\, P(r) \left\{ 1 - \frac{Q^2 r^2}{6} + \dots \right\} \\ &= 1 - \frac{Q^2}{6} \int_0^\infty dr\, r^2\, p(r) + \dots \end{aligned} \tag{1.22}$$

that, by comparing with Eq. (1.11), yields to

$$R_g^2 = \frac{1}{2} \int_0^\infty dr\, r^2\, p(r) \tag{1.23}$$

Let we consider the case of a particle with constant contrast $\Delta\rho$. The function $\delta\rho(\mathbf{r})$ can be written as $\Delta\rho s(\mathbf{r})$, where $s(\mathbf{r})$ is a function describing position and

shape of the particle which is one if the point $\mathbf{r}$ is into the particle and zero otherwise. By substituting, the Eq. (1.20) transforms to

$$P(r) = 4\pi r^2 \frac{1}{V_P^2} \int_{V_P} d\mathbf{r}_1 < s(\mathbf{r}_1 + \mathbf{r}) >_{\omega_r} . \tag{1.24}$$

This result shows that, for particle with constant contrast, the $P(r)$ is the distance distribution function which represents the probability density to find a vector having the first end in the particle point $\mathbf{r}_1$ and the second end again in the particle at distance r from $\mathbf{r}_1$.

If we develop the integral in the equation 1.24 considering separately the particle (core) and the volume of an internal shell of thickness r (which we call shell):

$$\begin{aligned} \int_{V_P} d\mathbf{r}_1 < s(\mathbf{r}_1 + \mathbf{r}) >_{\omega_r} &= \int_{\text{core}} d\mathbf{r}_1 < s(\mathbf{r}_1 + \mathbf{r}) >_{\omega_r} \\ &+ \int_{\text{shell}} d\mathbf{r}_1 < s(\mathbf{r}_1 + \mathbf{r}) >_{\omega_r}, \end{aligned} \tag{1.25}$$

The expression $< s(\mathbf{r}_1 + \mathbf{r}) >_{\omega_r} = \frac{1}{4\pi} \int d\omega_r s(\mathbf{r}_1 + \mathbf{r})$ represent the solid angle fraction from which $\mathbf{r}_1$ is linked to the particle at distance r. The core integral $< s(\mathbf{r}_1 + \mathbf{r}) >_{\omega_r}$ on $\mathbf{r}_1$ is 1, so $V_P - S_P r$. For the internal shell:

$$\int_{\text{shell}} d\mathbf{r}_1 < s(\mathbf{r}_1 + \mathbf{r}) >_{\omega_r} = S_P \int_0^r dx \ < s(x + \mathbf{r}) >_{\omega_r}, \tag{1.26}$$

where S_P is the surface of the particle and x the depth of the surface. Considering the integral on the solid angle:

$$\int_{V_P} d\mathbf{r}_1 < s(\mathbf{r}_1 + \mathbf{r}) >_{\omega_r} = V_P - S_P r + \frac{3}{4} S_P r = V_P (1 - \frac{S_P r}{4V_P}). \tag{1.27}$$

and $P(r)$ is:

$$P(r) = \frac{4\pi r^2}{V_P} \left(1 - \frac{S_P r}{4V_P} \right) + \ldots \tag{1.28}$$

that, inserted in the form factor expression, in function of r_{max}, that is the r value for which $P(r) = 0$:

$$\begin{aligned} P(Q) &= \frac{2\pi S_P}{Q^4 V_P^2} + \frac{A(Q r_{max})}{Q^3 V_P^2} \sin(Q r_{max}) \\ &+ \frac{B(Q r_{max})}{Q^3 V_P^2} \cos(Q r_{max}) + \ldots \qquad \text{for high } Q \text{ values.} \end{aligned} \tag{1.29}$$

The $P(Q)$ trend can be approximated by the Porod law:

$$P(Q) \approx \frac{2\pi S_P}{Q^4 V_P^2}. \tag{1.30}$$

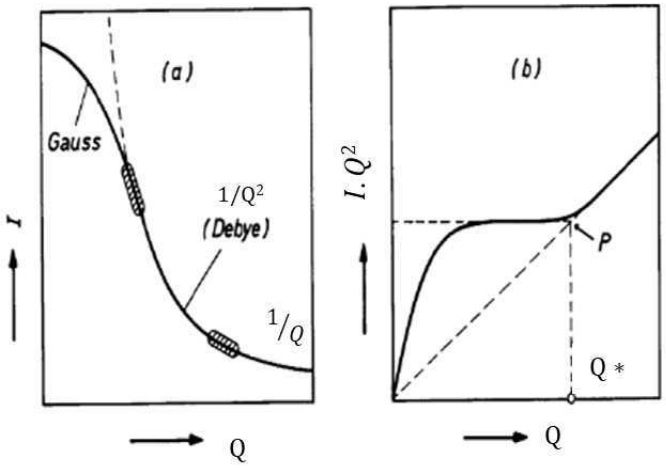

Figure 1.3: Schematic drawing of the scattering curve of a Gaussian coiled chain molecule, from [6].

1.2.2.4 Kratky plot

In the field of biological macromolecules one is usually concerned with omodisperse solutions of molecules with identical shape whose structures does not change with time. The Kratky plot, $I(Q) \cdot Q^2$ versus the Q plot, is a useful expression for the scattering profile to describe the structural characteristics of a chain molecule, and, consequently, is often used in polymer science [6]. The scattering curve of a chain is composed by three regions: a gaussian part at very low Q that is due to the overall shape of the globular particle, an intermediate $\frac{1}{Q^2}$ region operating from larger subsections of the molecule which can be visualized as random arrangements of chain elements. The outermost part of the curve will therefore have the shape of the scattering curve of a needle i.e $I \simeq \frac{1}{Q}$ if the chain is unfolded. Representing $I \cdot Q^2$ vs Q, the Gaussian region drops towards zero at $Q = 0$, the $1/Q$ tail end follows an ascending line the extension of which to the left passes through the origin (see Fig1.3). On the other hand, the scattering profile from a globular protein in the high Q values obeys Porod's law, that is, Q^{-4}. In this case, the Kratky plot should have a peak, and the peak position should depend on R_g. For protein solution, a peak in a Kratky plot indicates a compact globular structure, and the absence of a peak is an indication of a loss of compactness or globularity [7].

1.2.2.5 Genfit

Genfit is an open-source software developed in the research group of Molecular Biophysics in the Polytechnic University of Marche for the analysis of data obtained from small angle scattering (SAS) experiments of X-ray (SAXS) or neutron (SANS)[8], that will be widely used in this thesis. The program is written in Fortran and in input reads mono-dimensional scattering curves, that can be fitted a series of models. More than 50 models are available in the software, from simple asymptotic

behaviors to geometric or geometrical form factors of entire atomic structures. Some models provide both the presence of form factors and the presence of structural factors that take into account the interactions between the particles in solution. The parameters of each model can be linked to the chemical-physical conditions of the experiment by means of link functions which can be defined from time to time by the user thus changing the temperature, pressure, concentration, pH, ionic strength in the most suitable way for that specific fit. Thanks to these characteristics it is also possible to generate SAS theoretical curves based on these models or on the knowledge of the behavior of the species in solution with the aim of predicting the best experimental conditions to be explored in a future SAS experiment. The input SAS curve represents the macroscopic differential cross section, referred to as $I_{exp}(Q)$. Genfit minimize the χ^2 function analyzing one or several (global fit) SAS curves at the same time:

$$\chi^2 = \frac{1}{N_c} \sum_{c=1}^{N_c} \frac{1}{N_c} \sum_{i=1}^{N_{Q,c}} \left\{ \frac{I_{exp,c}(Q_i) - \hat{I}_c(Q_i)}{\sigma_c(Q_i)} \right\}^2 \tag{1.31}$$

where N_c is the number of SAS curves, $N_{Q,c}$ the number of Q points of the curve c and $\hat{I}_c(Q_i)$ is the model SAS curve determined from Genfit, σ_c is the standard deviation of the c curve. To take account of the presence of a possible background or some correction factors the model SAS curve is written as

$$\hat{I}_c(Q) = k_c I_c(Q) + B_c \tag{1.32}$$

I_c being the model SAS curve in absolute units, k_c the scaling factor and B the background. Generally speaking the model SAS curve can be written as a linear combination of M_c models

$$I_c(Q) = \sum_{m=1}^{M_c} w_{c,m} I_{c,m}(Q) \tag{1.33}$$

where $w_{c,m}$ is the weight of the m-th model, $I_{c,m}(Q)$ the curve determined for that model. Every model depends on different parameters that are obtained by the χ^2 minimization. The fitting parameters can be related to sample structural features, such us dimensions, shape, and scattering density. By means of the flags within the program it is possible to decide whether to fit or to keep them fixed. At the end of the calculation, Genfit generates different output files among which we find the best curve that represents the fit, the parameter file, the distribution function of polydisperse systems and Fourier transforms. The details of the principally used models will be illustrated in the following sections.

Models

Worm like model The unfolded or intrinsically disordered state of the protein monomer was described by statistical chains, such as the so-called worm-like model, based on the Kratky-Porod statistics. The corresponding form factor $P_{wlk}(Q)$, which

includes the effect of excluded volume, has been obtained by Pedersen and Schurtenberger through Montecarlo simulations, whose results have been given in terms of numerical approximations. $P_{wlk}(Q)$ is multiplied by a two-density level cylindrical cross section [9]. The unfolding protein form factor thus results:

$$P_{unf}(Q) = (2\pi L)^2 P_{wlk}(Q) \left[(\rho_s - \rho_0)(R_c + \delta)^2 \frac{J_1\left[q(R_c+\delta)\right]}{Q(R_c+\delta)} + (\rho_1 - \rho_s) R_c^2 \frac{J_1(QR_c)}{QR_c} \right]^2 \tag{1.34}$$

where L is the contour length of the chain, representative of the its extended length, R_c is the inner radius of the cross section that represents the mean half of the thickness of the protein chain, δ is the thickness of the solvation layer and $J_1(x)$ is the first order Bessel function. The parameters ρ_1, ρ_s and ρ_0 are the scattering length densities of the dry protein, of the hydration layer and of the bulk solvent, respectively. The worm-like form factor $P_{wlk}(Q)$ depends on L and on the statistical segment (Kuhn) length b, the average separation between two subsequent segments. The number of segments is simply given by the ratio $n_b = L/b$.

Cylinders The shape of early protofibrils, representing the first fibrillation states, and of the fibril-like aggregates, were described starting from cylinders form factor. The form factor of a cylinder is written as:

$$P_{cyl}(Q) = (2\pi R_{cyl}^2 H_{cyl})^2 (\rho_{cyl} - \rho_0)^2 \int_0^{\frac{\pi}{2}} d\beta sin\beta \left\{ \frac{sin\left(\frac{1}{2} Q H_{cyl} cos\beta\right)}{\frac{1}{2} Q H_{cyl} cos\beta} \frac{J_1(QR_{cyl} sin\beta)}{QR_{cyl} sin\beta} \right\}^2 \tag{1.35}$$

where R_{cyl} and H_{cyl} are the cylinder radius and length. The average scattering length density of the cylinder, ρ_{cyl} , is fixed to the average electron density of a protein, and the monomer aggregation number, N_{cyl}, is calculated from $N_{cyl} = \pi R_{cyl}^2 H_{cyl}/V_1$.

Bigger aggregates The fourth protein state (sph) is described by unspecific protein aggregates, which could reach very large dimensions. The signature of their presence is the asymptotic behavior at the lowest Q-values of the scattering curve, which could be interpreted by the tail of the form factor of large spherical shapes, well described by the Porod law,

$$P_{\rm sph}(Q) \quad = \quad \frac{2\pi\sigma_{\rm sph}}{Q^4} N_{\rm sph} V_1 (\rho_{\rm sph} - \rho_0)(\rho_1 - \rho_0) \tag{1.36}$$

where $\sigma_{\rm sph}$ is the surface-to-volume ratio of the spherical aggregates and $\rho_{\rm sph}$ is its average uniform scattering length density. To note, this law does not allow to get the aggregation number $N_{\rm sph}$. However, the fraction of dry protein in the aggregate can be easily determined by $\phi_{\rm sph} = \frac{\rho_{\rm sph} - \rho_0}{\rho_1 - \rho_0}$.

Form factor from a PDB structure To analyse SAXS curves with different models, it has often been considered the macroscopic differential scattering cross

section as a combination of the form factors corresponding to different states involved:

$$\frac{d\Sigma}{d\Omega}(Q) = \frac{cN_A}{M_1}\left[x_1 P_1(Q) + \frac{x_2}{N_2}P_2(Q) + ...\right] \tag{1.37}$$

where c is the protein mass concentration, N_A is Avogadro's number, M_1 is the monomer molecular weight, x_i is the fraction of monomers involved in the formation of the i-species, $P_i(Q)$ its form factor and N_i is the aggregation number of that species (which is 1 for unfolded monomers). The structure factor $S(Q)$ was approximated to unity due to the low protein concentration of the experiment.

SASMOL

Several models included in GENFIT are able to calculate the form factors of atomic structures on the basis of Protein Data Bank (PDB) files, taking into account the contribution of the solvation shell around the macromolecule. Some models are based on the SASMOL method [10, 11], which uses the spherical harmonic expansion of the scattering amplitudes, similar to the widely known CRYSOL software [12]. The main idea of SASMOL is to embed the macromolecule in a "tetrahedrical close-packed" lattice and assign the lattice positions in contact with the atoms of the macromolecule to hydration molecules. In this way, the scattering contribution of water molecules inside cavities or grooves is taken into account. For each of the PDB-based models, the GUI provides a facility where the user can load the PDB files [8].

1.3 Applications in the biological field for the characterization of proteins

Small-angle scattering have proved to be versatile techniques for the structural characterization of biological macromolecules [13]. Recent advances have made it possible to obtain accurate data in a relatively short time, thus permitting time-resolved studies [14]. The assessment of scattering curves can be obtained under low-contrast solvent conditions and in a wide region, leading to the possibility to investigate even complex objects like viruses [15, 16]. These developments have led to a breakthrough in the application of these techniques to the study of protein folding, enabling equilibrium and kinetic investigations [17, 18].
Since these techniques allow to approximately reproduce the physiological conditions in which the protein is, they can provide low resolution information on the tertiary and quaternary structure of proteins [19] and allow to study the intermediate structures from a polypeptide chain during its folding process. By SAS it is possible to characterize the process of folding/unfolding [20, 21], the conformational changes occurring after or during the activation of a certain process, the interactions with other molecules [22], and even the density of the hydration water [23].
Considering that the derivation of a more detailed and refined structure of the particles subjected to SAS measurements is rather complicated, the coupled use of complementary approaches has proved to be a powerful tool in the biological field. In particular, the potential benefits of combining SAXS and MD simulations were recently reviewed [24], with a focus on the development of algorithms able to refine protein structures in solution from SAXS data, based on restrained Molecular Dynamics (MD) results [25]. Another successful experimental match is between SAXS/SANS and NMR [26], while the combination of SAS data with experimental data from other techniques like electron and/or atomic force microscopy or fluorescence based techniques (as single-molecule FRET) is promising, too.
It is clear that SAS can be considered a very convenient technique to study protein fibrillation and the effects of inhibitors. SAS investigations have been extensively studied concerning the two most studied cases of proteins leading to fibrils: amyloid β peptide and α-synuclein [27, 28, 29, 30]. In most cases, model-free approaches demonstrate to be able to provide essential information.

Chapter 2

Amyloidogenic proteins

Contents

2.1 Introduction

Proteins, in unaltered conditions, are known to assume a well-defined three-dimensional conformation (folding), linked to the aminoacidic disposition, which constitutes its biologically active state. However, polypeptide chains can adopt a multitude of conformational states depending on surrounding conditions (pH, temperature, chemical agents), some of which may be thermodynamically more stable than the native conformation itself.
Protein misfolding disorders are usually caused by peptides that, characterized by a certain degree of meta-stability, create in particular conditions a population capable of giving rise to cytotoxic aggregates [31, 32]. The molecular mechanisms underlying this kind of aggregation and the cytotoxic rising effect are to date topics of fundamental importance in the context of multidisciplinary sectors, ranging between biology, medicine, chemistry and physics.
In the followings of this section, a brief preface on the state of the art for the proteins studied will be presented. Starting from the definition of intrinsically disordered proteins (IDPs, [33]) the two main proteins analyzed in this PhD thesis will be introduced: Aβ peptide and α-synuclein. These two proteins, that share the lack of a fixed three-dimensional structure, are both connected with neurodegenerative disorders, respectively Alzheimer's and Parkinson's diseases. It is wildely accepted that the formation of off-pathway fibrillar aggregates, compose the trigger of the entire pathological phenomena [34]. The current hypothesis regarding the

beginning of the neuropathology is focused on the role of small oligomers, which are considered more toxic than the monomers or than the mature insoluble amyloid fibrils [35, 36, 37]. The transient nature of the intermediate oligomers is equally challenging for the characterization of the toxic potential of these species, and thus a number of differently sized oligomers have been suggested as the cause of the diseases. This is why this issue remains on the agenda in the biophysical debate even if many efforts have been produced to elucidate the role of the separate species.
In the subsequent sections a preliminary characterization of Aβ peptide, in the two alloforms Aβ_{1-40} and Aβ_{1-42}, and α-synuclein will be presented, mainly by means of SAXS technique, but with the aid of microscopy and AFM techinques. The characteristics of two amyloidogenic proteins are presented in comparison with model proteins, that can gain an amyloid status if subjected to appropriate experimental conditions [38]. The proteins have been investigated in their native conformation and after the fibrillation protocol, to describe the final states of the processes.
The results are in good agreement with basic and recent literature [39, 40, 11] and, for the fibrillated state, with each others, confirming the similarity of the fibril structure regardless the native conformation of the protein. SAXS curve of Aβ_{1-40} monomer has never been observed, at my knowledge, however it results in good agreement with the recent SANS result of Zhang-Haagen *et al.* [41].
This discussion is presented here both as a portray of the characters of this work and to underlie the possible changes resulting from the interaction of the amyloidogenic proteins with biological as well as with chemical inhibitors, that will be presented in the following chapters.

2.1.1 Intrinsically disordered proteins

Knowledge about the proteins' function has always been correlated with the knowledge of the structure. It is in fact known that in well-defined proteins a well-defined tertiary structure has a fundamental role to allow them to carry out their biological function. This concept, over the years, has been validated by determining the crystallographic structure of numerous proteins and enzymes.
In recent decades, however, protein regions, which still perform a biological function, have been identified without any kind of well-defined tertiary structure [42, 33]. These segments can assume a defined structure following a link with a target molecule or they may never assume a defined tertiary arrangement, always remaining disordered [43]. The finding that a high percentage of proteins, encoded in the eukaryotic genome, is totally or partially disordered is the cause of a great change of perspective in structural and molecular biology. Indeed, numerous challenges aimed at a deeper understanding of the structural properties and the consequent functions of this new class of proteins, named Intrinsically Disordered Proteins or IDPs, have been undertaken [44, 45].
An intrinsically disordered protein (IDP) is thus a protein known to lack a fixed or ordered three-dimensional structure. IDPs cover a spectrum of states from fully unstructured to partially structured and include random coils, (pre-)molten glob-

ules, and large multi-domain proteins connected by flexible linkers. These proteins present numerous advantages in respect to well-defined globular ones: they have a greater interaction surface and a conformational flexibility that allows them to expose short parts of the polypeptide chain, making them able to interact with many other types of proteins and molecules. They also have several post-translational modifications that facilitate the adjustment of their functions and their stability within the cell, making them able to interact with their target with high specificity and low affinity [46].
Even if the major of the IDP proteins are non-pathological [47], in this set are highlighted two particular proteins linked to neurodegenerative diseases: the Aβ peptide, linked to Alzheimer's disease, and α-synuclein, linked to Parkinson's disease.

2.1.1.1 Alzheimer's disease and amyloid β peptide

Alzheimer's disease (AD) is a neurodegenerative disease characterized by the death of neurons in different areas of the cerebral cortex, resulting in loss of cognitive and behavioral function. It is the most common form of dementia, progressively disabling and with an onset that generally occurs in pre-senile age (over 65 years), although there are increasing cases of an insurgence at the age of 40 [49].

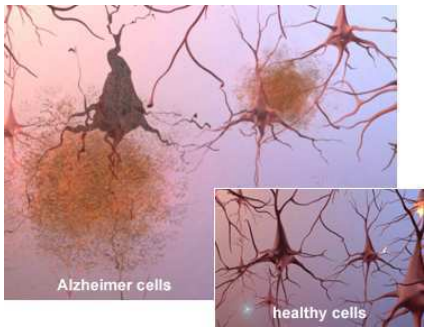

Figure 2.1: Sketch of healthy neuron cells vs Alzheimer's damaged cells, from [48].

One of the hallmarks of Alzheimer's disease is the formation of amyloid plaques and agglomeration of insoluble neurofibrillary clusters and tangles in the cell bodies of neurons [34]. A component of the tangles structures is the τ protein, a molecule involved in the development of various neurodegenerative diseases that have in common the degeneration of microtubules. Aβ is instead the constituent of the core region, consisting of fibrillar aggregates, of extracellular conformations, approximately spherical in shape and with a diameter between 50 and 200 μm, called amyloid plaques (neuritic or senile plaques), sketched in Fig. 2.1.
To explain the etiology and pathogenesis of Alzheimer's disease in 1992 the hypothesis of the amyloid cascade (see Fig. 2.2) has been proposed [50]. This hypothesis suggests that the mismetabolism of β-amyloid precursor protein is the initiating event in AD pathogenesis, subsequently leading to the aggregation of the β-amyloid protein. Formation of neuritic plaques instigates further pathological events, including the formation of the neurofibrillary tangles and disruption of synaptic connections, which lead to a reduction in neurotransmitters, death of tangle-bearing neurons and dementia. Thus, the formation of fibrillar aggregates, consisting of Aβ, composes, according to this theory, the trigger of the entire pathological phenomenon.
The Aβ monomer is a peptide of 38 - 42 residues and belongs to the intrinsically disordered protein family. It is normally produced and present in the brain and

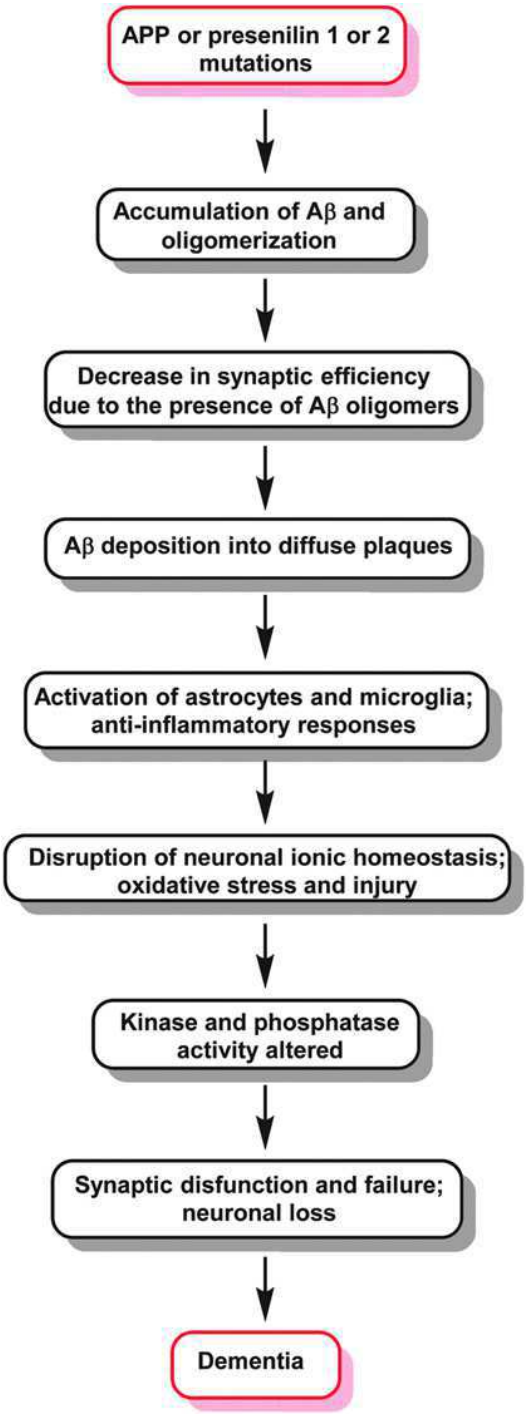

Figure 2.2: The amyloid cascade hypothesis [51], from [52].

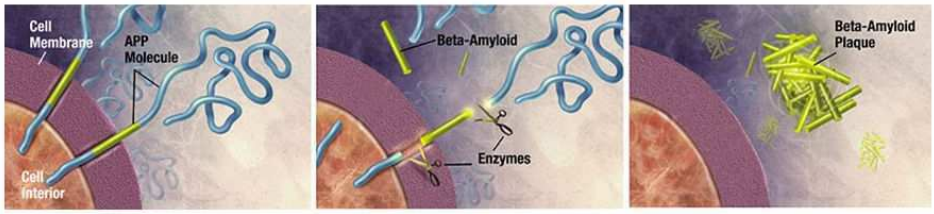

Figure 2.3: Enzymes action on APP that generates the Aβ peptide. From [53].

in the cefalorachidian liquor. The Aβ biosynthetic pathway provides for various reaction steps and involves the action of two proteases. The peptide is produced by proteolytic cutting starting from the Amyloid Precursor Protein (APP), an integral membrane protein of about 110 kDa expressed in many tissues and, more consistently, in neuronal cells at the synapse level. Its main function has not yet been fully clarified, but its implication in processes such as the regulation of synapse formation, neuronal plasticity and iron transport to the extracellular environment is known [54]. The fibrillation process of Aβ is considered to be related to changes in secondary structures leading to β-sheet formation, which proceeds via monomers aggregation into oligomers up to the formation of the mature amyloid fibers, according to different nucleation, elongation and fragmentation processes. Amyloid fibrils usually consist of 2-6 unbranched protofilaments, each about 2-5 nm in diameter, characterized by a cross-β spine, with β -strands perpendicular to the fibril axis and β-sheets along the length of the fibril [56], sketched in Fig. 2.4.
The current hypothesis regarding the triggering of the neuropathology is focused on the role of small Aβ oligomers, which are considered more toxic than the monomers or than the mature insoluble amyloid fibrils [57]. Nevertheless, the understanding of the molecular mechanisms leading to oligomers formation and to the onset of the pathology is still largely unknown, although different hypothesis have been prompted [35]. A proposed mechanism of fibrils formation depict the presence in the protein of a segment that can form a tightly complementary interface with an identical segment, which permits the formation of a steric zipper-two self-complementary β sheets that form the spine of an amyloid fibril [58].
Different experimental evidences assign to oligomers a central role in the development of diseases: they have been shown to interact with cell membranes, impairing their structural organization, destroying their selective ion permeability, leading to metabolic alterations (oxidative stress, Ca^{2+} homeostasis) that eventually culminate with neuronal cell death [59]. Binding of various amyloid oligomers with A11, an anti-amyloid oligomer conformation-specific antibody, revealed that, regardless of the primary protein structure, the amyloid oligomers present a generic conformation and suggested that the role of plasma membranes is critical for the toxicity of β-aggregation [60]. Recently, by studies in transgenic model mouse of Tg2676 of AD, it has been shown that lipid rafts constitute a site where Aβ oligomers might accumulate and cause toxicity in Alzheimer's disease [61, 62].

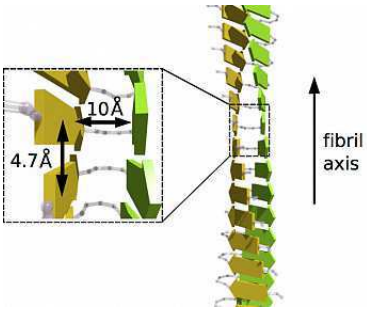

Figure 2.4: Figure 2: Scheme of the cross-β structure of a mature amyloid fibril. Each β-sheet is indicated by yellow or green color and shows a parallel alignment of the β-strands. From [55].

Aβ_{1-40} and Aβ_{1-42}: two distinct alloforms There are different alloforms of the Aβ peptide in tissues. The two principal alloforms found in amyloid plaques are 40 and 42 amino acids long and are called respectively Aβ_{1-40} and Aβ_{1-42}. Although the differences in the primary structure are minimal, these two species show very different clinical and biological behaviors. Even if the secreted concentration of Aβ_{1-42} is only 10% of that of Aβ_{1-40}, the longest alloform is predominant in the plaques of the cerebral parenchyma [63]. Aβ_{1-42} appears to be more neurotoxic than Aβ_{1-40} and kinetic studies seem to confirm that it forms fibrils much faster than the shorter peptide [64]. The two peptides affect each other's aggregation rates and toxic activities: *in vitro* studies have shown that they form mixed aggregates [65, 66]. Moreover, these peptides show different behaviors in the initial phases of the aggregation. Aβ_{1-42} seems to form predominantly hexameric aggregates, called paranuclei, with spheroidal radius structure around 2.5 nm [67], which coexist in equilibrium with the monomer. These aggregates they associate themselves to give protofibrillar and fibrillar structures. In contrast, structures analogous to the paranuclei of the Aβ_{1-42} peptide have not been identified for the peptide Aβ_{1-40}. Studies of introduction of mutations have suggested that the critical residue that promotes the initial oligomerization and formation of paranuclei is Ile-41, while Ala-42 would facilitate the association between paranuclei. In addition, oxidation of Met-35 blocks paranucleus formation but does not alter the Aβ_{1-40} oligomer size distribution [68].
The two species, however, after prolonged incubation, produce similar proto-fibrillar structures, hence the fundamental difference at the basis of the clinical differences between the two peptides would be the initial oligomerization immediately after the production of the peptides.

2.1.1.2 Parkinson's disease and α-synuclein

Parkinson's disease (PD) is the second most common neurodegenerative disorder after Alzheimer's disease and affects about 1% of the population over 60 years old [69].
The primary manifestations of Parkinson's disease are abnormalities of movement, including movement slowness, difficulties with gait and balance, and tremor. Non-motor symptoms are equally present and include disorders of mood and affect with apathy, anhedonia and depression, cognitive dysfunction and hallucinosis, as well as complex behavioral disorders [70]. Pathologically, PD is characterized by the prevailing death of the dopaminergic neurons in the *pars compacta* of the *substantia nigra* located in the midbrain. Moreover, proteins and lipids aggregates in Lewy

Bodies (LBs) and Lewy Neurites (LNs), were found also in other brain regions, such as the dorsal motor nucleus of the vagus, the nucleus basalis of Meynert, and the locus coeruleus [71]. In particular, Lewy Bodies are mainly constituted by ubiquitin and an aggregated form of the α-synuclein protein. Electron microscopy showed that α-synuclein present in Lewy Bodies and Lewy Neurites is organized into filaments 200-600 nm long and with a diameter of 5-10 nm [72], with α-synuclein filaments in LBs characterized by a β-sheet structure characteristic of amyloid fibrils [73]. The fact that α-synuclein is the major component of the aggregates and that mutations in the gene encoding for the protein lead to autosomal dominant forms of PD has attracted the attention for to unravel the causes of the mechanisms of the disease.
α-synuclein monomer is a small protein constituted by 140 amino acids that belongs to the synucleins family (α-synuclein, β-synuclein and γ-synuclein), that share a quite high sequence identity and similar expression pattern [74]. Synucleins are expressed primarily in neural tissue, mainly at presynaptic terminal in mammalian brains, and have in common a highly conserved α-helical lipid-binding motif with similarity to the class-A2 lipid-binding domains of the exchangeable apolipoproteins [75]. The primary structure of α-synuclein can be divided in three parts: N-terminus,

Figure 2.5: α-synuclein primary structure divided into N-terminus, NAC and C-terminus. Adapted from [76].

non-beta amyloid component (NAC) and C-terminus (Fig. 2.5). The first 60 amino acids, the N-terminus of the protein, form, along with the NAC region, an amphipathic α-helix responsible for α-synuclein interaction with lipidic membranes [77]. The single point mutations A30P, E46K and A53T responsible for familial form of PD are all located in this region, accounting for variation in protein-membrane interaction or in protein aggregation propensity.
The NAC fragment (61-95), constitutes the more hydrophobic region of α-synuclein and it is believed to be responsible for the primary intramolecular interactions that cause α-synuclein misfolding and aggregation [36]. This region promotes the formation of β-amyloid *in vivo*, acquiring a β-sheet structure when α-synuclein forms amyloid fibrils. The remaining part of the protein constitutes the C-terminus, which includes 14 acidic residues and does not acquire a defined secondary structure in solution, when α-synuclein is bound to the membranes or when it forms amyloid fibrils.
Extensive biophysical investigations provided evidence of the lack of a secondary structure when α-synuclein is isolated *in vitro*. For this reason, it has widely been classified as intrinsically disordered protein and, as a model IDP, in numerous studies, has aided in the development of many technologies used to characterize IDPs and arguably represents the most thoroughly analyzed IDP to date. Recent reports,

however, have challenged the disordered nature of α-synuclein inside cells and have instead proposed a physiologically relevant helical tetramer [78, 79]. Moreover, it has been shown that different solution condition can influence the protein aggregation, assembling into fibrils that exhibit considerable morphological heterogeneity [80]. Such polymorphism can lead to significant differences in fibrils height, width, periodicity, length and mechanical properties [81, 82]. Despite α-synuclein's rich biophysical history, a single coherent picture has not yet emerged concerning its *in vivo* structure, dynamics, and physiological roles.

2.1.2 Amyloid aggregation and fibrillogenesis

The non-pathogenic process of protein folding leads the peptide to assume a three-dimensional structure, thermodynamically stable and biologically active, defined as native conformation [83], dependent on the amino acid sequence and the environment in which the protein is expressed. A generic polypeptide chain, in the not folded conformation, possesses a high number of degrees of freedom which translates into a very high number of possible three-dimensional conformations. If to reach the native conformation the protein should probe each of the possible conformations, the whole process would require times of the order of 10^8 s [84]. Instead, it is known that the folding process takes place in terms of the order of milliseconds, with small differences correlated to the molecular weight of the particular molecule in question. This difference between theoretical predictions and *in vivo* observations was underlined by Levinthal, in 1969 [84]. Actually, the Levinthal paradox is solved by the consideration that not all the probabilities of the states are equal but there is a "bias" in respect to the native state [85]. Protein folding can be described as a stochastic process of intramolecular self-assembly driven by the establishment of noncovalent interactions such as electrostatic, hydrophobic, Van der Waals interactions and hydrogen bonds leading to the energetically most favorable conformation. There is no single way of reaching these states, but alternative routes that can be traced according to the free energy profile. This concept can be summarized by the so-called conformational funnel (Fig. 2.6). Protein folding is thus a hierarchical process that involves a progressive increase in the conformational stability of the protein, or a drastic decrease of the Gibbs free energy with respect to the unfolded state. Many studies, from the work of Anfinsen in 1972 [87], have been carried out on protein folding mechanisms both *in vivo* and *in vitro*, which have led to an understanding of the relationships between primary structure and free energy able to guarantee protein folding [31, 85]. Since the amyloid state is characterized by high kinetic and thermodynamic stability due to their characteristic structure, the process of forming amyloid fibrils can thus be considered as an alternative to the normal folding process and in competition with the latter. Moreover, this conformation can be adopted, in principle, from all existing peptide chains [83], not being strictly the exclusive prerogative of some amino acid compositions.
In the context of intramolecular interactions, the native conformation constitutes the most stable state from the energetic point of view and an absolute minimum in

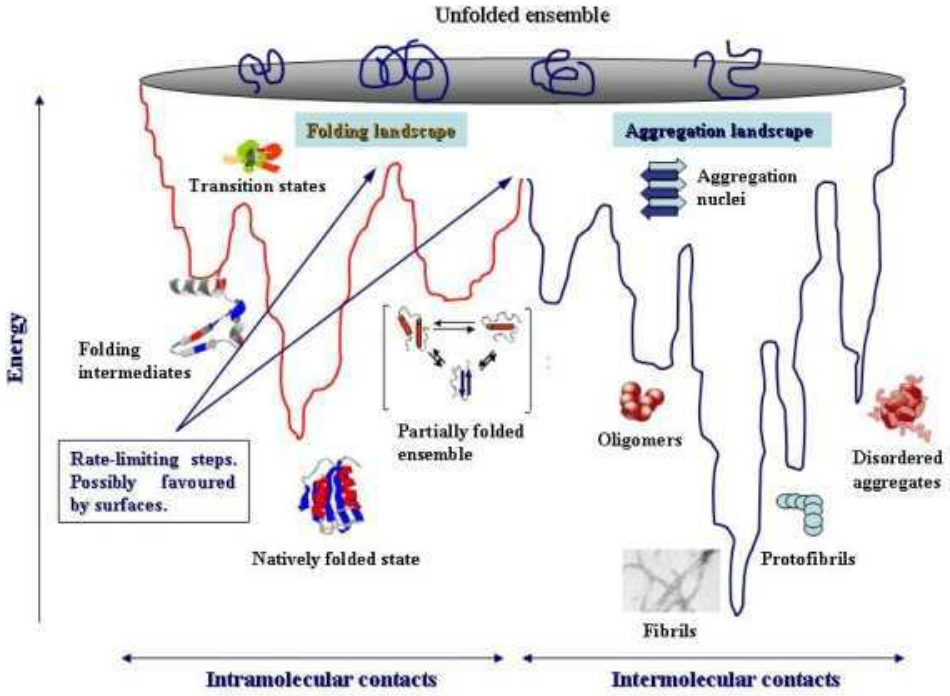

Figure 2.6: Combined protein folding/aggregation landscapes. Energy landscape model for protein folding (left, in red) and aggregation (right, in blue) starting from the unfolded ensemble. Different conformational states are available to a protein when stabilized by either intramolecular (monomeric protein) or intermolecular (aggregation intermediates and mature fibrils) contacts. The energy barriers can be lowered by suitable conditions such as interactions with other proteins. From [86].

the context of the conformational funnel (see Fig. 2.6). If we also consider intermolecular contacts in the context of aggregative phenomena, new minimum points are found. The native conformation becomes a point of relative energetic minimum, while the fibrillar state gains the status of absolute minimum. The amyloid state could therefore be thermodynamically more stable than the native conformation of many proteins, even under physiological conditions. Since the conversion of amyloid fibrils provides an increase in terms of intermolecular interactions, it follows that the formation of such aggregates is favored by high concentrations of peptide in unfolded or partially-unfolded states. In this framework the folded state could represent a metastable monomeric (or oligomeric) phase separated from the polymeric-fibrillar state by a potential energy barrier.

Fibrillogenesis is thus a very complex process, as it is the result of the formation

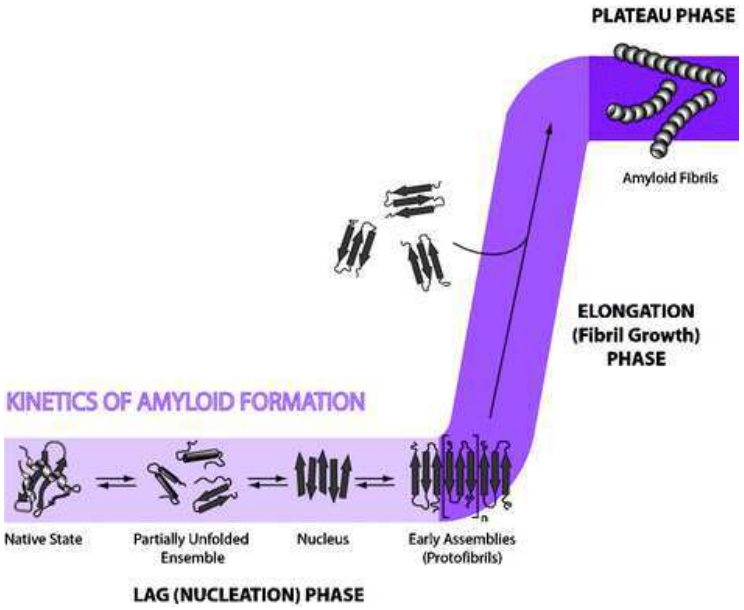

Figure 2.7: Schematic representation of the amyloid forming pathway. The nucleation dependent mechanism is represented: soluble prefibrillar oligomers or nuclei are formed during the lag phase, act as templates to sequester other aggregation-prone intermediates, leading to rapid fibril growth (represented by the exponential elongation phase) and subsequently, to the formation of insoluble mature amyloid fibrils. The plateau phase represents the steady state when maximum fibril growth has been reached. From [88].

of inter and intramolecular bonds that change the structure and conformation of the protein involved. The amyloid aggregative phenomena can be generally treated as a polymerization process that takes place in distinct and consequential phases, according to a nucleation and elongation mechanism (Fig. 2.7). An initial phase called nucleation (lag phase) is observed during which the peptides in solution usually undergo a conformational modification with consequent formation of oligomeric structures rich in β sheets (see Fig. 2.8). These aggregates are often called nuclei or

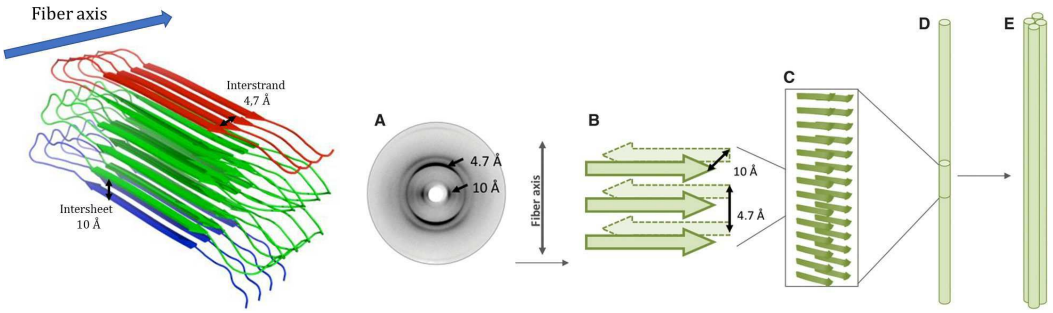

Figure 2.8: Left: ordered cross-β structure forms amyloid fibrils. Right: (A) The cross-β diffraction pattern obtained from amyloid fibrils which arises from the (B) cross-β structural core of the protofilament shown in (C). The protofilaments shown in (D) self-associate to form the more complex mature amyloid fibril (E). From [89].

seeds because they provide the basis for the subsequent assembly up to the formation of fibrils. Then follows a second phase, called elongation, during which the size of the aggregates grows exponentially with the formation of protofibrils and mature amyloid fibrils. Finally, a saturation is reached due to the establishment of a balance between the aggregates present in the solution and the oligomeric fraction available for the assembly. Since amyloid fibrils are insoluble and thermodynamically very stable the process is hardly reversible. Despite the differences between proteins in their native state, the corresponding amyloid fibrils appear to have in common the cross-β pattern. Unlike the native conformation, the three-dimensional structure of the fibrils is not dictated by the amino acid sequence, although the details inherent in structure and stability may be sequence specific: at the nanoscale, fibrils originating from different peptides have a high degree of structural homology [90]. Amyloid fibers are commonly 7-20 nm wide, but have a length that instead falls in the order of micrometers and are composed of multiple thin protofilaments that can be assembled in a variety of ways to create mature fibers. The characteristic X-ray reflection pattern at or near 4.75 Å indicates that protofilaments in the amyloid are organized in a β-fold (see Fig. 2.8).

This landscape has been extensively analyzed in recent years, highlighting more complex and articulated formation processes, which include secondary nucleations and depend from unseeded or seeded aggregation [91]. From the known model of Knowles group [35], in the absence of fibrils, all oligomers have to be generated through primary pathways, since secondary nucleation requires the presence of fibrils. Once a critical concentration of amyloid fibrils has formed, however, secondary nucleation overtakes primary nucleation as the major source of new oligomers, and further proliferation becomes exponential in nature due to positive feedback. The system finally reaches a critical concentration of fibrils, above which secondary nucleation becomes the dominant mechanism generating new aggregates.

As aggregation is a stochastic process, the reaction mixture will be highly complex and composed of several oligomeric species at any given time. Homogeneity of the

sample is not thought to occur until after the polymerization reaction is complete and even then, it is possible an instability in time. Furthermore, the composition of the reaction can be significantly modulated by physicochemical parameters, such as temperature, ionic strength and pH [38]. The presence of cosolvents influences the stability, solubility, binding, and crystallization of proteins [92]. In particular cations and anions affect these processes with widely varied effectiveness: the Hofmeister series ranks the relative influence of ions on the physical behavior of biomacromolecules as well as a wide variety of aqueous processes [93]. It is thus not surprising that independent studies of this highly dynamic reaction mixture have yielded a plethora of transient molecular species that have been claimed to occupy an essential position along this pathway [94]. The transient nature of the intermediate oligomers is equally challenging for the characterization of the toxic potential of these species, and thus a number of differently sized oligomers have been suggested as the cause of the diseases. This is the reason why, even if it has been differently studied, this issue remains on the agenda in the biophysical debate.
Amyloid aggregates may however have a gainful function, as in the case of bacteria where amyloid structures are involved in the formation and stabilization processes of biofilms [95]. Moreover, amyloid fibrils can give micro-organisms favorable characteristics such as mechanical resistance or increased virulence [96]. The cross-β architecture guarantees a remarkable stability to the fibrils as it allows the formation of an extended network of hydrogen bonds. For this reason, it has been proposed their possible use in designing novel nanostructured materials [97, 98, 99].

Model proteins The ability to form structures of amyloid nature is not a unique feature of proteins involved in protein misfolding diseases. Proteins of a different nature, even non-pathogenic, can gain an amyloid status if subjected to appropriate experimental conditions [100, 38]. These evidences have allowed to study the phenomenon of amyloid aggregation in a much more widespread way, using less precious and better known proteins as model proteins. For example, lysozyme, in this thesis the one extracted from eggs (hen egg white lysozyme, HEWL), homologous to the human protein, is a highly studied protein and characterized in detail in structural terms. Mutant lysozyme was found involved in hereditary systemic amyloidosis [101]. Aggregation of lysozyme was also observed *in vitro* in different experimental conditions that have in common the alteration of the native conformation due to thermal destabilization after incubation at acidic pH or the presence of denaturing agents or organic solvents [102, 103, 104].
Even insulin, a hormone protein, has been intensively examined as one of the best models among proteins that can form amyloid fibrils readily *in vitro* [105, 106]. Bovine serum albumin (BSA), β-lactoglobulin and cytochrome C can form aggregates with amyloid characteristic, rich of β-sheets structures [107, 108, 109].
In this thesis this characteristic has been exploited to deepen the mechanism of fibrillation *in vitro* in our laboratory and for preliminary studies on amyloid interactions.

2.2 Materials and methods

In this section, the details of the different techniques exploited to characterize amyloidogenic proteins will be presented, to introduce the experimental section to follow.

Protein fibrillation

Lysozyme (Hen Egg White Lysozyme, HEWL, Sigma Aldrich) has been dissolved in a 70 mM Glycine-HCl buffer at pH 2.7 containing NaCl (50 mM). The concentration of HEWL in solution, 100 μM for SAXS and 50 μM for fluorimetric measurements, has been evaluated spectrophotometrically at $\lambda = 280$ nm using a molar extinction coefficient of 38.94 L mol^{-1} cm^{-1}.The solution was incubated overnight in the absence of NaCl and salt was added immediately before the induction of thermal destabilization. Amyloid aggregates were produced by incubation of the sample at 65 °C under conditions of constant mechanical stirring (1100 rpm).
The α-synuclein was purified as a monomeric fraction from *Escherichia coli* as described in [110] from the Vendruscolo laboratory, Department of Chemistry, Cambridge. The different Aβ peptides were purchased lyophilized by Anaspec. Aβ_{1-40} was solubilized in NaOH 5 mM (Sigma-Aldrich), pH 10, sonicated and lyophilized according to Fezoui et al. protocol [111]. The lyophilized peptide was then dissolved in PBS (pH 7.4) and filtered through two filters in series having diameter of 0.20 mm (Millex-Lg) and 0.02 mm (Whatman) respectively, in order to eliminate large aggregates. The sample preparation was aseptically operated in a cold room at 4 ∘C. The Aβ_{1-40} concentration was determined by tyrosine absorption at 276 nm using an extinction coefficient of 1390 cm-1 M-1. Aβ_{1-42} aggregation was induced just by solubilizing the peptide in hesafluoroisopropanol (HFIP), that was evaporated using a gentle stream of nitrogen gas. The sample preparation was aseptically operated in a cold room at 4 °C. The protein was carried in ice to the beamline and dissolved just before the measurements in PBS.

Fluorescence and UV-Vis measurements

The aggregation kinetics of HEWL were monitored by fluorescence detection (50 μM) by Thioflavin T (5μM) at 485 nm and by absorbance detection (200 μM) by Congo Red (20 μM) in the UV-Vis spectral range. Fluorimeter parameters have been optimized by checking different emission/excitation slits, and finally analyzing the kinetics with 9:9 slits. All reagents have been purchased by Sigma Aldrich. A Perkin Elmer LS55 spectrofluorometer has been exploited for fluorescence measurements equipped with a thermostatic bath that kept the sample at constant temperature (20 °C).
A Cole Palmer spectrophotometer (67 series VU Visible Scanning spectrophotometer; Bibby Scientific Ltd., Stone, Staffordshire, UK) has been used for absorbance measurements at room temperature for Congo Red assays. The reported values are the average of three measurements and are obtained from intensity weighted

distributions.

SAXS

Experiments of Aβ_{1-42} and lysozyme were carried out at the Elettra synchrotron, Trieste. Measurements were carried out at 20 °C in capillaries of 1.5 mm outer diameter/0.01 mm wall thickness made from borosilicate (Hilgenberg, Maisfeld, Germany) enclosed within a thermostatic compartment connected to an external circulation bath and a thermal probe for temperature control. Two dimensional patterns were recorded by Pilatus3 1M detector system that is based on the CMOS hybrid pixel technology. The data were stored in TIF format and then directly processed with FIT2D [112]. Each sample has been measured 20 times with an acquisition time of 20 s and a rest time of 40 s for each step after a negative control for radiation damage. The sample-to-detector distance was set to 1.247 m, which provided wavenumbers Q between 0.1-4 nm^{-1}. α-synuclein and Aβ_{1-40} were carried out at the BM29 beamline in ESRF - the European Synchrotron Radiation Facility in Grenoble, France. SAXS patterns were recorded using a bidimensional Pilatus 1 M detector. The sample cell used is a 1.0 mm diameter quartz capillary, with a few tens of microns wall thickness. The transmitted intensity is monitored with a diode integrated in the beamstop and the intensity measured during data acquisition is used for normalization. Since the sample-detector distance was fixed at 2.867 m, the Q values ranged from 0.1 to 4.5 nm^{-1}. Each measurement lasted 1 s, followed by a dead time of 6 s in order to avoid radiation damage, and was repeated at least 10 times. Protein samples were carried in ice, and freshly prepared with the desired amount of curcumin-like compound. Aβ_{1-40} and Aβ_{1-42} concentrations have been analyzed at 270 μM and 200 μM respectively and α-synuclein at 50 μM. SAXS macroscopic differential scattering cross sections $d\Sigma/d\Omega(Q)$ (briefly referred to as scattering intensities) were obtained, where possible for the setup of the experiment, on an absolute scale (cm^{-1}) by calibrating via a water sample, subtracting the proper buffer contribution for each investigated condition, and correcting for the protein volume fraction, as previously described.

Optical microscopy

Samples have been withdrawn from the aggregation kinetics and deposited in a glass slide. For Congo Red stained observations, 20 μl of dye has been added on the slide and left to dry under a laboratory hood. For fluorescence microscopy analysis the same procedure has been followed without drying the sample and adding a ThT drop (5 μM) on the glass slide in a dark room before the measurement.
Fluorescence microscopy measurements have been carried out on a Zeiss Axio Imager 2 microscope (Carl Zeiss MicroImaging GmbH, Germany) while optical microscopy measurements have been performed with an Leitz Ortholux polarized light microscope.

Confocal Microscopy

Images of Aβ_{1-40} fibril bundles stained with Thioflavin T (ThT) were obtained using a Leica TCS SP5 inverted laser scanning confocal microscope (Leica Microsystems AG, Wetzlar, Germany) interfaced with an Ar laser for excitation at 458 nm and adopting a 63 x 1.4 numerical aperture oil immersion objective (Leica Microsystems) in oil immersions. Fibril bundles were left to settle for 20 min from the initial solution in 3.5 cm glass bottomed Petri dishes (WillCo-Dish, WillCo Wells, Amsterdam, the Netherlands) and then imaged therein. The excitation power was 50-200 mW at the objective, the line scanning speed was set to 400 Hz, and the wavelength collection range was between 470- 515 nm. Transmission images were obtained in differential image contrast mode (Nomarski image) using the same laser source.

AFM measurements

α-synuclein samples were placed on flat mica surfaces and allowed to dry for several hours in a desiccator under N_2 flow. AFM imaging was done at the Partnership for Soft Condensed Matter (PSCP) Atomic Force Microscopy Platform, Grenoble, at ambient conditions using an Asylum Research MFP-3D microscope equipped with a high-resolution tip (Bruker MSNL-10; radius 2 nm, spring constant 0.6 N/m) in tapping mode. The analysis of the AFM images was carried out using the Gwyddion 2.50 software [113]. Plane leveling and alignment of rows were done as corrections to the raw data.

2.3 Characterizations of protein structures and fibrillation processes

In this chapter, experimental results on the fibrillation of amyloidogenic proteins (α-synuclein and A$\beta_{1-40/42}$ peptides) are introduced. First of all, the characterization of the dynamics of amyloid formation has been analyzed by means of a model protein, i.e. lysozyme. Subsequently, a brief study of the starting (monomers) and final (fibrils) states of aggregation of α-synuclein and Aβ peptides is presented, to depict characteristics and differences of the primary targets of this PhD thesis.

2.3.1 Fibrillation of model protein

As stated before (section 2.1.2), every protein can, in principle, exhibit an amyloid state, under specific conditions. To investigate the kinetics of fibrillation, lysozyme (HEWL), a well known protein, has been employed. Its amyloid aggregation has been induced *in vitro* and investigated by classical biophysical techniques. In particular, the fibrillation of HEWL (50 μM) has been observed by means of Thioflavin T staining [114], 5μM (see Section 6.2) in presence of 50 mM NaCl [115, 116]. In

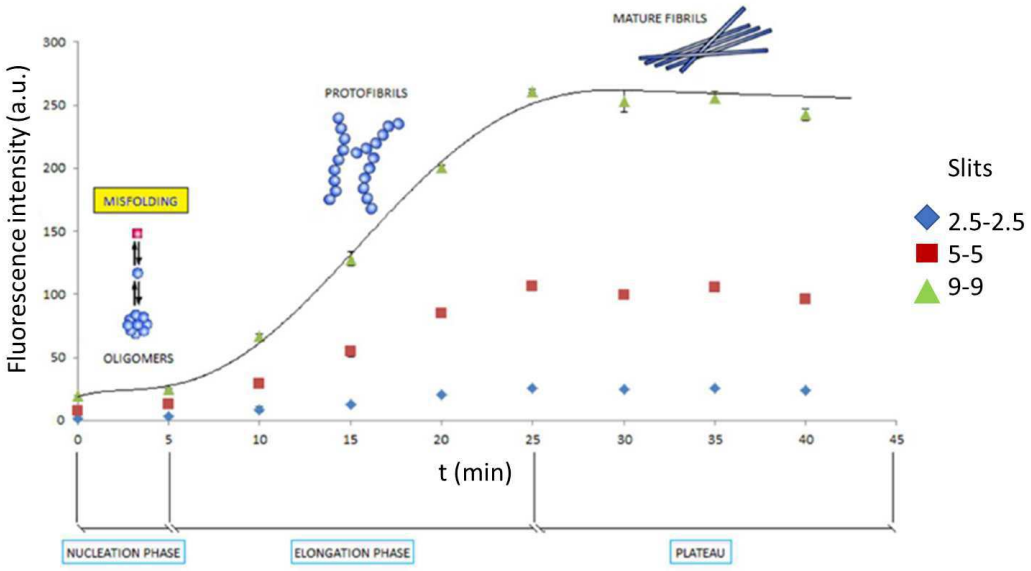

Figure 2.9: Evolution of the ThT (5 μM) fluorescence signal in lysozyme (50 μM) fibrillation pathway as a function of time and schematization of the nucleation and elongation process. In the view of optimizing the results, different fluorimeter slits have been exploited. The kinetic with different slits has been reported in different colors.

Fig. 2.9, the aggregation kinetic has been reported, highlighting the different phases of fibrillation. The Thioflavin T (ThT) signal increases with time, showing a trend

describable with a sigmoidal pattern:

$$I(t) = \frac{A_1 - A_2}{1 - exp^{\frac{(t-t_0)}{\Delta t}}} - A_2 \tag{2.1}$$

where A_1 is the initial value, set to zero for our analysis, A_2 is the final value, t_0 the nucleation phase and Δt the elongation phase. The saturation occurs after about 25 minutes (see Table 2.1). It is possible to distinguish a relatively short nucleation phase followed by an elongation phase (apparent growth rate $\tau = 1/\Delta t$ equal to about 0.05 min^{-1}). The very short lag phase occurs, on average, within 5 minutes from the beginning of the fibrillation process.
To avoid interaction of ThT staining with the amyloid formation [117], the same process has been observed with a spectrophotometric analysis with Congo Red (CR). Tissue amyloids have traditionally been defined as amorphous proteinaceous aggregates with distinctive tinctorial attributes after being exposed to alkaline solution of CR. They appear red at normal light but yellow/green ("apple green") between crossed polarizers (the complementary spectral color). Binding to amyloid induces a characteristic shift in CR maximal optical absorbance from 490 nm to 540 nm. The analysis of the results has been done considering the ratio between absorbance intensities at 490 nm, characteristic for Congo Red unbound, and 540 nm, characteristic of Congo Red bound to fibrils [118] (see Fig. 2.10, left). The kinetic has been performed in presence of 50 μM of NaCl and in absence of salt, known to speed up the kinetic of fibril formation [93].
As can be seen in Fig. 2.10 right, the kinetic without ions is slowed (black line) in respect to the one in presence of free-ions (green line). The lag phase of the sample with NaCl is consistent with Thioflavin T measurements (see Table 2.1) with an elongation phase of about 20 minutes. In absence of ionic strength, as expected, both elongation and nucleation phases are extended, and the apparent growth rate results lowered.
Even though the specificity of CR for amyloid fibrils only is still matter of debate

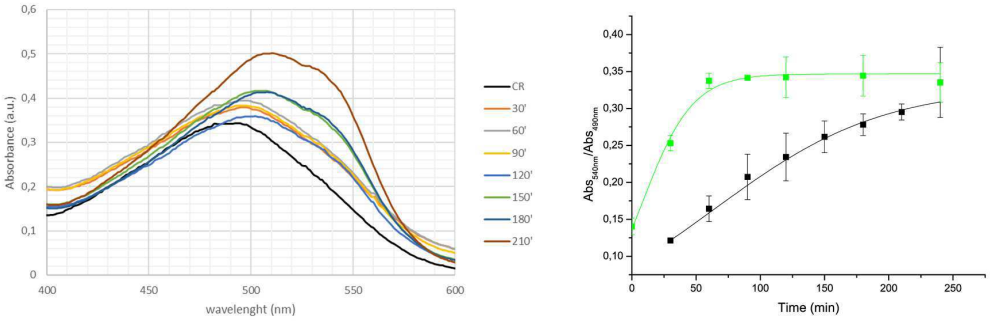

Figure 2.10: Left: Example of absorbance spectra of lysozyme (50 μM) with Congo Red staining monitored in time. Right: sigmoidal fitting of the ratio of the two characteristic Congo Red peaks of lysozyme without (black line) and with 50mM NaCl (green line).

Table 2.1: Sigmoidal fitting results of HEWL with ThT and Congo Red (CR) stainings. t_0 represent the nucleation phase, Δt the elongation phase and τ the growth rate.

	t_0	Δt	τ
	min	min	min^{-1}
ThT (50mM NaCl)	5 ± 2	25 ± 3	0.040 ± 0.005
CR (50mM NaCl)	8 ± 2	20 ± 2	0.050 ± 0.005
CR (0mM NaCl)	65 ± 1	65 ± 2	0.015 ± 0.005

[119], the concordance between the two techniques allows to define the characteristics times of the kinetic.
To obtain free-dye informations, SAXS measurements on the starting and final stages of lysozyme fibrillation has been performed at Elettra synchrotron, Trieste. The kinetic of fibrillation has been checked acquiring the curve at the beginning of the process and after 250 minutes, which was considered enough for fibrils formation (Fig. 2.11). The time zero curve is characteristic of a globular protein, and it allows to assert that lysozyme is present in solution in native conformation or, at most, in a state only partially destabilized before being subjected to the protocol of fibrillation. The time course of the SAXS curves shows an increase in intensity over time for the fibrillar sample. This signal evolution is evidenced by Kratky plots in Fig. 2.11. While at $t = 0$ the graph presents a single representative peak of a single conformational population in solution, at final stages it presents a modification of the low Q curve with the appearance of a slight peak indicative of the presence in solution of large structures. Exploiting a Guinier analysis (see Section 1.2.2.1), the average dimensions of the structures present in the two conformational populations highlighted by the Kratky plot have been estimated (Fig. 2.11, bottom). The gyration radius of the first stage of fibrillation is coherent with literature, resulting in R_g=1.5±0.1 nm [120], while for the fibrils the cross-radius in the Guinier rod-like approximation is R_c=7.5±0.1 nm.
To check the fibrillar nature of the sample, lysozyme fibers were observed with a fluorescence microscope, using ThT as fluorophore (see Fig. 2.12). The fibrillar structures are clearly distinguishable, the dimensions of which are comparable to the theoretical ones presented in section 2.1.2. It should be noted the presence of protofibrils arranged like a carpet under the fibril, captured in the right image. These complexes act as reservoirs for the fibrillation.

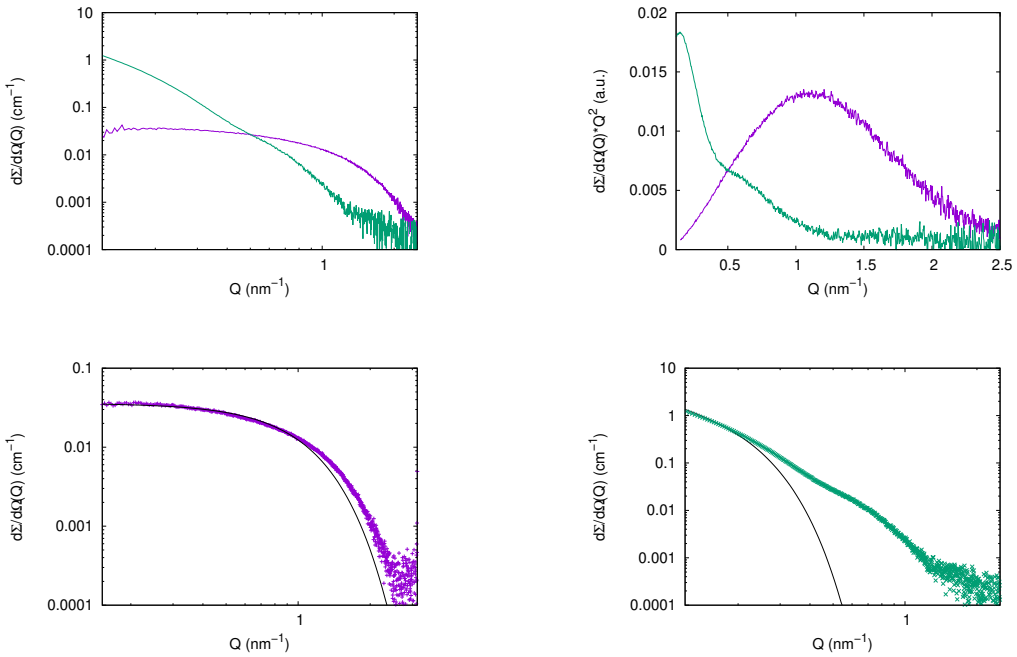

Figure 2.11: Measurements of lysozyme at 100 μM at initial (violet curve) and final (green curve) stage of fibrillation. SAXS curves are reported (top left) and their Kratky plots (top right), highlighting the different conformations of the two stages. In bottom, left and right, the Guinier fitting in classical approximation for native lysozyme (Q_{max}=0.8 nm^{-1}) and for rod-like particle for fibers (Q_{max}=0.2 nm^{-1}).

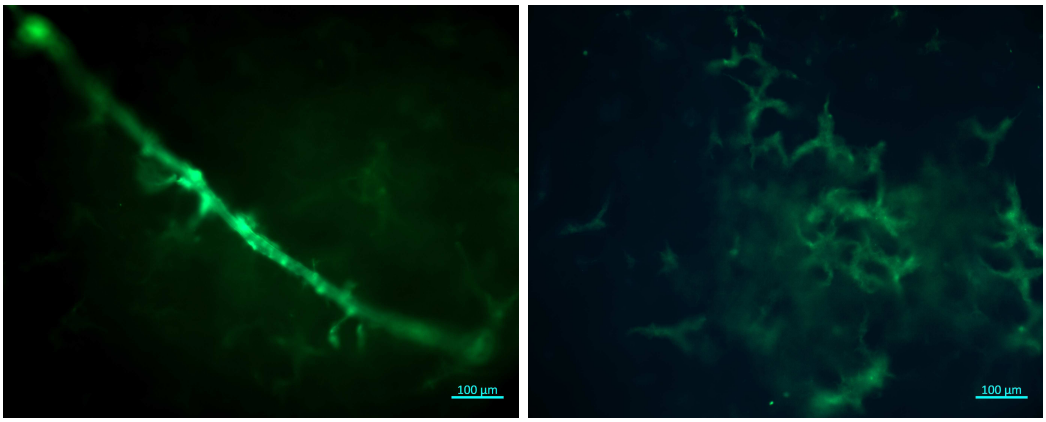

Figure 2.12: Lysozyme fibrils in presence of ThT after 3h of fibrillation kinetics. Scale bar: 100 μm.

2.3.2 Characterization of amyloidogenic proteins: initial states

The starting stage of the different amyloidogenic proteins (α-synuclein, Aβ_{1-40}, Aβ_{1-42}) have been analyzed principally by means of SAXS technique.
This discussion is needed both in order to learn about the initial conformation of these proteins and to observe the possible changes due to their interaction with biological as well as with chemical partners.

α-synuclein: SAXS curve obtained from α-synuclein in solution at neutral pH in phosphate buffer at 1 g/L concentration is reported in Fig. 2.13.
The Kratky plot nearby shows a not completely unfolded conformation. The Guinier analysis of spherical particle returns a gyration radius R$_g$=4.1±0.1 nm, effectively compatible with the size of the monomer reported in recent literature [82]. The SAXS curve has been also evaluated in the whole Q range adopting

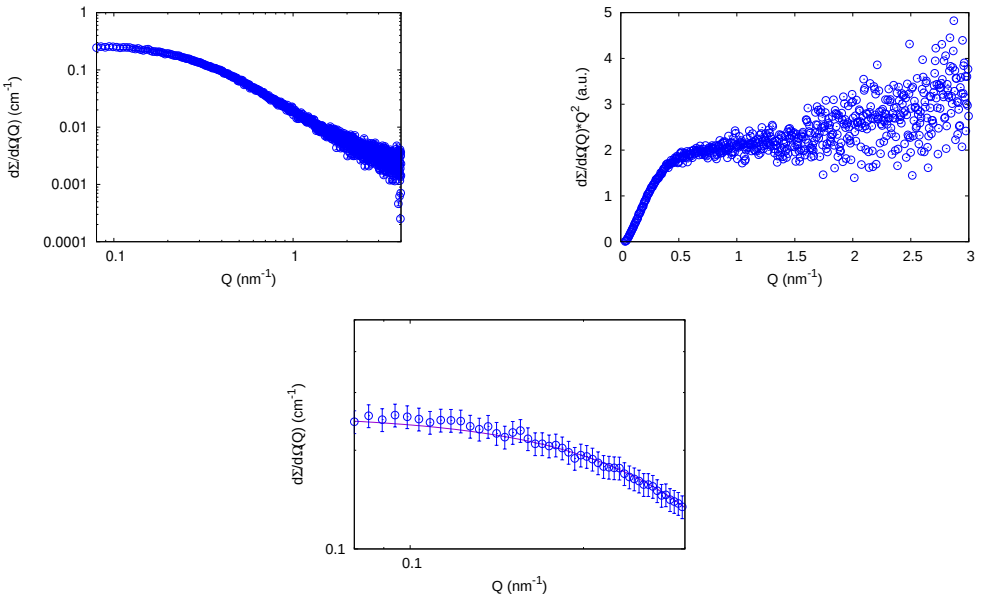

Figure 2.13: Top, α-synuclein monomer, 50 μM: scattering cross section and Kratky plot. Bottom, Guinier fitting for the gyration radius determination, Q_{max}=0.25 nm^{-1}.

a worm-like chain model [9], exploiting the Genfit software package (see section 1.2.2.5). This model is indeed suitable to describe the intrinsically disordered chain of monomeric proteins [121]. Since the electron density and the dry volume of the α-synuclein monomer can be determined using aminoacid literature data, the fitting parameters of the model reduce to the contour length L of the chain, the statistical Kuhn length b (which represents the separation between two adjacent rigid segments of the chain), the core radius R_w of the circular cross-section and the relative bulk mass density d_W of the hydration water. The best fit curve is

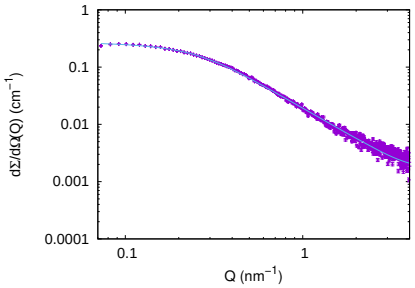

Figure 2.14: Fitting results of α-synuclein monomers with Genfit software, χ^2=1.1.

reported in Fig. 2.14, with a Kuhn length of b=1.2±0.5 nm, L=94.6±0.4 nm, R_w=0.44±0.01 nm and $d_W \simeq 1.08\%$.

For amyloid β-peptide, the analysis performed concerns the two allosteric forms: Aβ_{1-40} and Aβ_{1-42}.

Aβ_{1-40}: In Fig. 2.15 a measurement of the Aβ_{1-40} peptide has been reported, resembling the monomeric state. Effectively, the sample results in a very low gyration radius (R$_g$=1.62±0.09 nm). SAXS curve of the freshly prepared Aβ_{1-40} sample,

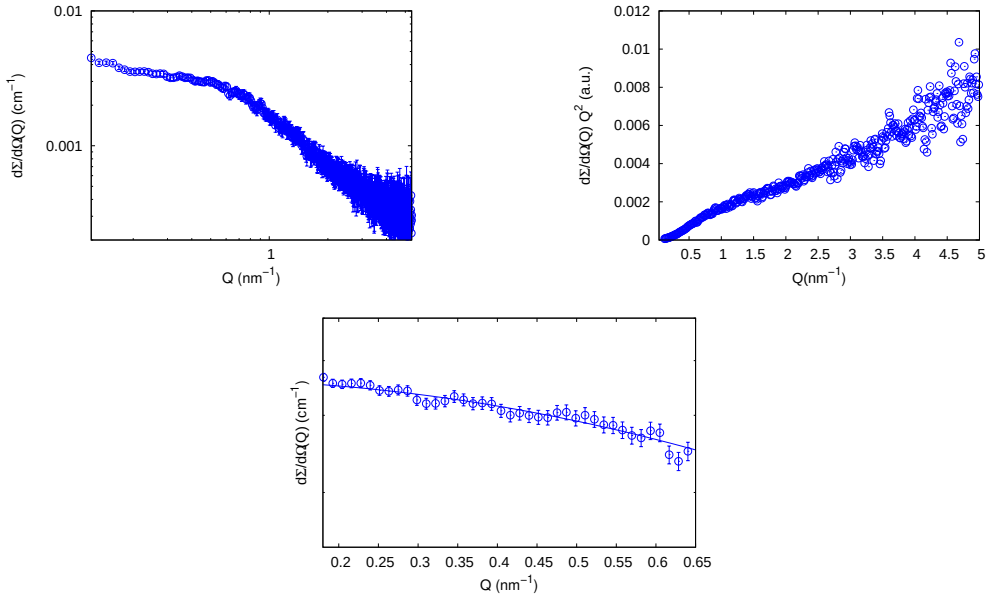

Figure 2.15: Aβ_{1-40} monomer (270 μM): top, SAXS curve, Kratky plots and, bottom, Guinier fitting, $Q_{max} = 0.6$ nm^{-1}.

as reported in Fig. 2.16, has been studied in the whole Q range by the worm-like form factor. To note, the fixed estimated value $V_1 = 5400$ Å^3 for the dry volume

of the Aβ_{1-40} monomer implies the constraint $V_1 = \pi R_w^2 L$. The best fit curve was obtained with b=2.0±0.5 nm R_w=0.41±0.01 nm and $d_W \simeq 1.05\%$, confirming that Aβ_{1-40} contains disordered single chains resulting from an ensemble of possible conformations.

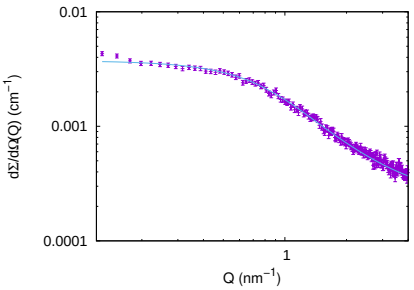

Figure 2.16: Aβ_{1-40} monomer (270 μM) theoretical fitting with Genfit software, χ^2=1.2.

Aβ_{1-42}: In analogy with the samples analyzed previously, the starting stage of Aβ_{1-42} peptide aggregation has been observed. Indeed, the shape of the SAXS curve does not suggest the presence of monomers, even compared with the monomers of Aβ_{1-40} presented previously (see Fig. 2.17, left). The approach with a classical Guinier fitting could not allow fine results, confirming a semi-aggregated trend of the sample. Even the fitting with the worm like approximation, used for the other

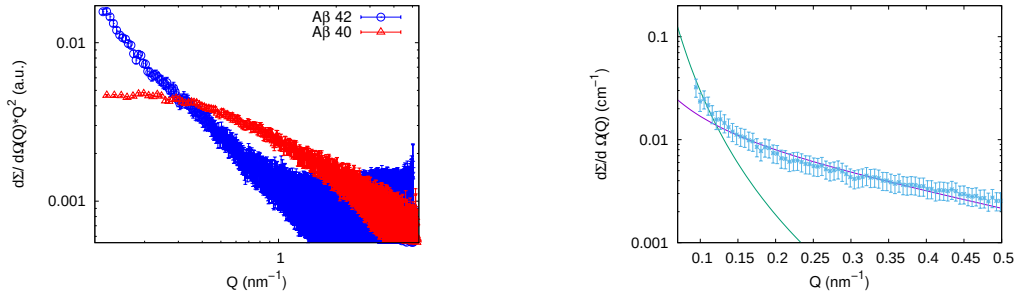

Figure 2.17: Left: Aβ_{1-42} initial measurement vs Aβ_{1-40} monomer, right:Aβ_{1-42} Guinier rod-like fitting: R$_c$=1.9±0.2 nm (200 μM). At very low Q values an aggregate tendency has been considered with a Porod like trend.

monomers, was not able to describe the initial state of this protein. It is necessary to exploit the rod-like approximation, so considering higher aggregates, giving a radius R$_c$=1.9±0.2 nm (Fig. 2.17). At very low Q values an aggregate trend has been considered with a Porod like trend and disregarded for the Guinier fitting. This confirms the higher aggregation propensity of Aβ_{1-42} in respect of Aβ_{1-40}.

2.3.3 Characterization of amyloidogenic protein: final states

The final fibrillar stages of the α-synuclein and Aβ_{1-40} and Aβ_{1-42} have been sampled, also in this case, in order to characterize the targets to which the inhibitory compounds will be added and to highlight the possible differences.

α-synuclein: SAXS curves corresponding to α-synuclein fibrils are clearly very different from the ones corresponding to the monomeric form in solution (see Fig. 2.18). Mature α-synuclein fibrils were measured by SAXS in several experimental sessions

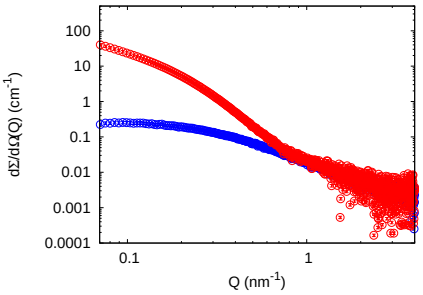

Figure 2.18: Fibers (red) and monomers (blue) of α-synuclein (50 μM).

in synchrotrons, according to the same protocol. However, since SAXS detects the overall structures in solution, we could detect some difference between fibrils samples, probably due to different degree of maturation (see Fig. 2.19 and 2.20) and to the evolution of the sample. The curves reported have been acquired with different degree of maturation and in different experimental sessions. The curves and the observation of Kratky plots reveal different conformations for the samples.
These differences can be highlighted with rod-like Guinier fittings (see 1.2.2.2), from which the resulting values for the cylinders radii are R_c=5.1±0.1 nm for the first sample, R_c=10±1 nm and R_c=12±1 nm for the samples at a different time (Fig. 2.19).

Table 2.2: Cylinders radii from theoretical analysis for α-synuclein fibers.

	R_1 (nm)	R_2 (nm)	Polydispersity (%)
Sample 1	5.2 ± 0.2	-	48 ± 5
Sample 2	13.0 ± 0.6	1.8 ± 0.1	48 ± 5
Sample 3	28.0 ± 0.5	1.7 ± 0.1	48 ± 5

Given these results, a theoretical fitting performed considering the presence of cylinders whose radius is polydisperse has been carried out, to better characterize the cylinders in solution (see Fig. 2.21). The results from the fitting return a great polydispersity for all the samples, ranging at 48±5 % , and are reported in Table 2.2. These results, in agreement with literature [39], highlight the evident inhomogeneity

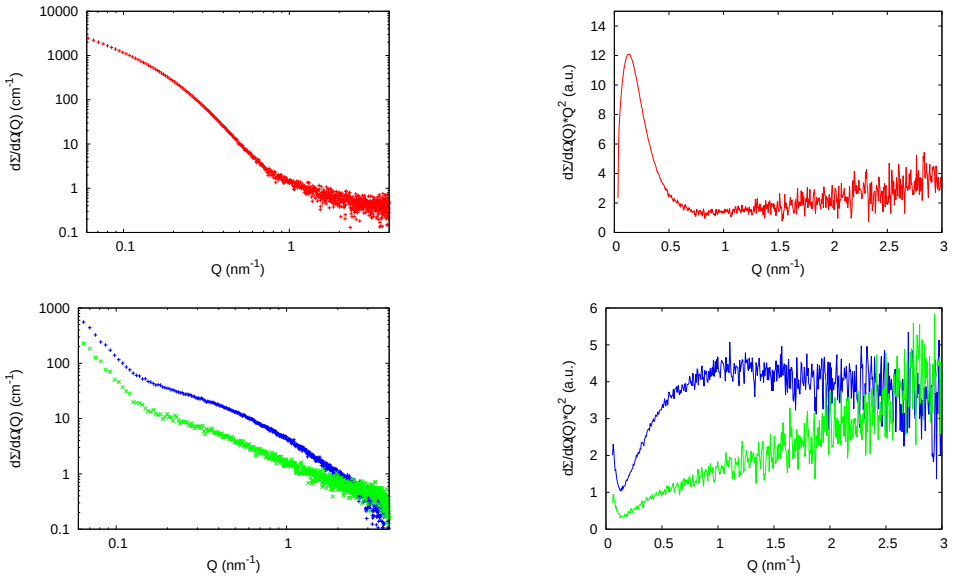

Figure 2.19: Left: α-synuclein fibers at different degree of maturation (red, blue and green) The green and blue curve showed a higher degree of homology so are reported together. Right, Kratky plot of the same samples.

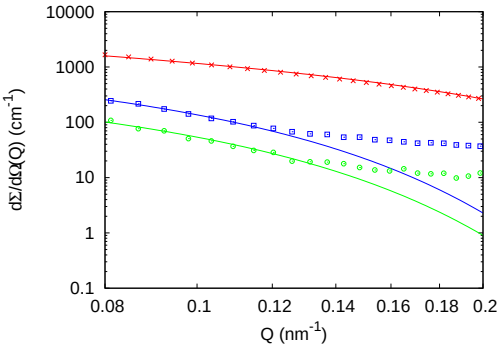

Figure 2.20: Fitting of α-synuclein fibers with a Guinier rod-like approximation. The maximum Q for the different samples are 0.2 nm^{-1} for the red curve and 0.12 nm^{-1} for the blue and the green curve.

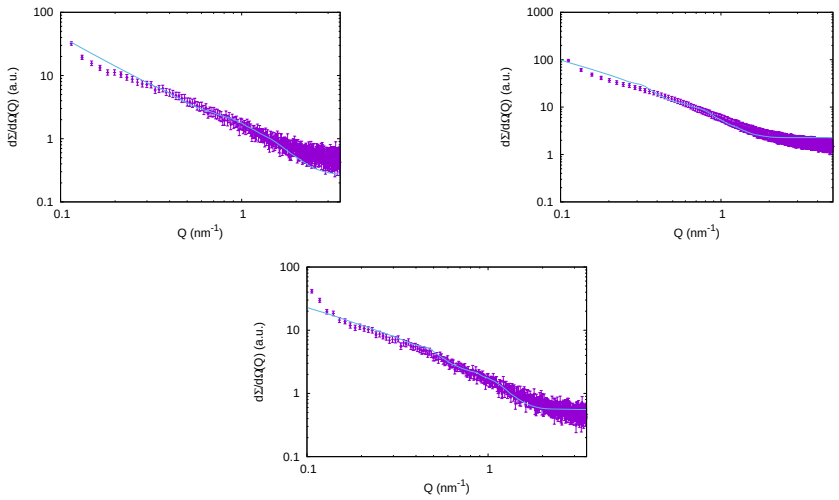

Figure 2.21: Genfit analysis of α fibers with cylinder model. Radii obtained are R_1=5.2±0.2 nm, R_1=13±6 nm and R_2=1.8±0.1 nm; R_1=28.7±0.5 nm and R_2=1.7±0.1 nm for the different samples, showing a great inhomogeneity in the evolution of the samples. χ^2=2.1, 2.5, 1.9 for each fitting curve.

of fibrils samples, since the evolutionary pattern can be different. The polydispersity has been confirmed by AFM microscopy at AFM platform in ESRF (Fig. 2.22, top).
In Fig. 2.22, bottom, profiles selected on the image are reported on the right. The mean dimensions observed are 50 nm in thickness and 10 nm height, compatible with mature fibrils [122, 123]. For Aβ_{1-40} and Aβ_{1-42}, discrete steps leading to the final states of fibrillation have been observed and compared.

Aβ_{1-40} : The overall shape of the SAXS curves of Aβ_{1-40} noticeably changes at increasing time after the sample preparation (Fig. 2.23). The best fit Guinier radii R_c are reported in Fig. 2.23.
SAXS curves corresponding to in solution Aβ_{1-40} during its aggregation were fitted in their low Q-range by adopting the Guinier approach for infinite rods, considering the formation of elongated cylindrical structures and thus confirming the expected presence of protofibrils and fibrils in solution. The cross section radii R_c obtained from this analysis are reported in Fig. 2.23, and they increase at increasing time as it could be expected.
The final step, considered characteristic of the mature fibril sample, was fitted considering the possible presence of fibrillar cylindrical structures and disordered aggregates. In fact two species in solution have been considered: cylinders of radius 2.3±0.4 nm and infinite height, given SAXS resolution, and disordered oligomers (3±1%) with aggregation number 16±5 (Fig. 2.24). The morphology of the largest species at the final stage of the aggregation kinetics was observed with confocal microscopy, with ThT staining (Fig. 2.25). Samples showed prevalently the presence of long fluorescent "sticks"; importantly, negligible background fluorescence was recorded indicating that these "sticks" account for the vast majority of ThT-

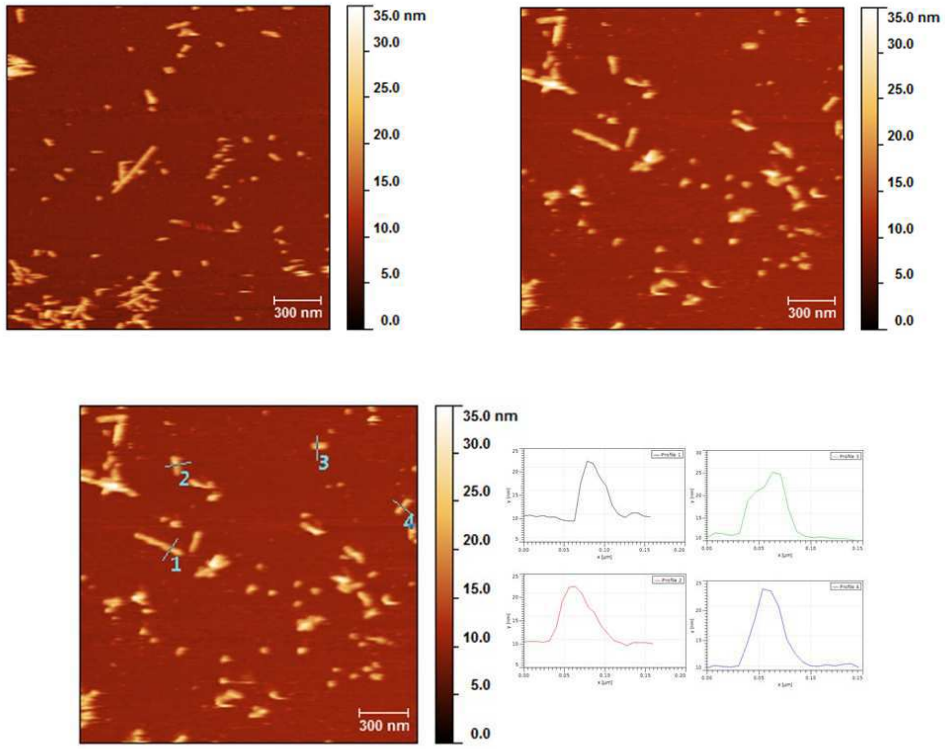

Figure 2.22: Top: AFM images of α-synuclein fibrils at 0.2 μM. Bottom: AFM images of the α- synuclein fibrils (left) and example profile of the selected regions (right). z-scale: 35 nm.

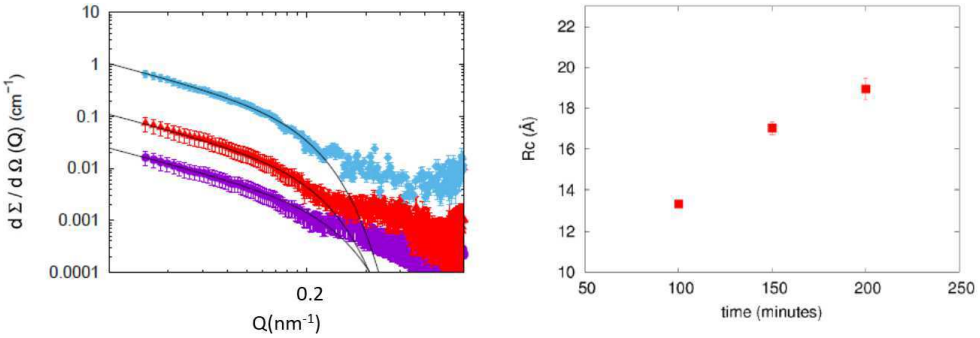

Figure 2.23: Guiner plots for rod-like particles of SAXS data corresponding to Aβ_{1-40} 270 μM, after 100, 150, and 200 minutes. Curves at increasing time are shifted for clarity by a factor 5i (with i=0 for time 100, i=1 for the measurement after 150 minutes, and so on). Continuous lines are the theoretical fitting corresponding to Guinier approximation for rod-like particles. Right: Time dependence of the radius of the cross-section, obtained by fitting SAXS curves corresponding to Aβ_{1-40} in solution.

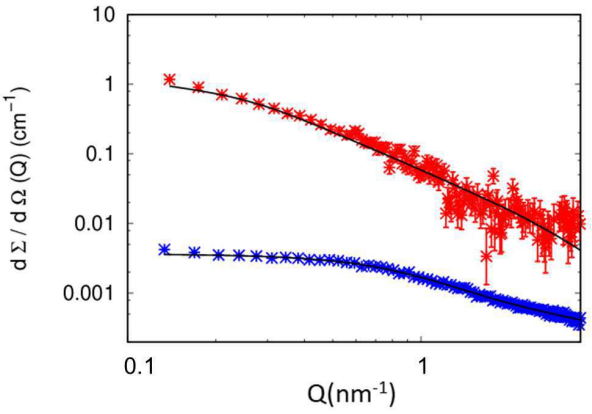

Figure 2.24: Aβ_{1-40} at the final stage (red) fitted with elongated objects model (black line). The monomer curve is reported for comparison (blue curve).

positive Aβ_{1-40} structures in solution [124]. Even more, mature fibrils of Aβ_{1-40}

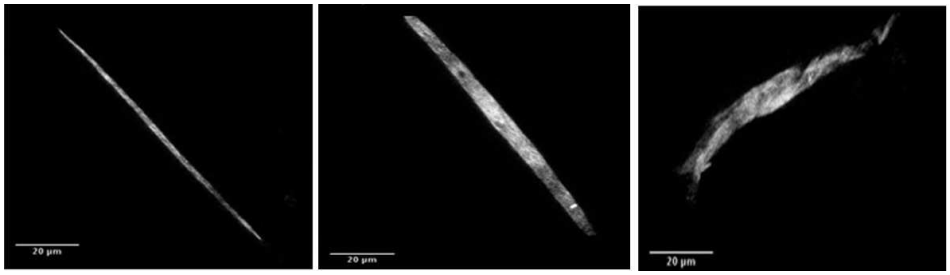

Figure 2.25: Fluorescence confocal images of ThT-stained Aβ_{1-40}. Scale bar 20 μm.

were observed with a microscope with polarized light. We highlighted the presence of fibrils with Congo Red staining. In Fig. 2.26 are represented what we can interpret in term of fibrils bundle, giving their dimensions (approximately 50±6 μm of thickness, see Fig. 2.26). In Fig. 2.27 the characteristic birefringence under polarized light is evidenced in large aggregates. Our results are in accordance with literature [125].

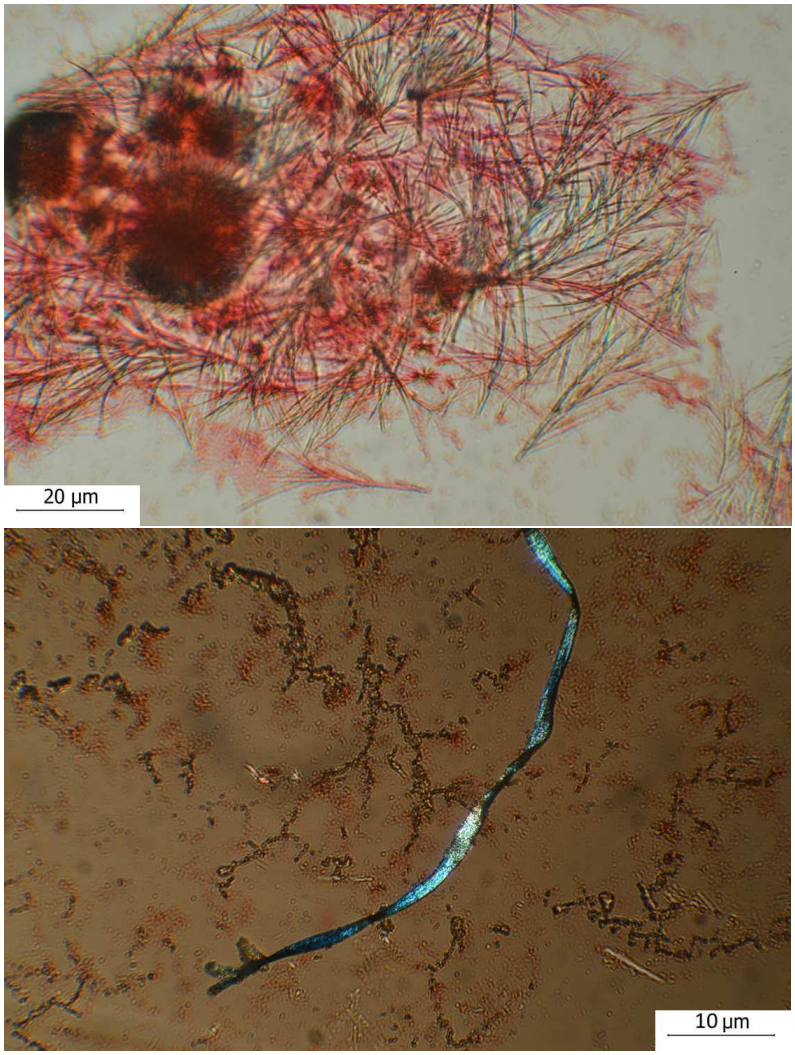

Figure 2.26: Top: Congo Red staining on a fibril bundle of Aβ_{1-40}. Scale bar 20 μm. Bottom: an isolated fiber, scale bar 10 μm.

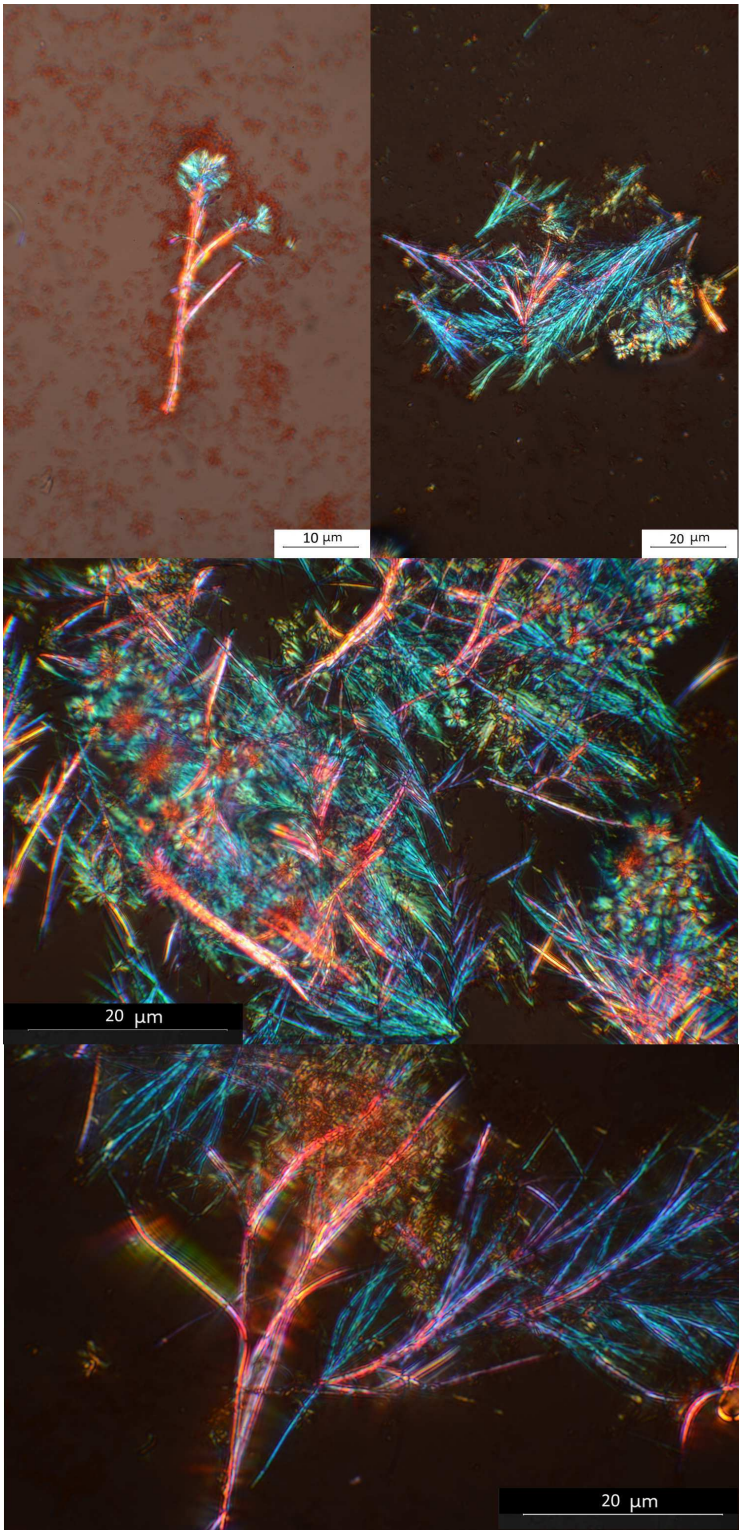

Figure 2.27: Aβ_{1-40} fibers observed in polarized light microscope.

Aβ_{1-42}: For Aβ_{1-42}, the set of SAXS curves shown in Fig. 2.28 shows a clear evolution in time, starting from a sample that, as said before, was yet in an aggregated state. It can be observed, in the prossimity of $Q = 0$, both an increase of the diffused intensity and an increase of the slope of the curve. Both phenomena indicate a growth in the average size of the particles present in the sample. The kinetic is very rapid, since in 120 minutes the system is aggregated and stable. In the Kratky plot, shown in Fig. 2.28 right, the lack of a maximum well defined above all in the kinetic starting curve indicates a low amount of compact species in solution. A transition occurs from a partially unfolded state to a more compact state. Given the propensity of the monomer Aβ_{1-42} for the aggregation, we can deduce that over time fibers of variable length form. Since the length of these fibers is greater than the size that our experimental apparatus allows us to analyze, data at the end of the kinetic are interpreted, as before, with a cylinder model (one-dimensional hypothesis). In this hypothesis the cross-sectional radius R_c resuts R_c=2.7±0.1 nm (see Figure 2.29). The Genfit analysis, considering an infinite cylinder, returns a radius of R=2.0±0.5 nm, see Fig. 2.29, but a very high polydispersion (48±2%). It has

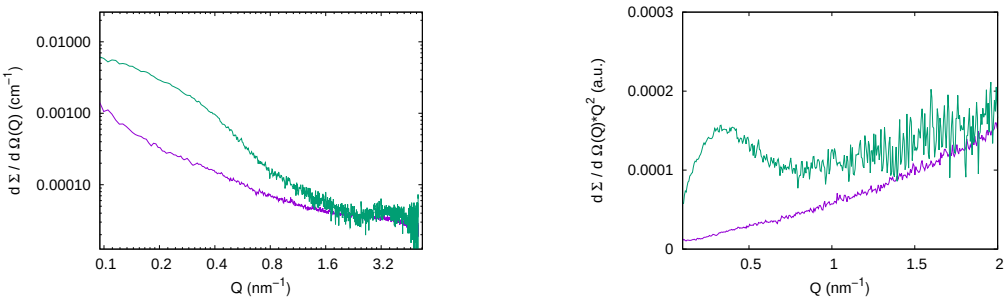

Figure 2.28: Aβ_{1-42} starting (violet) and final (green) conditions (200 μM). Right: Kratky plot representation of selected data.

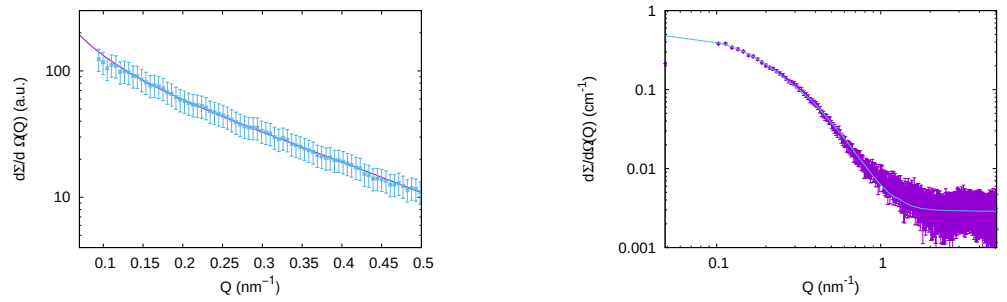

Figure 2.29: Aβ_{1-42} Guinier rod-like fitting: R_c=2.7±0.5 nm for the final stage of fibrillation. Aβ_{1-42} Genfit fitting with polydisperse cylinders model, $\chi^2 = 1.1$

been reported in the literature that the process of fibril formation, for example of

Aβ_{1-42} peptide [126], depends not only upon the specific conditions (ionic conditions, pH, temperature, mixing, etc.), as well as the manufacturing route (synthetic or recombinant), but also on the methods of synthesis and purification, even though all studied samples formed amyloid-like fibrils at pH 3-6, and the fibrils contained cross-β structures. For this reason, without prejudice to the characterization of the samples obtained so far by SAXS technique, for each interaction reported in the following chapters the reference protein will be the one measured in the same measurement session, to ensure a correct comparison.

Chapter 3

Hsp60 characterization and interactions

Contents

3.1 Introduction

Chronologically speaking, the discover of protein that assist the correct folding of other proteins in the cells has begun with the work of Georgopoulos and Hohn [127] in 1979, who identified a *groE* gene product of approximately 65 kDa that hydrolyzed ATP (Fig. 3.1). The term "molecular chaperones" was firstly utilized by Laskey in 1978, referring to the nucleoplasmin, a protein required for nucleosome assembly. In 1986, instead, Ellis used the term referring to "a class of cellular proteins whose function is to ensure that the folding of certain other polypeptide chains and their assembly into oligomeric structures occur correctly" [129] . During 80s, the genetics of bacterio-phage morphogenesis together with the synthesis of Rubisco in chloroplast lead to the knowledge of the existence of proteins that, contradictory in respect to Anfinsen's paradigm, have to assist the correct folding of protein inside the cells (helping them to climbing over the energy barriers, as depicted in Fig. 3.1 and illustrated in section 2.1.2).
The explanation for the cell's remarkable efficiency in promoting protein folding was yet individuated in chaperones, a class of proteins found in all organisms from bacteria to humans. Chaperones are located in every cellular compartment, bind

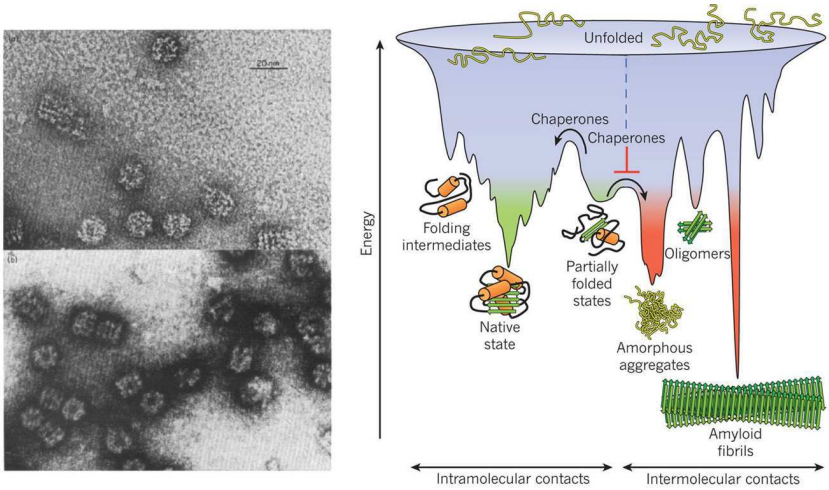

Figure 3.1: Left: Bright field and dark field of negatively stained preparation of groE complexes. From [127]. Right: the chaperones help the protein to reach the correct conformation in the energy landscape, from [128].

a wide range of proteins, and function in the general protein-folding mechanism of cells. They have also a broad range of conformations and molecular weights, and very different functions. From the very broad class of molecular chaperones, a narrower selection called "chaperonins" can be identified. Chaperonins are defined as the class of chaperones that assist in folding of (largely) newly synthesized proteins with the help of ATP. While the main role of chaperones is to maintain protein homeostasis, chaperonins have a more specific function. They are usually barrel shaped and have a hydrophobic chamber to facilitate folding without the effects of crowding (see Fig. 3.2). They are divided into two different subgroups, i.e. the type I and type II chaperonins. The first class is composed by proteins in Eubakteria and Eukarya (mitochondrial proteins) while the second class assemble Archaea and Eukarya (cytosolic) proteins. We concentrate our discussion on Type I, and specifically on human Hsp60. Heat shock proteins (Hsps), who owe their name to their upregulation immediately after a heat shock, play crucial roles in bio-synthesis, folding/unfolding, transport and assembly of other proteins.
Hereafter, a brief introduction to the structures of Hsp60 and GroEL will be presented, stressing the differences between the two forms of Hsp60 that can be found in human cells: the naïve and mitochondrial mtHsp60.
After this, experimental results on the in-solution structures of the chaperonins will be presented. In fact, even if the bacterial GroEL have been extensively studied [130, 131], the structure of human Hsp60 has been obtained only in 2015 [132] and in presence of the co-chaperonin. Even more, our SAXS results underline differences between GroEL in-solution and crystallographic structure, suggesting the need of a multidiciplinary approach (in this case MD and SAXS) to reveal the actual configuration in physiological conditions. After the reconstruction of GroEL and Hsp60,

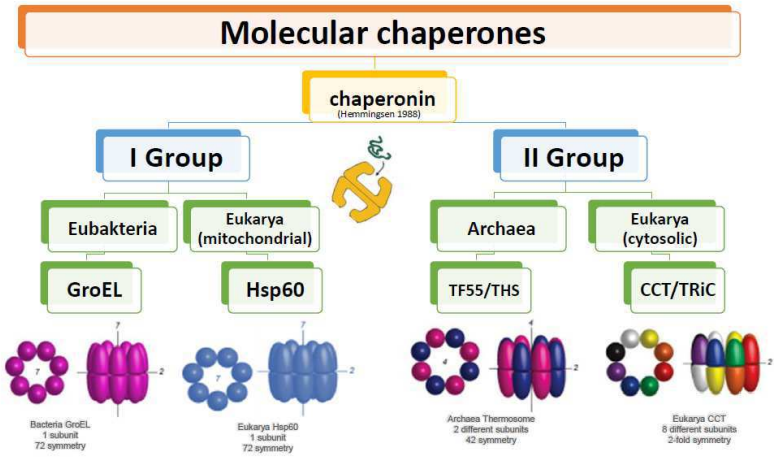

Figure 3.2: Classification of chaperonins in the class of molecular chaperones.

their stability has been considered and compared, by means of Circular Dichroism and SAXS. The stability and unfolding energy for the three proteins have been obtained, introducing a differentiation between the three proteins that can be addressed either to the different structure (the presence of a MIS tail in the naïve Hsp60) or to a different evolutionary pathway. Results reported in this section have been published in [19, 133, 134]. Further analysis will be conducted on the conformation and stability of the proteins in presence of their co-chaperonins and ATP. The last section is dedicated to a SAXS analysis of the interaction between mtHsp60 and Aβ_{1-42}. The results of Hsp60 action towards the fibrillation process of the peptide demonstrate the ability of the chaperone to target Aβ_{1-42} species responsible for the induction of amyloid protein assembly. Although the specific mechanisms by which the presence of the chaperone inhibits Aβ_{1-42} protein aggregates remain to be elucidated, this result further confirm the extraordinary potentiality of molecular chaperones in interfering with the crucial molecular steps leading to amyloid aggregation in neurodegeneration [135, 136] with an "unactivated" mechanism, i.e. without ATP. This result can be deepen coupling the "unactivated" effect with the active one, even in presence of the co-chaperonin.

3.1.1 Chaperonin structures

GroEL and Hsp60 are arranged in a tetradecameric structure with a barrel shape obtained by two stacked heptameric rings. Their correct functioning is also assisted by the 10 kDa co-chaperonin GroES for GroEL and Hsp10 for Hsp60, that act as a cap covering the central cavity of the tetradecamer (see Fig. 3.3, left). The client polypeptide to be folded interacts with the inner side of the central cavity by means of hydrophobic residues and ATP hydrolysis induces conformational changes (from *cis* to *trans* conformation, i.e. from the open cavity to receive the substrate

molecule to the closed cavity) [137]. After these changes, the chaperonin and the co-chaperonin separate and the correctly folded protein is released [138].
Each chaperonin monomer is constituted of three structural domains: the apical, intermediate and equatorial (see Fig. 3.3, right). The 547 aminoacids that compose

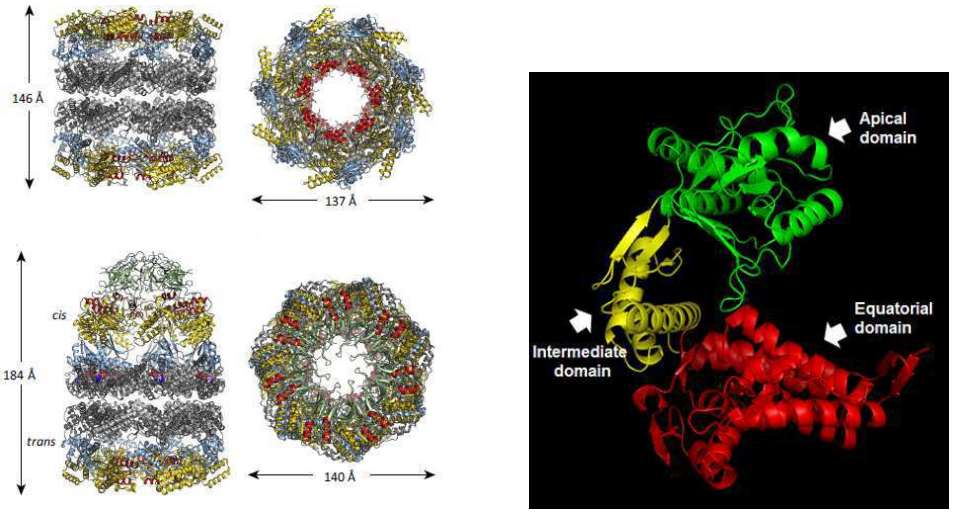

Figure 3.3: Left: in top sketches are represented crystal structures of GroEL (PDB code 1SS8). In the bottom sketches, views of GroEL in complex with the cofactor GroES (green) in the presence of ADP (PDB code 1PF9). The bound nucleotide is shown in space-filling mode, from [139]. Right: representative snapshot with the Hsp60 domains shown in green (apical), yellow (intermediate), red (equatorial). From [138].

the monomer, for GroEL and Hsp60, have different roles in binding the substrate protein and in creating the tertiary structure of tetradecamers and heptamers and link to the co-chaperonin [138]. In the panel shown in Fig. 3.4, a representation of the principal amino-acids involved in the GroEL structure is presented. In particular, there are highlighted hydrophobic/aromatic residues that contribute to substrate binding and in the binding of ATP/ADP (Fig. 3.4, top, left and center), the ones involved in the interaction between equatorial domains (Fig. 3.4, top right) and intermonomer–intraring contacts (Fig. 3.4, bottom). On the basis of data from the GroEL crystal structure and from the alignment of many diverse Hsp60 sequences from different species, including humans, various authors have identified highly conserved sequence segments and residues [141, 142]. The human Hsp60, but not GroEL, has cysteine residues (Cys237, Cys442 and Cys447), that can be interesting for developing Hsp60-binding compounds [138].

In a single cycle of ATP hydrolysis, GroEL, such as Hsp60, binds the substrate proteins in its inner cavity, is then capped by the GroES heptamers, binds and hydrolyzes 14 ATP folding the substrate protein and ejects the correctly folded components (Fig. 3.5), all in a matter of tens of seconds [143, 144]. After the substrate protein is bound in the cavity of the first inner cage and has been capped by the co-chaperonin, different scenarios have been depicted on the mechanism in

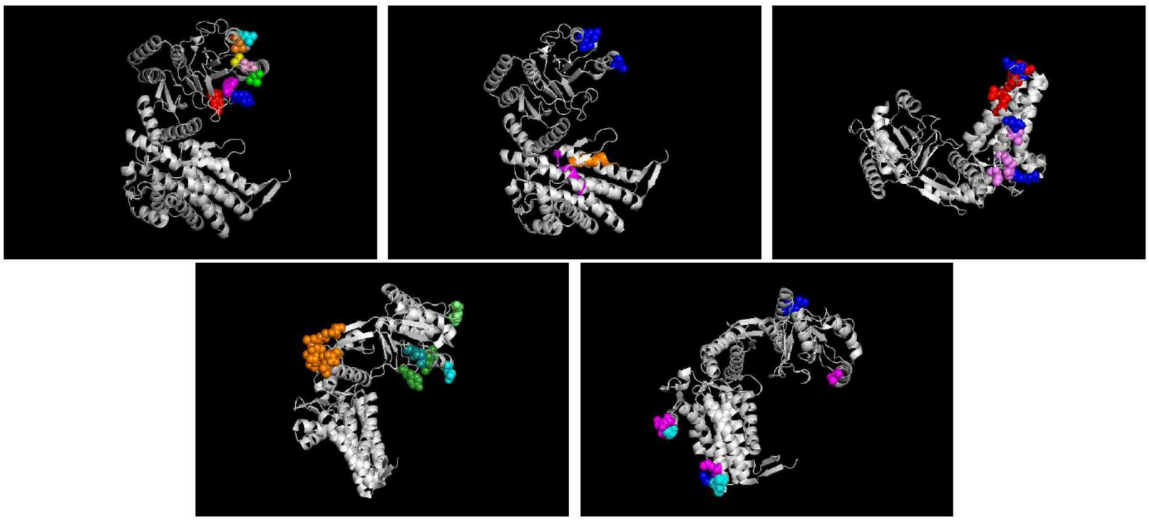

Figure 3.4: Top, left: Amino acids involved in substrate binding in Hsp60: Y199 red, Y203 blue, F204 magenta, L234 cyan, L237 orange-brown, L259 yellow, V263 pink and V264 green.
Top, center: the two highly conserved sequences: 52-DGVTVAKEI-60 (orange-brown), and 85-AGDGTTTATVL-95 (magenta) corresponding to the binding sites for Mg+/K+ and ATP/ADP and the hydrophobic conserved residues L234 and L237, and N265 on the surface of GroEL are shown in blue.
Top, right: hydrophobic contact residues I6, L73, L513, T517 and V521 (all in red) interact with hydrophobic residues V39, L40, I49 and I60 (all in light violet) on the opposite surface. The charged residues K4-E518 and E61-R36 (all in blue) also participate in the intermonomer-intraring interactions.
Bottom, left: intermonomer–intraring contacts of Y203, V263 and V264 in the apical domain (forest-green color) interact with D304, the unaligned position 305, and with G306 (lime green). E257 (cyan) on one surface interacts with R268 and G269 (teal) on the opposite surface. Conserved residues in contiguous intermediate domains at positions 181 – 183 and 383 – 389 (orange).
Bottom, right: the interactions between rings (V464, K105, E461 and E467 (all in magenta)) and the small residues A108, A109, and S463 (cyan). E434 and D345 are shown (both blue), which contribute to the salt-bridge K105-E434 and to allosteric switch.
The figures were generated using the PyMOL program [140].

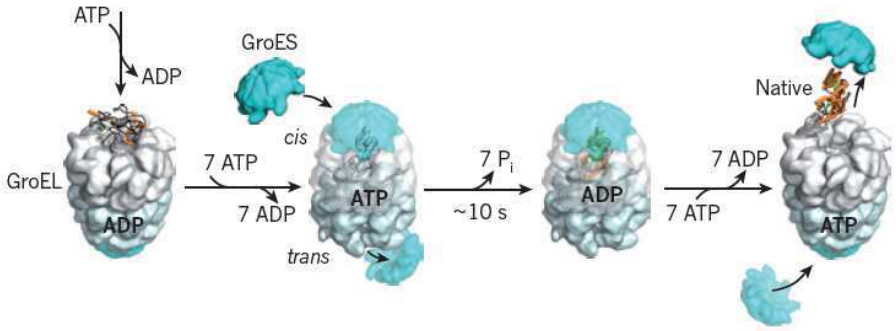

Figure 3.5: Substrate binding to GroEL with GroES. Structural model is based on PDB accession 1AON. From [128].

which the two folding chambers work [128], conflicting between an "asymmetric bullet cycle", in which each chamber functions alternatively and the possibility instead that both folding chambers can be working together and at the same time. Recent findings suggest the conversion of the symmetric, football-shaped GroEL-$GroES_2$ complex to the asymmetric, bullet-shaped GroEL-$GroES_1$ complex depending upon the stochastic hydrolysis of ATP and the development of nucleotide asymmetry between the rings [131]. Moreover, single-molecule analysis demonstrates that the first GroES to interact with GroEL is not necessarily the first one to dissociate from the symmetric complex and that the dissociation may occur randomly [145].

The folding mechanisms that have been proposed are strictly linked to the struc-

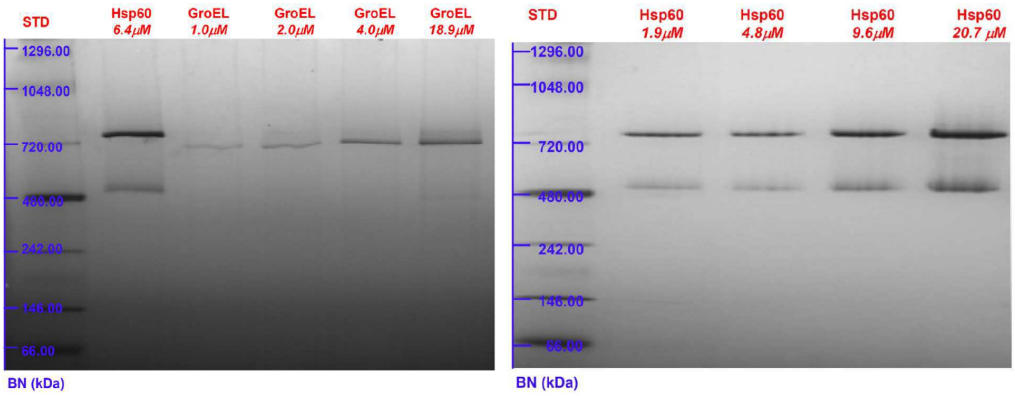

Figure 3.6: Left: Blue Native Polyacrylamide Gel Electrophoresis: comparison of Hsp60 with GroEL. Blue Native PAGE (4-16%) image of GroEL in the concentration range of 1.0-18.9 mM and Hsp60 protein at 6.4 mM; Right: Blue Native PAGE (4-16%) image of Hsp60 in the concentration range 1.9-4.8 mM. From [146].

tural arrangement of the proteins in solution. Nevertheless the high degree of homology, discrepancies have been found in the oligomeric equilibria of GroEL and Hsp60, giving the existence of Hsp60 as both a single and double-ringed football

shaped structure [147] and its dissociation in single heptameric rings and in 60kDa monomers [148]. More recently, structure and oligomeric state of the Hsp60, in absence of ATP and co-chaperonin, have been studied *in vitro* in a wide range of concentrations and with different biophysical techniques, in comparison with GroEL. Results have confirmed that it exists in solution in a dynamic equilibrium between two conformations: heptameric single rings and double ringed tetradecamers [146]. This is in contrast with GroEL behavior, that instead remains mostly in a tetradecameric barrel shaped form. As reported in Fig. 3.6, where Blue Native PAGE have been performed on the two chaperonins, while GroEL at different concentrations in the 1.0 to 18.9 mM range gives rise to a unique single band corresponding to the tetradecameric structure, the Hsp60 is resolved into two bands that can be attributed to the heptamers and tetradecamers. Similar structures were observed for the *Thermus thermophilus* chaperonin, as well [149]. This suggests that the human homologue may function alternating the two reaction mechanisms, where the tetradecamer exists as a football in its protein-folding state, but dissociates into two single rings in a certain amount at some point during the cycle.
The fact that the apo-protein has been observed in a single ringed conformation presents an intriguing challenge to the theory of chaperonin function. In addition, a better knowledge of Hsp60 structure and equilibrium in solution in comparison with the bacterial GroEL could shed new light on the functioning of homologue proteins in the different evolutionary patterns.

3.1.2 Two forms of Hsp60: the naïve and the mitochondrial one- Implications in diseases

Hsp60 is encoded and transcribed by a nuclear gene and translated in the cytosol. The newly translated ("naïve") polypeptide has a mitochondrial import signal (MIS), i.e. a sequence of 26 amino acids at the N-terminus that drives Hsp60 to the inside of mitochondria where the MIS is cleaved and the protein reaches the final conformation (mtHsp60, see Fig. 3.7). The different Hsp60s showed specific functional properties [150, 151, 152]. Even more, a peptide derived from the signal sequence MIS of human Hsp60 has been found to be present in human histocompatibility leukocyte antigen (HLA)-E and to be involved in the detection mechanism of stressed cells [146]. In situations like cancers or inflammatory pathologies, Hsp60 accumulates into the cytosol in its double form: the naïve that, once produced by the cell nucleus, never enters into mitochondria, and the mitochondrial one, secreted by the organella upon stress [153, 154]. Chandra *et al.* [155] demonstrated that in Jurkat and Hela cells, mtHsp60 directly interacts with procaspase-3 in cytosol enhancing caspase-3 maturation and activation in a pro apoptotic function, with or without mitochondrial release. mtHsp60 has been found associated with $\alpha 3\beta 1$-integrin, a protein involved in the adhesion of metastatic cancer cells [156]. In other systems that involve mainly naïve Hsp60 accumulation in cytosol, a classical chaperone role is supposed, since the protein knockdown is observed to favor cell death. In contrast to what happens for mtHsp60 case, in this case the peculiarity of Hsp60 bonding

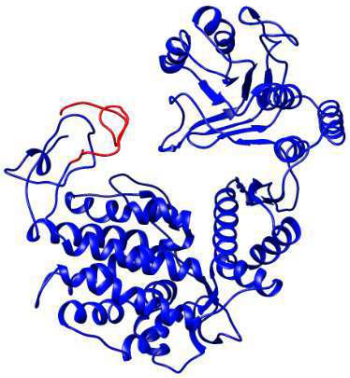

Figure 3.7: Naïve Hsp60: in red the MIS sequence is highlighted (MLRLPTVFRQ MRPVSRVLAP HLTRAY). The image is rendered using the structure from [19] and the UCSF Chimera package [157].

with procapsase-3 would embed protein activation inhibiting the apoptotic trigger. Collectively, these evidences suggest that there is a delicate equilibrium regulating the pro- and anti-apoptotic functions of Hsp60 in cells and tissues, that depends on mechanisms yet to be fully understood.

Since when the Hsp60 is imported into mitochondria, its folding and self-assembly from monomers to oligomeric species is mediated by functional pre-existing Hsp60 complexes that catalyze chaperonin folding in an ATP-dependent process [146], a study on the oligomeric equilibria of the two chaperonins, even in respect to GroEL, can allow to a deeper understanding of the folding mechanism *in vivo* and on the effective role of the chaperonin in the diseases and its therapeutic potentialities.

3.2 Materials and methods

In this section, the details of the different techniques exploited to characterize the chaperonins (mtHsp60, naïve Hsp60 and GroEL) structures, stabilities and interactions will be presented, to introduce the experimental section to follow. In particular, a software developed by the research group of Molecular Biophysics in the Polytechnic University of Marche for the specific reconstruction of assemblies in solution, starting from the experimental SAS curve and symmetries informations, QUAFIT, is displayed.

Proteins

The recombinant naïve Hsp60 was purchased from ATGen (Seongnam, South Korea) in stock solution at 16.0 μM (buffer 20 mM Tris pH 8.0 and 10% glycerol (w/w)). Lyophilized GroEL was obtained from SIGMA (St. Louis, MO, USA). As a step prior to the experiments, we verified that the chaperonins under analysis were able to properly work. Hence, ATP activities were measured by using the ImageJ Software, and they are (16.48±0.02) nmol ATP min^{-1} mg^{-1} for GroEL; (4.7±0.1) nmol min^{-1} mg^{-1} for naïve Hsp60; and (17.72±0.01) nmol ATP min^{-1} mg^{-1} for mitochondrial Hsp60 used as a protein reference (BostonBiochem). $A\beta_{1-42}$, purchased by Sigma Aldrich, was solubilized in hesafluoroisopropanol (HFIP), that was evaporated using a gentle stream of nitrogen gas. The protein was carried in ice to the beamline and dissolved just before the measurements in PBS.

Molecular dynamics and Principal Component Analysis

GroEL quaternary structure (PDB ID: 4AAR) was obtained from the protein data bank and ATP molecules were deleted. This analysis has been mainly performed by Angelo Spinello in Palumbo Piccionello research group, Department of Chemistry, set in the University of Palermo. The GroEL monomer used in the following simulations was taken from this structure. The tertiary structure of the Hsp60 monomer was predicted using Swiss-Model Software. The missing monomer residues were folded using ROSETTA modeling software and then added to the N- and C-endings of the model with the software Maestro. The fragment library was obtained from Robetta server. All MD simulations were carried out through the GROMACS 4.6.5 software package, by following a recently reported procedure. Amber ff99SB-ILDN force field was used. A triclinic box of TIP3P water molecules was added around the protein to a depth of 0.7 nm on each side. The charge of the protein was neutralized and other Na^+ and Cl^- ions were added to set the solution ionic strength to about 0.20 M. Explicit solvent simulations were performed in the isothermal-isobaric NPT ensemble, at a temperature of 300 K, under control of a velocity rescaling thermostat. The particle mesh Ewald method was used to describe long-range electrostatic interactions. The time step for integration was 2 fs and all covalent bonds were constrained with the LINCS algorithm. There were two temperature coupling groups in these simulations, the first for the protein and the second for water and ions.

Preliminary energy minimizations were run for 5000 steps with the steepest descend algorithm. During the equilibration, the protein system was harmonically restrained with a force constant of 1000 kJ mol^{-1} nm^{-2}, gradually relaxed into five consecutive steps of 100 ps each, to 500, 200, 100 and 50 kJ mol^{-1} nm^{-2}. RMSD were referred to the starting configurations of MD.
Principal component analysis (PCA) was obtained by diagonalizing the covariance matrix, which is built from the atomic fluctuations in a MD trajectory where overall translational and rotational motions have been removed. The monomer backbone atoms were used to construct the protein covariance matrices. Upon diagonalization of this matrix, a set of eigenvalues and eigenvectors was obtained. The eigenvectors correspond to directions in a 3N-dimensional space, and motions along a single eigenvector correspond to concerted fluctuations of atoms. The eigenvalues of the covariance matrix represent the total mean square fluctuation of the system along the corresponding eigenvectors. If eigenvectors are ordered according to their decreasing eigenvalues, the firsts describe the largest scale correlated motions. The trajectories were analysed using VMD software.

SAXS

SAXS measurements of naïve Hsp60 and GroEL were performed at ID02 beamline at the European Synchrotron Radiation Facility (ESRF) in Grenoble, France. The explored Q-range covers between 0.1 and 3 nm^{-1}, being the sample to detector distance set to 1.5 m. Experiments were carried out at 20 °C and 37 °C using a sealed 2 mm diameter quartz capillary enclosed within a thermostatic compartment connected to an external circulation bath and a thermal probe for temperature control. Both naïve Hsp60 and GroEL solutions were measured at the weight concentrations c=3 g/L, while the concentration of mtHsp60 was c=1 g/L and Aβ_{1-42} c=200 μM. Every measurement was performed for 100 ms, and followed by a dead time of 3 s in order to avoid radiation damage. Final SAXS $d\Sigma/d\Omega(Q)$ curves evidenced that both GroEL and Hsp60 show no difference in the temperature range 20-37°C.
SAXS data of mtHsp60, and mtHsp60 with Aβ_{1-42} were collected at the Austrian beamline of Elettra Synchrotron in Trieste, Italy [158]. Measurements were carried out at 20 °C in capillaries of 1.5 mm outer diameter/0.01 mm wall thickness made from borosilicate (Hilgenberg, Maisfeld, Germany) enclosed within a thermostatic compartment connected to an external circulation bath and a thermal probe for temperature control. We measured each sample 20 times with an acquisition time of 20 s and a rest time of 40 s for each step after a negative control for radiation damage and checked for consistency with literature values before usage. In both the experimental set up, two dimensional patterns were recorded by Pilatus3 1M detector system that is based on the CMOS hybrid pixel technology. The protein macroscopic differential scattering cross section, $d\Sigma/d\Omega(Q)$, was determined by subtracting from the protein in solution signal the one of the buffer, corrected by its volume fraction in the protein solution. We carefully checked each set of scattering pattern and performed the average after a positive control over radiation damage.

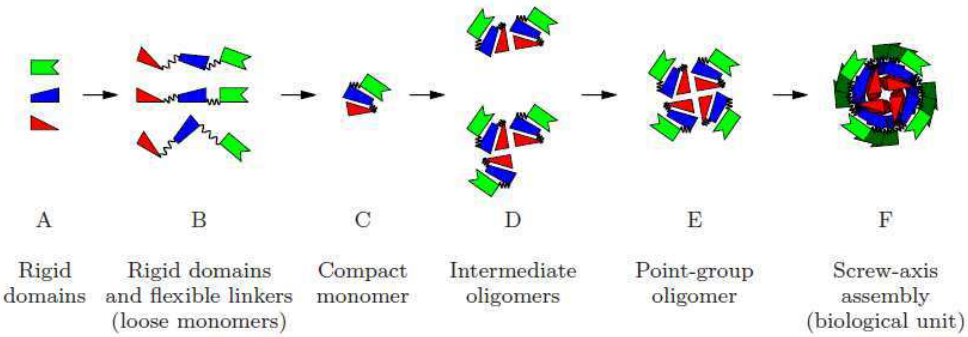

Figure 3.8: The biological assembly from the monomer to the quaternary structure

Circular Dichroism

CD spectra for the unfolding studies in Guanidine Hydrochloride (GdnHCl) were measured on a JASCO J-810 spectropolarimeter (CNR, Palermo) at 20 °C, with a 20 nm/min scan rate and 1 nm resolution, using a 0.5 mm optical path length. Protein concentration in samples at different GdnHCl concentrations was c = 0.05 g/L for GroEL and c = 0.1 g/L for Hsp60s. In order to minimize errors due to protein concentration the unfolding was evidenced by the ratio of CD signals at two different wavelengths (λ = 212 nm and λ = 223 nm).

QUAFIT

Theory

The QUAFIT method [159] allows to determine the quaternary structure of biological macromolecular assemblies by analyzing x-ray or neutron small-angle scattering data. The method is based on the idea that asymmetric monomers, formed by rigid domains of known atomic structure possibly connected by flexible linkers of known sequence, are assembled according to a point-group symmetry combined with a screw axis (see Fig. 3.8). QUAFIT establishes the form factor P(Q) of the assembly that better reproduces the macroscopic differential scattering-cross section provided by a SAS in-solution experiment as a function of the scattering vector modulus Q. The structural parameters that define the configuration of the assembly depends on the rigid domains ($d = 1...N_{RD}$) and on the flexible linkers assigned to the structure ($f = 1...N_{FL}$) and are defined by a) the three translation coordinates $\mathbf{u}_d \equiv u_d, \alpha_{u_d}, \beta_{u_d}$ and the three orientation coordinates $\omega_d \equiv \alpha_d, \beta_d, \gamma_d$, i.e. the Euler angles, for each of the N_{RD} rigid domain; b) a set of dihedral angles Γ_f for each flexible linker; c) two Ramachandran angles ϕ_g and ψ_g for each residue g and the torsion angle χ_g of the side group, the rotation angle α_{scr} around the screw axis and the translational distance d_{scr} along the axis. The form factor of the assembly

is the orientational average of its squared amplitude

$$P(Q) \equiv \left\langle |F(Q)|^2 \right\rangle_{\omega_Q} = \frac{1}{4\pi} \sum_{l=0}^{L} \sum_{m=-l}^{l} |F_{l,m}(Q)|^2 \tag{3.1}$$

where $< ... >_{\omega_q}$ denotes the average over the polar angles ω_q of the scattering vector Q, and $F_{l,m}(Q)$ is the spherical tensor (with rank l and component m) of the assembly excess amplitude expanded in spherical harmonics up to the maximum rank L. This tensor can be written in terms of the individual tensors for the isolated assembly, the solvent displaced by the assembly, and the solvation shells of the assembly,

$$F_{l,m}(Q) = \sum_{j} c_j \Psi^j_{l,m}(Q) \tag{3.2}$$

where c_j contains the scattering length densities of the solvent, ρ_0, and of the solvation shells, ρ_s; $\Psi^j_{l,m}(Q)$is obtained by summing the amplitudes $\Psi^{d,j}_{l,m}(Q)$ and $\Psi^{f,j}_{l,m}(Q)$ respectively of rigid domains and flexible linkers, which should have been formerly symmetrized according to all the point group and screw axis operations

$$\Psi^j_{l,m}(Q) = \sum_{d=1}^{N_{RD}} \Psi^{d,j}_{l,m}(Q) + \sum_{f=1}^{N_{FL}} \Psi^{f,j}_{l,m}(Q) \tag{3.3}$$

Different controls allows to avoid non-consistent solutions.
In the backbone control of not superimposition of the structure, a first test consist in the control that the linker the distance $r_{f,k,k'}$ between two atoms k and k' of the backbone not covalently bound is lower than the sum of their van der Waals radii r_{vk} and $r_{vk'}$, respectively. The backbone control of all the linkers is carried out using a term of backbone penalty of the monomer, which should be minimized

$$U_{bb} = w_{bb} \sum_{f=1}^{N_{FL}} \sum_{k>k'} H(r_{vk} + r_{vk'} - r_{f,kk'}) \tag{3.4}$$

where $H(x)$ is the Heaviside step function and w_{bb} an arbitrary penalty weight. In analogy, a second test regards the overlap between the side groups of the residues g and $g0$. In analogy with the backbone penalty, the side-group penalty term has the expression:

$$U_{side} = w_{side} \sum_{f=1}^{N_{FL}} \sum_{g>g'} H(r_{scg} + r_{scg'} - r_{f,gg'}) \tag{3.5}$$

where r_{scg} is the effective radius of the g-side group and $r_{f,gg'}$ is the distance between the geometrical centers, $u_{f,g}$ and $u_{f,g'}$, of the two groups g and g', w_{side} is an arbitrary penalty weight.
To control the capability of the linker to connect two rigid domains, in the QUAFIT algorithm, the left-end of the f-linker is attached with the right-end of a chain belonging to the d-domain. On the contrary, the right-end of the f-linker is connected

to the left-end chain of a d'-domain only for some values of the set of dihedral angles Γ_f . Four representative atoms of the right-end residue of the f-linker are hence taken under control by calculating the average distances r_f between their positions (denoted as $u'_{f,R,k}$ and those they should take to ensure proper connections ($u_{f;R;k}$)),

$$r_f = \frac{1}{4}\sum_{k=1}^{4} |u'_{f,R,k} - u_{f,R,k}| \tag{3.6}$$

The connection control of all the linkers is then performed introducing a monomer elastic energy term that should be minimized

$$U_{conn} = \frac{1}{2} K \sum_{f=1}^{N_{FL}} r_f^2 \tag{3.7}$$

where K in the generalized elastic force constant. The optimum configuration of rigid domains within the assembly should avoid any overlap among them, but should also maintain the continuity of the whole structure. The crucial point is to find the shortest approaching distance ("Contact Distance") of two intrinsically asymmetric RDs.
The shape of a rigid domain is defined by the probability $G_d(r)$ that an atom in position r belongs to the d-RD:

$$G_d(r) = \sum_{k=1}^{N_{ad}} e^{-\frac{\pi |r - r_k|^2}{v_k^{2/3}}} \tag{3.8}$$

where r_k is the position of the k atom out of N_d atoms of the rigid domain, v_k is the relative core volume, defined in terms of the Van der Waals radius $r_{v,k}$. The overlap volume between d and d' rigid domains can be written as:

$$V_{d,d'}(\omega_d, \omega_{d'}, r_{d,d'}) = \sum_{l_1,l_2=0}^{L'} \sum_{l_3=|l_1-l_2|}^{l-1+l_2} \sum_{k_1=-l_1}^{l_1} \sum_{k_2=-l_2}^{l_2} [\phi_{dd'}]_{k_1,k_2}^{l_1,l_2,l_3}(r_{d,d'}) S_{k_1,k_2}^{l_1,l_2,l_3 *}(\omega_d, \omega_{d'}, \omega_{r_{dd'}}) \tag{3.9}$$

where $S_{k_1,k_2}^{l_1,l_2,l_3 *}(\omega_d, \omega_{d'}, \omega_{r_{dd'}})$ are the Stone's rotational invariants, an expansion basis set of orthogonal functions in the space of eight angular variables. Contact distances are invariant under reference system rotation: hence, they can be expanded in series of Stone Invariants,

$$\sigma_{d,d'}(\omega_d, \omega_{d'}, \omega_{r_{d,d'}}) = \sum_{l_1,l_2=0}^{L'} \sum_{l_3=|l_1-l_2|}^{l-1+l_2} \sum_{k_1=-l_1}^{l_1} \sum_{k_2=-l_2}^{l_2} [\sigma_{dd'}]_{k_1,k_2}^{l_1,l_2,l_3}(r_{d,d'}) S_{k_1,k_2}^{l_1,l_2,l_3 *}(\omega_d, \omega_{d'}, \omega_{r_{dd'}}) \tag{3.10}$$

they are defined as the minimum approaching distances $r_{dd'}$ to which corresponds to a small value ($\simeq$30 Å^3) of the overlap volume $V_{dd'}(\omega_d, \omega_{d'}, r_{dd'})$. Expansion coef-

ficients are independent of any positional or orientational coordinates

$$[\sigma_{dd'}]_{k_1,k_2}^{l_1,l_2,l_3} = (2l_1+1)^{\frac{1}{2}l_2-l_1-l_3}(-1)^{k_1+l_2}\sum_{m_2=-l_2}^{l_2} C(l_2,l_3,l_1;m_2,k-1-m_2)\times$$
$$\times\frac{(2l_2+1)(2l_3+1)}{32\pi^3}\int d\omega_{d'}d\omega_{r_{dd'}}\sigma_{dd'}(\{0,0,0\},\omega_{d'},\omega_{r_{dd'}})D^{l_2^*}_{m_2,k_2}(\omega_{d'})D^{l_3^*}_{k_3,0}(\omega_{r_{dd'}}) \tag{3.11}$$

They can be used in to easily obtain the Contact Distances between d-RD and d'-RD for any arbitrary combination of the eight angular variables, allowing a suitable implementation of the method in a SAS data fitting program. The Stone's invariants expansions are among the first parameters the software calculates and can be time consuming depending on the dimension of the assembly.
The Lennard Jones potential, based on the shape anisotropy, is defined in terms of $sigma_{dd'}$:

$$U_{LJ,dd'}(\omega_d,\omega_{d'},r_{d,d'}) = 4\varepsilon_{dd'}\left\{\left[\frac{\sigma_{dd'}(\omega_d,\omega_{d'}\omega r_{dd'})}{r_{dd'}}\right]^{12} - \left[\frac{\sigma_{dd'}(\omega_d,\omega_{d'}\omega r_{dd'}}{r_{dd'}})\right]^{6}\right\} \tag{3.12}$$

It describes both the short-range attraction between RDs and their strong repulsion due to the forbidden overlap, and where $\varepsilon_{dd'}$ is the depth of the potential well (in arbitrary units). We can thus introduce the Lennard-Jones domain-domain potential of the assembly,

$$U_{RD,RD} = \frac{\sum_{p=1}^{N_p} m(dd')_p U_{LJ,dd'_p}(\omega_d,\omega_{d'}\omega r_{dd'})}{\sum_{p=1}^{N_p} m_{dd'_p}} \tag{3.13}$$

being $m_{dd'_p}$ the multiplicity of the p^{th} pair of RD. In analogy, two new terms (the Lennard-Jones domain-linker potential of the assembly, $U_{RD,FL}$, and the Lennard-Jones linker-linker potential of the assembly, $U_{FL,FL}$) are introduced.
The optimum configuration is found by minimizing the target functional H defined as

$$H = \chi^2 + U_{linkers} + U_{overlaps} \tag{3.14}$$

Where $U_{linkers} = U_{bb} + U_{side} + U_{conn}$, $U_{overlaps} = U_{RD,RD} + U_{RD,FL} + U_{FL,FL} and$

$$\chi^2 = \frac{1}{N_Q - 1}\sum_{k=1}^{N_Q}\left\{\frac{\frac{d\Sigma}{d\Omega_{exp}}(Q_k) - \frac{d\Sigma}{d\Omega}(Q_k)}{\sigma_{exp}(Q_k)}\right\}^2 \tag{3.15}$$

where $\frac{d\Sigma}{d\Omega_exp}(Q_k)$ is the macroscopic differential scattering cross section at the k^{th} out of N_Q points of the experimental SAS curve, with uncertainty $\sigma_{exp}(Q_k)$, $\frac{d\Sigma}{d\Omega_exp}(Q_k)$ is the model scattering cross section at the same point provided by the QUAFIT method. In the case of assemblies uniformly distributed over a discrete number N_{conf} of different configurations, which share the same rotational point group G

and the same number N_t of rototranslations around the screw axis,the form factor is a simple average over all the configurations,

$$P(Q) = \frac{1}{N_{conf}} \sum_{k=1}^{N_{conf}} P_k(Q) \tag{3.16}$$

Similar expression are defined for the averages of the different potentials. An oligomerization intermediate is defined as a point-group oligomer in which not all the symmetrical positions are occupied by monomers. The complete oligomer can be assumed to form according to a hierarchical assembling of all the possible intermediates. In the case of weak association forces, all intermediates together with the complete oligomer will be simultaneously present in solution. The SAS curve of such a complex system constituted by N_{obj} possible particles is

$$\frac{d\Sigma}{d\Omega}(Q) = \frac{cN_A}{M_{w,m}} \sum_{j=1}^{N_{obj}} \frac{x_j}{N_{agg_j}} P_j(Q) + B \tag{3.17}$$

where N_{agg_j} is the aggregation number of the $j-th$ particle, x_j is the fraction of the whole biomolecule mass involved in the formation of the $j-th$ particle.

Quafit in naïve Hsp60 structure

For GroEL reconstruction, according the MD results and on the basis of the PDB 4AAR structure, two units constituting the monomer have been considered as rigid domains (RDs). The first RD includes the N- and the C-terminus referred to as equatorial and intermediate domains. It is defined from residue 1 to 187 and from 377 and 524. The second RD includes the amino acids from 192 to 372. As a consequence, the two RDs result to be connected by two flexible linkers, both arranged by 4 amino acids. The first FL, defined by the sequence DVVE, connects the residue 187 of the first RD to the 192 of the second RD. The other FL (AGGV) connects the residue 372 of the second RD to the 377 of the first RD. This monomer can form tetradecamers based on the symmetry point-group D7.
The reconstruction of the Hsp60 structure has been performed by dividing the monomer unit, constituted by 573 residues, in three RDs. The first RD includes N- and C-termini and encompasses residues from 1 to 22 and from 553 to 573. The second RD is from residue 27 to 210 and from 401 to 547. The third RD, from 215 to 396, is the apical red domain. Accordingly, four FLs are defined. The first FL, sequenced as TRAY, connects the residue 22 of the first RD to the 27 of the second one. The second FL (LEII) is from residue 210 of the second RD to the 215 of the third one. The third and the fourth FLs (LSDG and EIPKE, respectively) connect residues 396 (third RD) and 401 (second RD) and residues 547 (second RD) and 553 (first RD). A unique optimized structure of the monomer is assembled according to the symmetry groups D7 and C7 to define the quaternary structure of the

```
********************** Input Data File for Quafit 4.0 **********************

OPTIMIZATION PARAMETERS %%%%%%%%%%%%%%%%%%%%%%%%%%%%%%%%%%%%%%%%%%%%%%%%%%%

Number of Cycles per Sub-Run .........:5
Maximum Number of Sub-Run ............:50
Hypothetical Final H(X) ..............:0.02
Constant Value of T* (if not 0.0) ....:0.0
Iterations Number for Error Analysis .: 0
Maximum Rank L for [A^i][l,m](Q) .....:7
Maximum Rank L for [A^i]^S[l,m](Q) ...:7
Maximum Rank L for S[l1,l2,l3,k1,k2] .: 3
Maximum Q of A[l,m](Q) ...............:0.3
Number of Q's for A[l,m](Q) ..........:120
TCP Packing Distance (Angs.) .........:2.8
Number of Hydration Shells ...........: 1
Well Depth of LJ potential (epsilon) .: 5.0
Force Constant of Linker's Ends (K) ..: 0.15
Linker Lateral Chains Overlap Penalty : 1.
Two linkers CA-CA Overlap Penalty ....: 1.
CA linker - Domains Overlap Penalty ..: 1.
.....................................:
Number of Zeros for Integration ......: 32
Number of Bins for Integration .......: 1
Number of Points for 3D Plots ........: 31
Reference Temperature (Celsius) ......:0.0
Reference Pressure (bar) .............:1.0
Stone Exp. Contact Dist. Family Name .:chaperonin/s_abeta_12_2_
Stone Exp. Contact Dist. Flag (1/0) ..:0
A[l,m] Calculation Flag (1/0) ........:1
Dummy Atom Shell Determination .......:1
Read HETATM atoms in PDB file (1/0) ..:0
Free / Thermod.-linked fractions (1/0):1
Optimisation free fraction (1/0) ......0
Plot Random Contact Distances (1/0) ..:0
No-Overlap test connected-RD (1/0) ...:0
Mixed D5/C5 symmetry (1/0) ...........:0
Exponent alpha of power-law error fu..:0.8
Reduction contact distances (Angs.) ..:0.0
```

Figure 3.9: Example of the input file for QUAFIT routine

```
**************** Amino acid Constraints
 AA |RD|SS|POL| Atom|Coord.vector r_i |     Condition     |Val,Name,Vec.u_d |Fact.Val.|Method|   K    |Name  |Flag
    |FL|  |   |     |x,y,z,r,a,b,rc,ac|=,>,>=,<,<=,max,min|x,y,z,r,a,b,rc,ac|         |st,el |        |      |1/0
2    1  1  1    CA      r                    <=           r               0.25      el      1.0            1
524  1  1  1    CA      r                    <=           r               0.25      el      1.0            1
2    1  1  1    CA      z                    <            0.0                       el      1.0            1
524  1  1  1    CA      z                    <            0.0                       el      1.0            1
******** Pairs of Amino acid Constraints
i:AA|RD|SS|POL|i:Atom|j:AA|RD|SS|POL|j:Atom|Coord.vector r_ij|     Condition     |Val,Name,Vec.u_dd|Fact.Val.|Method|   K    |Name  |Flag
    |FL|  |   |     |    |FL|  |   |     |x,y,z,r,a,b,rc,ac|=,>,>=,<,<=,max,min|x,y,z,r,a,b,rc,ac|         |st,el |        |      |1/0
 2   1  1   1   CA    193  2  1   1    CA          r                   >                20.                 el      1.0            1
```

Figure 3.10: Constraints on aminoacids position and on aminoacids relative distance

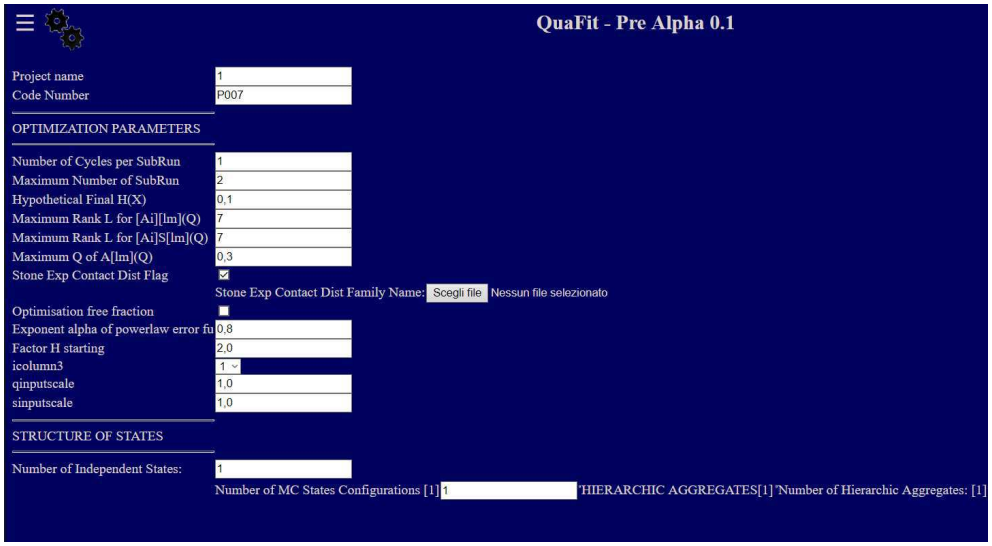

Figure 3.11: Quafit screenshot from https://somo.chem.utk.edu/quafit/

tetradecamer and the heptamer, respectively. The set of geometrical parameters optimized by QUAFIT includes the three polar coordinates of the geometrical center of each RD, the three Euler angles defining the orientation of each RD, the three dihedral angles that define the conformation of each residue belonging to each FL (two Ramachandran angles for the backbone and one angle for the side chain group). Moreover, in the case of Hsp60, QUAFIT also optimizes the molecular fraction of monomers forming tetradecamer. The maximum rank L of the spherical harmonics expansion of the partial X-ray scattering amplitudes has been fixed to 7. Contact distances among pairs of RDs are expanded in series of Stone's rotational invariant up to a maxim rank L'=3. SAXS curves have been analyzed in the whole range of Q. With the information illustrated in section 3.1.1, different resulting structures were excluded, even with a low χ^2.
When the analysis of the structure has been proposed the software was installed on a University server. It took in input a .dat file with specified all the parameters to allow the reconstruction and the SAXS curve (Fig. 3.9). During this analysis the software was implemented to refine the structure adding some constraints between known atoms and aminoacids (see Fig. 3.10). Nowadays, the software is implemented in a software platform (see Fig. 3.11), to allow the accessibility for registered users (https://genapp.rocks).

3.3 Characterization and stabilities of chaperonins

Given the shown importance of the determination of these proteins' structure, firstly the in solution shape of GroEL, and after that of naïve Hsp60 in comparison with GroEL, have been reconstructed and are presented in this section. After this, the denaturation path of GroEL, naïve and mtHsp60 against a chemical agent (Guanidine Hydrochloride, GdnHCl) will be characterized, to obtain information on their relative oligomeric stabilities.

3.3.1 Characterization of GroEL and naïve Hsp60

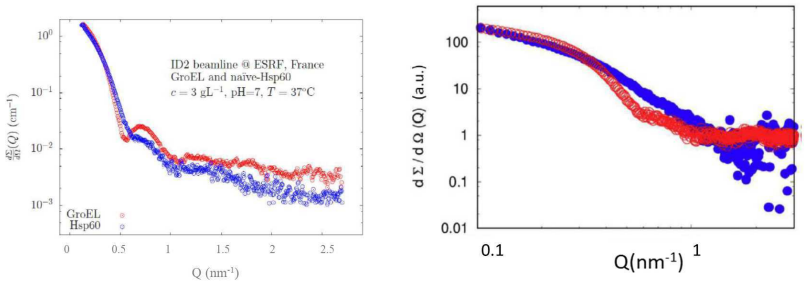

Figure 3.12: Left: differences in the structures of GroEL (red) and naïve Hsp60 (blue), measurements performed at ESRF, BM29 biosaxs line. Right: differences between naïve (blue) and mtHsp60 (red), measurements performed in Elettra synchrotron, Trieste.

In this context we used SAXS to obtain information on the conformation of the chaperonines in solution and refined our analysis with the aid of other techniques, in particular of Circular Dichroism (CD) and Molecular dynamics (MD) [19].
A first SAXS experimental observation of the proteins in solution shows different features for GroEL and naïve Hsp60, and for naïve and mtHsp60, even if at low resolution (Fig. 3.12). This result turned out to be interesting for the three proteins and in particular for to determine the structure of GroEL in physiological conditions. In fact, although several crystallographic structures of GroEL are deposited in the Protein Data Bank, these differences could not be interpreted with any of the PDB reconstructed present in literature (applying the SASMOL approach included in the Genfit software package, see section 1.2.2.5 and [8], which uses the spherical harmonic expansion of the scattering amplitudes, similar to the widely known CRYSOL software, as reported in Fig. 3.13, upper panel).
GroEL SAXS experimental curve, anyway, looks similar to the one obtained by Arai et al. [160], confirming the accuracy of our experimental results and suggesting that significant differences between solution and crystallographic GroEL structures exist. Since both tetradecameric and heptameric GroEL PDB structures are reported, an attempt to fit the SAXS curve by combining the presence of both oligomers in solution was done: no combination of these quaternary structures could satisfactorily fit the experimental data (Fig. 3.13, bottom panel). In particular, while the position of

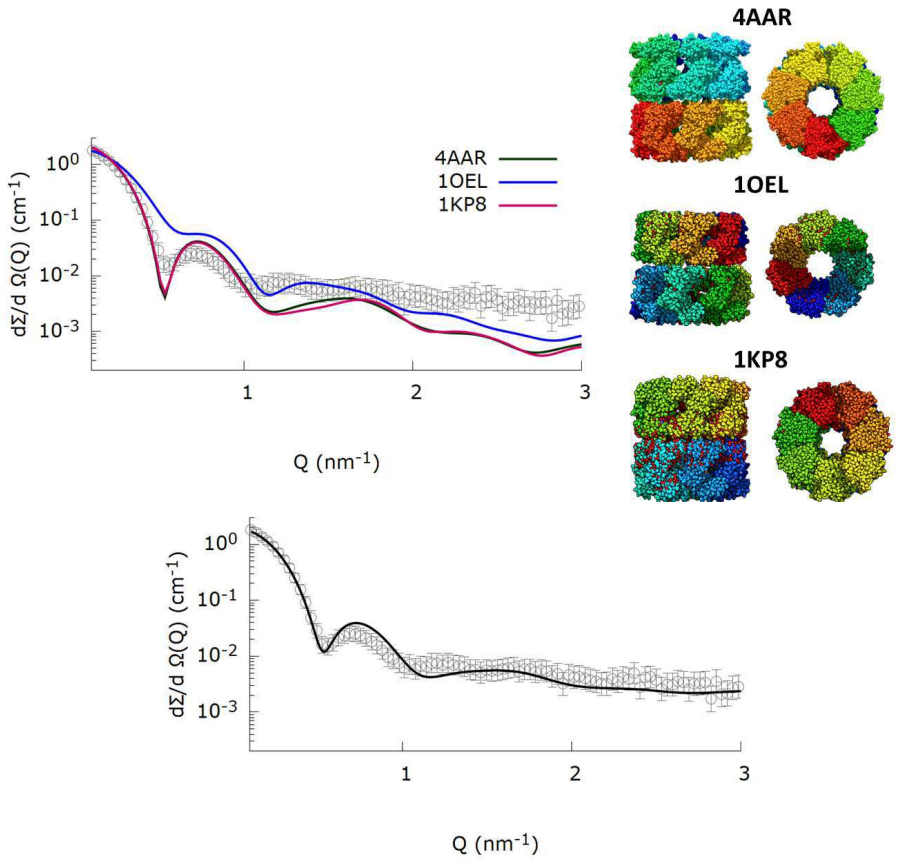

Figure 3.13: SAXS experimental profiles of GroEL (open circles, c=3 gL-1) with tentative fitting curves obtained from the crystallographic structures indicated in the legend (Top), and from a combination (Bottom) of tetradecamers and heptamers from the 4AAR PDB structure computed by the GENFIT software [8]

the first minimum at $Q \simeq 0.5$ nm^{-1} is well fitted, its shape and intensity is not adequately reproduced. As showed in literature [146], GroEL do not present in solution an equilibrium between heptamers and tetradecamers but a unique tetradecameric state. The GroEL overall shape in solution was hence reconstructed starting from SAXS data.

3.3.2 GroEL structure in solution

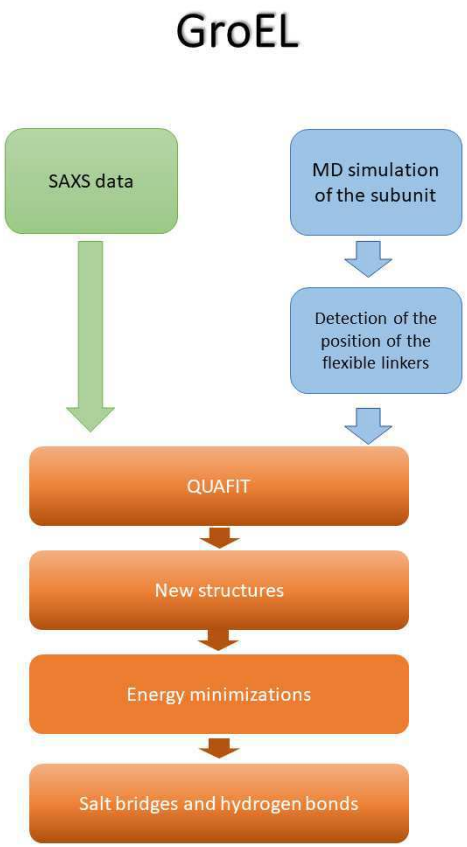

Figure 3.14: Workflow for GroEL reconstruction

Since all-atom MD simulations on GroEL tetradecameric barrel-shaped structure (PDB ID: 4AAR) resulted to be a non-suitable procedure to reach an acceptable fitting of SAXS data within reasonable time, being extremely time consuming, to

provide the structure of the chaperonin GroEL in aqueous solution under physiological conditions, the flexibility of the monomer of GroEL has been exploited [161, 130] to explore its conformation. Starting from the monomer from the 4AAR PDB entry, its flexibility was investigated by means of MD simulations, and the structure of the tetradecamer was reconstructed by simultaneously finding the best conformation of the MD modified flexible monomer and the best positioning of the tetradecameric structure, assembled according to the D7 point group symmetry, satisfying the fitting of the experimental SAXS curve (for a schematic representation of method's workflow see Fig. 3.14). To determine the position of flexible linkers, a 300 ns MD

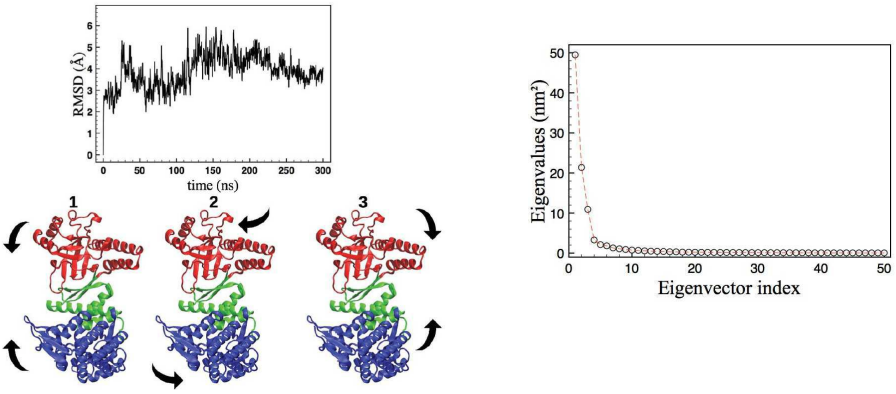

Figure 3.15: Left: RMSD plot of the Cα atoms of the GroEL subunit (Top). Schematic representation of the relative domains motion along the first three eigenvectors (Bottom). GroEL domains are highlighted by different colors, i.e. equatorial (blue), intermediate (green) and apical (red) domains, respectively. Right: Eigenvalues of the first 50 eigenvectors relative to the PCA from 300ns MD of GroEL subunit.

simulation on the GroEL monomer extracted from the ring T of 4AAR PDB entry has been performed. The RMSD relative to the starting configuration is depicted in Fig. 3.15 left, showing that the isolated subunit explores a wide conformational space, also in the absence of bound ATP molecule. Monomer's flexibility modes, evidenced by means of the principal component analysis (PCA), reveal the presence of three principal eigenvectors, out of fifty, relative to the main conformational fluctuations (see Fig. 3.15, right). Representatively, the relative movements of these eigenvectors are schematically depicted in Fig. 3.15, bottom left. The QUAFIT analysis [159] to reconstruct tetradecamers starting from the PDB of the monomer have been performed (see section 3.2) considering two flexible linkers in the border region between the apical and the intermediate domains (the two linkers are composed by residues 188-191 and 373-376, respectively). Interestingly, in the isolated monomer the apical domain (shown in red in Fig. 3.15) can move with respect to the equatorial (blue) and intermediate (green) domains, which result to be tightly bound, as already evidenced within the tetradecameric structure, thus confirming the choice of the flexible linkers as the hinge of these relative movements. Furthermore, a residue root mean square fluctuations (RMSF) analysis confirms that selected se-

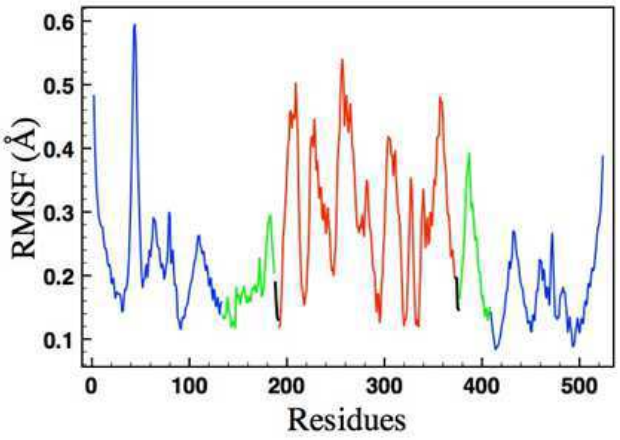

Figure 3.16: Residue root mean square fluctuations (RMSF) analysis

quences corresponded to fluctuation minima at the interface of the rigid domains (see Fig. 3.16). Using the QUAFIT method, according to the strategy described in section 3.2, two different structures of the tetradecamer (A and B), both able to best fit the experimental SAXS curve, have been obtained. To check the accuracy of this choice, GroEL's SAXS data were analyzed by QUAFIT method considering the monomer as a single rigid domain: the fitting, reported below in Fig. 3.25, gave a worse solution at lower values of Q, with a reduced χ^2=2.31. Best fitting curves and different views of the A and B structures are reported in Fig. 3.17. Corresponding reduced χ^2 measuring the quality of data fitting for A and B solutions are 1.38 and 1.13, respectively. By comparing tetradecamer's size, we could observe that, although the oligomers are quite similar concerning external dimension (gyration's radius and barrel axes), the size of the internal cavity is considerably smaller for structures A and B than for 4AAR (see below). This feature could be explained by comparing the monomers from each oligomeric structure. In fact, in solution the apical domain seems to adopt a tilted conformation, with respect to that of the monomer extracted from 4AAR, orienting this domain toward the center of the barrel. Notably, these conformational changes are representative of the bending mode relative to the first eigenvector evidenced by the PCA reported in Fig. 3.15, right. As evidenced by the Ramachandran's plot, where the torsional angles ϕ and ψ of the residues are plotted, structural changes due to chain flexibility, imposed during the fitting process, did not dramatically distort the protein backbone (Fig. 3.18). Interestingly, the resulting structure presents several new hydrogen bonds and salt bridges (see Fig. 3.19) between adjacent subunits of the same ring (intra-ring salt bridges), involving residues Asn229-Glu238 in the apical region, and Lys80-Asp41 in the equatorial domain. Notably, two repeated inter-ring hydrogen bonds were also detected between Asn437-Glu434, in the equatorial domain. In Fig. 3.20 a section of the GroEL cavity (PDB: 4AAR) is compared with that of GroEL structure obtained by SAXS experiments in solution, as described above. Two essential differences are highlighted: i) the size of the two access windows and ii) the shape of

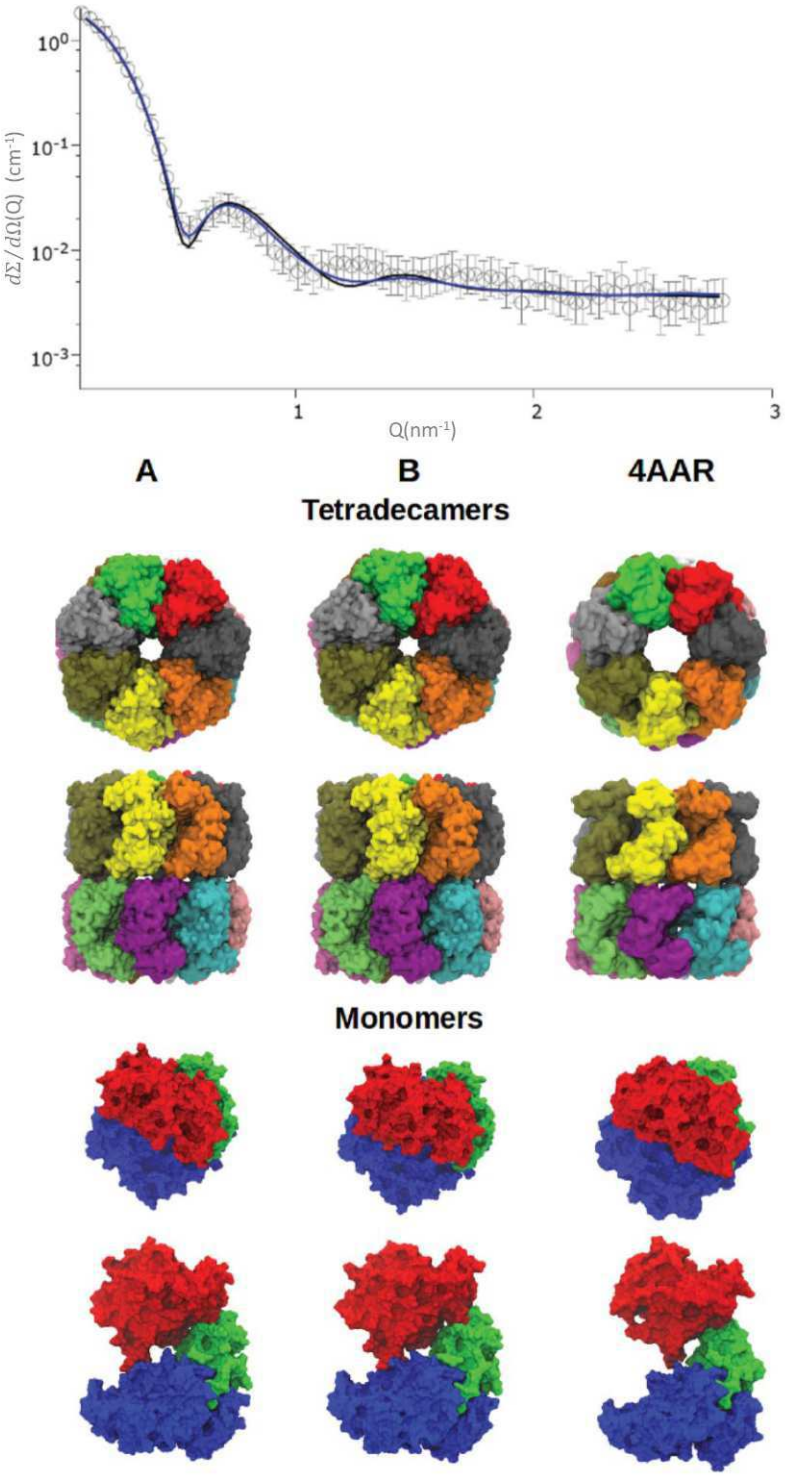

Figure 3.17: Fit and reconstruction of GroEL

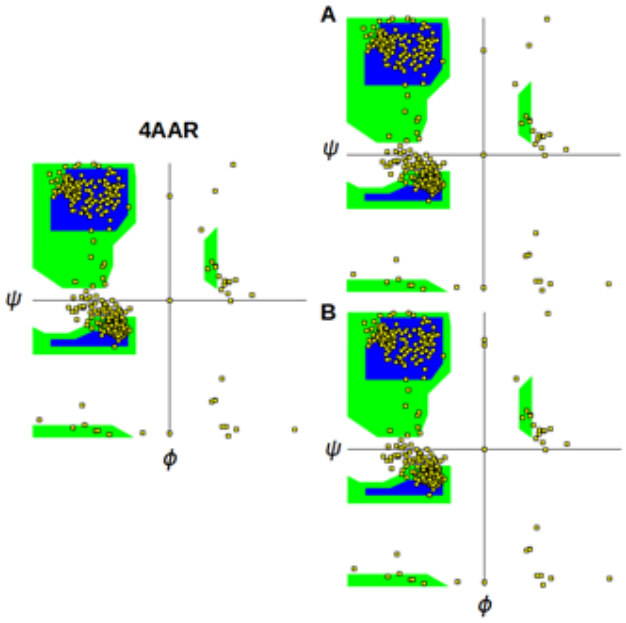

Figure 3.18: Ramachandran's plot for the crystallographic (4AAR) (left) and the solution structures (right) of GroEL.

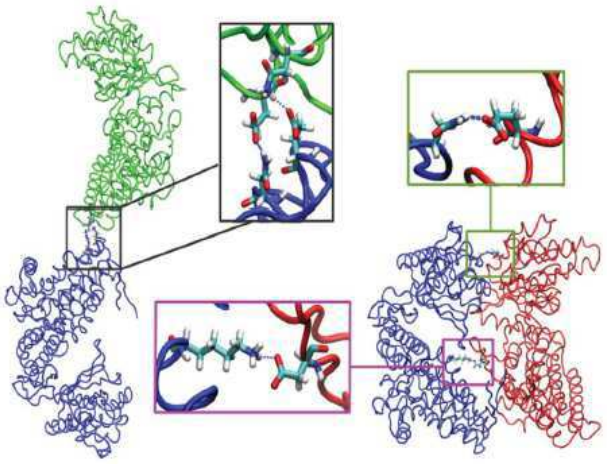

Figure 3.19: Inter-ring (left) and intra-ring (right) salt bridges between the GroEL subunits in solution; involved residues are represented as balls-and-sticks

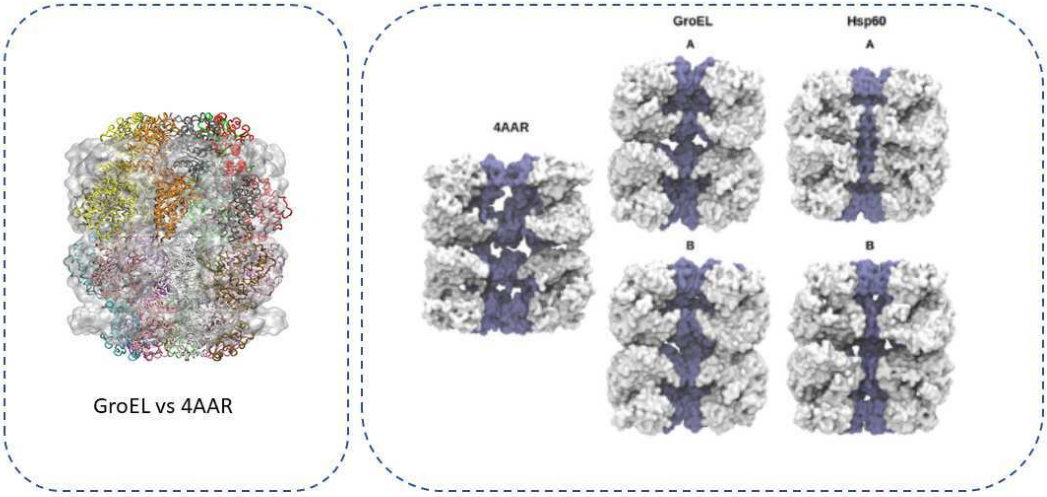

Figure 3.20: Cavities of 4AAR in the solid state (left), and of the solution structures of GroEL (center) and Hsp60 (right).

the internal chamber, where the client unfolded protein is hosted for undergoing the folding process. In fact, the in-solution structure presents a smaller window of about 2 nm compared to that of the high-resolution solid state structures, such as 4AAR. This feature induces us to suggest a role of GroEL, not only for recognition of client proteins, but also for the initial denaturation step, forcing the nascent polypeptide to pass through this tighter entrance. On the other hand, the cavity's size was estimated by counting the number of water molecules inside each heptameric ring (see e.g. Fig. 3.21) for 4AAR (6591), GroEL-A (4136), GroEL-B (3968), Hsp60-A (5147) and Hsp60-B (4349). These results show in solution a shrinking of available volume for the client proteins.

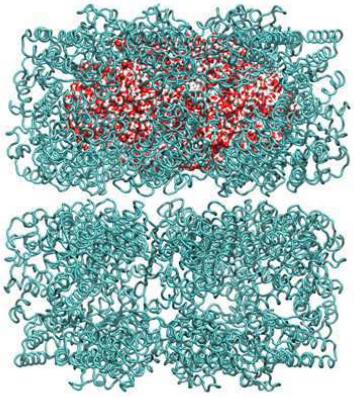

Figure 3.21: Water molecules inside the single ring (heptamer) cavity of GroEL A structure (4136).

3.3.3 Naïve Hsp60 structure in solution

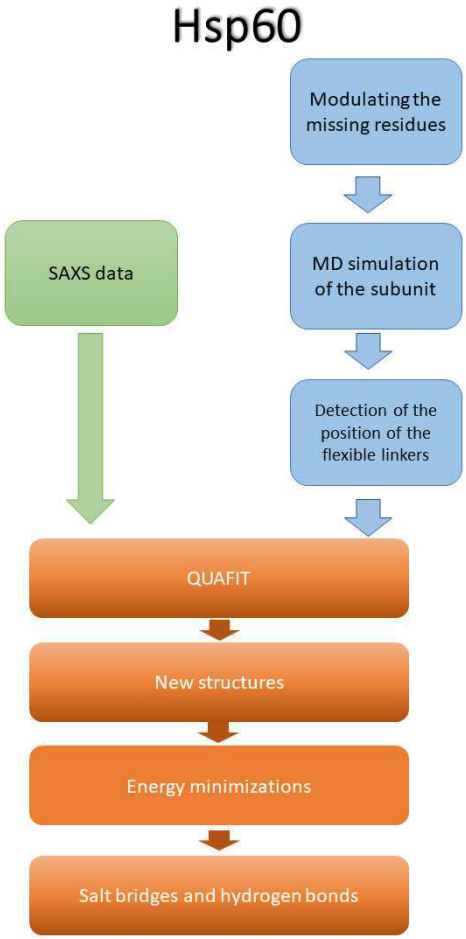

Figure 3.22: Workflow for naïve Hsp60 reconstruction

Naïve Hsp60 structure has been reconstructed, starting from the obtained in solution monomer of GroEL from the previous analysis. The monomer was reconstructed by homology modeling, the missing residues (MIS and unresolved C-terminal aa) were modeled through the ROSETTA software (see section 3.2). Following the same approach used to study the structure of GroEL in solution (see workflow in Fig. 3.22), 200 ns of MD simulation have been performed for the reconstructed Hsp60 monomer. A representative snapshot, at about 150 ns, is shown in Fig. 3.23b, with the attached MIS highlighted in cyan. The presence of these additional C- and N-terminal sequences clearly impose an intrinsic stiffness to the

monomer structure, as observed from the RMSD plot after 120 ns (Fig. 3.23a). In

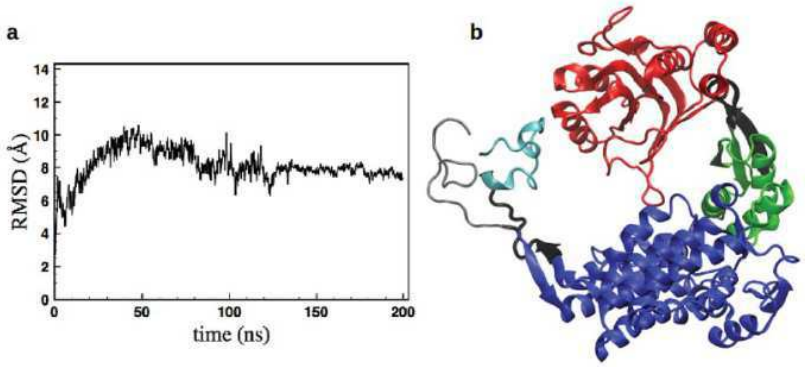

Figure 3.23: a) RMSD plot of the Cα atoms of the naïve Hsp60 subunit; b) Representative snapshot with the Hsp60 domains shown in red (apical), green (intermediate), blue (equatorial), the MIS and C-terminal sequences in cyan and in grey, respectively. The four flexible linkers are also shown in black.

compliance with the approach followed for GroEL reconstruction and considering the added sequence, the Hsp60 monomer used within QUAFIT has been divided in three rigid domains: the apical (shown in red in Fig. 3.23b), the combination of equatorial and intermediate fragments (blue and green) and the set of N- and C- endings folded with ROSETTA (cyan and gray). Hence four flexible linkers have been defined. Two of them are in the region between the apical and the intermediate domains (as in the case of GroEL) and are composed by residues from 211 to 214 and from 397 to 400, respectively. The other two flexible linkers, connecting the N- and C-ending domain to the equatorial-intermediate domains, are from residues 23 to 26 and from 548 to 55. Moreover, we have considered that, unlike GroEL, naïve Hsp60 in solution can simultaneously be present as a mixture of tetradecamers and heptamers. Consequently, the QUAFIT software package allowed us to obtain best fitting of experimental SAXS data with tetradecameric and heptameric structures using the flexible monomer model as their building block (Fig. 3.24). Nevertheless, we had performed QUAFIT analysis even in the hypothesis of a unique tetradecameric population, but the bad fitting quality (Fig. 3.25) confirmed the simultaneous presence of two quaternary structures in solution. Two best structures (A and B) obtained with QUAFIT are reported in Fig. 3.24, together with their corresponding best fit curves (corresponding χ^2 are 1.28 and 1.31, respectively). Due to the presence of the MIS sequences, the structures of the monomer A and B, seen in Fig. 3.24, result more compact than the ones for GroEL, confirming the stable RMSD values shown in the last 80 ns of the MD simulation for the isolated subunit. Also, for Hsp60 the entrance of the folding chamber is notably smaller. Moreover, the MIS sequences are located inside the folding cavity, thus leading apparently to a reduced space available for the guest proteins (see Figs. 3.17 and 3.24). Nevertheless, the presence of amino acidic chains inside the cavities surprisingly allows the entrance of

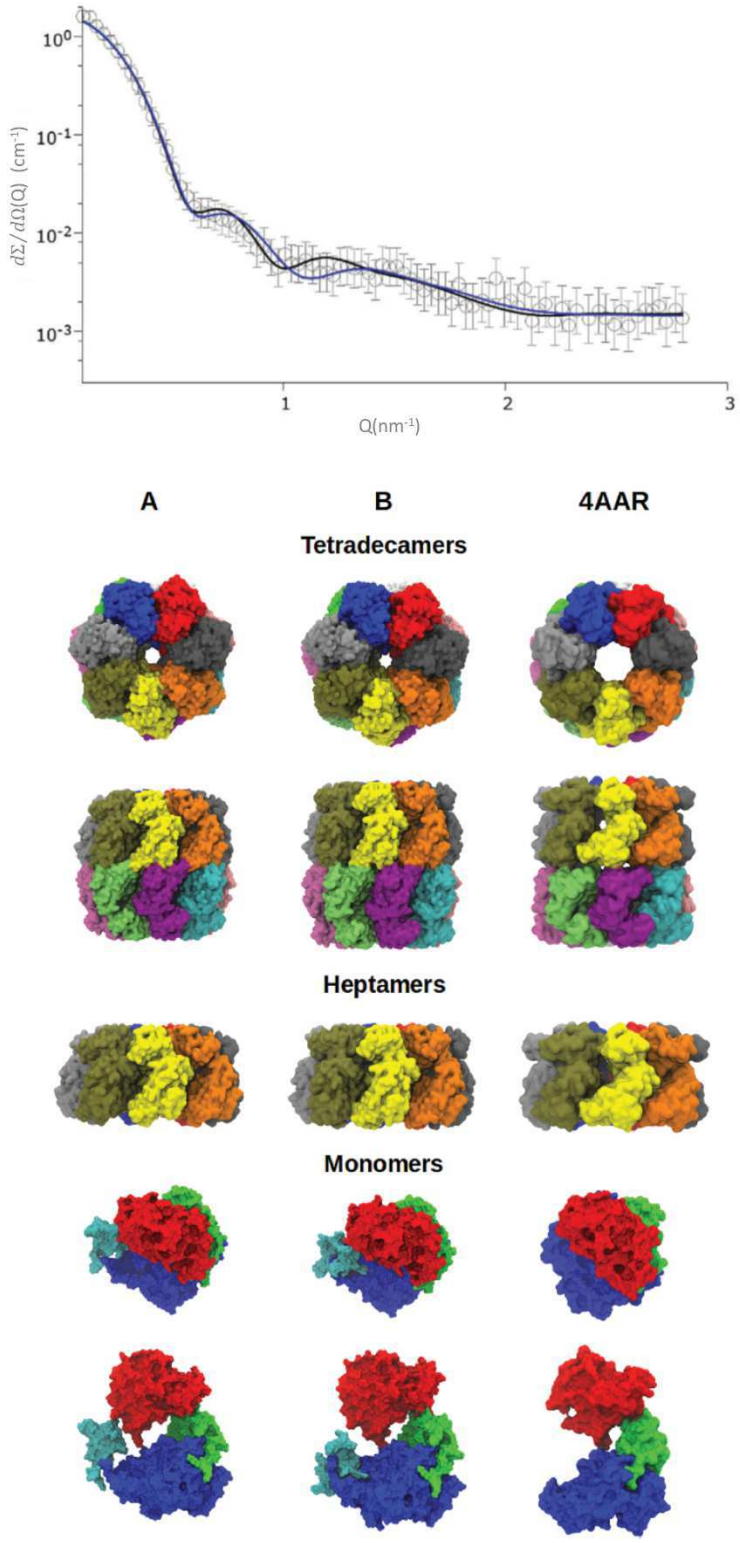

Figure 3.24: Fit and reconstructions of naïve Hsp60

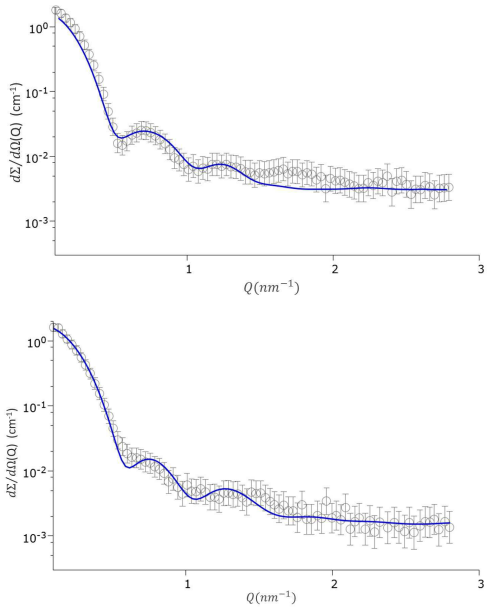

Figure 3.25: Tentative fitting of, top, GroEL with only rigid monomers ($\chi^2 = 2.31$) and, bottom, naïve Hsp60 with only tetradecamers ($\chi^2 = 1.81$).

a larger number of water molecules compared to GroEL A and B (see above). This result can depend on the different exposed aminoacid in the cavity, maybe more hydrophobic than in the previous structure. Non-covalent interactions in structure

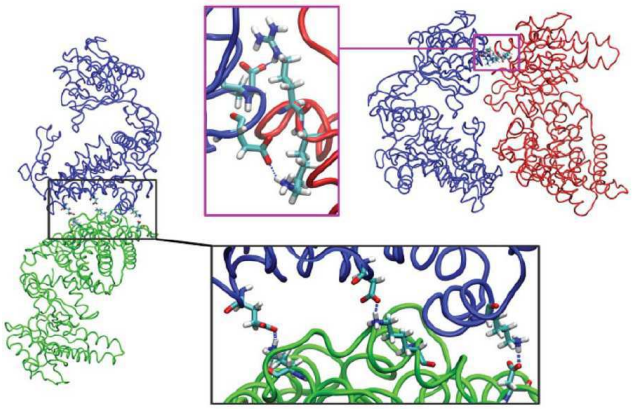

Figure 3.26: Salt bridges in naïve Hsp60

A have been representatively analyzed. In particular, several salt bridges were found (see Fig. 3.26) involving residues Glu281-Arg268. Recently, the naïve Hsp60 crystallographic structure has been published, but just in complex with Hsp10 [132]. In Fig. 3.27 are reported the comparisons with our structure. In respect to Nisemblat's one [162], our in solution structure is more compact (lower of about 1 nm in height

and higher of about 2 nm in thickness), and the inner cavity results less spacious. However, these effects could be attributed to the fact we are not in presence of bound Hsp10.
In conclusion, we obtained the structures of GroEL and naïve Hsp60 in solution by means of a combined SAXS-MD study. Those results clearly confirm for the Hsp60 case the co-existence of tetradecamers and heptamers and the exclusive tetradecameric structure of GroEL.

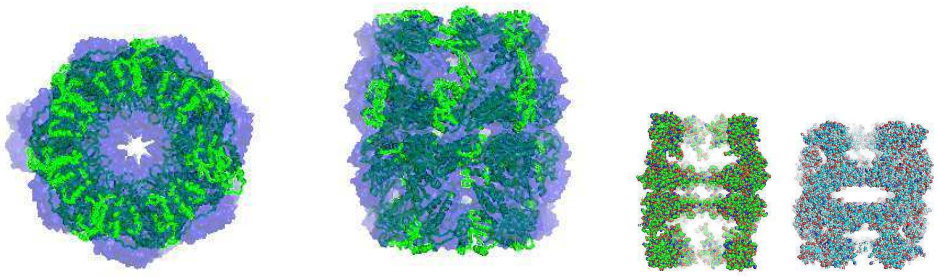

Figure 3.27: Left: the new structure (green, from [132]) is compared with our result (blue). Right: the inner cavities are compared: crystallographic, blue vs our in solution reconstruction, green.

3.3.4 Chemical stabilities

These findings prompted to wonder if there were any differences in the oligomeric stability of the three proteins considered (the bacterial and the human homologues, mtHsp60 and naïve Hsp60) [134, 133]. The attention has been then focused on the stability characteristics of Hsp60s in order to further elucidate the structural basis underlying Hsp60 functions, and providing information relevant to support, in general, a relationship between stability and function [163]. In this light, a study of the effect of guanidinium hydrochloride (GdnHCl) in solution has been conducted to provide information on naïve and mtHsp60 stability in parallel with GroEL, whose chemical unfolding mechanism by denaturing agents has been previously characterized by several biophysical techniques [160, 164, 165, 166]. To deepen the experimental investigation, the unfolding of the chaperonins has been followed by CD and SAXS (see sections 3.2).
Results obtained by CD (CNR, Palermo) provided thermodynamic informations on the unfolding of the three proteins [133]. Far-UV CD spectra at different denaturant concentrations are reported in Fig. 3.28. When the amide polypeptide bonds are aligned in regular arrays, such as α-helices or β-sheets, they have characteristic spectra. For example, proteins with high contents of α-helices have characteristic bands at approximately 223 and 212 nm. In the simple two-states approximation [167], the experimental CD spectrum is considered a linear combination of the CD spectra of a unique folded (F) state and a unique unfolded (U) state and the ratio between their

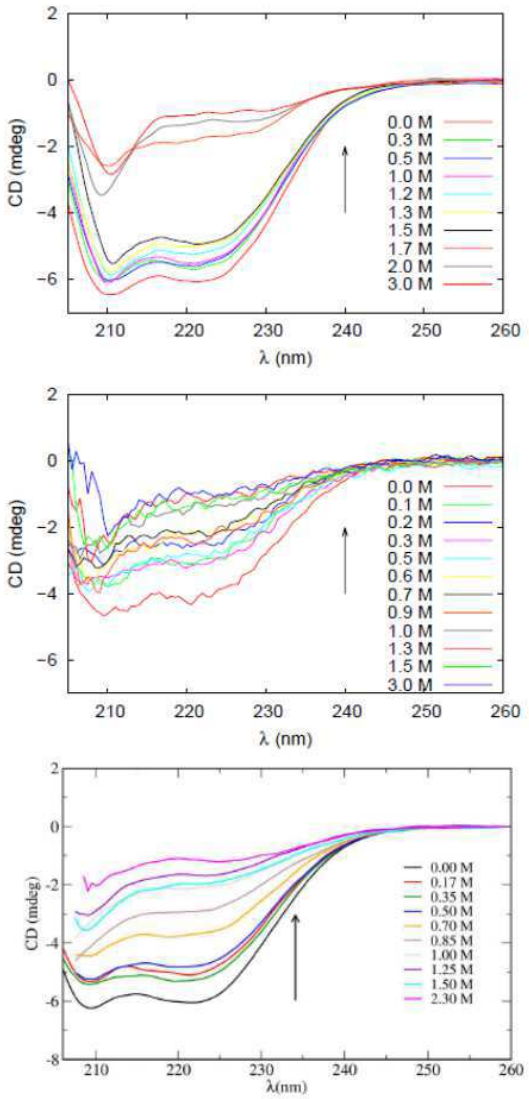

Figure 3.28: Circular Dichroism (CD) spectra from top to bottom of GroEL, naïve Hsp60 and mtHsp60 in the absence and in the presence of increasing concentrations of GdnHCl. The concentrations of GdnHCl are reported in the legend.

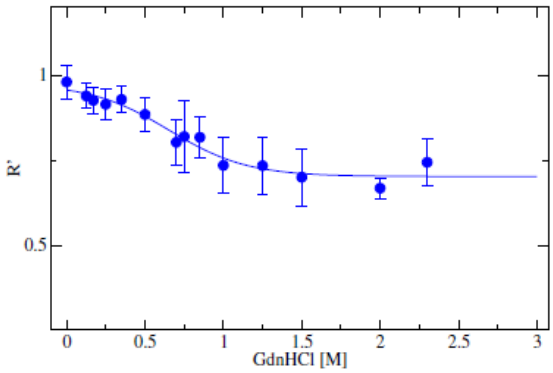

Figure 3.29: R' values of mtHsp60 in function of denaturant concentration for mtHsp60 (from Equation 3.18).

molar concentrations defines the unfolding equilibrium constant, $K_{\text{unf}} = [U]/[F]$. The associated unfolding free energy is assumed to have a linear dependence on the GdnHCl molarity in solution, $\Delta G_{\text{unf}} = -RT \log K_{\text{unf}} = \Delta G_0 - m\,[\text{GdnHCl}]$, R being the gas constant and T the absolute temperature [168]. On these grounds, the ratio R' between the CD values at 212 nm and at 223 nm, reported in Fig. 3.29 for mtHsp60 as an example, can be analyzed according to the expression:

$$R' = \frac{CD_{223\,\text{nm}}}{CD_{212\,\text{nm}}} = \frac{A + Be^{-\Delta G_{unf}/\boldsymbol{RT}}}{C + e^{-\Delta G_{unf}/\boldsymbol{RT}}}, \tag{3.18}$$

where A, B and C are parameter linked to the extrapolation of the values of the spectra at the completely unfolded stage and in absence of the denaturant, hence in the pure native state. In order to reduce the number of fitting parameters, the factors A and C have been fixed to the values derived from CD data in the initial and final plateau region. Results of the analysis of the whole set of CD spectra are summarized in Table 1. The fraction of unfolded proteins, $f_U = [U]/([U] + [F])$, was then obtained from the fitting parameters and is plotted as a function of [GdnHCl] in Fig. 3.30. The observation of the evolution of $f_U([GdnHCl])$ as a function of GdnHCl concentration reveals that the unfolding of mtHsp60 is early and less cooperative than the one relative to naïve Hsp60. Different to the case of GroEL, both of them seem to undergo a gradual unfolding without a single cooperative event although this behavior is more pronounced for mtHsp60.

As a second step, the stability of the three chaperonins against GdnHCl was examined by SAXS experiments. In order to confirm the compactness of in-solution mtHsp60, SAXS data are reported in Kratky plots, i.e. $(d\Sigma/d\Omega(Q) \cdot Q^2)$ as a function of Q. In Fig. 3.31 both Hsp60s SAXS fingerprints are reported. They present a broad peak, whose Q-position changes for each species. Naïve Hsp60 SAXS spectrum in the form of Kratky plot shows a peak at lower Q values in respect to that corresponding to mtHsp60, clearly indicating that the average dimensions of naïve species are larger than the others, since the peak position is inversely proportional

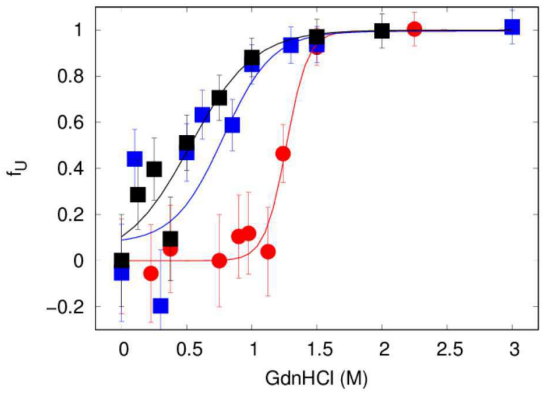

Figure 3.30: Fraction of naïve (blue), mitochondrial (black) Hsp60 and GroEL (red) unfolded protein plotted as a function of GdnHCl concentration. Theoretical fits to the data are derived from Equation 3.18 and from [133].

Table 3.1: CD analysis results on thermodynamic parameters for mtHsp60, naïveHsp60 and GroEL [134].

	A	B	C	ΔG_0 (KJ/mol)	m (KJ·L/mol^2)
mtHsp60	3.4	0.70 ± 0.02	3.5	3.3 ± 0.8	10 ± 2
naïve Hsp60	3.7	0.70 ± 0.01	3.6	10 ± 1	16 ± 1
GroEL	1.63	0.40 ± 0.03	1.74	37 ± 7	29 ± 6

to in-solution particle dimensions. We associate this evidence to an enrichment of mtHSP60 heptamers compared to the naïve form. Hence, SAXS curves obtained at increasing GdnHCl contents between 0 and 2.0 M are analyzed by considering the possible simultaneous presence of tetradecamers, heptamers, monomers and unfolded species. SAXS curve corresponding to native mtHsp60, i.e. without GdnHCl, is analyzed without the presence of unfolded species. The theoretical macroscopical differential scattering cross section can be expressed as the sum of the contributions due to each species, as discussed in section 1.2.2.5. Hence, the macroscopical differential scattering cross section results:

$$\frac{d\Sigma}{d\Omega}(Q) = \frac{c}{M_1} N_A [x_1 P_1(Q) + \frac{1}{7} x_7 P_7(Q) + \frac{1}{14} x_{14} P_{14}(Q) + \frac{1}{N_{agg}} x_U P_U(Q)] \quad (3.19)$$

where M_1 is monomer molecular weight, N_A is Avogadro's number, x_1, x_7, x_{14}, and x_U are the fractions of protein molecules occurring as monomers, heptamers, tetradecamers and unfolded species, respectively. $P_1(Q)$, $P_7(Q)$, and $P_{14}(Q)$ are accordingly the form factors corresponding to mtHsp60 monomers, heptamers and tetradecamers. $P_U(Q)$ is the Pedersen-Schurtenberger worm-like chain form factor

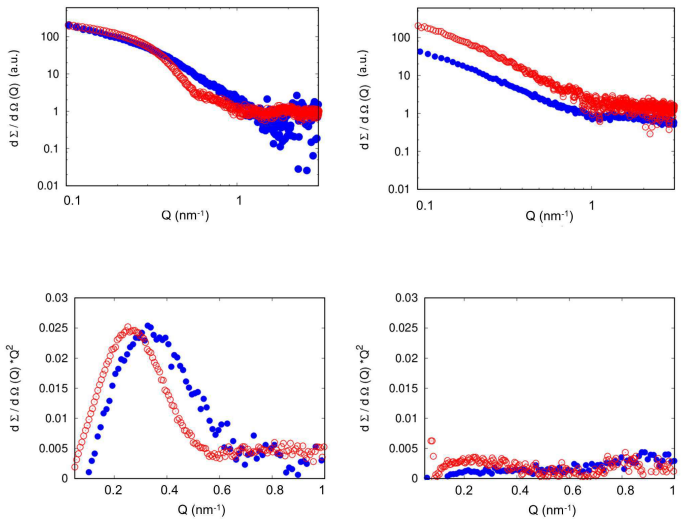

Figure 3.31: Top left: log-log plots of SAXS data corresponding to mitochondrial (blue circles) and cytoplasmatic (red empty circles) Hsp60 at 0M GdnHCl; right: log-log plots corresponding to 1.5M GdnHCl. Bottom left: Kratky plots of mitochondrial (blue circles) and cytoplasmatic (red empty circles) Hsp60 at 0M GdnHCl; right: same data at 1.5M GdnHCl.

multiplied by a two-electron density level cross section for the protein chain as used in previous studies [121] and N_{agg} is the aggregation number of monomers arranged in the worm-like species. Protein form factors corresponding to tetradecamers, heptamers and monomers were obtained by adopting the PDB arising from [19], by considering the shortage of MIS, and by taking into account water molecules positions at the hydration shell of each oligomer, according to the SASMOL approach [10], see section 1.2.2.5. The mass density of proteins first hydration shell was considered a fitting parameter and resulted to be incremented of $\simeq (12 \pm 2)$ % in agreement with literature results [23]. The average aggregation number results to be $\simeq (9 \pm 6)$. Given the relative low concentration c of the protein in solution (1 g/L) and because the relatively high molecular weight of the investigated species, we expect a small particle number density in solution. Consequently, the interactions should be considered neglectable and the effective structure factor approximated to unity. SAXS curve fitting was performed by using GENFIT software package [8]. Experimental macroscopical differential cross sections obtained for mtHsp60 at increasing GdnHCl concentrations are reported in Fig. 3.32 together with their theoretical fitting, which results to be satisfactory in the whole Q-range. This can allow to distinguish between heptamers, close one to each other, and tetradecamers, thus keeping information about tetradecameric dissociation at increasing GdnHCl. As a result, the fraction of protein molecules which occur in each oligomeric species is reported in Fig. 3.33. The protein dissociation appears as a cooperative phenomenon between different oligomeric species in solution, and in particular hep-

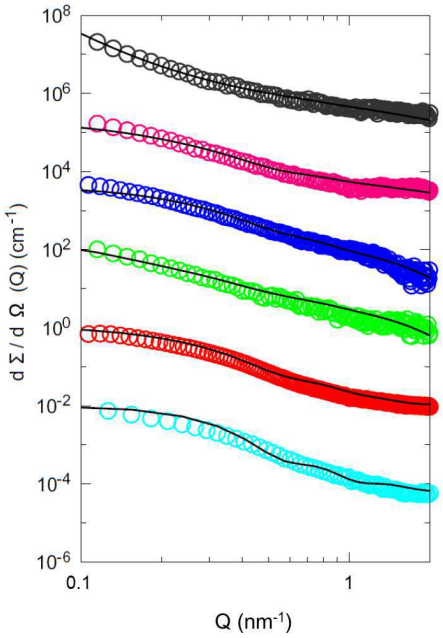

Figure 3.32: SAXS experimental curves and theoretical fitting (black lines) for mtHsp60 (1 mg/mL) are reported at increasing denaturant concentration, from 0 M GdnHCl (cyan circles), 0.25 M (red circles), 0.75 M (green circles), 1 M (blue circles), 1.5 M (pink circles), 2 M (black circles). Curves are scaled for sake of clarity.

tamers and tetradecamers co-participate to the formation of monomers and unfolded species. From the unfolding fraction is possible to obtain thermodynamic informations on the process. In Fig. 3.34 the unfolded fraction for mtHsp60 in comparison with naïve Hsp60 as a function of GdnHCl concentration are reported. Similarly to what observed by CD, unfolding for mtHsp60 occurs earlier, thus confirming its lower stability. Since $\Delta G_{unf} = \Delta G_0 - m[GdnHCl]$, where we consider the unfolding free energy to have a linear dependence on GdnHCl molarity in solution, and $\Delta G_{unf} = -RTln([U]/[F])$, the parameters ΔG_0 and m are obtained from the resulting unfolded species. The reference unfolding free energy resulted to be $\Delta G_0 = 13 \pm 3\ kJ/mol$ and $m = 10 \pm 3\ kJ/(mol^2 L)$. ΔG_0 provided by SAXS results on mtHsp60 is about the half of the one obtained for naïve Hsp60 [133].

Table 3.2: CD and SAXS results in comparison for thermodynamic stability values [134].

	ΔG_0 (KJ/mol)		m (KJ·L/mol^2)	
	SAXS	CD	SAXS	CD
mtHsp60	13 ± 3	3.3 ± 0.8	10 ± 3	10 ± 2
naïve Hsp60	23 ± 7	10 ± 1	14 ± 5	16 ± 1
GroEL	42 ± 10	37 ± 7	22 ± 5	29 ± 6

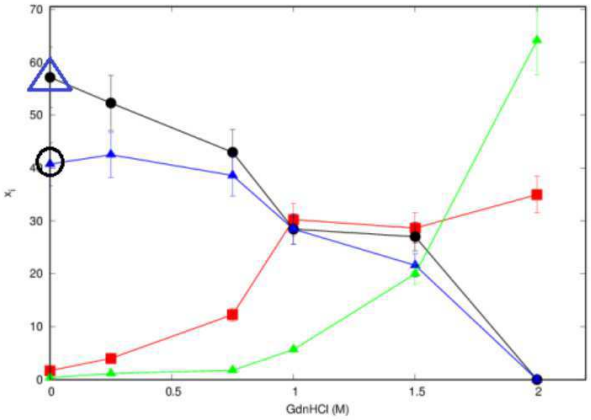

Figure 3.33: SAXS results reporting the protein molecules fractions occurring as different oligomeric species. Full points refer to mtHsp60 monomers (red squares), heptamers (black circles), tetradecamers (blue triangles) and unfolded species (green triangles), versus GdnHCl content. Note that SAXS curves corresponding to Hsp60 without GdnHCl were fitted considering the unique presence of tetradecamers, heptamers and monomers in solution. The superimposed black circle and the blue triangle at 0M GdnHCl represent respectively the fraction of heptamers and tetradecamers in naïve Hsp60 [133].

The results obtained from the two techniques are in accordance predicting a major stability for the bacterial protein and a growing less stability form naïve Hsp60 to mtHsp60 (Table 3.2). The lower stability of human protein can suggest a different mechanism of functioning that have been evolutionary awarded towards a greater flexibility in different condition. It is worth of noting that two of the four residues, R452, E461, S463 and V464 that are essential for double ring formation in GroEL, are different in the correspondent Hsp60 positions [169]. In addition, Hsp60 can function as an efficient "one stroke engine" *in vivo*, and a single ring is sufficient for productive chaperonin-mediated folding [169]. In this perspective, our findings well fit the general "stability-function" hypothesis, by which protein functional residues are not optimal for protein stability [163]. We can speculate that also for chaperonin 60, the evolution has been driven by mutations which lead to new protein functions by providing higher flexibility to the protein, but come at a cost to protein stability. Organisms evolve by balancing the advantage of accepting more functional substitutions with the possible cost of effects on protein stability [170].

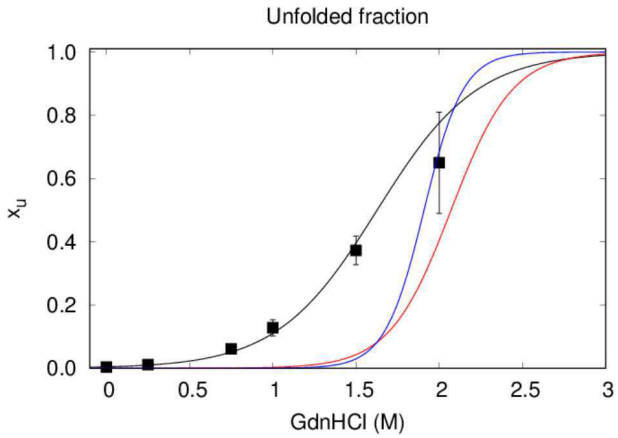

Figure 3.34: Experimental points corresponding to the fraction of mtHsp60 (black) unfolded proteins as a function of GdnHCl content, in comparison with naïve Hsp60 unfolding profile (red) and GroEL (blue) as revealed by SAXS from [133]. Lines are the theoretical fitting performed by considering the unfolding free energy.

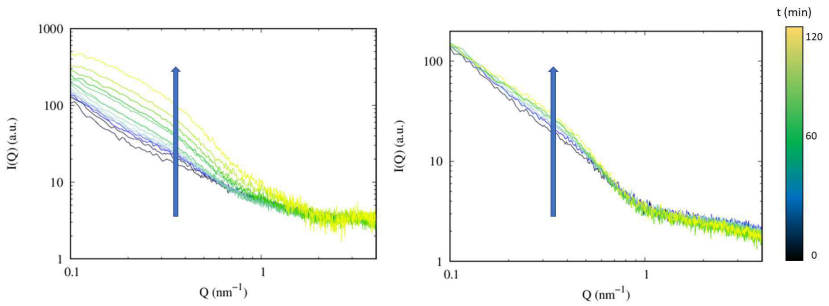

Figure 3.35: Time evolution of 200μM Aβ_{1-42} alone, left, and in presence of mtHsp60 (4μM), right.

3.4 Hsp60 interactions with Aβ peptide

Finally, in this section, the effects of mtHsp60 on Aβ peptide aggregation are presented, to illustrate the inhibitory effect of this chaperonin on the Aβ_{1-42} fibrillation pathway.

As introduced in Section 2, Alzheimer's and Parkinson's diseases are characterized by the presence, in brain tissues and in Lewy bodies respectively, of amyloid fibrils and prefibrillar aggregates, originated by off-pathway conformational changes. Modifications in chaperones expression, however, can alter the neurotoxicity of oligomers and fibrils, suggesting possible therapeutic strategies (Section 3.1.2). Moreover, it has been found by NMR measurements that GroEL suppresses Aβ_{1-40} amyloid formation by interacting with its two hydrophobic segments Leu17-Ala21 and Ala30-Val36, key residues in fibril formation [171].

In this framework, mtHsp60-Aβ_{1-42} aggregation kinetics was followed in time, to observe the non-activated interaction of the chaperonin with the peptide.

Time resolved SAXS measurements allowed to monitor the aggregation process of the Aβ_{1-42} (200 μM) in time, alone and in the presence of mtHsp60 (4 μM) for about two hours (Fig. 3.35). An evolution in time for the samples with and without chaperonin can be observed, inferring the presence, at the initial state, of a distribution of oligomers not yet in an equilibrium state that proceed during the folding pathway. Nevertheless, the sample with mtHsp60 seems to be inhibited in its evolution, since the differences between the starting and the end point seem to be less evident.

In order to better understand these phenomena, firstly we observed Kratky plots ($I(Q)\cdot Q^2$ vs Q, see Section 1.2.2.4) in order to gain a model-free result. The sample with Aβ_{1-42} alone (Fig. 3.36, left) shows an evolution from unfolded to globular and compact structures, and a progressive shift of the peak from higher to lower values of Q, indicating an increase in the mean dimensions of the system.

The sample with the addition of mtHsp60 (Fig. 3.36, right) seems to start from a more compact condition, showing a peak at 0.4 nm^{-1}, given from the coexistence of tetradecameric mtHsp60 in solution (Fig. 3.36). Instead the evolution of the signal proceeds in a less accentuated way towards bigger structures. At the end of the

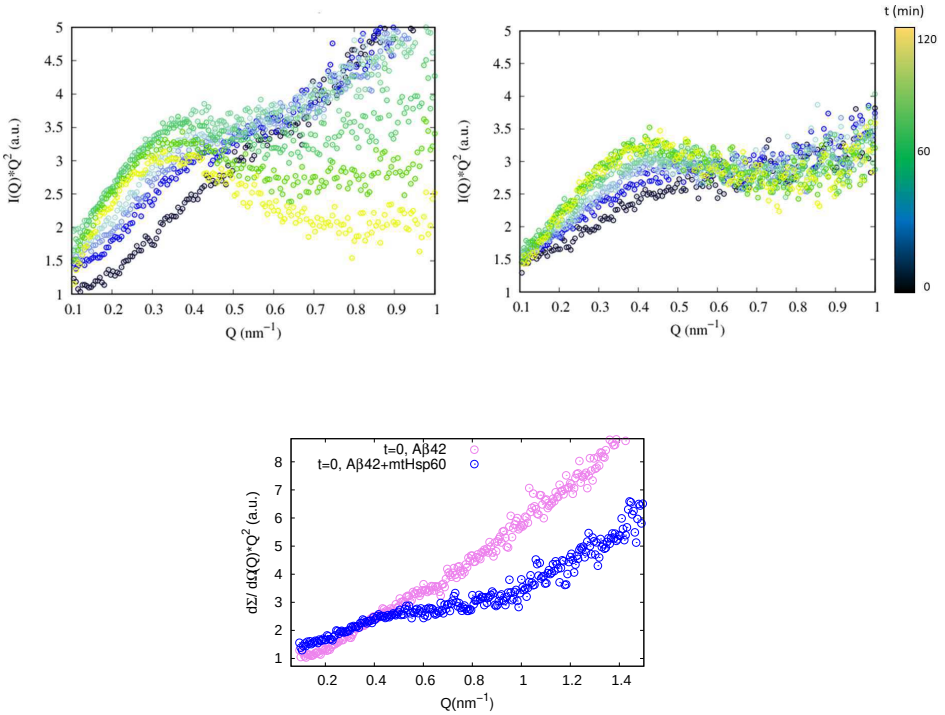

Figure 3.36: Top: Time evolution of SAXS curves in form of Kratky plots for Aβ_{1-42} (200μM), left and Aβ_{1-42} with mtHsp60 (4μM), right. Bottom: focus on Kratky plots of the two samples at the starting point, highlighting the presence of mtHsp60 from the peak at $\simeq 0.4$ nm^{-1}

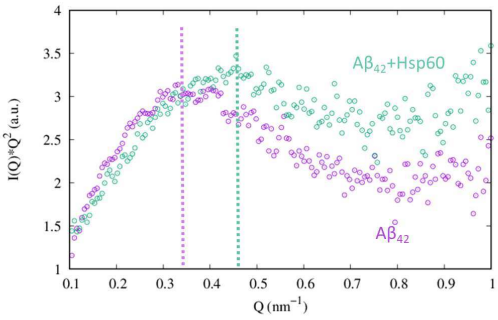

Figure 3.37: Final states of the Aβ_{1-42} peptide alone (violet) and in presence of mtHsp60 (green) from the representation in form of Kratky plots of SAXS curves.

recorded kinetic the peak for the two systems show significant difference in the position, illustrating an inhibitory effect for the chaperonin (Fig. 3.37). Time resolved measurements reveal that mtHsp60 is able to modify the peptide aggregation pattern, inhibiting the aggregation process. The effect of mtHsp60 on Aβ aggregation has been analyzed recently, showing a striking effect of the chaperonin towards a complete blocking of the progression of the fibrillation [136], see Fig. 3.38 in which a Thioflavin T fluorescence experiment has been reported: the increase of the signal of Aβ_{1-40} alone is completely inhibited in presence of mtHsp60 even after 24 hours. The experiments in literature [136] have been performed at lower concentrations and in presence of Aβ_{1-40} instead of Aβ_{1-42}. The differences between our results could be charged on these differences of concentration and type of peptide, since the Aβ_{1-42} has a more rapid time dependence. In fact, the starting point of our kinetics could not be considered as composed of only monomers (see Fig. 2.17, where the Aβ_{1-40} and Aβ_{1-42} peptide are reported at the earliest stage of measurement performed). It is possible that the action of the mtHsp60 is more effective when the population of protein in solution is monodisperse and there are no seeds for secondary nucleation growth.

To test the effect of the chaperonin on mature fibrils, SAXS curves have been acquired, in time, on a sample of yet formed Aβ_{1-42} fibers with the delayed addition of mtHsp60: the chaperonin has been included in the sample after the peptide has been free to aggregate.

It can be seen from Fig. 3.39, bottom, that SAXS curves show small differences in time evolution. Interestingly, the Kratky plots show an evolution of the signal toward the formation of bigger aggregates at very low Q values. This result points out a possible interaction mechanism of Hsp60 toward amyloid fibrils and and highlights the multiple applications of the chaperone with respect to the formation of different oligomeric species, as will be observed also see for the Hsp70.

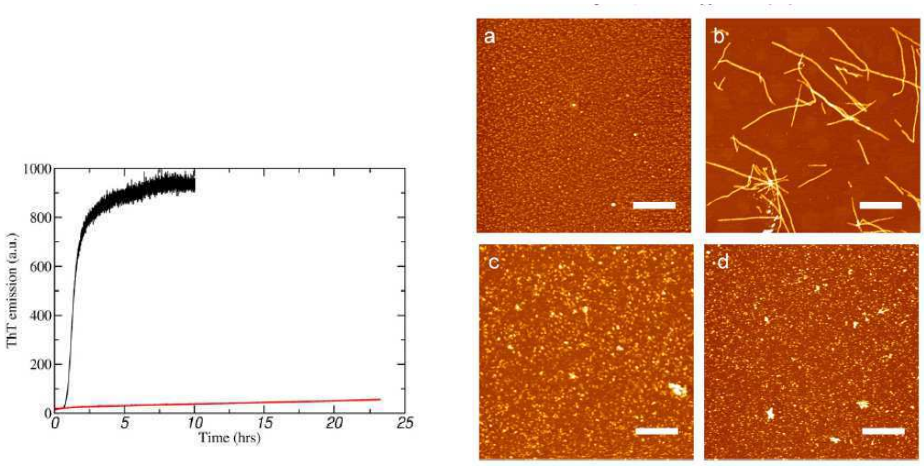

Figure 3.38: Form [136]. Left: Thioflavin T measurement on 50 μM Aβ_{1-40} with the addition of 40 μM mtHsp60. Right: AFM measurements of Aβ species formed in the presence of mtHsp60 under amyloid aggregation conditions: a) and b) 50 μM of Aβ_{1-40} at the starting and final stage of fibrillation and c) and d) 50 μM of Aβ_{1-40} with 2μM at the starting and final stage of fibrillation. Scale bar 1 μm, z-range for a, b, c: 7 nm, for d: 9.6 nm.

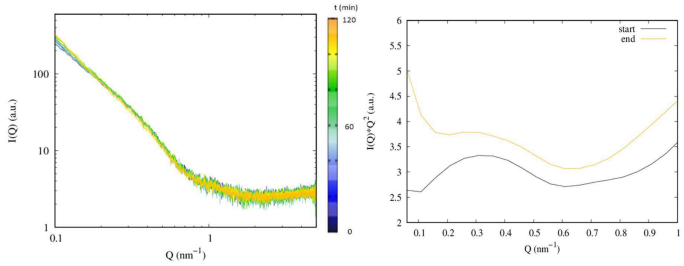

Figure 3.39: Left: interaction of mtHsp60 with already formed fibrils of Aβ_{1-42}. Right: Kratky plots of starting and ending stages of mtHsp60 with already formed fibrils of Aβ_{1-42}, highlighting a slightly modification in time.

Chapter 4

Hsp70 characterization and interactions

Contents

4.1 Introduction

Even more attention has been posed, in recent years, on the study of molecular chaperones, with the aim to enhance their specificity in the treatment of various diseases [172]. In fact, as introduced in section 3.1 for Hsp60, their connection with the onset of different pathologies is an experimental evidence. In the brains of patients affected by Alzheimer's Disease (AD), an increased level in the expression of another particular molecular chaperone, the Hsp70, has been reported, suggesting its potential role the in the pathogenesis [152, 173].
Furthermore, there are evidences that indicate an inhibitory effect of Hsp70 on α-synuclein, the protein linked to Lewy bodies in Parkinson's disease [174, 175].
Characterizing the interactions of Hsp70 with amyloid proteins linked to the onset of neurodegenerative diseases could thus help to identify the molecular mechanisms underlying the pathologies and possible therapeutical strategies.
Moreover, very recently, different research groups designed and produced engineered chaperones (GHsp70), capable to selectively bind specific proteins and to inhibit their misfolded aggregation pattern [176].
The study here presented aims to deepen the understanding of the effect of wild type and engineered Hsp70 on the fibrillogenesis of Aβ_{1-42} amyloid peptide and α-synuclein, investigating the structure and kinetics of amyloids-GHsp70 complexes.
Before the experimental section, a brief introduction on the structure and functioning of the wild type Hsp70 is presented, with the description of the engineered proteins analyzed.

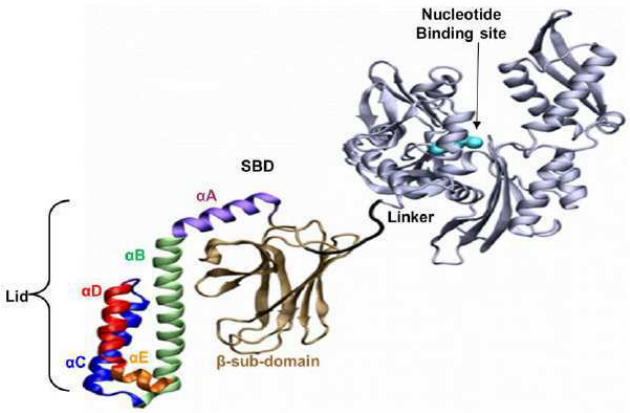

Figure 4.1: Wild type Hsp70 domains, from [177].

Wild type Hsp70 consists of two structurally distinct domains connected by a linker (Fig. 4.1). The N-terminal nucleotide-binding domain (NBD), which in *Homo Sapiens* Hsp70 corresponds to residues 1-383, binds to ATP and hydrolyzes it to ADP. Such ATPase domain has a conventional nucleotide-binding fold, that is the "actin fold" found in different proteins where aminoacid residues form a cleft into which ATP is bound [178]. This binding promotes a conformational change that closes the cleft [179]. The substrate binding domain (SBD) corresponds to residues 397-641 and can interact and transiently associate with short linear peptide segments of folding intermediates. The SBD can be further subdivided into a β-sandwich region (residues 397-507) named substrate binding subdomain or β-subdomain and an α-helical subdomain (residues 508-641), composed of five α-helices (namely, A, B, C, D and E) that governs substrate affinity of the chaperone. The peptide-binding site, which lies between the two β-sheets, is hydrophobic in nature and contains a deep pocket capped by the helices. The helical subdomain has been suggested to regulate the kinetics of substrate binding and act as a "lid" for the substrate binding pocket. In fact, a lidless variant of DnaK, the bacterial Hsp70 homologue, has been reported to be unable to stimulate the refolding of chemically denatured firefly luciferase [180]. When an Hsp70 protein is ATP bound, the lid is open and peptides bind and release relatively rapidly (see Fig. 4.2). The helical subdomain shows specificity for hydrophobic residues, particularly leucine. When Hsp70 proteins are ADP bound, the lid is closed, and peptides are tightly bound to the substrate binding domain. The two domains are connected by a short linker segment (6 residues), which is highly conserved. Also, there is a C-terminal intrinsically disordered region of 26 residues [176].

Given the natural predisposition of Hsp70 towards the correct folding of proteins, this chaperone has been selected as a possible tool to inhibit amyloid formation [181]. Furthermore, it has been observed that in absence of ATP or ADP, Hsp70 showed the same inhibitory effect, indicating a nucleotide-independent interaction [182]. The presence of an unactivated mechanism can propose Hsp70 as a simple

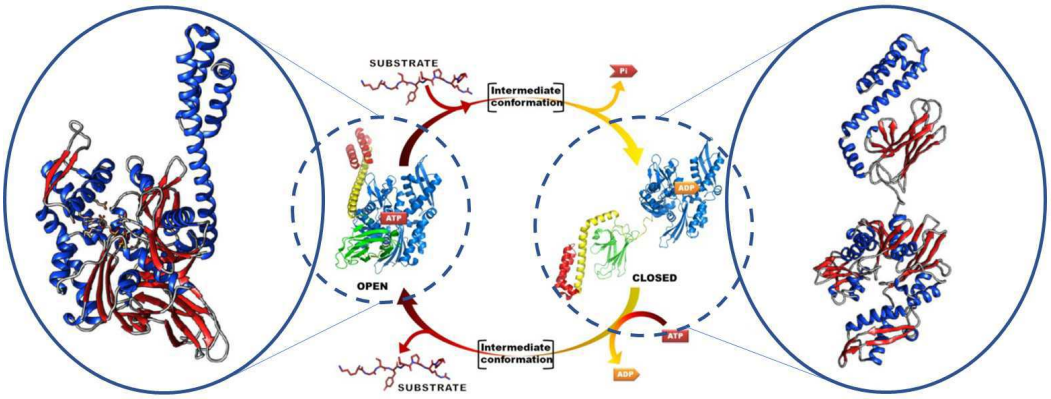

Figure 4.2: Sketch of ATPase cycle of Hsp70: binding of ATP to the NBD of Hsp70 opens the lid over the substrate-binding domain and allows substrate to bind. ATP hydrolysis, catalyzed by various co-chaperones leads to the closing of lid and trapping substrate in the substrate binding pocket. PDB structures are rendered with USCF Chimera software [157].

and powerful tool for therapeutic purposes. Moreover, the realization of engineered proteins with enhanced interaction capability has been exploited in recent years to obtain proteins or antibodies that bind specifically target disordered regions [183, 184, 185].

Actually, the details of the substrate binding mechanism remain still unclear and the nature of possible interactions with substrate proteins is not yet fully resolved. Even the oligomeric stability of the chaperone has been analyzed just recently [186], correlating its stability with the sequence composition and to the secondary structure. In this work, in addition of wild type Hsp70 (Hsp70WT or 70WT), two grafted proteins produced to specifically bind with pathogenic proteins have been studied, produced by the Vendruscolo laboratory, Department of Chemistry, Cambridge [176].

To obtain these particular proteins, an additional binding site for a specific epitope has been introduced in a target protein into Hsp70, with the purpose of selectively increase the affinity of Hsp70 for that target, while maintaining unaltered its functionality. The engineered protein was obtained adding at the C terminus peptides which are termed "complementary peptides" (see Fig. 4.3). This strategy has already been applied before in literature [176, 187, 188, 189] to obtain a tool for inhibiting toxic protein aggregation associated with conformational disorders such as Alzheimer's and Huntington's diseases. With this approach, the Hsp70 variants retain the wild-type sequence, and so the binding site, but have an additional peptide, which binds to the target protein, identified with the analysis of the interactions between amino acid sequences in the Protein Data Bank (PDB) [189] and grafted at the end of the disordered C-terminus of the molecular chaperone. As a result, the C-terminus of the engineered Hsp70 mutants effectively acts like a "fishing line", with a hook (the complementary peptide, colored green in Fig. 4.3b),

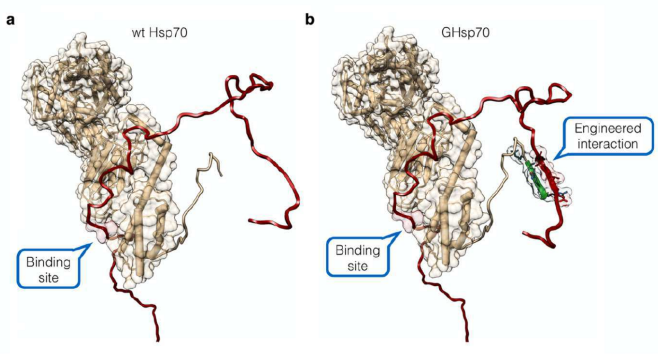

Protein variant	Complementary peptide	Target sequence
GHsp70NAC	EILVSYQ	EQVTNVG (α-synuclein residues 61-67)
GHsp70-Aβ	FKLSVIT	QKLVFFA (Aβ42 residues 15-22)

Figure 4.3: Design of the grafted proteins: representation of wild-type Hsp70 (wt Hsp70, panel a) and the grafted form (GHsp70) (b) bound to α-synuclein (colored red in both panels). In the table are reported the target sequences and the complementary peptides exploited for the linker [176].

that selectively binds the specific epitope on the target protein, thus creating the "engineered interaction" shown in Fig. 4.3b. The complementary peptides, reported in Fig. 4.3 were designed to target a part of the NAC region of α-synuclein (see Section 2.1.1.2) and the Aβ peptide.
Our analysis of the three forms of Hsp70 has been performed principally by means of SAXS, to analyze the differences of the chaperones in solution and their effects on the fibrillation pathway of Aβ peptide and α-synuclein.

4.2 Materials and methods

In this section, the details of the different techniques exploited to characterize the Hsp70s structures and interactions with Aβ_{1-42} and α-synuclein are presented, to introduce the experimental results in the following section.

Protein production

The α-synuclein was purified as a monomeric fraction from *Escherichia coli* as described in [110] from the Vendruscolo laboratory, Department of Chemistry, Cambridge. Aβ_{1-42} was solubilized in hesafluoroisopropanol (HFIP), that was evaporated using a gentle stream of nitrogen gas. The protein was carried in ice to the beamline and dissolved just before the measurements in PBS. As reported in [176, 189], the different complementary peptides were grafted at the C-terminal end of human Hsp70 (human Hsp70 1A, GenBank entry NP005336) by mutagenic polymerase chain reaction (PCR) with phosphorylated oligonucleotides (for details see [176]). Protein concentrations (1:1 Hsp70:amyloids, 50 μM) were determined by absorbance measurements at 280 nm using theoretical extinction coefficients calculated with ExPASy ProtParam [190].

SAXS

Small Angle X-ray Scattering (SAXS) experiments were carried out at the BM29 beamline in ESRF - the European Synchrotron Radiation Facility in Grenoble, France and repeated, for chaperones alone, in Elettra synchrotron, Trieste. Protein samples were carried in ice, and freshly prepared in the beamline. SAXS patterns were recorded using a bidimensional Pilatus 1 M detector. The sample cell used is a 1.0 mm diameter quartz capillary, with a few tens of microns wall thickness. To minimize the dose and the consequent radiation damage, protein solutions were only irradiated during data collection using a fast experimental shutter located 4 m upstream of the sample, thus controlling the acquisition time. Since the sample-detector distance was fixed at 2.867 m, the Q values ranged from 0.1 to 4.5 nm^{-1}. Each measurement lasted 1 s, followed by a dead time of 6 s in order to avoid radiation damage, and was repeated at least 10 times.

AFM measurements

After dilution (1:1000, until 0.05 μM) in appropriate buffer, α-synuclein and GHsp70NAC samples were placed on flat mica surfaces and allowed to dry for several hours in a desiccator under N_2 flow. AFM imaging was done at the Partnership for Soft Condensed Matter (PSCP) Atomic Force Microscopy Platform, Grenoble at ambient conditions using an Asylum Research MFP-3D microscope equipped with a high-resolution tip (Bruker MSNL-10; radius 2 nm, spring constant 0.6 N/m) in tapping mode. The analysis of the AFM images was carried out using the Gwyddion

2.50 software [113]. Plane leveling and alignment of rows were done as corrections to the raw data.

4.3 Characterization of wild type and grafted Hsp70s structures

First of all, the three protein variants have been analyzed, by means of SAXS techniques, to determine their configuration and stability in solution, as reported in the following.
In Fig. 4.4, SAXS curves of wild type Hsp70 (Hsp70WT), GHsp70NAC (70NAC) and GHsp70AB (70AB) are reported. The features of the three proteins seem to be very close one to each other and show very similar characteristics at higher Q values, while in the 0-0.3 nm^{-1} range they differ one from each other. Since Hsp70 has two different spatial arrangement, the first check that has been conducted concerns the possibility that these differences arise from the ADP/ATP bound conformations of the monomers, in case the proteins privileged one of the two arrangements (shown previously in Fig. 4.2). With this aim, the trends are

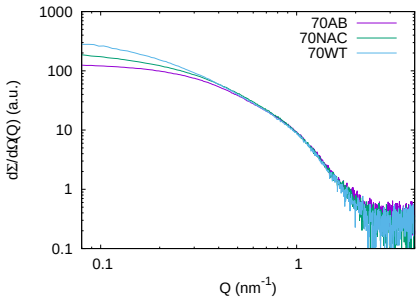

Figure 4.4: SAXS curves of Wild Type Hsp70 25 μM (violet line), and the two grafted peptides GHsp70NAC 60 μ M (green line) and GHsp70AB 60 μM (blue line), scaled for the comparison.

compared in Fig. 4.5 to the theoretical reconstruction from PDB entry 2KHO of DnaK ADP bound and the ATP-bound conformation from 4B9Q [191], obtained by applying the SASMOL approach included in the Genfit software package [8], as briefly reported in section 1.2.2.5. The two theoretical curves show a low-Q trend very similar, while at intermediate values the two conformations differ, and in particular, the open conformation deviates from the others while the closed conformation adheres to the trend of the experimental curves. It can be deduced that the 2KHO is the most suitable arrangement for the fitting of our data.
Despite this, at low Q values the experimental curves differ from the reconstructed one. In particular the curve that mostly differs from the wild type Hsp70 theoretical reconstruction is the experimental curve of wild type Hsp70.

To control if such differences refer to a different oligomeric stability at the same concentration, SAXS curve of Hsp70WT were obtained varying protein concentration from 25 to 200 μM (Fig. 4.6). When Hsp70WT concentration is higher than 100 μM, Fig. 4.6, the curve changes noticeably, depending probably on the formation of larger aggregates. Even Kratky plots highlight the differences

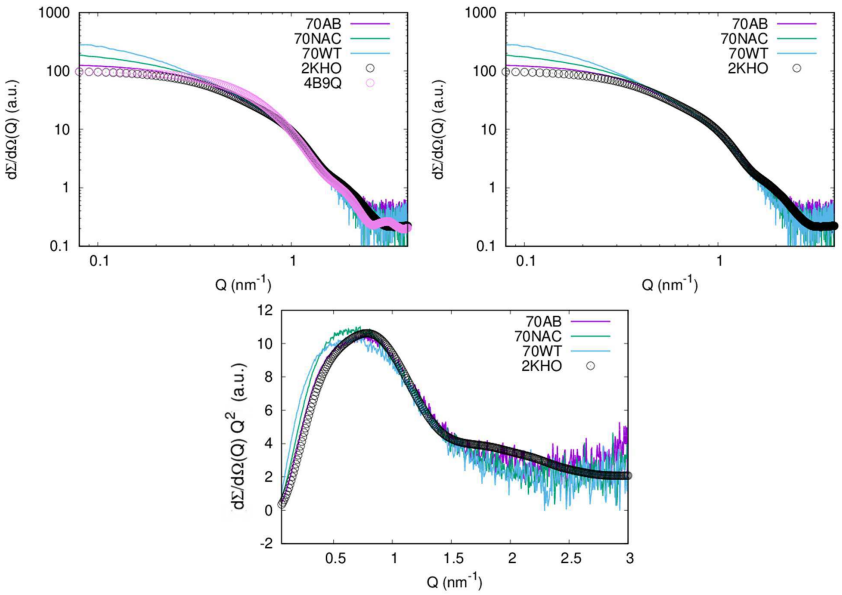

Figure 4.5: Top: Comparison between the Hsp70 variants at 50 μM and the reconstructed curve from the monomer of 2KHO PDB entry and 4B9Q [191], to show the chosen PDB structure and right, comparison with only the reconstructed curve 2KHO. Bottom: Kratky plots of the studied chaperones and reconstructed curve of 2KHO

.

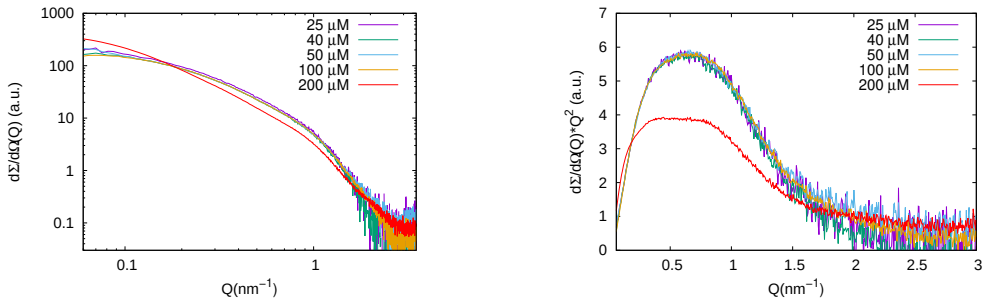

Figure 4.6: Left: wild type Hsp70 at different concentrations (in the legend). The curves are scaled to note the differences in shape, referring to the 25 μM curve, with appropriate scaling factor depending on the concentration. Right: Kratky plots of the same chaperones.

showing a shift towards lower Q values, so to higher dimensions. To stress this effect, the curves at the two extremes of concentrations, i.e. 25 μM and 200 μM have been analyzed considering two peaks with two Gaussian distributions (the minimum replica allowed by the fitting). While the high-Q peak is conserved in both concentrations (at 0.77±0.02 nm^{-1}), the low-Q peak shifts from 0.40±0.02 nm^{-1} for the 25 μM sample to 0.30±0.03 nm^{-1} for the 200 μM sample (see Fig. 4.7). Even the area occupied by this peak shifts from 6% to the 9%, suggesting an increasing amount of aggregated structures. This result is in agreement with previous analytical size-exclusion chromatography (SEC) results [186], reported in Fig. 4.7, that prove that increasing Hsp70 concentration increase the oligomeric distribution of the protein, starting from a monomeric distribution at 70 μM to a co-presence of aggregates at 220 μM.
Given these experimental results, in the 25-100 μM range, where the experimental curves have the same features, the differences between wild type and grafted proteins cannot be attributed to concentration effects. The observed differences can be therefore attributed to an intrinsic polydispersion of the sample.

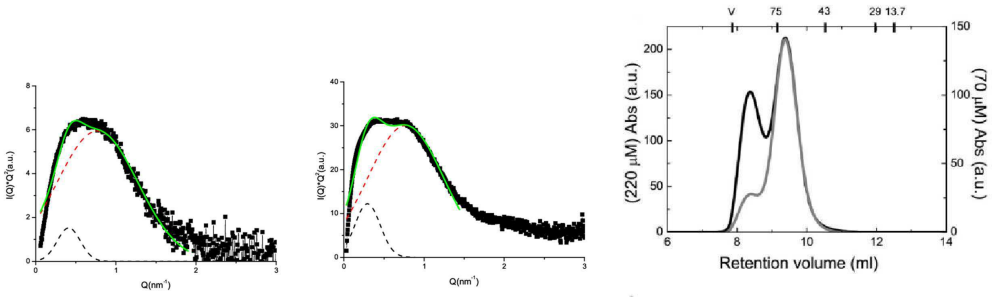

Figure 4.7: Left: Gaussian fitting (green line) of Hsp70WT at 50 μM and 200 μM, respectively. Right: analytical SEC analysis of wild type Hsp70 at protein concentrations of 220 μM (black line) and 70 μM (grey line). At the top of the chromatogram the molecular weights of standard proteins: conalbumin (75 kDa), ovalbumin (43 kDa), carbonic anhydrase (29 kDa) and ribonuclease A (13.7 kDa). Reported from [186].

Table 4.1: Gyration radii for Hsp70 from the Guinier and P(r) analysis.

	R (Hsp70WT)	R (GHsp70NAC)	R (GHsp70AB)
	nm	nm	nm
Guinier analysis	8.3 ± 0.3	6.5 ± 0.1	4.5 ± 0.1
P(r)	8.1 ± 0.5	6.5 ± 0.1	4.2 ± 0.2
theoretical Guinier	3.14 - 2.90 ± 0.01		

To characterize the oligomeric composition of the protein variants, an analysis of the differences between grafted and wild type chaperones has been performed with $P(r)$ distributions, normalized by the areas, obtained with GNOM software

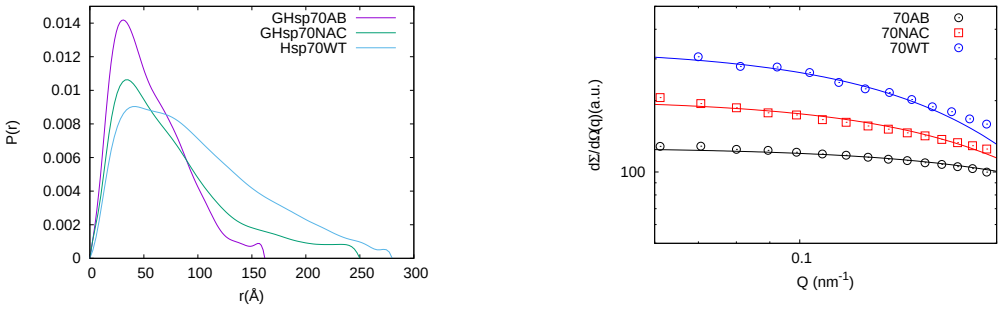

Figure 4.8: Left: P(r) analysis for Hsp70WT, GHsp70NAC and GHsp70AB, D_{max} are, respectively, 29.0, 25.0 and 16.2 nm. Curves have been normalized by the area and are in arbitrary units. Right: Guinier analysis for the three Hsp70 in comparison, Q_{max}=0.14 nm^{-1} for wild type, Q_{max}=0.2 nm^{-1} for grafted proteins.

[192] and reported in Fig. 4.8, left. Gyration radii from this analysis are reported in Table 4.1. The radii increase starting from GHsp70AB to wild type, that, in particular, reaches the higher values. The two engineered proteins, and especially GHsp70AB, seem to be more monodisperse, with dimensions similar to the reported radius for wild type Hsp70 in literature, that is 3.7±0.1 nm [193]. The represented curves suggest the hypothesis of increasing aggregates, shifting from engineered to wild type Hsp70. The SAXS curves have been analyzed even with a classical Guinier fitting for compact structures (Fig. 4.8). With the Guinier approximation a set of gyration radii consistent with $P(r)$ has been determined (Table 4.1), while the theoretical one obtained from the Guinier fitting of the curve deduced from the PDBs, ranges between 3.14±0.01 nm and 2.90±0.01 nm depending on the open (4B9Q) or closed (2KHO) conformation. It can be deduced that GHsp70AB seems to have the most monodisperse distribution, while the deviation of the wild type sample curve implies the presence of low weight oligomers, probably dimers.
With these premises we analyzed the Hsp70s data with Genfit software, considering an aggregation number up to the most polydisperse situation from literature [186], that is monomers, dimers, trimers and tetramers (for details on the Genfit model see Section 4.2 and 1.2.2.5). As expected, the two grafted proteins return a good fit considering only a monomeric composition for GHsp70AB and GHsp70NAC (Fig. 4.9) while for Hsp70WT at 50μM a satisfactory fit was obtained (see Fig. 4.10) considering a very low concentration (1%) of dimers, comparable to what reported in literature [186]. The same fitting has been obtained on Hsp70WT at 200 μM. Here the presence of oligomers results higher, with a percentage of monomers (27%), dimers (38%), trimers (16%) and tetramers (18%) (see Fig. 4.10).

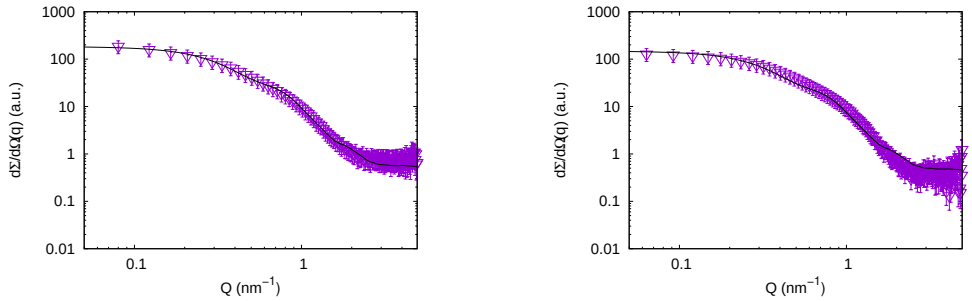

Figure 4.9: GHsp70NAC and GHsp70AB fitting with Genfit software: the fitting is satisfactory considering only monomers with $\chi^2 = 0.2$ and $\chi^2 = 1.2$ respectively.

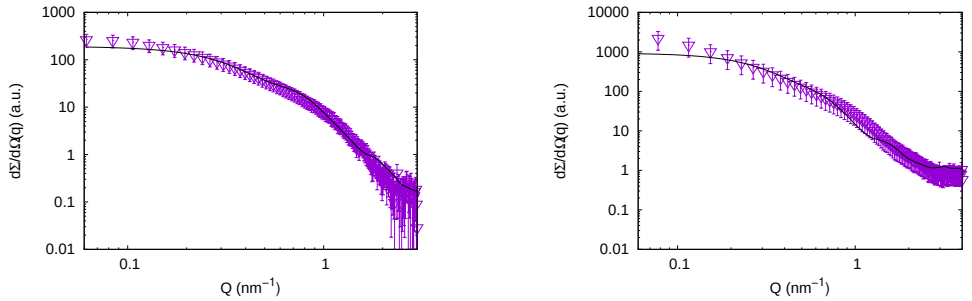

Figure 4.10: Left: Hsp70WT 50 μM fitting with Genfit analysis, χ^2=1.3. Monomers are 99%, dimers 1%. Right: Hsp70WT 200μM in which are considered monomers (27%), dimers (38%), trimers (16%) and tetramers (18%), χ^2=1.6.

4.4 Hsp70's interactions with amyloids

The interactions of the variants of Hsp70 with different species of amyloid beta peptides have been studied by means of SAXS technique. Hsp70s interactions toward the different conformations of these peptides were observed at increasing time, until 24 hours. The comparisons between the effect of the different proteins have been carried out observing the data in form of Kratky plots and, where appropriate, highlighted by the representation of the difference between the curve of the two Kratky plots in different times. With this representation is possible to better notice the different population arising in the evolution, identifying the Q-range of the modifications.
In the following, the interaction of GHsp70NAC with α-synuclein monomers and the effect of Hsp70WT on fibrils compared with the one of the grafted Hsp70 will be depicted.

4.4.1 GHsp70NAC with α-synuclein monomers

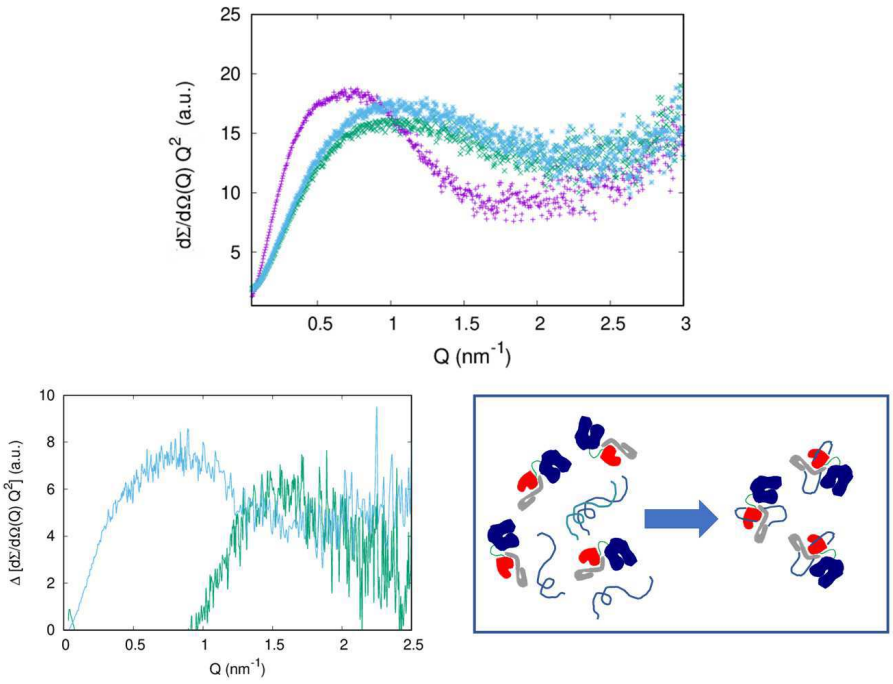

Figure 4.11: Top: GHsp70NAC with α monomers (1:1). Bottom left: Comparison between specific (GHsp70NAC, green line) and aspecific (GHsp70AB, blue line) effect on α-synuclein monomers. The curves have been obtained subtracting at the Kratky plots of the samples at 24h the plot of the one at time 0. In this way the resulting peak can highlight the Q range of the population emerging in time evolution. Right: graphical sketch for the suggested mechanism displayed by the shift in Kratky plots.

The effect of the grafted protein in respect of α-synuclein monomers is showed in Fig. 4.11 top, in the form of Kratky plot. The three curves represent the evolution of the signal of the complex during time, starting from the violet curve reaching the light blue one after approximately 24 hours. There is a concrete shift of the peak towards higher values of Q (Fig. 4.11). Highlighting the evolution in time, a difference between Kratky plots have been represented in Fig. 4.11, bottom left, subtracting at the Kratky plots of the samples at 24h the plot of the one at time 0, for GHsp70NAC and GHsp70AB. In this way the resulting peak represent the population that arises from the interaction between the chaperones and the α-synuclein monomer. In this representation, the peculiar shift for GHsp70NAC is evidenced by the position of the green curve in Fig. 4.11, that emphasize the formation of a population of approximately 4 nm. This effect can be attributed to a dissociating effect of the grafted protein with respect to low molecular weight oligomers of α-synuclein and to the encapsulation of the disordered monomers in a tight structure with GHsp70NAC (see the graphical sketch in Fig. 4.11). The effect, in this intensity, is peculiar for GHsp70NAC, while the aspecific interaction of GHsp70AB seems to involve different populations.
Such results, obtained by SAXS, confirm and support the Thioflavin T (ThT) fluorescence results reported in literature [176, 182], excluding the possible interference of ThT in the mechanisms underlying the inhibitory effects of Hsp70 [194], the intrinsic Hsp70 little fluorescence [182] and the formation of amorphous aggregates.

4.4.2 Hsp70 effects on fibers

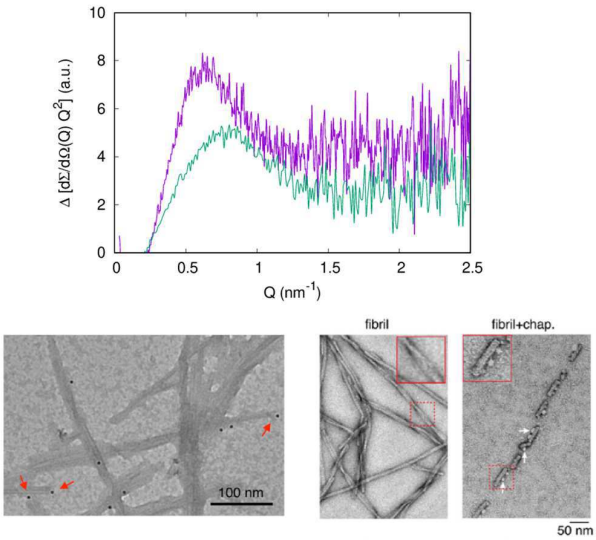

Figure 4.12: Top: difference in Kratky plots between Hsp70WT and α-synuclein (violet curve) and β fibers (green curve). Bottom left: Immunogold-TEM images of α-synuclein fibrils in the presence of Hsp70; arrows show examples of bound Hsp70 to fibril ends, from [195]; Bottom right: untreated α-synuclein fibrils and α-synuclein fibrils from full chaperone system disassembly reaction. Aligned short fibrils appear decorated with globular structures (right, white arrows). Reproduced from [196].

In order to shed light into the mechanism of the intrinsic anti-aggregation activity of Hsp70 and the specific inhibitory contributions of the interactions between Hsp70 and various α-synuclein and Aβ_{1-42} aggregated species, we investigated the effect of the three Hsp70s on these structures at physiological pH.
First of all, the Hsp70WT interacts with the amyloid fibrils formed from Aβ_{1-42} and the ones from α-synuclein, showing a common interaction with both the samples. In Fig. 4.12 the differences between the Kratky plots of Hsp70WT fibers are reported (violet line for Aβ_{1-42} fibers and green line for α-synuclein fibers). It can be noticed the rise of a peak in the Q range of 0.5-1.2 nm^{-1}, consistent with a new population in solution, whose average dimension should be of about 50-100 nm. The disaggregating effect can be hence interpreted in a detaching effect of the ends of the fibrils made by the chaperones, allowing the formation of small fragments. This hypothesis has been reported in literature [195, 196], and several experimental techniques, including TEM (Fig. 4.12), have been exploited to check this hypothesis on α-synuclein fibers. The binding of Hsp70 to proteins is considered hydrophobically-driven [197] and it is interesting to note that the dimensions of aggregates detached from Hsp70 are smaller for α-synuclein than for Aβ_{1-42} peptide, even if the two monomers are inverted in size. This effect can be related to the observation of smaller radii for α-synuclein fibrils with respect to Aβ_{1-42} peptide (see Sections 2.3.2 and 2.3.3)

suggesting an effective interaction with fibril bundle instead of single monomers. Considering the cylinder radii for the fibrils reported in sections 2.3.2 and 2.3.3 and the peaks of the Kratky plots as proportional to the radii of the structures, it can be obtained that the rate of the heights of the cylinders detached from α-synuclein is approximately 4 times the ones of Aβ_{1-42}.
The engineered Hsp70s were designed to interact with monomers of the amyloidogenic proteins, given the grafting of the specific peptide, but showed an effect even on mature fibrils. Even more, in contrast to what might be expected, the effect of grafted Hsp70 with respect to the wild type one, resembles to compete with the wild type "aspecific" effect. The formation of the populations at 0.5-1.2 nm^{-1} is lowered with GHsp70AB and almost suppressed for GHsp70NAC. In both cases instead a peak between 0 and 0.5 nm^{-1} arise, and appear to be more pronounced in the interactions with α-synuclein fibers than with Aβ_{1-42} fibers. It can be suggested that two different mechanisms, more than competing, are subsequent in the binding with the fibrils, with a first detaching effect and a secondary interaction with the fragments. The lower Q value peak can be attributed to soluble amorphous aggregates of α-synuclein and Hsp70, since they are not detected with fluorescence techniques [176]. The peak at 0.12±0.02 nm^{-1} can be identified as characteristic for the grafted interaction (obtained with a Gaussian fit of the curve between 0 and 0.5nm^{-1}) and the one at 0.7±0.1 nm^{-1} for Aβ_{1-42} fibrils and 0.9±0.1 nm^{-1} for α-synuclein fibrils typical of wild type interaction (even here with a Gaussian analysis). In order to evaluate the kind of prevalent interactions, the rate "G/wt" between the intensities of the two peaks can be considered as an indication of the specificity/aspecificity of the affinity. If the value is lower than 1, the aspecific effect is predominant, while if it is higher than 1 the grafted mechanism is more efficient. The rates are reported in Table 4.2. We obtain the higher G/WT rate for GHsp70NAC with α-synuclein fibrils and a high value for GHsp70AB with Aβ_{1-42} fibrils: these rates suggest a preference of the specific action mechanism of the grafted protein with respect to the aspecific one of the WT species. For GHsp70AB with α-synuclein we obtain a poised rate, while for Hsp70NAC with Aβ_{1-42} the rate value suggests an higher effect of the aspecific component with respect to the grafted one.
A possible interpretation of this behavior can be a two-phase mechanism in which

Table 4.2: G/WT rates for the interactions between engineered proteins and fibrils.

	α-synuclein fibers	Aβ_{1-42} fibers
GHsp70NAC	4.3 ± 1.3	0.8 ± 0.2
GHsp70AB	1.2 ± 0.4	1.5 ± 0.4

the chaperone, in an aspecific mechanism, detaches cylinders from the bundles of fibrils and then, particularly in the case of complementary peptides associated to the target, the grafted peptide connects this fragments with a soluble linker, forming very high weight populations. These wider aggregates are not detected by ThT and

in high dilution are dispersed. In this way the population arising from the interaction with the "wild type" mechanism disappears in favor of bigger aggregates. To check this hypothesis, AFM measurements have been performed on GHsp70NAC on α-synuclein fibers, in parallel with SAXS measurements at the Atomic Force Microscopy Platform on ESRF facility. Since the unevenness of fibrils in solution (as showed in Chapter 2), depending on the aging and the environmental conditions of the sample, the availability of an *in situ* instrument with which to measure the same SAXS sample acquires importance, conferring reliability to the obtained results.

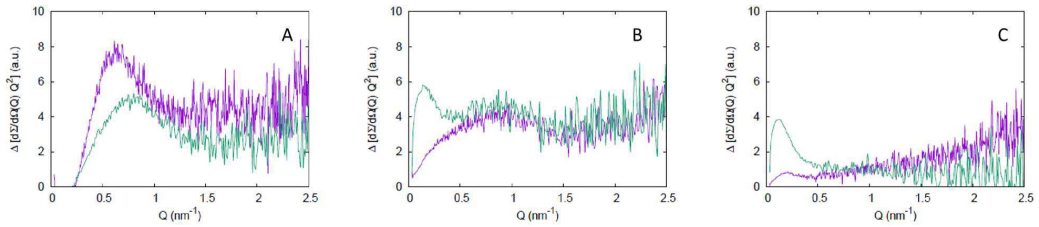

Figure 4.13: Differences in Kratky plots highlighting the two mechanisms underlying the interaction of the Hsp70s with the fibrils, starting from Hsp70WT (A), to GHsp70AB (B) and GHsp70NAC (C) with Aβ_{1-42} fibers (green line) and α-synuclein fibers (violet lines). It can be seen that the populations created by the Hsp70WT proteins are conserved in a lower efficiency in the grafted Hsp70, interacting instead with the formation of a population at very low Q values.

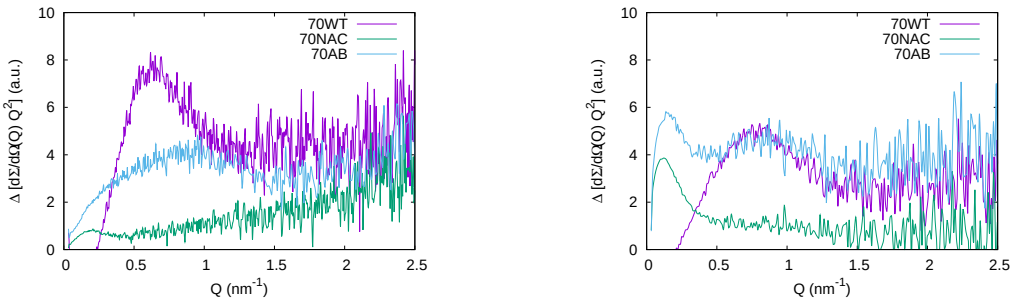

Figure 4.14: Aβ_{1-42} fibers, left, and α fibers, right, in interaction with the three chaperones: Hsp70 wild type (violet line), GHsp70NAC (green line) and GHsp70AB (blue line).

In Fig. 4.15, AFM images of α-synuclein fibrils alone (top) and of α-synuclein fibrils with GHsp70NAC (bottom) are reported. As it can be seen, the effect of Hsp70NAC on α-synuclein fibers is evident and results in a diminishing of fibers in the samples. This observation is in accordance with the supposed effect of GHsp70NAC of converting part of fibrils in soluble oligomers, with a specific-aspecific mechanism. These aggregates are not visible in AFM measurements, vanishing in the initial dilution of the samples. Such chaperone action has been shown in [197], where the binding of Hsp70 to prefibrillar species results in a

distribution shift from insoluble to soluble forms of α-synuclein.

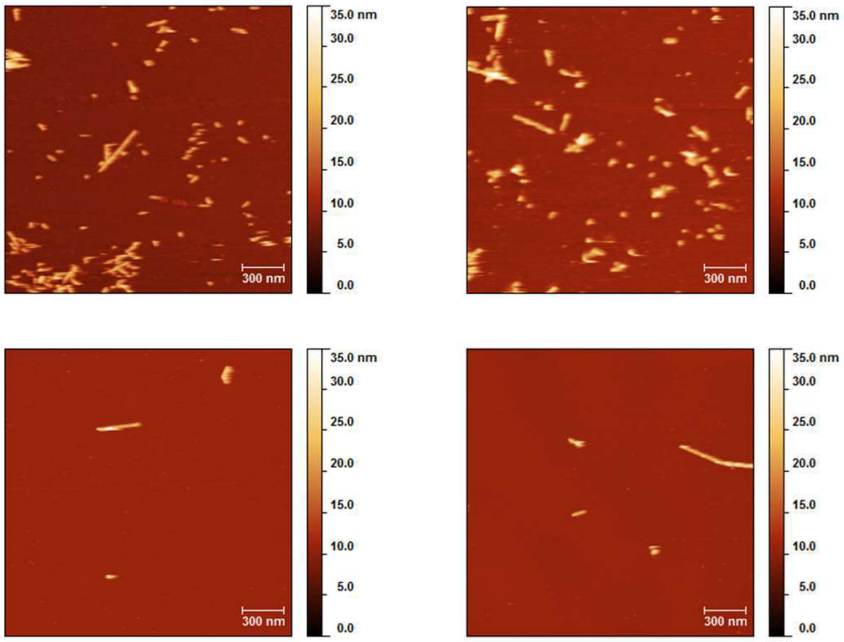

Figure 4.15: AFM images of α-synuclein fibrils alone (top) and of α-synuclein fibrils in interaction with GHsp70NAC (bottom). z-range: 35nm.

In Fig. 4.16, AFM profiles of the detected structures have been reported, showing mean dimensions of approximately 40 nm in thickness, compatible with bundle of fibrils in both samples. AFM measurements, avoiding the presence of bias linked to dyes such as ThT, confirms and complements SAXS measurements, giving informations on the three-dimensional structure of aggregates in solution.
The overall analysis is coherent with previous studies on the action of Hsp70 and GHsp70s on monomers of α-synuclein and β amyloid, and deepens the interaction with fibrils, suggesting a possible candidate for the therapy of neurodegenerative diseases and probing the mechanisms of link between chaperones and complex structures such as fibrillary aggregates.

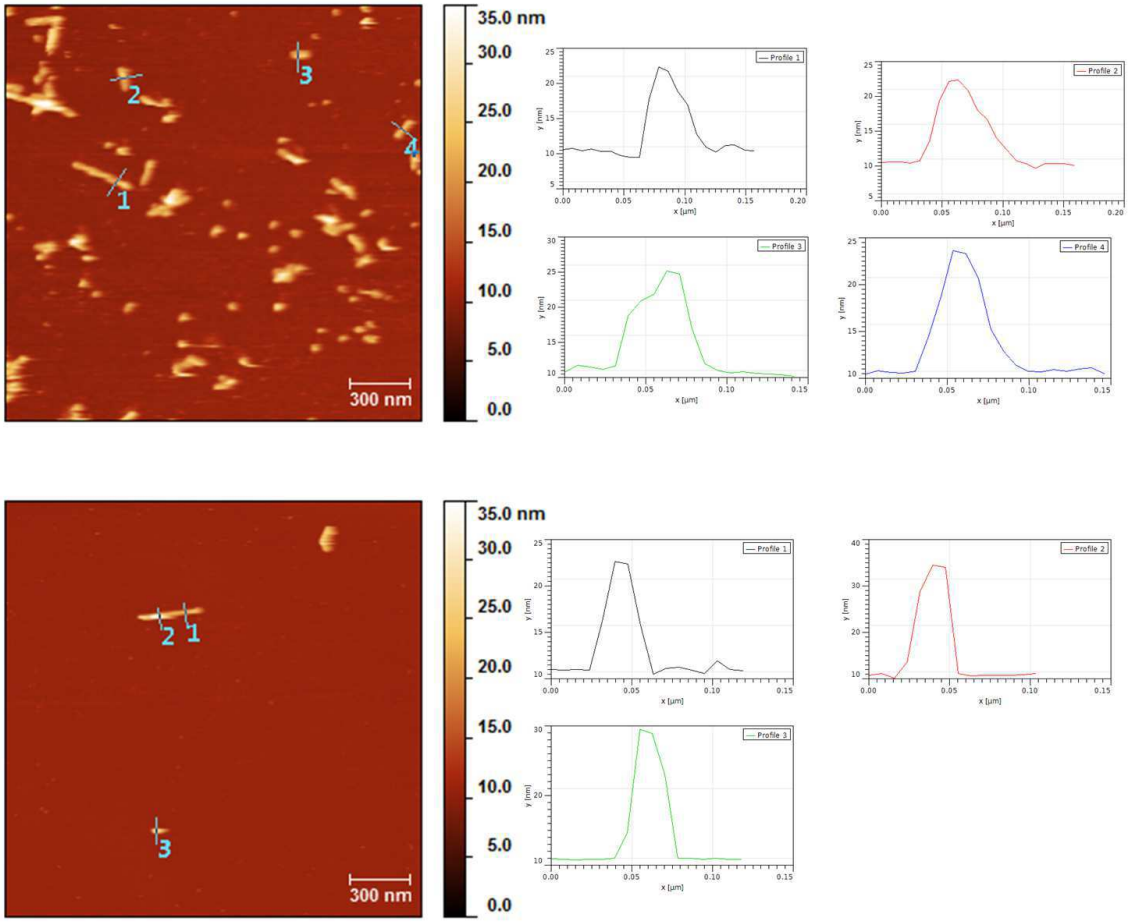

Figure 4.16: AFM images of the α-synuclein fibrils (top) and α fibers with GHsp70NAC (bottom), each with the selected profiles on the side. z-range: 35 nm.

Chapter 5

The effect of curcumin-like compounds on Aβ aggregation

Contents

5.1 Introduction

Curcumin is a molecule (diferulomethane) naturally found the turmeric root, with polyphenolic molecular structure similar to other plant pigments (e.g. extracted from grapes (resveratrol), or in green tea (catechins)). There are substantial $in-vitro$ data indicating that curcumin has antioxidant and anti-inflammatory activity [198]. Moreover, studies of Alzheimer's disease (AD) indicate a direct effect of curcumin in decreasing the amyloid pathology of AD [199, 200, 201]. As the widespread use as a food additive, curcumin was considered a promising agent in the treatment and/or prevention of AD [202]. Nonetheless, the idea of using curcumin for therapeutic purposes presents huge limitations inherent to its poor solubility, stability and ability to permeate the blood-brain barrier (BBB). For these reasons it would be opportune to synthesize compounds with the same ability of curcumin to bind Aβ peptide, but that do not present stability and bio-availability problems, allowing a real applicability in the treatment of the disease. In this sense, the replacement of 1,3-dicarbonilic nuclei with heterocyclic isosteres is a promising strategy, which has already allowed the identification of isoxazole and pyrazole derivatives capable to bind the peptide Aβ fibrils in the same manner as curcumin [203].
Here is presented a multi-disciplinary study that starts from the design of curcumin-like compounds, presenting the key chemical features required for inhibiting amyloid beta aggregation, and achieves to report the effects of these compounds in the $in-vitro$ aggregation of amyloid beta peptide [204].

Compounds design was performed in order to increase curcumin stability and capacity to penetrate the blood-brain barrier via an *in silico* drug-design by Antonio Palumbo Piccionello research group, Department of Chemistry, set in the University of Palermo. The chemo-informatic screening was performed through the calculation of molecular descriptors, able to highlight the drug-like profile. Computational design highlights two different scaffolds, namely, distiryl-1,2,4-oxadiazoles and distiryl-1,3,4-oxadiazoles, which were easily synthesized in good yields. $in-vitro$ experiments, include Synchrotron SAXS and fluorescence spectroscopy. The fluorescence spectroscopy was performed in the NEST laboratory in Pisa, in tight collaboration with Dr Antonella Battisti. In-solution experiments revealed that these compounds modify amyloid beta peptide aggregation pattern not only in the secondary structures, but even in terms of structures' dimension. The *in-vitro* cytotoxicity potential of the synthesized compounds was performed on a model neuronal cell line (LAN5) revealing, similarly to curcumin, a low cytotoxicity below 10 mM.
Results reported in this section have been published in [204].

5.2 Materials and methods

The different techniques exploited for the studies on curcumin-like compounds and interactions are hereafter presented, to introduce the experimental section to follow.

Samples preparation

The lyophilized synthetic peptide Aβ_{1-40} (Anaspec) was solubilized in NaOH 5 mM (Sigma-Aldrich), pH 10, and sonicated and lyophilized according to the Fezoui *et al.* protocol [111]. The lyophilized peptide was then dissolved in PBS (pH 7.4) and filtered through two filters in series with diameters of 0.20 mm (Millex-Lg) and 0.02 mm (Whatman), in order to eliminate large aggregates. The sample preparation was aseptically operated in a cold room at 4 °C. The Aβ_{1-40} concentration was determined using tyrosine absorption at 276 nm using an extinction coefficient of 1390 $cm^{-1}M^{-1}$. Compounds **7** and **4** were dissolved in DMSO. Absorption and fluorescence spectra for compounds **7** and **4** were registered at different times in order to assess their stability and the absence of fluorescence interference for the following spectroscopic measurements. The final samples containing Aβ_{1-40} and curcumin compounds were obtained by appropriate aseptic mixing of the solutions and were used immediately for the aggregation kinetics experiment.

Aggregation kinetics for spectroscopic experiments

Aggregation was induced by incubating 75 mM Aβ_{1-40} in the presence and absence of 7.5 mM curcumin compounds (**4** or **7**), in 0.1M phosphate buffer solution (PBS, pH 7.4), 1%DMSO, for 6 h at 45 °C under continuous magnetic stirring in the thermostatic cell holder of a FLUOROMAX 4 HORIBA Jobin Yvon spectrofluorometer (NEST, Scuola Normale Superiore and NANO-CNR, Pisa). The aggregation process was monitored by setting both the excitation and the emission monochromators at 405 nm and measuring the light diffusion at 90° [205, 206]. The illuminated volume was a cylinder of 20 mL, with the total volume of the solution in the microcuvette being 800 mL. For such a large volume, fluctuations of diffused light reflect a very small number of large particles floating in the solution. Assuming a Poisson distribution, we may estimate that in 20 mL fluctuations should arise from a particle concentration as low as $\simeq 10^{-17}$ M. Therefore, we can safely assume that monomers and small oligomers are the largely predominant species in our systems.

Thioflavin T fluorescence

Thioflavin T (ThT) fluorescence emission was monitored using a FLUOROMAX 4 HORIBA-Jobin Yvon spectrofluorimeter (NEST, Scuola Normale Superiore and NANO-CNR, Pisa). The excitation and emission wavelengths were 450 and 485 nm, respectively, with slit widths of 2 nm. The ThT concentration was 5 mM. In particular, for each sample 50 mL of 75 mM Aβ_{1-40} with and without 7.5 mM

curcumin compounds was added to 850 mL of a ThT solution with 5 mM final concentration. Thus, we reached 4 mM Aβ_{1-40} and 5 mM ThT final concentrations.

Confocal Microscopy

Images of Aβ_{1-40} fibril bundles, and compound **4**-Aβ_{1-40} and compound **7**-Aβ_{1-40} complexes stained with ThT, were obtained using a Leica TCS SP5 inverted laser scanning confocal microscope (Leica Microsystems AG, Wetzlar, Germany) interfaced with an Ar laser for excitation at 458 nm and adopting a 63 x 1.4 numerical aperture oil immersion objective (Leica Microsystems) in oil immersions (NEST, Scuola Normale Superiore and NANO-CNR, Pisa). Fibril bundles, and compound **4**-Aβ_{1-40} and compound **7**-Aβ_{1-40} complexes were left to settle for 20 min from the initial solution in 3.5 cm glass bottomed Petri dishes (WillCo-Dish, WillCo Wells, Amsterdam, the Netherlands) and then imaged therein. The excitation power was 50-200 mW at the objective, the line scanning speed was set to 400 Hz, and the wavelength collection range was between 470-515 nm. Transmission images were obtained in differential image contrast mode (Nomarski image) using the same laser source.

SAXS

SAXS experiments of Aβ_{1-40} were carried out at the BM29 beamline in ESRF - the European Synchrotron Radiation Facility in Grenoble, France. Protein samples were carried in ice, and freshly prepared with the desired amount of curcumin-like compound. Aβ_{1-40} concentration was spectrophotometrically checked to be 270 μM. Each sample was measured at 37 °C. SAXS patterns were recorded using a bidimensional Pilatus 1 M detector. The sample cell used is a 1.0 mm diameter quartz capillary, with a few tens of microns wall thickness. On BM29, data collection on protein solutions is possible in a wide temperature range via an automated sample changer. After each measurement protein samples are stored at 37 °C, without stirring. To minimize the dose and the consequent radiation damage, protein solutions were only irradiated during data collection using a fast experimental shutter located 4 m upstream of the sample, thus controlling the acquisition time. The transmitted intensity is monitored with a diode integrated in the beamstop and the intensity measured during data acquisition is used for normalization. Since the sample-detector distance was fixed at 2.867 m, the Q values ranged from 0.01 to 0.45 Å^{-1}. SAXS macroscopic differential scattering cross sections dΣ/dΩ(Q) (briefly referred to as scattering intensities) were obtained on an absolute scale (cm^{-1}) by calibrating via a water sample, subtracting the proper buffer contribution for each investigated condition, and correcting for the protein volume fraction, as previously described. Each measurement lasted 1 s, followed by a dead time of 6 s in order to avoid radiation damage, and was repeated at least 10 times.

Biological evaluation

The cytotoxicity of the compounds and their effect on Aβ_{1-40} aggregation *in vitro*, were studied on the LAN5 neuroblastoma cell line through an MTT assay (BioNec, University of Palermo). Cells were treated with both compounds **4** and **7** at 1 and 5 mM doses, respectively. Taking into account the cytotoxicity potential of Aβ_{1-40} in aggregated species, LAN5 cells were treated using aliquots taken during Aβ_{1-40} aggregation kinetics at 50 mM in the absence and presence of the oxadiazoles **4** and **7**, each one at 5 mM. Aβ_{1-40} aliquots were sampled after different incubation times. The experiments were carried out under the same conditions as the Rayleigh experiment, but using an Aβ_{1-40} concentration of 50 mM. The Aβ amyloid aggregation kinetics were followed at a controlled temperature (37 °C) and under stirring (200 rpm) at 50 mM. The samples for cytotoxicity assays were collected at the beginning, after 30 minutes, and after two hours of kinetics experiments, and were diluted in a medium at 5 mM of Aβ. To assess cell viability after 24 h of treatment, the MTT (3-(4,5- dimethylthiazol-2-yl-2,5-diphenyl tetrazolium bromide)) assay (Sigma-Aldrich) was performed as previously reported.

5.3 Curcumin like compound: design and interactions

Here an analysis on curcumin-like compounds realization and interaction will be presented, starting from the characterization and design of curcumin derivatives proceeding to the analysis of interaction with Aβ_{1-40} peptide.

5.3.1 Drug design of curcumin-like compounds

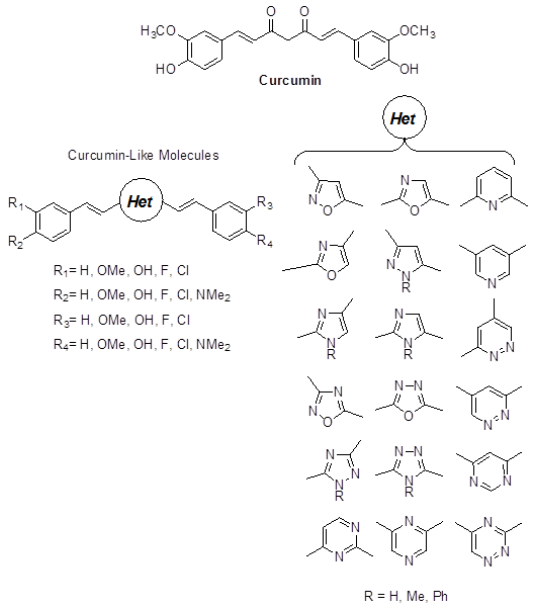

Figure 5.1: Structure of curcumin and dataset for the generation of the curcumin-like database.

The *in silico* study was based on the design of structures, related to curcumin, characterized by the substitution of the di-ketonic core of the molecule with a more stable, planar heterocycle (see Fig. 5.1): a large library with new compounds presenting the curcumin-like structure was generated. The chemo-informatic screening was accomplished by means of the software package Maestro Schröedinger, through the calculation of molecular descriptors able to highlight the drug-like profile of new molecules. From this screening, the database was reduced to about 700 compounds possessing the requested features. These compounds were used for the following step of Docking with the biological target, a pentamer of Aβ (PDB: 2BEG, Fig. 5.3) [207], given the absence of oligomer of PDB in literature. Docking poses revealed the preference for a binding on the saddle near Met35 (see Fig. 5.2), a previously proposed binding site for curcumin and other aggregation's inhibitors [208] and the preference of curcumin to interact with the lateral oligomer region, nearby the 17-21 aminoacid residues, as previously experimentally observed for curcumin as well as for other aggregation inhibitors, such as Hsp70 in Section 4.1 [209].
Six compounds, between 50 selected by the docking, binding the Met35 region with

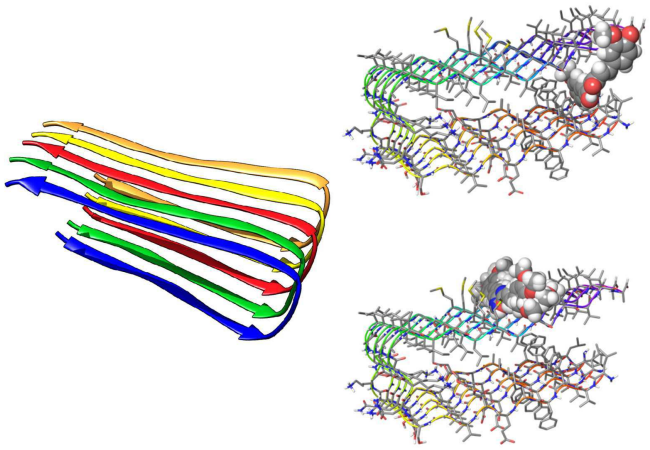

Figure 5.2: Left: the biological target used for drug design (a pentamer of Aβ_{1-42}), PDB:2BEG from [207], image realization with Chimera USCF software [157]. Right: Docking poses for curcumin (top) and for selected compounds (bottom) binding saddle nearby Met35.

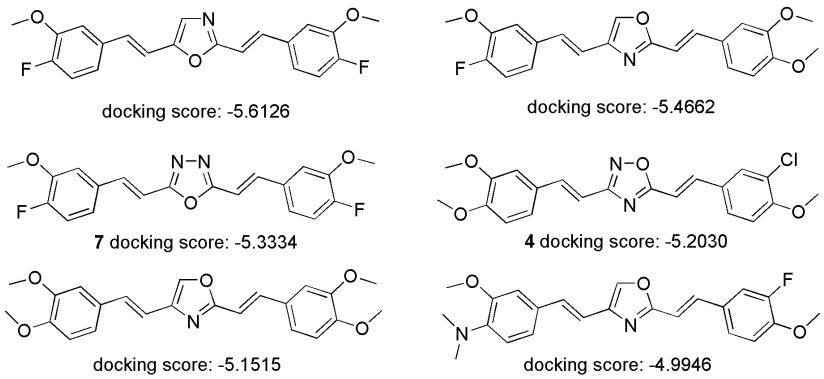

Figure 5.3: Structures of selected curcumin-like compounds. Docking score for curcumin was -3.92.

higher score (see Fig. 5.3) have been considered. Evaluation about synthetic feasibility and preliminary attempted synthesis, allowed the selection of two compounds. These compounds are two different oxadiazoles regio-isomers, which where both obtained through conventional cyclization reaction. In particular, the 1,2,4-oxadiazole derivative, that we called **4**, was obtained by following the conventional amidoxime route [210], while the 1,3,4-oxadiazole regio-isomer **7** was obtained from the construction of a diacylhydrazine derivative followed by cyclization (see Schemes 5.1). Both compounds were obtained in good overall yields and with all double bonds with *trans* geometry.

In order to assess whether compound **4** and compound **7** were able to directly interact with Aβ_{1-40} and to influence its aggregation process, the self-assembly kinetics in the presence and in the absence of either compound have been monitored.

Scheme 5.1 Synthesis of compound **4** and **7**.

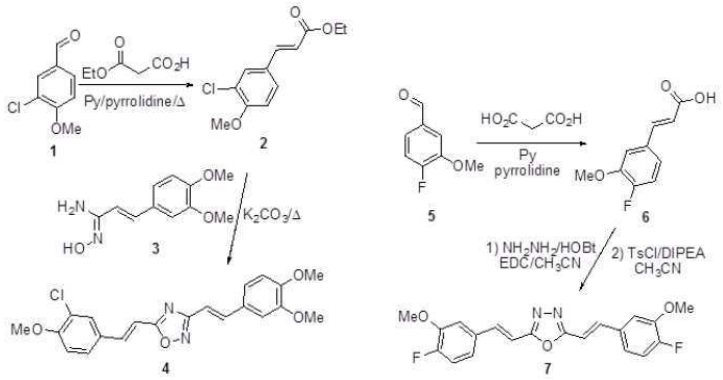

5.3.2 *In vitro* aggregation

First of all, to detect the specific formation of β-strands aggregates in amyloid fibrils at the end of the kinetics, Thioflavin T (ThT) assay has been performed [115, 116]. The fluorescent dye has been added to different samples only at the end of the kinetic, to avoid bias of the exogenous compound for the kinetic of aggregation and for the effect of the curcumin-like compound itself [211, 212]. In Fig. 5.4, left,

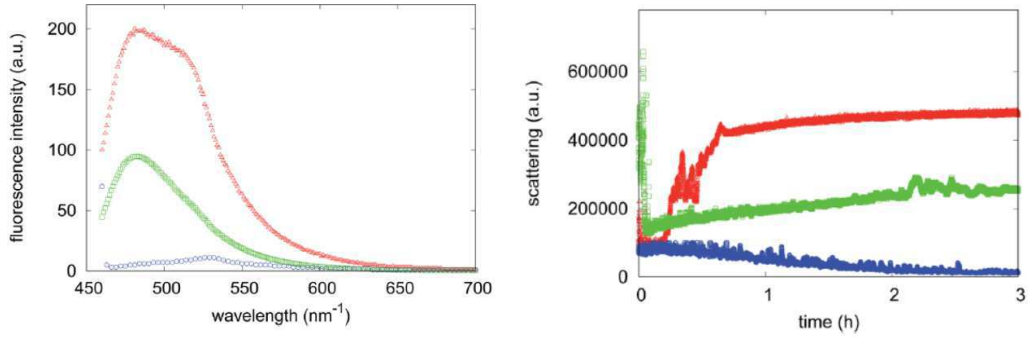

Figure 5.4: Left: Fluorescence spectra of ThT bound, at the end of the aggregation process, at 75 μM Aβ_{1-40} alone (triangles) and in the presence of 7.5 μM of compound **4** (circles) or compound **7** (squares). Right: Aggregation kinetics obtained by Rayleight scattering of 75 μM Aβ_{1-40} alone (triangles) and in presence of 7.5 μM compound **4** (circles) or compound **7** (squares).

fluorescence spectra of ThT bound to Aβ_{1-40} are reported at the end of the fibrillogenesis kinetics in absence and presence of synthesized compounds. A significant reduction in ThT emission can be detected in samples with compound **4**, whereas a less marked reduction in fluorescence maximum is registered in the presence of compound **7**. Since ThT fluorescence intensity is proportional to the amyloid structures formed [114], this suggests a different interaction of the two compounds with Aβ_{1-40}. In order to qualitatively evaluate the morphology and the differences of the species at the final stage of the aggregation kinetics, confocal microscopy was

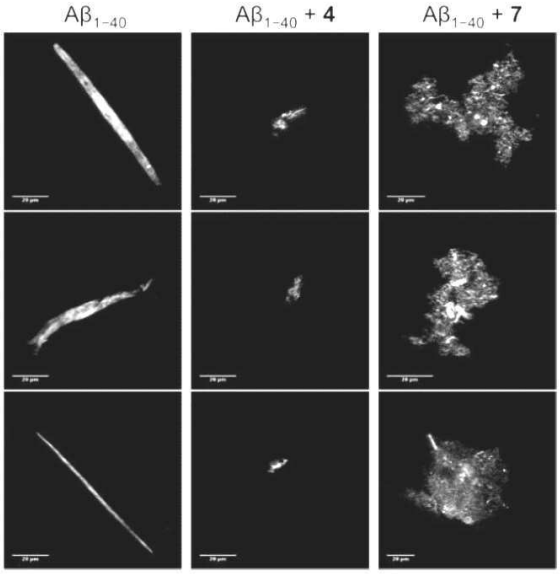

Figure 5.5: Fluorescence confocal images of ThT-stained Aβ_{1-40} (left), commented in 2.3.3 and reported as reference, compound **4**-treated Aβ_{1-40} (center) and compound **7**-treated Aβ_{1-40} (right) after 6 hours of incubation. Scale bar: 20 μm, as reported in the legend.

performed on aliquots of the solutions used for the kinetics experiments. Samples were stained with ThT, left to settle down in glass-bottom dishes in order to allow the aggregates precipitating, and then imaged. Fig. 5.5 shows images acquired at the final stage of incubation of Aβ_{1-40} with or without the curcumin derivatives. The peptide sample treated with compound **4** does not reveal a massive presence of amyloid fibers or large conglomerations, whilst a prevalent formation of small amorphous aggregates is observed. Larger aggregates are instead detected in the presence of compound **7**.

Given the proportionality between the light scattering intensity and the size of all the species in solution, the kinetics of samples incubated under amyloid protocol conditions have been observed monitoring the behavior of Rayleigh scattering peak, so in a free-dye approach. Fig. 5.4 shows the time course of the Rayleigh peak intensity during the aggregation kinetics of 75 μM Aβ_{1-40} incubated at 45 °C, alone or in the presence of compound **4** or compound **7**. The Aβ_{1-40} peptide aggregation kinetics follows a sigmoidal profile characteristic of a typical nucleation-polymerization process where the plateau corresponds to the completion of the aggregation process, and its limit value is related to the properties of the aggregates formed at the end of the process. In the presence of compound **4** (see circular symbols in Fig. 5.4, right), no significant change of light scattering intensity can be observed for the sample up to 3 hours from the beginning of the process, suggesting that the aggregation is inhibited by the compound, even if the sensibility of the technique cannot ensure the absence of low molecular weight oligomers. When the sample is incubated in the presence of compound **7** (see square symbols in Fig. 5.4) the inhibition of the

aggregation seems to be not so drastic. However, the assembly rate and the final amount of final aggregates are significantly reduced. In addition, no lag phase can be observed, thus suggesting that compound **7** is able to perturb the aggregation route of Aβ_{1-40} in respect to the one of compound **4** and of Aβ_{1-40} alone. These

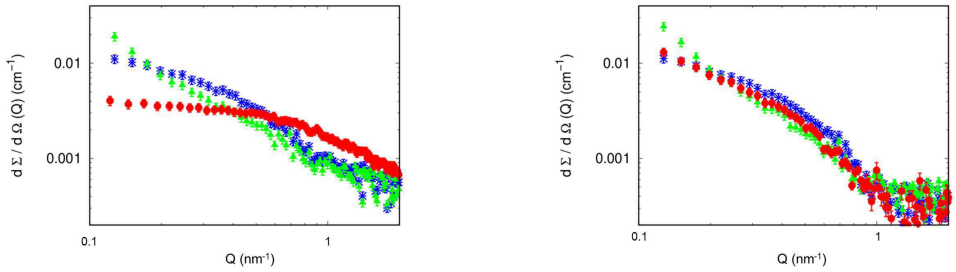

Figure 5.6: Left: SAXS curves of 270 μM Aβ_{1-40} just after the fresh preparation without any compound (red), with compound **4** (blue) and with compound **7** (green), each one in molar ratio 1:1 with Aβ_{1-40}. Right: SAXS curves corresponding to the same samples with the same color legend, after 200 minutes from preparation.

experimental results indicate that while compound **4** is able to strongly inhibit the aggregation of Aβ_{1-40} peptide toward the formation of amyloid aggregates, compound **7** alters the aggregation pattern redirecting a portion of monomers towards non-amyloid states.

To investigate at a molecular level the effect of each compound on the aggregation kinetics of Aβ_{1-40} , SAXS curves of 270 μM Aβ_{1-40} in the absence and in the presence of compound **4** or compound **7** (both in 1:1 molar ratio) were recorded immediately after their fresh preparation (time 0) and after 100, 150 and 200 min from the preparation. Experimental curves corresponding to two compounds with Aβ_{1-40} are reported in Fig. 5.6, left, and compared to the one of Aβ_{1-40} alone. First of all, it can be noticed that the scattering intensity a $Q \simeq 0$ increases adding compounds in solution (green and blue points in respect to red ones). Since at the same protein weight concentration values the cross section is proportional to the molecular weight of the average particles in solution [213], it is clear that both the compounds induce immediately an aggregation on Aβ_{1-40} peptide, given the very small dimensions of the compounds alone. Even more the overall shape of SAXS curve is different in presence of compounds and between compound **4** and **7**. On the other side, SAXS data of compounds **4** and **7**, in molar ratio 1:1 with Aβ_{1-40} monomers evidence a sudden modification and a different kinetic pattern of the peptide aggregation state. The final stage of Aβ_{1-40} peptide aggregation in presence and in absence of the compounds shows appreciable differences, as reported in Fig. 5.6, right panel. In fact, the Q-range between 0.3 and 0.6 nm^{-1} show noticeable differences between Aβ_{1-40} and Aβ_{1-40} with compound **4**, at lower Q are clear the differences with the peptide with compound **7** and the peptide alone.

More in details, while the SAXS curve of the peptide alone 100 min after the prepa-

ration was best fitted according to the Guinier approach for long cylinders representative of fibrillar species, as reported in chapter 2.3, this approximation failed fitting the corresponding data in the presence of both compounds at any time. However, the standard Guinier approximation related to unspecific spherical-like particles can successfully fit the low Q trend of all the experimental curves in the presence of compounds **4** and **7**, as shown by the linear trend of the plots log $\frac{d\Sigma}{d\Omega}(Q)$ vs. Q^2 reported in Fig. 5.7. The best fit Guinier radii R_g are reported in Fig. 5.7, bottom: in presence of both compounds we observe that the average dimensions of the particles in solution is increasing versus time.

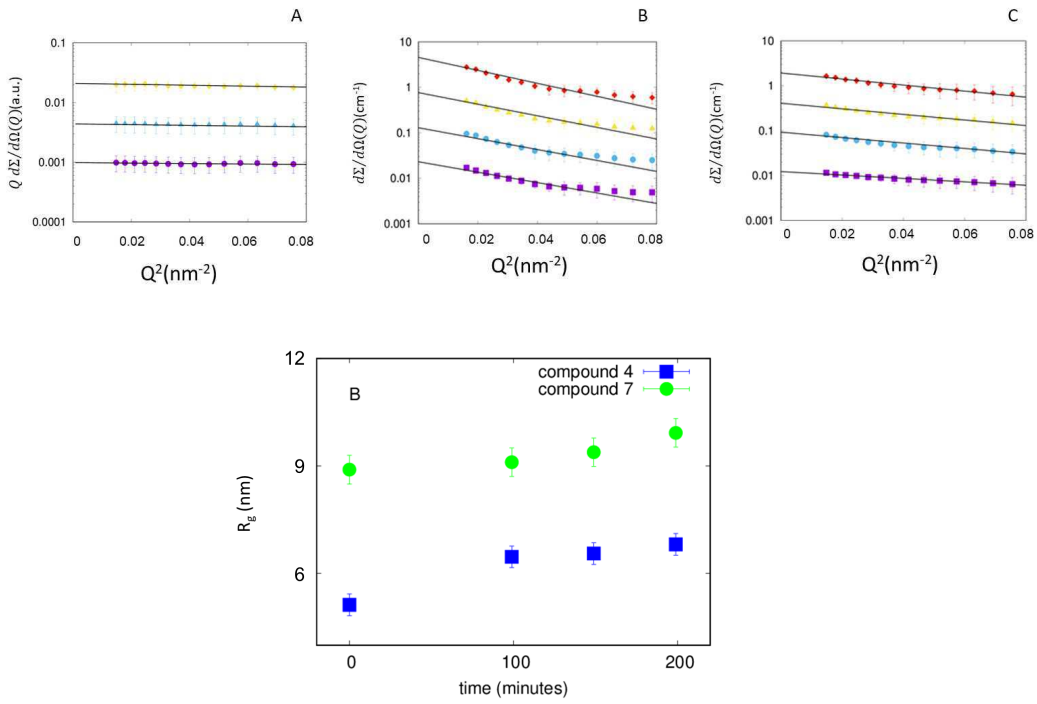

Figure 5.7: Top: Guinier plots for spherical particles of SAXS curves corresponding to Aβ in presence of compound 4 (B) and 7 (C) (ratio 1:1) compared with Guinier approximation for rod particle for Aβ_{1-40} alone (A, see Section 2.3.2), all obtained at time 0 (violet squares), and after 100 (blue circles), 150 (yellow triangles), and 200 (red diamonds) minutes. Curves at increasing time are shifted for clarity by a factor 5i (with i=0 for time 100, i=1 for the measurement after 150 minutes, and so on). Continuous lines represent the theoretical fitting.
Bottom: Time dependence of the gyration radii resulting by fitting SAXS curves corresponding to Aβ_{1-40} in presence of compounds **4** (blue) and **7** (green), as in the legend.

These model-free approaches enabled us to evaluate that both compounds **4** and **7** immediately modify Aβ_{1-40} aggregation state and provided the average dimensions of the particles in solution in each specific case. However, model-free methods do not provide a complete description of the species present in solution. Hence a further SAXS data analysis by Genfit software [8] was performed considering the

simultaneous presence in solution of disordered chains (unf) and cylinders (cyl), considering the scattering cross section as

$$\frac{d\Sigma}{d\Omega}(Q) = \frac{cN_A}{M_1}\left[x_{unf}P_{unf}(Q) + \frac{x_{cyl}}{N_{cyl}}P_{cyl}(Q)\right] \tag{5.1}$$

where c is the protein mass concentration, N_A is Avogadro's number, M_1 is the monomer molecular weight, x_i is the fraction of monomers involved in the formation of the i-species, $P_i(Q)$ its form factor and N_i is the aggregation number of that species (which is 1 for unfolded monomers). The structure factor $S(Q)$ was approximated to unity due to the low protein concentration of the experiment (see 1.2.2.5). This analysis has been performed considering the results obtained with the other techniques, in particular microscopy images, suggesting a polymorphism in the samples (Fig. 5.5). Results are reported in Fig. 5.8 and summarized in Fig. 5.9 in respect to Aβ_{1-40} alone and point out a description of the different species in solution. While in the final investigated time step of Aβ_{1-40} peptide aggregation

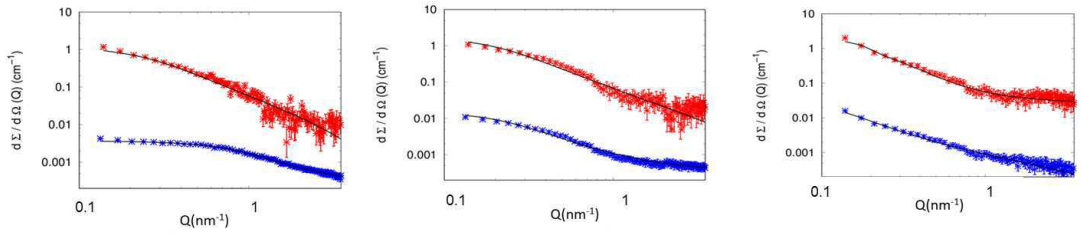

Figure 5.8: Starting (blue) and final (red) stages of Aβ alone (left), Aβ in presence of compound **4** (middle), Aβ in presence of compound **7** (right). Black lines represent the fitting obtained with worm like model (one population with aggregation number 1 for Aβ alone and two population for Aβ with compounds 4 and 7) and cylinders. Curves are scaled for sake of clarity (10^2 factor) to evidence the fitting in the whole range of Q.

the predominant object in solution resembles the cylindrical shape, confirming the fibrillar pattern, in the final step of aggregation in presence of compounds the results are clearly different. Compound **4** determines the prevalent presence of disordered aggregates, with just a low percentage of cylinders. On the contrary, compound **7** decreases the development of cylindrical species, in respect to the case of just Aβ_{1-40} in solution, in favor of disordered species. These findings are in agreement with the other experimental techniques, showing a strong inhibiting action of compound **4** and an interaction of compound **7** with amyloid formation, as pointed out from the fluorescence microscopy (see Fig. 5.5) and Rayleight scattering (see Fig. 5.4).
Finally, a biological analysis of the effects of the two curcumin-like compounds was carried out. To follow the internalization of the compound associated with Aβ-peptide, red-labeled Aβ_{1-40} (AβHF) was used to follow peptide uptake in Neuronal-type SH-SY5Y cells (Fig. 5.10). Cells treated with AβHF were monitored over time; after 2-3 hours of incubation at 37 °C the peptide started to concentrate in intracellular vesicles. The peptide was administered to cells treated with different probes, too. The peptide did not accumulate on the plasma membrane, it was slowly inter-

	Aβ40	Compound 7+Aβ40	Compound 4+Aβ40
start	1 worm like n_{agg}=1	2 worm like: 25±2%, n_{agg}=2±1 75±8%, n_{agg}=13±2	2 worm like: 0,10±0,03%, n_{agg}=2±1 99,8±0,5%, n_{agg}=13±3
end	3±1% worm like: n_{agg}=16±5 97±8% cylinder: R=2.3±0.4 nm h>150 nm	31±4% worm like: n_{agg}=17±5 69±7% cylinder: R=2.8±0.6 Å h>150 nm	95±9% worm like: n_{agg}=16±5 5±1% cylinder: R=2.8±0.4 Å h>150 nm

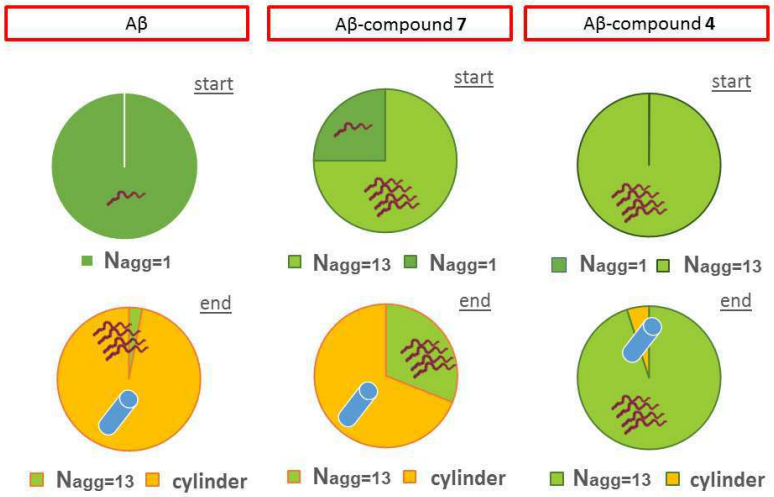

Figure 5.9: Table (top) of remarkable parameters and schematic representation (bottom) of SAXS fitting analysis on starting and final data of Aβ_{1-40} and Aβ_{1-40} with compounds **7** and **4**. SAXS curves were analyzed considering a combination of the form factors corresponding to the fibril-like cylinders states and unfolded species to describe respectively final and initial stages. In table the percentage of each species obtained from the fitting is reported, for the worm like model the aggregation number of segments(N_{agg}) and for cylinder model the radii (r) and the cylinders length (h, always undetectable by the technique). The presence of the two compounds lead to a different behavior in the final stages, where the fraction of cylinders in solution decrease from Aβ_{1-40} alone for both compounds, more noticeably in presence of compound **4**.

nalized in vesicles that after 24 h partially colocalize with lysosomes.
Further analyses have been performed on LAN5 cells, treated using aliquots taken during aggregation kinetic of the peptide alone or in presence of the compounds in a 10:1 peptide/compound ratio (Fig. 5.11). Cells were treated with both compounds and revealed a low cytotoxicity for both compounds **4** and **7** at 1 μM, particularly small for the last one. Conversely the addition of compounds at higher concentration (5 μM) raised a potential cytotoxicity, and specifically compound **4** reduced the cell viability at 5 μM (Fig. 5.11). From previous studies performed under the same conditions, we consider in the sample the prevalence of oligomeric

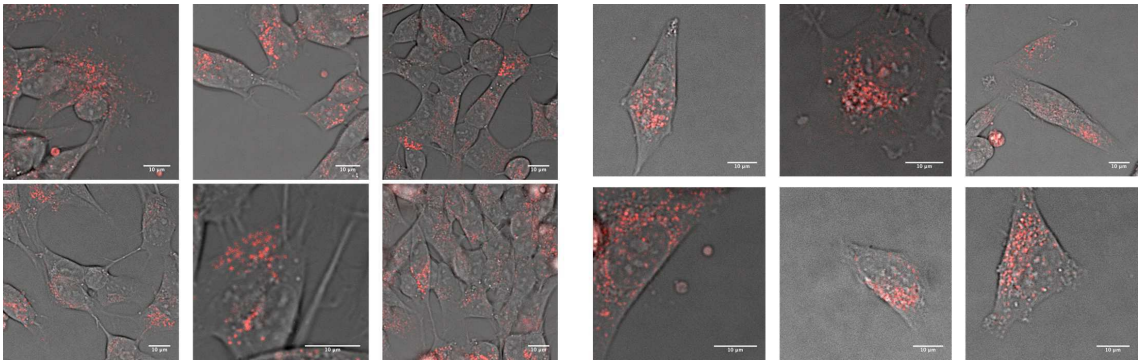

Figure 5.10: Efficient internalization of complexes constituted of curcumin derivatives and Aβ-peptide in SH-SY5Y cells. Scale bar 10 μm.

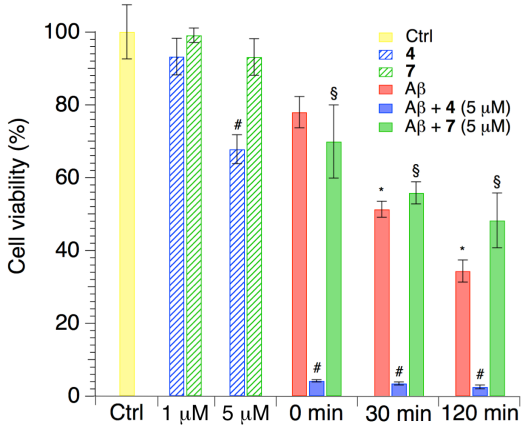

Figure 5.11: Histograms showing the percentage of cell viability after treatments with Aβ_{1-40} and the compounds alone or in combination. Results obtained for compound **4** and **7** corresponding at 1 hour from the beginning of the aggregation process: *p$<$0.001 vs Ctrl; §p$<$0.001 vs Ctrl, 1μM and 5μM; #p$<$0.001 vs Ctrl and 1μM.

species [214]. As expected, Aβ increase its toxicity along its aggregation kinetic due to the formation of toxic oligomeric species. Interestingly, compound **7** is able to counterbalance the formation of toxic oligomers, probably modifying the aggregation pathway toward less toxic aggregates, because after 2 hours is able to slightly reduce the Aβ_{1-40}-induced toxicity. On the other hand, co-administration of compound **4** clearly enhances Aβ_{1-40} toxicity. The latter effect could probably be explained by the higher presence of toxic oligomers in the medium, due to the inhibitory effect of compound **4** on the peptide aggregation into less noxious amyloid fibrils.

5.3.3 Induced Fit Docking

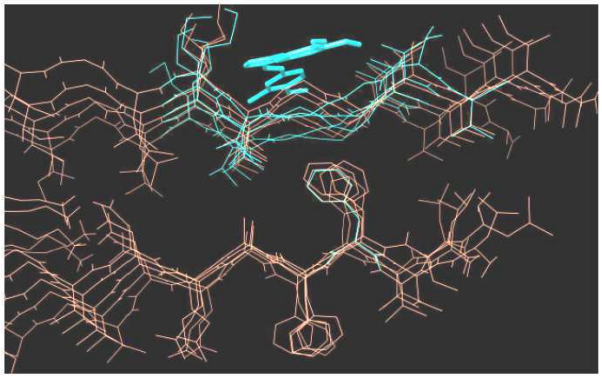

Figure 5.12: IFD pose for compound **4** bound to Aβ_{1-40} (turquoise) and unbound Aβ_{1-40} (orange) (PDB: 2BEG). In the presence of **4**, Gly37-Gly38 are compressed by the ligand and loss the zigzag conformation.

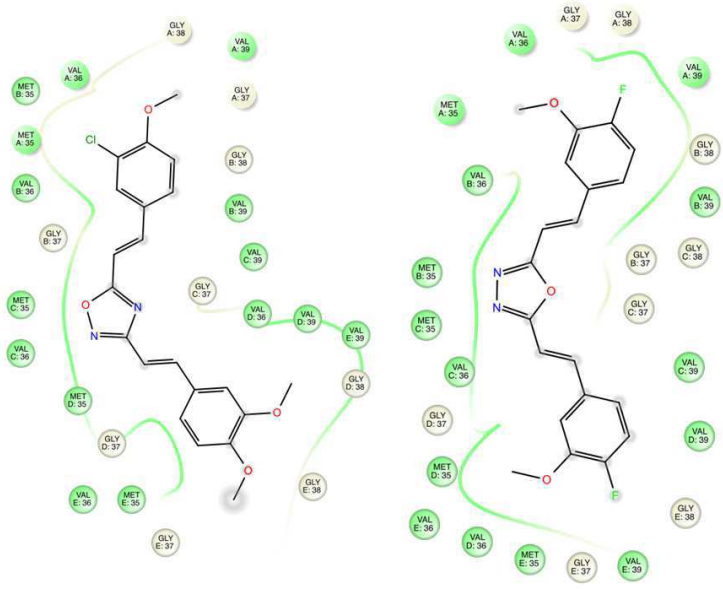

Figure 5.13: Interaction maps derived from IFD poses for compound **4** (left) and compound **7** (right) bound to chain A (PDB: 2BEG).

Because this different behavior of **4** and **7** was experimentally proved, a further analysis of the compounds binding mode was performed by means of Induced Fit Docking (IFD). IFD results showed that the binding of compounds **4** and **7** occur in a similar way in terms of involved amino acids and non-covalent interactions. According to IFD, both compounds bind Aβ in a saddle between Met35 and Val39, by means of hydrophobic interactions (see Fig. 5.12 and 5.13). The conformation of investigated compounds into the binding site is almost similar in terms of

molecule's orientation and conformation around rotable bonds. On the other side, a clear difference could be envisaged with compound **4** concerning Gly36-Gly37 conformation in comparison to the starting pentameric structure. In fact, in the presence of bound **4**, the peptide backbone seems compressed, thus perturb the β-sheet motif. In the presence of compounds **7**, the zigzag β-sheet motif is partially preserved (see Fig. 5.14). Hence, IFD results suggest that while compound **7** could

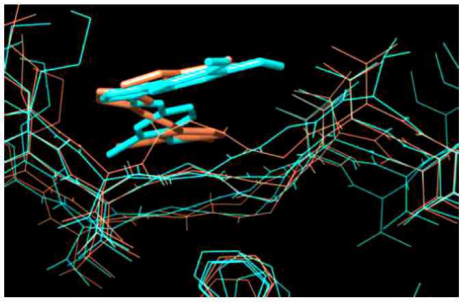

Figure 5.14: IFD poses for compound **4** (turquoise) and **7** (orange) bound to Aβ pentamer (PDB: 2BEG). In the presence of **7**, the pristine zigzag conformation of Gly37-Gly38 is partially preserved.

just interfere with Aβ aggregation avoiding packing of oligomers along fibril major axis, due to steric hindrance, compound **4** could also interfere with the formation of the β-sheet motif, unfortunately thus allowing the formation of toxic off-pathway structures.

In conclusion, both the compounds **4** and **7** interact with Aβ_{1-40} fibrillogenesis. They give rise to aggregates with different morphologies as well as with different cytotoxic potential. This result can be exploited to different aims. Taking into account as basic requirement the low cytotoxic impact of a drug, compound **7** could be deemed to be a promising candidate even considering the outrightness of its effect on Aβ_{1-40}. On the other hand, compound **4** triggers a lower peptide aggregation, featured by a higher cytotoxicity. This hypothesis is in agreement with our biological analysis: compound **4**, linking to Aβ_{1-40} oligomeric toxic species, inhibits the formation of large aggregates, but its addition to the amyloid peptide may induce a higher concentration of small toxic oligomers, thus producing a collapse in cell viability. The eventuality here described does not completely rule out the interest toward compound **4**. It is possible, in fact, to consider its use toward studies for the identification of toxic oligomers, coupling it to a removal treatment after the binding.

Chapter 6

Lipid-protein interactions

Contents

6.1 Introduction

A well-established mechanism in neurodegenerative disease etiology involves the neuronal membrane damage as a consequence to the seeding and growth of amyloidogenic aggregates onto the lipid bilayer. In particular, it has been reported that Aβ is able to bind the ganglioside GM1, expressed in lipid rafts on the extracellular surface, particularly on synaptic membranes [215]. The complex GM1-Aβ *in vivo* has been identified in cerebral cortices from AD and Down's syndrome subjects, while it was not detected in controls [216]. Substantial evidence suggests that small, prefibrillar oligomers, forming at the beginning of the aggregation process potentially act as synaptotoxins towards the cellular membrane [217, 218, 37]. The understanding of amyloid peptides interaction with cellular membranes is thus between the major molecular challenges among the efforts against Alzheimer's disease. In this study the interactions of the liposomes with both monomers and an early aggregated protein solution is presented. The liposomes (LUV) exploited represent a good model of neural membrane, with raft components, like cholesterol and GM1, natural effective charge (POPS) and lipid main component (POPC).
The experimental section follows two approaches: a first study of the effect of monomeric and oligomeric species of model proteins on the lipid bilayer by means of fluorescence spectroscopy, and a second study of the interaction of Aβ peptide on lipid membranes by means of Neutron Spin Echo (NSE). In particular, the fluorescence experiment has been designed in accordance with literature [219], exploiting the quenching effect of a fluorophore, i.e. carboxyluorescein, inside LUVs. With this

device, an eventual leakage of the membrane by amyloid fibrils of model proteins can be observed by a sudden increase in the fluorescence signal. On the nanometer scale, however, undulations of the lipid bilayer are experimentally much more difficult to probe. Few spectroscopic techniques offer the spatial and temporal resolution needed. NSE is capable of probing direct measurements of bilayer undulation with spin echo experiments, allowing access to the bilayer's bending modulus [220, 221, 222]. This admitted getting information on the mechanism through which Aβ species can influence membrane functionality. Moreover, to better understand such mechanism, but also in the perspective of a therapy search, the role of mtHsp60 was investigated by the study of the interaction of the liposomes with the same early aggregated Aβ peptide solution, maturated in the presence of mtHsp60.
The NSE-SANS study is part of a manuscript in submission. The results reveal an effective interaction of oligomers on the membrane integrity, showing a disruption of the membrane in presence of oligomers only. Even more, Aβ peptide induces variations in the dynamic properties of membranes, that are even more marked in the presence of Aβ oligomers considered the most toxic forms.

6.2 Materials and methods

In this section, the samples investigated and the techniques used are reported, dividing them into samples and techniques for the fluorescence analysis and for Neutron Spin Echo measurements.

Spectrofluorometer experiment

The Large Unilamellar Vescicles (LUVs) were produced by repeated extrusions, through a 100 nm pore filter of a solution containing multilamellar vesicles (MLVs) of POPC and POPS (POPC: POPS = 9: 1) in 10 mM HEPES buffer, containing Carboxyfluorescein (10 mM) at pH 7.4, as indicated in literature [219]. The excess of carboxyfluorescein outside the LUV has been cleaned up by column chromatography (with HiTrap® Desalting Columns with Sephadex G-25 as gel filtration medium) and subsequent dialysis in the appropriate buffer. Since the quenching effect was the key point of the fluorescence experiment, a quenching calibration of carboxyfluorescein has been done, reported in Fig. 6.1

Hen egg white lysozyme (HEWL), has been purchased by Sigma Aldrich and dis-

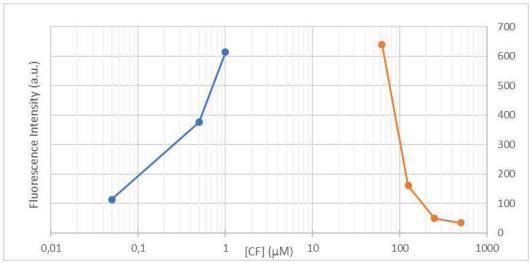

Figure 6.1: Carboxyfluorescein quenching in function of concentration.

solved in glycine buffer 70 mM at a stock concentration of 50 μM. The aggregation process of lysozyme was previously monitored by ThT fluorescence (see section 2.2), in order to prepare and characterize the solution to be used for the interaction studies with LUV.

A Perkin Elmer LS55 spectrofluorometer (Polytechnic University of Marche) has been exploited for fluorescence measurements equipped with a thermostatic bath that kept the sample at constant temperature (20 °C).

The LUV presence has been checked in terms of the size by Dynamic Light Scattering (DLS), in Polytechnic University of Marche. For light scattering measurements, a Malvern NanoZetaSizer apparatus, equipped with a 5 mW He-Ne laser, was employed. The reported values are the average of several measurements and are obtained from intensity weighted distributions.

The GUV preparation has been obtained following the literature, with the electroformation method [223]. An amount of 20 μL of a 2 mg/mL lipid (POPC and POPS in 9:1 rate) dissolved in chloroform solution was spread on the surfaces of two conductive glasses (coated with fluorine tin oxide), which were left under vacuum to

remove all traces of the organic solvent. The glasses were placed with their conductive sides facing each other and separated by a 2 mm thick Teflon frame to form a chamber which was filled with 10 mM carboxyfluorescein solution. The glass plates were connected to a function generator and an alternating current of 1 V with a 10 Hz frequency was applied for about 2 h. The solution obtained from this process has been checked to contain GUVs with an optical microscope. The sample has been purified with a dialysis overnight in HEPES buffer and then controlled again with the microscope to ensure the stability of the system. Fluorescence microscopy measurement have been carried out on a Zeiss Axio Imager 2 microscope (Carl Zeiss MicroImaging GmbH, Germany) while optical microscopy measurements have been performed with an Leitz Ortholux polarized light microscope, in Polytechnic University of Marche.

Neutron Spin Echo experiment

Lipids (POPC and POPS) cholesterol and bovine brain GM1 were purchased from Sigma Aldrich (Milan, Italy), and were used without any further purification. Amyloid β-peptide 1-40 (Aβ_{1-40}) peptide was purchased by ANASPEC. mtHsp60 was purchased by Atgen, Korea. LUV, Aβ_{1-40} and mtHsp60 solutions, were prepared and characterized in double, by using both H_2O and D_2O buffers as solvent. LUVs were made from films of a binary lipid combination of mono-unsaturated POPC:POPS (9:1), with cholesterol and bovine brain GM1, 95% w/w of PC:PS:Chol (81%:9%:10% w/w respectively) and 5% w/w of GM1. The solvent was then evaporated with a gently nitrogen flow and films were left under vacuum overnight. Afterward, dried films were solubilized both with 50 mM phosphate buffer with 20 mM NaCl prepared with H_2O or D_2O to obtain a concentration of about 9 mg/ml. Complete hydration of the lipid material in the aqueous solvents was obtained by several freeze/thawing cycles. After a two hours equilibration, liposomes were extruded by applying the suspension to a Lipofast extruder (Avestin, Mannheim, Germany), with a polycarbonate membrane filter with 100 nm pore and 31 extrusion steps.

Aβ_{1-40} was dissolved in 50mM phosphate buffer with 20mM NaCl and after a sequential filtration with Millex LG 200 nm and Amicon 20 nm filters the concentration was determined and brought to 45μM. An aliquot of this solution was characterized and used as Aβ_{1-40} monomer, the resting part was aggregated at T=37 °C under stirring at 200rpm. The aggregation time for NSE, t_1 (65min), corresponding to the oligomers reach condition, was chosen both considering previous studies and after characterization of time sampling aliquots during the whole aggregation process, up to the final plateau state, showing the formation of mature fibrils, both in D_2O and H_2O samples. The characterization was performed by fluorescence and F-UV circular dichroism (CNR, Palermo) to follow also the conformational changes during the aggregation process. Without and with mtHsp60 aliquots of solution right after mixing (t_0) and for comparison after t_1=65min of incubation time were withdrawn to be mixed with the liposomes. The final liposomes and Aβ_{1-40} concentrations were 5.9 mM and 22.5 mM for all the samples, with lipid:Aβ_{1-40} ratio

of about 260:1 and when present Aβ:mtHsp60 ratio was 20:1.

NSE neutron-scattering experiments were conducted on the IN15 spin-echo spectrometers located at the Institut Laue Langevin in Grenoble, France. Neutron spin-echo spectroscopy measures the real part of the normalized intermediate scattering function $P_{NSE}(Q,t) = Re[I(Q)/I(0)] = \frac{\int S(Q,\omega)cos\omega t d\omega}{\int S(Q,\omega)d\omega}$, a quantity that varies from 0 to 1, where Q is the total momentum transferred to the sample, $S(Q,\omega)$ is the dynamic structure factor, which gives the probability that an incident neutron is scattered by the sample with a momentum transfer Q and energy transfer ω. The selected wavelength was 10 Å, with a maximum spin echo time of 194 ns in a Q-range $0.029 < Q < 0.115$ Å^{-1}. The samples were contained in the quartz cells with 1mm path length.

SANS measurements were carried out on the lowest momentum transfer and lowest background SANS instrument, D11, at the Institut Laue-Langevin (ILL), Grenoble, France [224]. We recorded spectra at three sample-detector distances (1.4, 8.0, and 34 m) and by using 8 Å wavelength neutrons. The investigated wave vector modulus Q ranged from 0.0025 to 0.55 Å^{-1}. Samples were measured at room temperature in a 1 mm thick quartz cell. Experimental detector counts were corrected for background from buffer, sample cell, and electronic noise by conventional procedures. The two-dimensional isotropic scattering spectra were corrected for detector efficiency by dividing by the incoherent scattering spectra of pure water and azimuthally averaged, too. The resulting macroscopic differential scattering cross section are reported in absolute units (cm^{-1}).

6.3 Model protein fibrillation and interaction with membrane

6.3.1 Fluorometric analysis of membrane-protein interactions

The aim of our analysis is to analyze the interactions between different protein structures and model lipid systems, i.e. large and giant unilamellar vesicle (LUV and GUV), in order to reproduce the interaction between a neuronal membrane and the different species of amyloid oligomers formed neurodegenerative disease. In this framework, we adapted and improved a protocol to quantitatively study the effects of proteins with LUVs in solution, by using fluorescence spectroscopy. The effect of peptide interaction on membrane stability has been studied monitoring the 5,6-carboxyfluorescein (CF) leakage from liposomes composed of POPC/POPS. The fluorophore is included in the vesicles at high concentrations, in such a way to quench its fluorescence. If the protein interacts with the membrane and there is a leakage effect, there is a dispersion of the fluorophore in the surrounding environment, so that it dilutes and recovers its fluorescence ability.
The choice of LUVs and GUVs as a biological membrane model has been carried out considering the relative ease with which they are obtained and their characteristic of being unilamellar system, therefore constituting a good model of natural biological membranes. Fluorometric measurements have been carried out, obtaining informations with a statistical relevance, in respect, for example of direct microscopy. Nevertheless, optical and fluorescence microscopy have been employed to check the correct internalization of the fluorophore in the vesicles. Various protocols already exist and have been exploited to produce vesicle populations of homogeneous size with high entrapment efficiency [225, 223]. After direct observation of GUVs with an optical microscope analysis (example image in Fig. 6.2), the correct encapsulation of the desired amount of fluorophore, that is to quench the fluorescence effectively inside the GUV, and not around it, has been ensured with fluorescence microscopy (Fig. 6.2). As can be seen, the interior of the vesicle results black at the microscope, confirming the quenching of the fluorophore inside the liposome and the effectiveness of the method.
Instead, to control LUVs dimensions and integrity, a DLS analysis has been performed, to check sample size distribution and integrity before fluorescence spectroscopy investigation (see Fig. 6.3). The release of carboxyfluorescein due to the possible breakdown of liposomes has been monitored by a fluorescence assay at a wavelength of 520 nm (Fig. 6.4, top). At the end of the interaction the Triton X-100 detergent 10% (w/v) was added in order to induce the destruction of all the suspended vesicles. The system has been always previously checked adding an amount of Triton X-100 to the liposome sample and observing the increase of fluorescence as the liposomes are disrupted.

Amyloids fibril formation of lysozyme has been previously characterized with Thioflavin T and Congo Red staining to control the formation of correct amyloid structures, and from the sample used in the fluorometric experiment an amount of

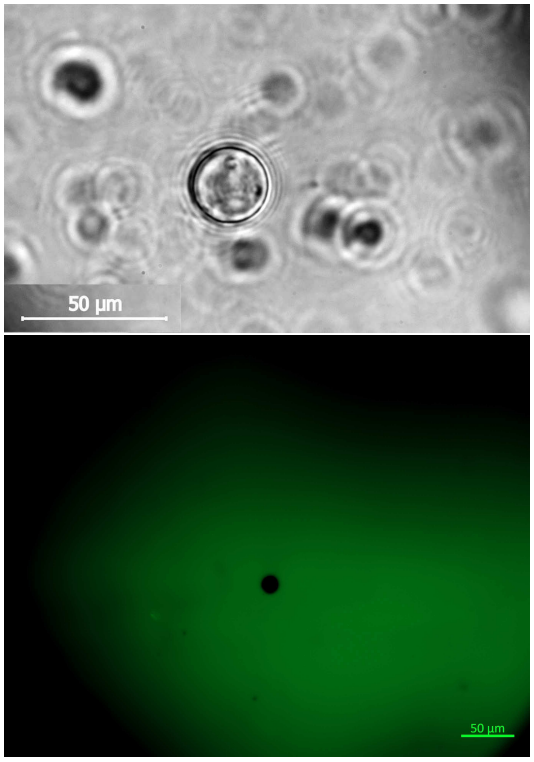

Figure 6.2: Top: GUV optical microscopy image. Bottom: GUV filled with quenching CF, obtained with fluorescence microscopy.

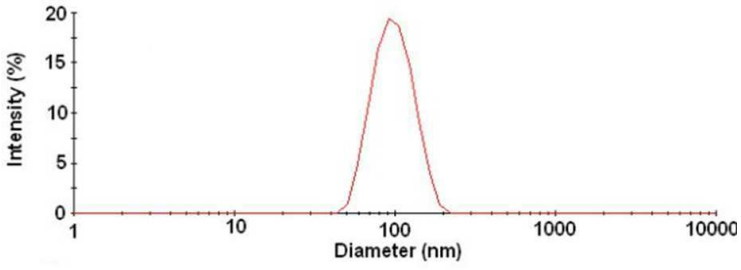

Figure 6.3: DLS distribution of LUVs in solution.

fibrils has been withdrawn and observed with Congo Red at the optical microscopy. After all the controls, the experiment has been performed adding preformed fibrils at the sample of LUV filled with carboxyfluorescein. The data obtained clearly show that the amyloid aggregates, oligomers and fibrils, are able to interact with the membrane, destroying the vesicles. Native proteins neglect LUVs, without interfering with the lipid membrane.

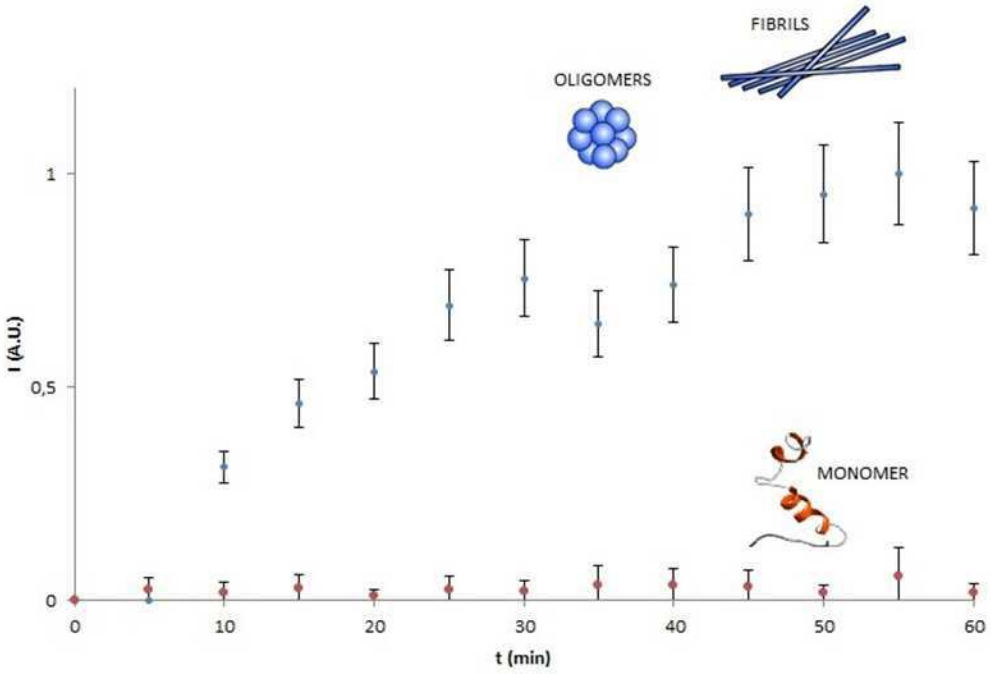

Figure 6.4: Interaction between vesicles and aggregates present in solution at the end of the fibrillation protocol (blue) and lysozyme in native conformation (red). Fibrils and monomers (0.4 μM) were added to the system at the beginning of the experiment and the system has been monitored in time.

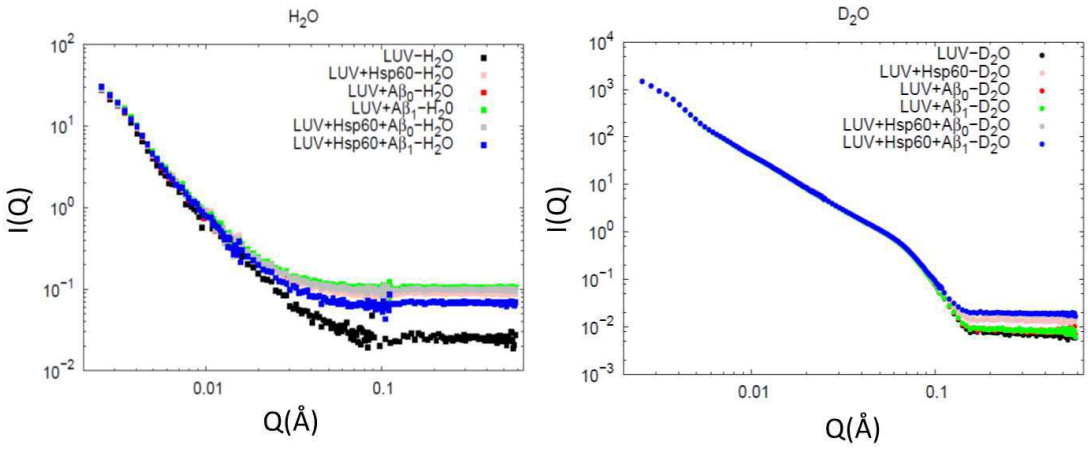

Figure 6.5: SANS experimental data in H_2O and D_2O.

6.4 Neutron Spin Echo characterization of membrane-protein interactions

To observe changes in the dynamics of membrane in presence and absence of the protein, it has been used the Neutron Spin Echo technique, a well-suited experimental approach for a direct investigation of local lipid bilayer undulation dynamics and the membranes' corresponding mechanical properties [226]. NSE is a dynamic method ideal for studies of the thermal fluctuations of the biomembranes because its correlation times (0,1 ns to 100 ns) and lenght scales (10-10^3 Å) [227, 228]. As introduced before NSE spectroscopy measures the real part of the normalized intermediate scattering function $P_{NSE}(Q,t) = Re[I(Q)/I(0)] = \frac{\int S(Q,\omega)cos\omega t d\omega}{\int S(Q,\omega)d\omega}$, where Q is the total momentum transferred to the sample, $S(Q,\omega)$ is the dynamic structure factor, which gives the probability that an incident neutron is scattered by the sample with a momentum transfer Q and energy transfer ω. A previous SANS characterization of the samples has been performed to evaluate the structure factor $S(Q)$ obtained in D_2O and possible structural changes induced by the two species of Aβ_{1-40} and by the chaperone to the LUV. The resulting macroscopic differential scattering cross section are shown in Fig. 6.5.

Curvature free energy of elastic membranes is commonly expressed by the Helfrich Hamiltonian [229], while the fluctuation dynamics of microemulsion droplets are depicted by Milner and Safran [230]. The normal bending modes of the flexible interface are coupled to the viscous friction exerted by the suspending medium with a single exponential decay $exp^{(-\Gamma t)}$ with a relaxation rate of $\Gamma = \frac{k_c}{4\eta}q^3$, where η is the effective viscosity of the solvent medium and k_c the bending rigidity [228]. In this manner, faster interfacial film relaxations are assigned to stiffer membranes. While well suited to describe data from soft interfaces, this expression fails to accurately account for the dynamics of phospholipid vesicles. Zilman and Granek introduced a model to describe curvature shape fluctuations of freely suspended flat phospho-

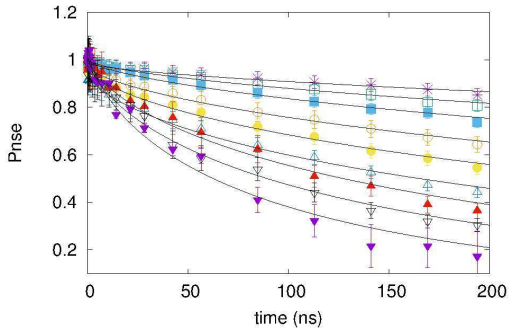

Figure 6.6: Fitting of the normalized scattering functions against Fourier time obtained by NSE at different Q values (0.29, 0.39, 0.50, 0.61, 0.72, 0.83, 0.93, 1.04, 1.15 nm^{-1}) for vesicles alone made in D_2O from Equation 6.1, reported as example.

lipid bilayers [231]. On the local length scales probed by the NSE experiment, the lipid bilayer of a vesicle is approximately flat. The Zilman-Granek model takes into account a coupling of the bending modes and local diffusion processes: in a rigid membrane with a bilayer bending rigidity of $k_c >> K_BT$, less free volume can be explored by individual molecules; this means that the relaxation rate for a coupled process of undulation and local curvature will increase, whereas the average amplitude of the modes will decrease. The anomalous subdiffusive relaxation of the bending motions is described by a stretched exponential decay:

$$P_{nse}(Q,t) = P_{nse}(Q,0)e^{-(\Gamma t)^{2/3}} \tag{6.1}$$

where Γ is the relaxation rate. In Fig. 6.6 the decay and the fitting of liposomes alone is reported as an example. The relaxation rate is related to the bending elasticity as

$$\Gamma(Q) = 0.025\gamma_k \left(\frac{K_BT}{k_c}\right)^{1/2} \frac{K_BT}{\eta} Q^3 \tag{6.2}$$

where η is solvent viscosity and the factor γ_k originates from averaging over the angle between the wavevector and the plaquette surface normal, K_B is the Boltzmann's constant and T the temperature. γ_k approaches unity when $k_c/K_BT >> 1$. The viscosity is assumed as three times the viscosity of D_2O at 20° as reported in [232]. The anomalous dependence on k_c is explained as a result of two competing effects: the increase of the undulation relaxation rate and the decrease of the average undulation amplitude both with increasing stiffness k_c. While a stiffer membrane subject to a random thermally activated undulation will relax faster to its flat state, it is less efficient in exploring volume, so that one has to wait a longer time for an empty solvent blob to be filled up by membrane material [231].
In order to test the effect of amyloid oligomers on LUVs, $A\beta_{1-40}$ solution has been incubated at 37 °C under stirring at a 200 rpm, a protocol that ensures the formation of amyloid on-pathway species [233]. Aliquots from the sample were removed at different times from the beginning of the process (t_0=0, t_1=30

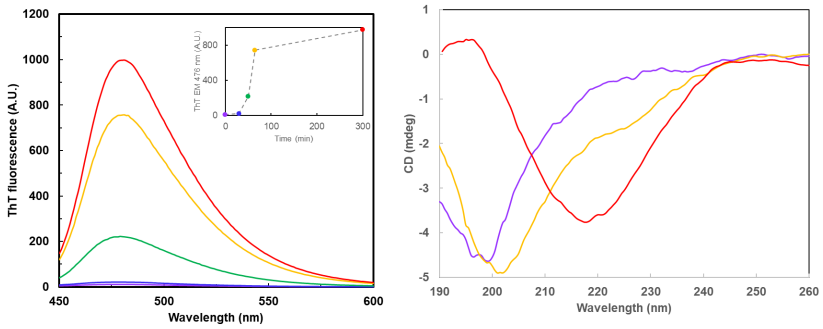

Figure 6.7: Left: fluorescence spectra of ThT in 50 μM Aβ_{1-40} collected at different times from the beginning of the incubation at 37°C under stirring. Times are t_0=0 min (violet), t_1=30 min (blue), t_2=50 min (green), t_3= 65 min (yellow) and t_4=300 min (red). In the inset, the emission maximum at 476 nm is shown as a function of time. Right: circular dichroism spectra of 50 μM Aβ_{1-40} at the beginning of the aggregation process t_0=0 min (violet), at a time t_3= 65 min (yellow), corresponding to oligomers formation, and at and t_4=300 min (red) the end of the process.

min, t_2=50 min, t_3=65 min, t_4=300 min) and the amyloid species formation was monitored by Thioflavin T fluorescence (Fig. 6.7). At t_3=65 min, the ThT fluorescence corresponds to the growth phase of the fibrillation kinetics profile (Fig. 6.7 inset), with maximum emission that reached about 75% of the signal arising from mature fibrils at 300 min. In fact, the CD spectrum of species formed after 300 min presents a minimum at 222 nm, as expected for a protein with cross-β structure, thus indicating the completion of fibril formation in the sample (Fig. 6.7). At t_3=65 min, CD spectrum reveals a transition unordered-β structure not yet completed for Aβ_{1-40} peptide with the minimum slightly shifted from the initial one.

6.4.1 Effect of Aβ_{1-40} on lipid membranes

The species selected by means of ThT are heterogeneous prefibrillar oligomeric species, which are supposed to be the most pathogenic amyloid forms for their ability to interact with cell membranes, impair calcium homeostasis and induce apoptosis or necrosis in cells. As concerns the interaction with Aβ_{1-40}, the results show an increase of membranes rigidity in the presence of the amyloid peptide (see Fig. 6.8). The effect is small when the dynamics of LUVs is analyzed with Aβ_{1-40} collected at t_0. However, it is much more significant in the presence of Aβ_{1-40} oligomers which cause an increase in the bending module that results almost doubled compared to control. The significant increase of the bending modulus k_c by incubation of LUVs with Aβ_{1-40} peptide respect to liposome control is correlated to a membrane bending deformation, and thus a change in the bilayer curvature due to protein-membrane interactions [234]. This result is in agreement with other studies performed on bilayer lipids by other techniques and with NSE findings previously reported by Hirai [30, 235].

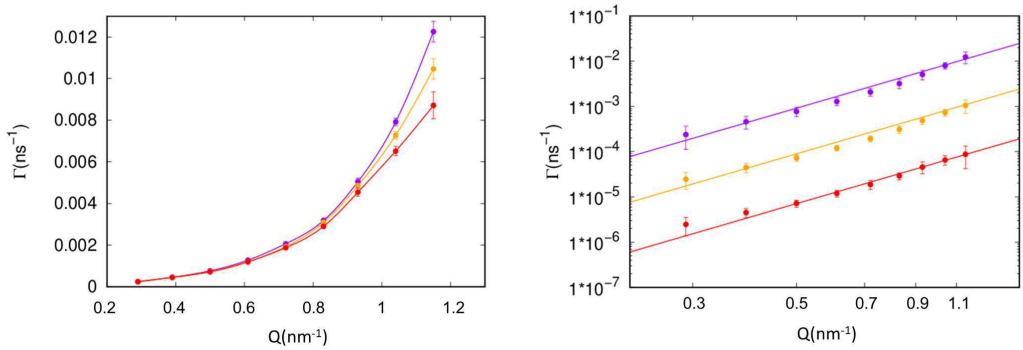

Figure 6.8: Left: relaxation rate Γ of membranes alone (violet), liposomes Aβ_{1-40} monomer, liposomes with Aβ oligomers (red) as a function of the scattering vector Q. Right: relaxation rate Γ as a function of Q in a log-log scale. Curves have been scaled for sake of clarity. Solid lines represent the fits from equation 6.2.

6.4.2 Effect of Hsp60 on membrane-protein interactions

As next step, the effect on LUV dynamics of Aβ_{1-40} species produced by the incubation of the peptide with the human chaperonin mtHsp60 has been analyzed. Aβ_{1-40} has been incubated in the presence of Hsp60 at 37 °C and under stirring. The same sample was brought into contact with LUVs for subsequent NSE analysis. In Fig. 6.9 are reported $\Gamma(Q)$ values in function of Q for liposomes with Aβ_{1-40} incubated in the presence of Hsp60 at the beginning of the aggregation protocol and after 65 minutes. The fitting of equation 6.2 are represented in Fig. 6.9 and values are reported in Table 6.1. Very interestingly the chaperonin reverses the rigidity increase caused by Aβ_{1-40} oligomers, placing the bending modulus in an intermediate value between the LUV (hence in their stable conformation), and the LUV with Aβ_{1-40} (hence in a possible toxic essay). Instead Aβ_{1-40} incubated with mtHsp60 and collected at $t3$ does not significantly changes the LUV bending module in respect to Aβ_{1-40} monomers.

In Fig. 6.9, left, are reported $\Gamma(Q)$ values in function of Q. The fitting from equation 6.2 are represented in Fig. 6.9 right and values obtained are reported in table 6.1. The results of LUV's bending modulus are in accordance with literature [236]. It seems that the rigidity of the membrane is increased in presence of the peptide and that the chaperonin reverses this process, placing the bending modulus in an intermediate value between the LUV alone and the LUV with Aβ_{1-40}.

The overall results confirm that the interaction with LUVs is especially due to oligomeric prefibrillar species which cause significant variations in the mechanical properties of lipid bilayers and show that aggregates produced by the incubation with Hsp60 are not so efficient in affecting features of membranes.

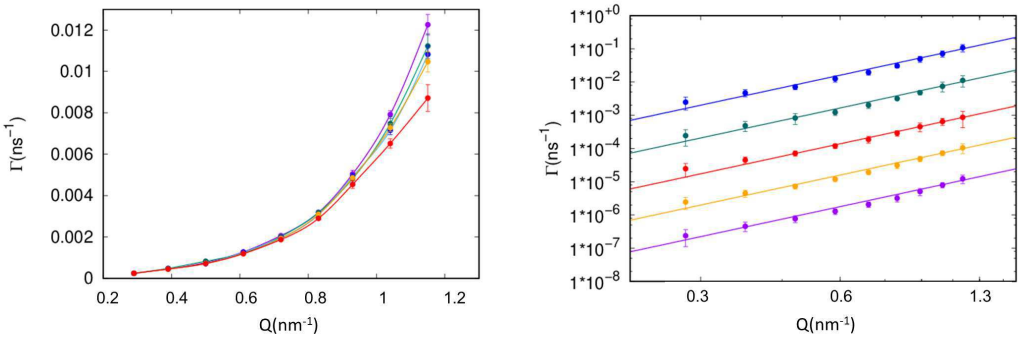

Figure 6.9: Left: Relaxation rate $\Gamma(Q)$ of membranes alone (violet), liposomes with mtHsp60 and Aβ_{1-40} monomer and fibrils (green and blue), liposomes with Aβ_{1-40} monomer (yellow), and Aβ_{1-40} fibrils (red) as a function of the scattering vector Q. Experimental points are connected with lines just to guide the eye. Right: Relaxation rate Γ as a function of the scattering vector Q. Solid lines represent the fits from equation 6.2.

Table 6.1: Bending moduli of liposomes alone and in presence of Aβ_{1-40} and mtHsp60

Sample	$k_c(10^{-19})J$
Liposomes	0.55 ± 0.06
Aβ_{1-40} mono	0.70 ± 0.04
Aβ_{1-40} oligo	0.92 ± 0.03
mtHsp60+Aβ_{1-40} mono	0.64 ± 0.05
mtHsp60+Aβ_{1-40} oligo	0.66 ± 0.05

Conclusions

In the last decades, the study of the mechanisms inducing amyloid fibril formation has involved several experimental and theoretical biophysical approaches [237, 238]. Many efforts have been made by scientist at the borderline between biology, chemistry, biochemistry and physics in order to understand why and in which way a protein starts its amyloidogenic pattern [239, 240]. This fundamental research issue is evolving in parallel to the development of drugs able to modify protein self assembly towards amyloid fibrils [241, 242]. SAXS experiments demonstrated to be suitable methods to investigate protein amyloidogenesis and the possible effects of inhibitors, being an in-solution technique, requiring low amount of sample and giving the possibility of a good time-resolution, in the case of Synchrotron SAXS, making it possible to follow the aggregation pattern [14]. For this reason, this technique has been chosen for this PhD work. In particular by means of SAXS technique the interaction of chaperones and chemical compounds with amiloidogenic proteins have been explored.

Taking advantage of combining SAXS and MD techniques [25], the resolution at atomic level of two oligomeric structures revealed some new structural features of GroEL and naïve-Hsp60 in solution [19]. The stability by chemical denaturation of the human chaperonins mtHsp60 and naïve Hsp60 have been analyzed and compared to that of its bacterial homologue, GroEL [134, 133]. The overall results have shown that Hsp60 is clearly less stable than its bacterial homolog: it dissociates at lower denaturant concentrations, it presents a smaller free energy change in the absence of denaturant and its dissociation is not as cooperative as the GroEL one. Moreover, the denaturation of Hsp60 tetradecamers involves single ring formation, while GroEL disassembly has no heptameric intermediate. A better knowledge of the Hsp60 structure and equilibrium in solution in comparison with the bacterial GroEL can give some hints on the functioning of homologue proteins in the different evolutionary patterns [243]. Furthermore, whereas in naïve Hsp60 the prevalence of 14mer species can be observed, the equilibrium is shifted towards heptamers for mtHsp60 under the same conditions in solution. Probably this different oligomeric equilibrium, confirmed by the analysis of SAXS curves in the absence of denaturant, is partially responsible for the differences in stability found between mitochondrial Hsp60 and naïve one, confirming, as happens for GroEL, the prevalence of tetradecamers higher stability to naïve Hsp60. Apart from the oligomeric organization, the influence of Mitochondrial Import Sequence in reinforcing Hsp60 protein monomeric structure cannot be excluded. Like the other targeting signals for mitochondria, chloroplasts, or the ER [244], also Hsp60 MIT presents over-representation of positively charged residues, like arginine. Even more, secondary structure prediction tools [245] reveal that Hsp60 MIS involves an α helical domain in proximity to the N-terminus of the protein. The presence of this helical tail is able to stabilize adjacent residues that, in the absence of the

same, present higher disorder content.
The results of Hsp60 action towards the fibrillation process of Aβ_{1-42} peptide demonstrate the ability of the chaperone to target Aβ_{1-42} species responsible for the induction of amyloid protein assembly. Although the specific mechanisms by which the presence of the chaperone inhibits Aβ_{1-42} protein aggregates remain to be elucidated, this result further confirm the extraordinary potentiality of molecular chaperones in interfering with the crucial molecular steps leading to amyloid aggregation in neurodegeneration [135, 136]. Once the Aβ_{1-42} active seeds are recruited through hydrophobic interactions in the presence of only off-pathway species, the highly prone to aggregate Aβ_{1-42} peptide lower its rate to form new seeds and subsequently to fibrillate.
Together with Hsp60, another molecular chaperone has been observed in the interaction with Aβ_{1-40} and α-synuclein: the Hsp70. Its action towards amyloid aggregation have been exploited, confirming its effectiveness in modifying the aggregation pattern of α-synuclein [174]. Employing specifically designed proteins, the affinity and the antiaggregation activity of the molecular chaperone for a target protein have been enhanced [176]. A preferential binding mechanism between the engineered Hsp70 and α-synuclein governs the inhibition of the early stages of aggregation. Towards fibril formation two different mechanisms seems to arise, one linked to the wild type Hsp70, disaggregating fibers of α-synuclein and β amyloid, and a specific mechanism typical of grafted proteins that interact directly with these fragments reverting them in soluble aggregates. The tight balance between these factors, therefore, could be a key aspect of the suppression of pathogenic events, including the nucleation and spreading of aggregate formation by molecular chaperones, and could also be an important aspect to consider in the design of future therapeutic agents targeted towards misfolding diseases.
In the context of chemical inhibitors, curcumin-like compounds effect has been investigated. This study integrates different research efforts focused on the development of small molecules able to interfere with amyloid β peptide uncontrolled aggregation [202]. The newly synthesized compounds were designed according to the same principles and provided equivalent promising impact on Aβ_{1-40} according to the scoring states resulting from docking [246]. The *in vitro* studies on the real effects of these compounds presented interesting prospects. Firstly, both the compounds **4** and **7** succeed in modifying Aβ_{1-40} fibrillogenesis. However, they give rise to aggregates with different morphologies as well as with different cytotoxic potential. Taking into account as basic requirement the low cytotoxic impact of a drug, compound **7** could be deemed to be more promising than **4**, which presents a high cytotoxic potential. Experimental biophysical results account for an immediate effect of compound **7** on Aβ_{1-40}, and for a moderate peptide aggregation in presence of this compound. On the other hand, compound **4** triggers a lower peptide aggregation, featured by an higher cytotoxicity. These results suggest that compound **4** can be able to link Aβ_{1-40} oligomeric toxic species and in some way to shelve their natural tendency to aggregate into amyloid fibrils. This hypothesis is in agreement with the biological analysis: if compound **4** inhibits

the formation of large aggregates, then its addition to the amyloid peptide may induce a higher concentration of small toxic oligomers, thus producing a collapse in cell viability. The eventuality here described does not completely rule out the interest toward compound **4**. In fact, it is possible to consider its use toward analysis for the identification of toxic oligomers. In fact, if the action of potential therapeutic agents produces intermediates of fibrillation and/or products of fibril disaggregation, then their accumulation could be harmful. In this respect, a careful usage of tetracycline as fibril inhibitor is indicated because of the accumulation of toxic precursors [247].
The study on the effects of the Aβ_{1-40} oligomers on Large Unilamellar Vesicles (LUVs) dynamics and on the role of the human chaperonin Hsp60 in influencing these effects, suggests several observations. First, incubation with Aβ peptide significantly increase the bending modulus k_c of LUVs, representing how the membrane responds to bending deformations, with direct implications of bilayer curvature to protein-membrane interactions [234, 227]. This effect was strongly marked when LUVs were in contact with oligomeric species produced during in vitro Aβ_{1-40} amyloid aggregation. The increase in the bending modulus would be associated to the formation of pores with high modulus, and would became more marked at further higher concentrations, due to significant interpore interaction. In the "channel hypothesis" on Aβ amyloid toxicity [248], Aβ oligomers would share their mechanisms of toxicity with antimicrobial peptides in their ability to insert in the membranes and thus to leading ion channels or pores formation considered a cause of neurodegeneration [249]. To provide a methodological tool with potential applications in therapeutic field, after having characterized, the bending properties of LUVs incubated with Aβ species upon the incubation of the peptide with a human chaperonin Hsp60 under the same experimental conditions of control have been tested. Very interestingly, in this case, no significant increase in the bending modulus was found for Hsp60-Aβ peptide collected at the time corresponding to control oligomers in respect to initial species. This effect can be the result of a protecting direct effect of Hsp60 on the membranes [250] or of the action exerted by the chaperonin on amyloid seeds, inhibiting the route for amyloid on pathway formation, simultaneously blocking the formation of the fold features that induce membranes stiffening associated to toxicity of amyloid species [251]. In both cases, this study confirms the extraordinary anti-amyloidogenic nature of the human chaperonin Hsp60, rendering it highly promising in design of beneficial strategies for neurodegeneration.

In conclusion, different compounds interacting with amyloidogenic proteins have been tested, even in presence of model membrane or cellular environments, with the purpose of better understand the process of aggregation and identify the means to counteract the onset of serious pathologies. This analysis has led to highlight several promising strategies, to identify the characteristics of new or less studied molecules and to emphasize the strengths to be exploited to draw each type of intervention. Biophysical and molecular analysis needs an *in vivo* application to be validated

but they can provide work cues for and perspectives of action in an applicative therapeutic field.

Appendix A

Nanocarriers for drug delivery

Polyamine phosphate nanoparticles (PANs) have an interesting potential for the delivery of large therapeutics i.e. plasmids, siRNAs, which can be complexed with the polyamines before nanoparticle formation [252, 253]. PANs are formed on a simple and straightforward one step procedure, involving the mixing of polyamines solutions and phosphate ions, driven by electrostatic interactions and hydrogen bonding between the positively charged amines groups of the polyamines and the negatively charged phosphate ions (see Fig. A.1). It has been shown that PANs, prepared from

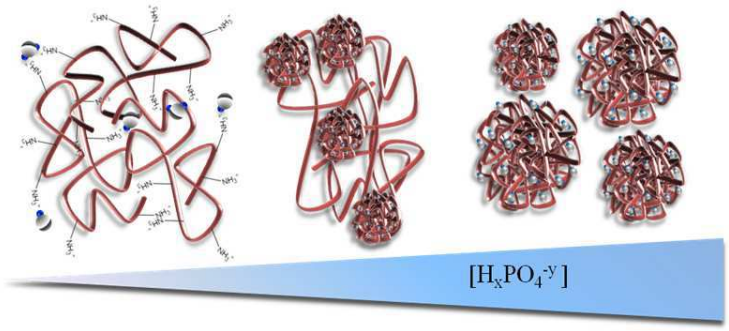

Figure A.1: Sketch of PANs formation.

poly(allylamine)hydrochloride and phosphate buffer (PB) are stable in moderate basic pHs and disassemble at acidic pHs and pHs over 9 [254]. Therefore, PANs will be stable in bloodstream and cell media but dissolve in endosomes once uptaken in cells. This response to the pH and the capacity of the polyamines of complexing negatively charged molecules makes PANs particularly appealing for their use as vectors for drug delivery. The ionic strength also plays an important role in the association of the polyamine chains as the charged polymers tend to coil with increasing ionic strength. At low ionic strength chains are more extended. The state of the chains, extended or coiled, can impact on the way that the chains are linked among them in the presence of the phosphate ions [255, 256]. The formation and growth of PANs has been evaluated as a function of the concentration of phosphate ions and ionic strength by measuring scattering intensity by SAXS.

SAXS allowed to trace the formation of the PANs at low phosphate concentration and learn about the nucleation process between phosphates and polyamines that leads to the generation of the nanoparticles. SAXS measurements were performed for samples prepared by mixing PAH, 1 mg/mL, with PB at concentrations from 1

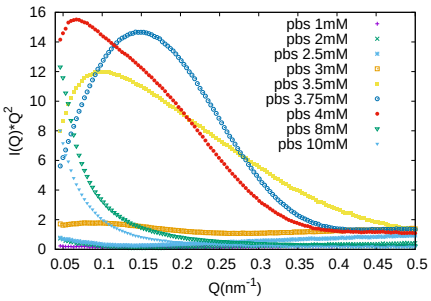

Figure A.2: Kratky plots of SAXS experimental curves as a function of phosphate buffer concentration.

to 10 mM. Kratky plots do not evidence a bell-shape peak at low Q characteristic of compact objects in solution (see Fig. A.2) below 4 mM PB, while at higher PB concentrations the plots suggest the presence of compact objects. Therefore, SAXS spectra were fitted by considering the simultaneous presence of flexible polymers and spheres made of the same polymers. Fitting was performed considering the theoretical approach for flexible disordered polymers developed by Pedersen-Schurtenberger (see Section 1.2.2.5), reported in Fig. A.3. Fitting results show an increasing in the Kuhn length with PB concentration to reach a constant value comparable with the size of the PANs (see Fig. A.3). The increase in Kuhn length for increasing PB concentrations, below the complete formation of particle spheres, tells us that the polymer becomes stiffer by association with phosphate groups. In particular, Kuhn lengths are ≃8 nm without PB and almost double when PANs appear in solution. This means that the polymer loses conformational freedom as the concentration of

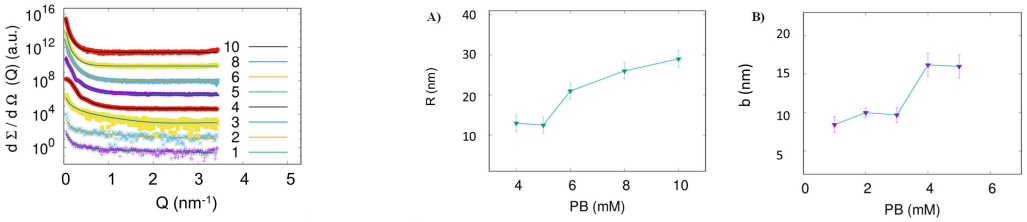

Figure A.3: SAXS experimental curves as a function of phosphate buffer concentration, together with their theoretical fitting. All experimental conditions refer to PAH 1 mg/mL and increasing phosphate buffer (PB) content as indicated in the legend in mM units. From bottom to top PB molarity increases. Curves are scaled for clarity. Right: Average spheres radii, R (nm) obtained with Genfit analysis, considering spheres in solution at increasing phosphate buffer concentration. B) Kuhn lengths, b (nm) corresponding to disordered polymers for the formation of PANs in phosphate buffer.

phosphates increases in solution. The increase in the Kuhn length is concomitant with the formation of polymer spheres. Once the polymer is only present as spher-

ical particles the Kuhn length does not change.
The same analysis has been repeated with different buffers and changing the ionic strength of the system (see Fig. A.4). Different buffers show the same trend in PANs formation, at different molar values of phosphate. Increasing the ionic strength of the media during PANs preparation impacts on the size and stability of the nanoparticles. Instability of PANs at high ionic strength is related to the screening of charges on the polyamines/phosphate complexes that weakens the interaction between phosphates and polyamines.

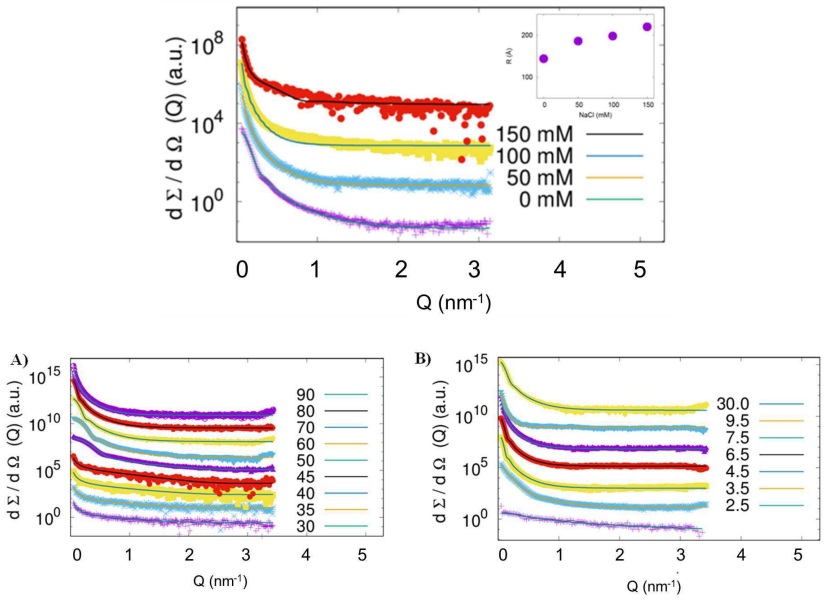

Figure A.4: Top: SAXS curves, scaled for the sake of clarity, correspond to the same PB conditions and NaCl concentration as in the legend. In the inset the average radii of PANS are reported vs NaCl content in solution. Bottom: SAXS experimental curves and theoretical fitting as a function of the phosphate concentration for PAH exposed to a single phosphate component from PB. A) SAXS curves of PAH at 1 mg/mL prepared in presence of increasing concentrations of KH2PO4 (mM). B) SAXS curves of PAH at 1 mg/mL prepared in presence of increasing concentrations of Na2HPO4 [mM].

By means of SAXS is possible to study the organization of polymer chains during their nucleation into nanoparticles, exploiting the Genfit software with the worm-like model. Most interesting, we can observe how the Kuhn length of the polyamines changes while the amount of PB in solution increases till 5 mM, the PB concentration at which all the polymer is forming rigid spheres. The changes in Kuhn length as the concentration of phosphate ions increase hint on the evolution of the conformational freedom of polymer chains and their bending rigidity (elastic module) while nanoparticles are nucleating.
In conclusion, the formation of polyamine phosphate nanoparticles (PAH, PANs) have been analyzed by means of complementary techniques. Polyamines, already

identified as excellent vectors for the polyamine transport system mediated cell import process, also emerged for their ability to specifically convey a bioactive functionality into mitochondria. SAXS studies show how the nucleation of the PAH chains with the phosphate ions results in a progressive decrease in conformational freedom and an increase in bending rigidity for the polymer as evidenced by the increase in the Kuhn length as the phosphate buffer concentration increases. These results give a deeper insight on the process of formation of supramolecular polyamine phosphate nanoparticles and in the decrease of conformation freedom and the increase in stiffness that polymer undergo during their nucleation through amine phosphate interactions. The increase in the Kuhn length with buffer concentration shows in an elegant way the changes in the state of the polymer from a random walk configuration to a condensed state as in PANs.
This study, implemented by DLS and TEM analysis is part of a manuscript in submission.

Materials and methods

PANs Poly(allylamine) hydrochloride salt (PAH) (MW: $15 \cdot 10^{3}$ g/mol), Phosphate Buffer (PB), Sodium Phosphate dibasic (Na_2HPO_4), Potassium Phosphate monobasic (KH_2PO_4), Hydrochloric Acid (HCl), Sodium Hydroxide (NaOH) and Sodium Chloride (NaCl) were purchased from Sigma-Aldrich. Polyelectrolyte stock solutions and all subsequent diluted precursor solutions were prepared with MilliQ deionized water. Grids and supports of copper and osmium tetroxide were obtained from Electron Microscopy Sciences (USA).

SAXS SAXS experiments were performed at the Elettra Synchrotron, Trieste. Temperature was kept at 20 °C during measurements. SAXS patterns were recorded using a PILATUS detector. The distance from the sample to the detector was set to 1.5 m, in order to obtain a Q-range from 0.08 to 3.4 nm^{-1} with $\lambda = 0.995$ Åthe X-ray wavelength. The incident and transmitted intensities have been simultaneously recorded with the aim of obtaining data in an absolute scale. Hence, normalized SAXS patterns were azimuthally averaged to obtain one-dimension profiles of scattered intensity. The buffer contribution was subtracted, taking as data for the buffer the scattering of the water solutions of phosphate and salts before addition of polyamines for each investigated condition. Each measurement was performed for 10 s, followed by a dead time of 2 s in order to avoid radiation damage, and repeated at least 20 times.

Appendix B

Small Angle Scattering theory

The fundamentals of SAS are herein presented following the texts [4] and [257]. The geometry of a Small Angle Scattering experiment is sketched in Fig.1.1. A probe with energy E affects the sample and is scattered by an angle θ. The incoming particle can be represented as a plain wave:

$$\psi_0(r) = exp(i\mathbf{kr}) \tag{B.1}$$

where $k = \frac{2\pi}{\lambda}$ is the wavevector, and its motion is described by the Schroëdinger equation of the interactions between the probe and the target, and can be written as

$$(\nabla^2 + k^2)\psi(\mathbf{r}) = \phi(\mathbf{r})\psi(\mathbf{r}) \tag{B.2}$$

where $\phi(r)$ is the reduced potential of the interaction and together with k, the wave vector, depends on the type of technique. The solution of the equation in the Born approximation (or single scattering approximation) is

$$\psi_{out}(\mathbf{r}) = e^{i\mathbf{kr}} - \frac{1}{4\pi}\frac{e^{ikr}}{r}\hat{\phi}(\mathbf{Q}) \tag{B.3}$$

where the first term represents the incident plain wave and the second the spherical scattering wave modulated by a "diffusion amplitude" represented by the Fourier transform of the reduced interaction potential. Considering the scattering cross section $d\Sigma/d\Omega$ defined as the number of particles on the detector on the number of incident particles for unit of solid angle and time, and that the number of scattered particles depend on the interaction between the probe and the sample, the differential cross section depends on the Fourier transform of the reduced potential of interaction:

$$\frac{d\sigma}{d\Omega} = \left(\frac{1}{4\pi}\right)^2 |\hat{\phi}(Q)|^2 \tag{B.4}$$

Even more, the scattering cross section of different probes can be described by the equation:

$$\frac{d\sigma}{d\Omega} = \sum_{i,j} \left\langle f_i^* f_j F_i^*(Q) F_j(Q) e^{-i\mathbf{Q}\cdot(\mathbf{R}_i - \mathbf{R}_j)} \right\rangle_{\omega_k, r_k} \tag{B.5}$$

where $F_i(Q)$ is a scattering length, with f_i a normalization factor, connected with the i_{th} atom/molecule and has the dimension of a lenght. It usually depends on Q and is dependent on the probe that is is used.

Assuming that the configurations are independent from their positions we can separate the mean on the position from the mean fo the orientations:

$$\frac{d\sigma}{d\Omega} = \left\langle \sum_{i,j} f_i^* f_j F_i^*(Q) F_j(Q) \right\rangle_{\omega_k} \left\langle e^{-i\mathbf{Q}\cdot(\mathbf{R}_i - \mathbf{R}_j} \right\rangle_{r_k} \tag{B.6}$$

Considering that the atoms of the target have different scattering lenghts, F_i can be written as:

$$F_i = \langle F \rangle + \delta F_i \tag{B.7}$$

in which

$$\begin{cases} \langle F \rangle = \frac{1}{N} \sum_i^N F_i \\ \delta F_i = F_i - \langle F \rangle \end{cases} \tag{B.8}$$

The deviations from the mean square value $\langle F \rangle$ are uncorrelated from the atoms positions, i.e. $\langle \delta F \rangle = 0$, $\langle \delta F_i^* \delta F_j \rangle = \delta_{i,j} \left\langle |\delta F|^2 \right\rangle = \delta_{i,j} \left\langle (F_i - \bar{F})^2 \right\rangle$ and

$$S_{ij}(Q) = \frac{1}{N} \left\langle \rho_Q \rho_Q^* \right\rangle = \frac{1}{N} \sum_{i,j} \left\langle e^{-i\mathbf{Q}\cdot(\mathbf{R}_i - \mathbf{R}_j)} \right\rangle \tag{B.9}$$

$$\frac{d\sigma}{d\Omega} = \sum_{i,j} \left(N f_i^* f_j < F >^2 (Q) S_{i,j}(Q) + N f_i^* f_j < \delta F^2(Q) > \delta_{i,j} S_{i,j}(Q) \right) \tag{B.10}$$

that is

$$\frac{d\sigma}{d\Omega} = \sum_{i,j} \left(< F >^2 (Q) + < \delta\ F^2(Q) > \delta_{i,j} \right) f^2 N S_{i,j}(Q) = \sum_{i,j} N f^2 < F^2 > S_{i,j}(Q) \tag{B.11}$$

Starting from these general considerations it is possible to easily obtain the scattering cross sections for SANS and SAXS experiments, as reported in the sections below.

B.1 SANS

A SANS experiment employs thermic neutrons, i.e. a neutron beam at the temperature of 290 K, corresponding to a distribution of kinetic energies centered at 0.025 eV. The scattering of such neutrons by the targeted sample is mediated by strong interaction: i.e. each neutron interacts with point-like atoms. Neutron scattering occurs as a result of the interaction with the atomic nuclei. The scattering potential $V(\mathbf{r})$ can thus be approximated by a sum of δ-function pseudopotentials [257]:

$$V(\mathbf{r}) = \frac{2\pi\hbar^2}{m} \sum_{i=1}^{N} b_i \delta(\mathbf{r} - \mathbf{r_i}) \tag{B.12}$$

where $\mathbf{r_i}$ is the position of the i^{-th} nucleus and b_i is the scattering length of the i^{-th} nucleus. The reduced potential is linked, for massive particles, to the interaction

potential from the relation $\phi(\mathbf{r}) = \frac{2m}{\hbar^2}V(\mathbf{r})$ and is therefore given by:

$$\phi(\mathbf{r}) = \frac{2m}{\hbar^2}V(\mathbf{r}) = 4\pi \sum_i b_i \delta(\mathbf{r} - \mathbf{R}) \tag{B.13}$$

with the scattering lengths $F_i = b_i$ (see equation B.6). From Equation B.4:

$$\frac{d\Sigma}{d\Omega} = \left(\frac{1}{4\pi}\right)^2 \langle |\phi(Q)|^2 \rangle = \left\langle \sum_{i,j} b_i b_j^* e^{i\mathbf{Q}(\mathbf{R_i} - \mathbf{R_j}} \right\rangle \tag{B.14}$$

As stated in Equation B.10, the scattering cross section can be divided in two contributions, one connected to the mean value of the scattering length density and another linked to the fluctuations:

$$\frac{d\sigma}{d\Omega} = \left(\frac{d\sigma}{d\Omega}\right)_{coherent} + \left(\frac{d\sigma}{d\Omega}\right)_{incoherent} \tag{B.15}$$

where

$$\begin{cases} \left(\frac{d\sigma}{d\Omega}\right)_{coherent} = N \left\langle (\delta F)^2 \right\rangle = N \left\langle (\delta b)^2 \right\rangle \\ \left(\frac{d\sigma}{d\Omega}\right)_{incoherent} = N < F >^2 S(\mathbf{Q}) = N < b >^2 S(\mathbf{Q}) \end{cases} \tag{B.16}$$

The subscript refers to coherent and incoherent scattering. Informations about the structure of the system is contained entirely within the coherent contribution to the cross section: there is no incoherent contribution if the sample consists of one isotropic species of zero nuclear spin. In the absence of inchoerent scattering the cross section for scattering is

$$\left(\frac{d\sigma}{d\Omega}\right) = Nb^2 S(\mathbf{Q}) \tag{B.17}$$

where Nb^2 is the cross section for a system of N independent nuclei and $S(\mathbf{Q})$ represents the effect of spatial correlations.

B.2 SAXS

In a SAXS experiment the probe is a beam of photons with energy ranging from 1 to 30 keV. The general definition of the scattered intensity $I(\mathbf{Q})$, derived in appendix B, is given by the squared three-dimensional Fourier transform of the electron density, $\rho(\mathbf{r})$ per unit volume [6],

$$I(\mathbf{Q}) = \frac{1}{V} \left\langle \left| \int_V d\mathbf{r}\ \rho(\mathbf{r}) e^{i\mathbf{Q}\cdot\mathbf{r}} \right|^2 \right\rangle, \tag{B.18}$$

where V is the irradiated sample volume and the angular bracket $< \cdots >$ represents an ensemble (or time) average over all possible positions and orientations of the particles in the system. The electron density can be written as [258]

$$\rho(\mathbf{r}) = \delta\rho(\mathbf{r}) + \rho_0, \tag{B.19}$$

where ρ_0 is a uniform average value calculated over a volume larger than the resolution volume. The master equation (B.18) transforms to

$$\begin{aligned} I(\mathbf{Q}) &= \frac{1}{V}\left\langle \left| \int_V d\mathbf{r}\ [\delta\rho(\mathbf{r}) + \rho_0] e^{i\mathbf{Q}\cdot\mathbf{r}} \right|^2 \right\rangle \\ &= \frac{1}{V}\left\langle \left| \int_V d\mathbf{r}\ \delta\rho(\mathbf{r}) e^{i\mathbf{Q}\cdot\mathbf{r}} + \rho_0 \int_V d\mathbf{r}\ e^{i\mathbf{Q}\cdot\mathbf{r}} \right|^2 \right\rangle \end{aligned} \tag{B.20}$$

With the property $\frac{1}{(2\pi)^3}\int d\mathbf{r}\ e^{i\mathbf{Q}\cdot\mathbf{r}} = \delta(\mathbf{Q})$, where $\delta(\mathbf{Q})$ is the Dirac delta function, we can write

$$I(\mathbf{Q}) = \frac{1}{V}\left\langle \left| \int_V d\mathbf{r}\ \delta\rho(\mathbf{r}) e^{i\mathbf{Q}\cdot\mathbf{r}} + \rho_0 (2\pi)^3 \delta(\mathbf{Q}) \right|^2 \right\rangle \tag{B.21}$$

The contribution of $\delta(\mathbf{Q})$ to the scattering intensity is of no consequence because it is identically zero except when $\mathbf{Q} = 0$, that is, except for radiation not being scattered by the particles. The distribution of scattering centres in the i-th particle can be described in the reciprocal space by defining the *form factor*,

$$F_i(\mathbf{Q}) = \frac{1}{f_i}\int_{V_i} d\mathbf{r}\, \delta\rho_i(\mathbf{r})\, e^{i\mathbf{Q}\cdot\mathbf{r}} \tag{B.22}$$

$$f_i = \int_{V_i} d\mathbf{r}\, \delta\rho_i(\mathbf{r}), \tag{B.23}$$

where V_i is the volume of the scattering particle i. Clearly it results $F_i(\mathbf{Q}) = 1$.

In the case in which the orientation and the position of the $k-th$ particle are not mutually dependent, then:

$$\frac{d\sigma}{d\Omega} = \frac{1}{V}\sum_{i=1}^{N_P} f_i^2 < F_i^2(\mathbf{Q}) >_{\omega_i} \tag{B.24}$$

$$+ \frac{1}{V}\sum_{i=1}^{N_P}\sum_{j\neq i}^{N_P} f_i f_j < F_i(\mathbf{Q}) >_{\omega_i} < F_j^*(\mathbf{Q}) >_{\omega_j} < e^{i\mathbf{Q}\cdot(\mathbf{R}_i - \mathbf{R}_j)} >_{\mathbf{R}_i,\mathbf{R}_j} . \tag{B.25}$$

and using the definition of correlation function $g(\mathbf{R}_i, \mathbf{R}_j)$ which depends exclusively from the distance $\mathbf{R}_{ij} = \mathbf{R}_i - \mathbf{R}_j$ we can write that:

$$\begin{aligned} < e^{i\mathbf{Q}\cdot(\mathbf{R}_i - \mathbf{R}_j)} >_{\mathbf{R}_i,\mathbf{R}_j} &= \frac{1}{V}\int_V d\mathbf{R}_{ij}\, g(\mathbf{R}_{ij})\, e^{i\mathbf{Q}\cdot\mathbf{R}_{ij}} \\ &= \frac{1}{V}\int_V d\mathbf{R}_{ij}\, [g(\mathbf{R}_{ij}) - 1]\, e^{i\mathbf{Q}\cdot\mathbf{R}_{ij}} + \frac{1}{V}\int_V d\mathbf{R}_{ij}\, e^{i\mathbf{Q}\cdot\mathbf{R}_{ij}} \\ &= \frac{1}{V}\int_V d\mathbf{R}_{ij}\, h(\mathbf{R}_{ij})\, e^{i\mathbf{Q}\cdot\mathbf{R}_{ij}} + \frac{(2\pi)^3}{V}\delta(\mathbf{Q}), \end{aligned} \tag{B.26}$$

where we introduced $h(\mathbf{R}_{ij}) = g(\mathbf{R}_{ij}) - 1$ which is the total correlation function. We reach the expression of the scattering intensity:

$$\begin{aligned}\frac{d\sigma}{d\Omega} &= \frac{1}{V}\sum_{i=1}^{N_P} f_i^2 < F_i^2(\mathbf{Q}) >_{\omega_i} \\ &+ \frac{1}{V^2}\sum_{i=1}^{N_P}\sum_{j\neq i}^{N_P} f_i f_j < F_i(\mathbf{Q}) >_{\omega_i} < F_j^*(\mathbf{Q}) >_{\omega_j} \tilde{h}_{ij}(\mathbf{Q}),\end{aligned} \tag{B.27}$$

where $\tilde{h}_{ij}(\mathbf{Q})$ is the tridimentional Fourier transform of the total correlation function.

The Equation B.27 is valid in general and can be extended to the case of identical particles such as n species in solution. If we now hypothesize that the interaction between different particles has a spherical symmetry, hence the orientation of the particle is isotropic:

$$\begin{aligned}I(Q) &= \sum_{\alpha=1}^{p} n_\alpha f_\alpha^2 [< F_\alpha^2(\mathbf{Q}) >_{\omega_Q} - < F_\alpha(\mathbf{Q}) >_{\omega_Q}^2] + \\ &+ \sum_{\alpha=1}^{p}\sum_{\beta=1}^{p} \sqrt{n_\alpha n_\beta} f_\alpha f_\beta < F_\alpha(\mathbf{Q}) >_{\omega_Q} < F_\beta^*(\mathbf{Q}) >_{\omega_Q} S_{\alpha\beta}(Q)\end{aligned} \tag{B.28}$$

where the mean value has been obtained not on the single particle orientation but on the polar angles of the vector $\mathbf{Q}$, where p is the number of the different species in solution. The isotropic structure factor is:

$$\begin{aligned}S_{\alpha\beta}(Q) &= \delta_{\alpha,\beta} + \sqrt{n_\alpha n_\beta}\, \tilde{h}_{\alpha\beta}(Q) = \\ &= \delta_{\alpha,\beta} + \sqrt{n_\alpha n_\beta}\, 4\pi \int_0^\infty r^2 dr h_{\alpha\beta}(r) \frac{\sin(Qr)}{Qr}\end{aligned} \tag{B.29}$$

In most of the Small Angle Scattering experiments on proteins, given the resolution that we can obtain experimentally, we can consider each particle as an object with a uniform scattering density ρ_i immersed in a scattering length density solvent ρ_0. Working in very diluted conditions (the protein concentration is approximately 1% by weight), we can hypothesize that ρ_0 is the average scattering length density of the system and the function $\delta\rho_i(\mathbf{r})$ can be replaced by the constant $\Delta\rho_i = \rho_i - \rho_0$in the equations (B.22-B.23):

$$F_i(\mathbf{Q}) = \frac{1}{V_i}\int_{V_i} d\mathbf{r}\, e^{i\mathbf{Q}\cdot\mathbf{r}} \tag{B.30}$$

$$f_i = V_i \Delta\rho_i. \tag{B.31}$$

In the case of spherical particles with a density of length of uniform scattering, the expression of diffuse intensity becomes:

$$I(Q) = \sum_{\alpha,\beta=1}^{p} \sqrt{n_\alpha n_\beta} f_\alpha f_\beta F_\alpha(Q) F_\beta(Q) S_{\alpha\beta}(Q) \tag{B.32}$$

where the form factor for a sphere of radius R:

$$F(Q,R) = \Phi(QR) \quad = \quad 3\frac{\sin(QR) - (QR)\cos(QR)}{(QR)^3}. \tag{B.33}$$

The diffuse intensity will become

$$I(Q) \quad = \quad \sum_{\alpha,\beta=1}^{p} \sqrt{n_\alpha n_\beta}\Delta\rho_\alpha\Delta\rho_\beta V_\alpha V_\beta \Phi(QR_\alpha)\Phi(QR_\beta)S_{\alpha\beta}(Q), \tag{B.34}$$

where the structure factor is

$$S(Q) \quad = \quad \frac{\sum_{\alpha,\beta=1}^{p} \sqrt{n_\alpha n_\beta}\Delta\rho_\alpha\Delta\rho_\beta V_\alpha V_\beta \Phi(QR_\alpha)\Phi(QR_\beta)S_{\alpha\beta}(Q)}{\sum_{\alpha=1}^{p} n_\alpha(\Delta\rho_\alpha)^2 V_\alpha^2 \Phi^2(QR_\alpha)}. \tag{B.35}$$

When we are dealing with even more diluted systems ($n_\alpha \to 0$), then we can approximate the structure factor $S_{\alpha\beta}$ simply with the function $\delta_{\alpha,\beta}$ as we assume that the particles spread the radiation independently of each other. In the simplest case of a very diluted, monodispersed, two-phase, e in isotropic approximation, the diffuse scattering intensity is simply:

$$I(Q) \quad = \quad n_P(\Delta\rho)^2 V_P^2 P(Q), \tag{B.36}$$

where V_P is the single particle volume. Considering these approximations valid, it is easy to see that by means of the small angle diffusion technique is possible to obtain information about the structure of the object investigated. Different form factors are reported in Figure B.1, showing that different objects with the same overall dimension result in very different SAS shapes.

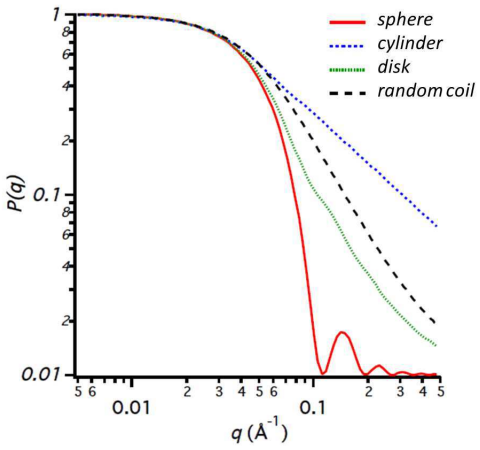

Figure B.1: Form factors for some simple geometries having the same gyration radius of 30 Å, from Igor simulations [259].

B.3 Derivation of SAXS reduced potential

Consider an electromagnetic plain wave with an incident electric field E_0 on a free electron. The electron starts oscillating and emit radiations. We are studying the electric filed emitted in a generic point, very far from the electron and from its oscillation core (Dipole approximation) and at a distance bigger then λ of radiation (enough to see the electromagnetic field as radiation in the observation point). From Maxwell's equations, with ρ and J the density of charge and the current of the target electron:

$$\begin{cases} \nabla \mathbf{E} = \frac{\rho}{\varepsilon_0} \\ \nabla \times \mathbf{E} = -\frac{\partial \mathbf{B}}{\partial t} \\ \nabla \mathbf{B} = 0 \\ \nabla \times \mathbf{B} = \frac{1}{c^2}\left(\frac{\partial \mathbf{E}}{\partial t} + \frac{\mathbf{J}}{\varepsilon_0}\right) \end{cases} \tag{B.37}$$

$$\begin{cases} E(\mathbf{r},t) = -\nabla\phi(\mathbf{r},t) - \frac{\partial \mathbf{A}(\mathbf{r},t)}{\partial t} \\ \mathbf{B}(\mathbf{r},t) = \nabla \times \mathbf{A}(\mathbf{r},t) \end{cases} \tag{B.38}$$

$$\nabla(\nabla \mathbf{A}) - \nabla^2 A = -\frac{1}{c^2}\left(\nabla\frac{\partial\phi}{\partial t} + \frac{\partial^2 A}{\partial t^2} - \frac{J}{\varepsilon_0}\right) \tag{B.39}$$

$$\begin{cases} \frac{1}{c^2}\frac{\partial^2\phi}{\partial t^2} - \nabla^2\phi = \frac{1}{c^2}\frac{\partial}{\partial t}\left(c^2\nabla\mathbf{A} + \partial\phi\partial t\right) + \frac{\rho}{\varepsilon_0} \\ \frac{1}{c^2}\frac{\partial^2 A}{\partial t^2} - \nabla^2 A = \frac{1}{c^2}\nabla\left(c^2\nabla\mathbf{A} + \partial\phi\partial t\right) + \frac{J}{c^2\varepsilon_0} \end{cases} \tag{B.40}$$

choosing the gauge $c^2\nabla\mathbf{A} + \frac{\partial\phi}{\partial t}$

$$\begin{cases} \frac{1}{c^2}\frac{\partial^2\phi}{\partial t^2} - \nabla^2\phi = \frac{\rho}{\varepsilon_0} \\ \frac{1}{c^2}\frac{\partial^2 A}{\partial t^2} - \nabla^2 A = \frac{\mathbf{J}}{c^2\varepsilon_0} \end{cases} \tag{B.41}$$

where $\mathbf{A}$ gives the distribution of charge density in the sample. For to evaluate the electric field in the observation point, it is necessary to consider that the electromagnetic waves are transverse: $E \perp B \perp \hat{k}'$, where $\hat{k}'$ is the propagation versor. It can be easily seen that $|E| = c\,|B|$. Solving the equation for $\mathbf{A}$ it can be found a relation between the current and the vector potential, considering r as the distance detector-target and r'' the position of the scattering atom in respect to the mass center

$$\mathbf{A}(\mathbf{r},t) = \frac{1}{4\pi\varepsilon_0 c^2}\int d^3r'' \frac{\mathbf{J}(r''; t - \frac{|\mathbf{r}-\mathbf{r}''|}{c})}{|\mathbf{r}-\mathbf{r}''|} \tag{B.42}$$

In this way it has been defined a delayed vector potential: fields propagates with finite velocity v, the measurement at time t depends on the position of the electron at the time before, i.e. $t' = t - \frac{|\mathbf{r}-\mathbf{r}''|}{c}$. Since $r >> r''$: $|\mathbf{r}-\mathbf{r}''| \simeq |r| - \frac{\mathbf{r}\cdot\mathbf{r}''}{|\mathbf{r}|} \simeq r$

$$\mathbf{A}(\mathbf{r},t) = \frac{1}{4\pi\varepsilon_0 c^2 r}\int d^3r'' \mathbf{J}(r''; t - \frac{r}{c}) \tag{B.43}$$

but the current density of the electron is the product between its velocity and the charge density $\mathbf{J} = \rho\mathbf{v}$

$$\int d^3r''\mathbf{J}(r'', t - \frac{r}{c}) = \int d^3r''\rho(r'', t')v(r'', t') = e\mathbf{v}_e(t') = e\frac{d\mathbf{r}_e}{dt'} = \dot{p}(t') \tag{B.44}$$

where $\mathbf{p} = e\mathbf{r}_e$ as the electronic dipole moment associated to the electron. If we assume the incident radiation to be polarized linearly in z, so that $\mathbf{p}$ and $\mathbf{A}$ have only one component:

$$A_z(\mathbf{r}, t') = \frac{1}{4\pi\varepsilon_0 c^2 r}\dot{p}_z(t') \tag{B.45}$$

$$\begin{cases} B_x = \frac{\partial A_z}{\partial y} \\ B_y = \frac{\partial A_z}{\partial x} \\ B_z = 0 \end{cases} \tag{B.46}$$

$$\begin{cases} B_x = \frac{\partial A_z}{\partial y} = \left(\frac{y}{r}\right)\frac{\partial A_z}{\partial r} = \frac{y}{4\pi\varepsilon_0 c^2 r^2}\left(\frac{\partial \dot{p}_z(t')}{\partial r}\frac{1}{r} - \frac{1}{r^2}\dot{p}_z(t')\right) = \frac{y}{4\pi\varepsilon_0 c^2 r^2}\frac{\partial t'}{\partial r}\frac{\partial \dot{p}_z(t')}{\partial t'} = -\frac{y}{4\pi\varepsilon_0 c^3 r^2}\ddot{p}_z(t') \\ B_y = -\frac{\partial A_z}{\partial x} = \left(\frac{1}{4\pi\varepsilon_0 c^3 r}\right)\left(\frac{x}{r}\right)\ddot{p}_z(t') \end{cases} \tag{B.47}$$

Generalizing

$$\mathbf{B} = \left(\frac{1}{4\pi\varepsilon_0 c^3 r}\right)\ddot{\mathbf{p}}(t') \times \hat{r} \tag{B.48}$$

$$|\mathbf{E}| = c|\mathbf{B}| = \left(\frac{1}{4\pi\varepsilon_0 c^3 r}\right)\ddot{p}(t')\sin\theta \tag{B.49}$$

where θ is the angle between the incident and the scattered wave. Considering an incident field $E(\mathbf{r}, t') = E_0 e^{i\omega t'}$

$$\ddot{\mathbf{p}} = e\ddot{\mathbf{r}} = e\left(\frac{e\mathbf{E}}{m}\right) = \frac{e^2}{m}\mathbf{E_0}e^{i\omega(t-\frac{r}{c})} = \frac{e^2}{m}\mathbf{E_0}e^{-ikr}e^{i\omega t} \tag{B.50}$$

$$|\mathbf{E}| = \left(\frac{e^2}{4\pi\varepsilon_0 c^2 m}\right)\left(\frac{e^{-ikr}}{r}\right)E_0 e^{+i\omega t}\sin\theta \tag{B.51}$$

in which $r_0 = \frac{e^2}{4\pi\varepsilon_0 c^2 m} = \frac{e^2}{mc^2}$ is the classical radius of the electron. In this way

$$\frac{I(\mathbf{r})}{I_0} = \frac{|\mathbf{E}|^2}{|E_0|^2} = r_0^2\frac{1}{r^2}\sin^2\theta \tag{B.52}$$

and since te intensity emitted by an accelerated electron is $I = \frac{\Delta E}{\Delta\Sigma\Delta t}$ and the flux $J = \frac{\Delta N}{\Delta\Sigma\delta t}$, $\frac{I(\mathbf{r})}{I_0} = \frac{\mathbf{J}(\mathbf{r})\cdot\hat{r}}{J_0}$

$$\frac{d\sigma}{d\Omega} = \frac{\mathbf{J}(r)\cdot\hat{r}}{J_0}r^2 = r_0^2 sin^2\theta \equiv \left(\frac{1}{4\pi}\right)^2\left\langle|\phi(Q)|^2\right\rangle \tag{B.53}$$

$$\left(\frac{d\sigma}{d\Omega}\right) = r_0^2\sin^2\theta \tag{B.54}$$

and the reduced potential

$$\phi(\mathbf{Q}) = 4\pi r_0 \sin\theta e^{i\mathbf{Q}\cdot\mathbf{R}_i} \tag{B.55}$$

$$\phi(\mathbf{r}) = 4\pi r_0 \sin\theta \delta(\mathbf{r} - \mathbf{R}_i) \tag{B.56}$$

If more atoms are considered, i being the index for the atom and $\rho_i(\mathbf{r})$ the numeric density of the electrons around the i^{-th} nucleus, in the classical elastic approximation of Thompson:

$$\begin{cases} \phi(\mathbf{r}) = 4\pi r_0 \sin\theta \sum_i \rho_i(\mathbf{r} - \mathbf{R}_i) \\ \phi(\mathbf{Q}) = 4\pi r_0 \sin\theta \sum_i \hat{\rho}_i(\mathbf{Q}) e^{i\mathbf{Q}\mathbf{R}_i} \end{cases} \tag{B.57}$$

in which θ is the angle between the direction of the electric field of the electromagnetic incident wave and the direction of the diffuse wave, $\hat{\rho}_i(\mathbf{Q}) = \int d^3 r e^{i\mathbf{Q}\mathbf{r}} \rho_i(\mathbf{r})$. From Equation B.53:

$$\frac{d\sigma}{d\Omega} = \left(\frac{e^2}{mc^2}\right)^2 (\hat{n}\hat{n}')^2 \left\langle \sum_{i,j} \hat{\rho}_i^*(Q)\hat{\rho}_j(Q) e^{-i\mathbf{Q}\mathbf{R_i}} e^{i\mathbf{Q}\mathbf{R_j}} \right\rangle \tag{B.58}$$

where $\sin\theta = \hat{n}\hat{n}'$ and $\hat{n}$, $\hat{n}'$ the directions of the scattered and incident beam. We can define

$$F_i(Q) = \frac{e^2}{mc^2} \frac{(\hat{n}\hat{n}')\hat{\rho}_i(\mathbf{Q})}{f_i} \tag{B.59}$$

the scattering length density characteristic of X-rays, where f_i is the normalization. From Equation B.11 we obtain:

$$\frac{d\sigma}{d\Omega} = n_p < (\Delta\rho V_P)^2 > P(Q)S(Q) \tag{B.60}$$

where $n_P = N_P/V$ is the global number density and $< (\Delta\rho V_P)^2 >$ represent an average square electron number per particle

$$< (\Delta\rho V_P)^2 > = \frac{1}{N_P} \sum_{i=1}^{N_P} f_i^2 \tag{B.61}$$

Bibliography

[1] USA University of California, Santa Barbara. Materials research laboratory at UCSB, cited June 2018. (Cited on page 6.)

[2] Loïc Barré. Contribution of Small-Angle X-Ray and Neutron Scattering (SAXS and SANS) to the characterization of natural nanomaterials. In *X-ray and Neutron Techniques for Nanomaterials Characterization*, pages 665–716. Springer, 2016. (Cited on page 6.)

[3] Brian R. Pauw. How to do a perfect SAXS measurement. 2011. (Cited on page 8.)

[4] Otto Glatter and Otto Kratky. *Small angle X-ray scattering*. Academic press, 1982. (Cited on pages 10 and 149.)

[5] André Guinier and Gérard Fournet. *Small angle scattering of X-ray*. Wiley, New York, 1955. (Cited on page 10.)

[6] Ingrid Pilz, Otto Glatter, and Otto Kratky. Small-angle X-ray scattering. *Methods in Enzymology*, 61:148–249, 1979. (Cited on pages 13 and 151.)

[7] Mikio Kataoka, Yoshihisa Hagihara, Ken'ichi Mihara, and Yuji Goto. Molten globule of Cytochrome C studied by Small Angle X-ray Scattering. *Journal of Molecular Biology*, 229(3):591 – 596, 1993. (Cited on page 13.)

[8] Francesco Spinozzi, Claudio Ferrero, Maria Grazia Ortore, Alejandro De Maria Antolinos, and Paolo Mariani. Genfit: software for the analysis of small-angle X-ray and neutron scattering data of macromolecules in solution. *Journal of applied crystallography*, 47(3):1132–1139, 2014. (Cited on pages 13, 16, 68, 69, 85, 99 and 121.)

[9] Jan Skov Pedersen and Peter Schurtenberger. Scattering functions of semiflexible polymers with and without excluded volume effects. *Macromolecules*, 29:7602–7612, 1996. (Cited on pages 15 and 38.)

[10] Maria Grazia Ortore, Francesco Spinozzi, Paolo Mariani, Alessandro Paciaroni, Leandro Barbosa, Heinz Amenitsch, Milos Steinhart, Jaques Ollivier, and Daniela Russo. Combining structure and dynamics: non-denaturing high-pressure effect on lysozyme in solution. *Journal of the Royal Society Interface*, 6:S619–S634, 2009. (Cited on pages 16 and 85.)

[11] Maria Grazia Ortore, Paolo Mariani, Flavio Carsughi, Stefania Cinelli, Giuseppe Onori, José Teixeira, and Francesco Spinozzi. Preferential solvation of lysozyme in water/ethanol mixtures. *The Journal of chemical physics*, 135(24):12B620, 2011. (Cited on pages 16 and 20.)

[12] Dmitri Svergun, Claudio Barberato, and Michel H. J. Koch. CRYSOL - a program to evaluate X-ray solution scattering of biological macromolecules from atomic coordinates. *Journal of Applied Crystallography*, 28:768–773, 1995. (Cited on page 16.)

[13] Paolo Mariani, Francesco Spinozzi, Francesco Federiconi, Maria Grazia Ortore, Heinz Amenitsch, Lea Spindler, and Irena Drevensek-Olenik. Guanosine quadruplexes in solution: A Small-Angle X-ray Scattering analysis of temperature effects on self-assembling of deoxyguanosine monophosphate. *Journal of Nucleic Acids*, 2010, 2010. (Cited on page 17.)

[14] Matteo Levantino, Briony A. Yorke, Diana C.F. Monteiro, Marco Cammarata, and Arwen R. Pearson. Using synchrotrons and XFELs for time-resolved X-ray crystallography and solution scattering experiments on biomolecules. *Current Opinion in Structural Biology*, 35:41 – 48, 2015. (Cited on pages 17 and 141.)

[15] Amy K. Manocchi, Soenke Seifert, Byeongdu Lee, and Hyunmin Yi. In situ small-angle X-ray scattering analysis of palladium nanoparticle growth on tobacco mosaic virus nanotemplates. *Langmuir*, 27(11):7052–7058, 2011. PMID: 21520923. (Cited on page 17.)

[16] Didier Law-Hine, Anil K. Sahoo, Virginie Bailleux, Mehdi Zeghal, Sylvain Prevost, Prabal K. Maiti, Stephane Bressanelli, Doru Constantin, and Guillaume Tresset. Reconstruction of the disassembly pathway of an icosahedral viral capsid and shape determination of two successive intermediates. *The Journal of Physical Chemistry Letters*, 6(17):3471–3476, 2015. (Cited on page 17.)

[17] Lois Pollack, Mark W. Tate, Nicholas C. Darnton, James B. Knight, Sol M. Gruner, William A. Eaton, and Robert H. Austin. Compactness of the denatured state of a fast-folding protein measured by submillisecond small-angle X-ray scattering. *Proceedings of the National Academy of Sciences*, 96(18):10115–10117, 1999. (Cited on page 17.)

[18] Tsuyoshi Konuma, Tetsunari Kimura, Shuzo Matsumoto, Yuji Goto, Tetsuro Fujisawa, Alan R. Fersht, and Satoshi Takahashi. Time-resolved Small-Angle X-ray Scattering study of the folding dynamics of barnase. *Journal of Molecular Biology*, 405(5):1284 – 1294, 2011. (Cited on page 17.)

[19] Angelo Spinello, Maria Grazia Ortore, Francesco Spinozzi, Caterina Ricci, Giampaolo Barone, Antonella Marino Gammazza, and Antonio Palumbo Piccionello. Quaternary structures of GroEL and naïve-Hsp60 chaperonins in solution: a combined SAXS-MD study. *RSC Advances*, 5:49871–49879, 2015. (Cited on pages 17, 53, 58, 68, 85 and 141.)

[20] David Eliezer, Patricia A. Jennings, Peter E. Wright, Sebastian Doniach, Hodgson Keith O., and Tsuruta Hiro. The radius of gyration of an apomyoglobin folding intermediate. *Science*, 270(5235):487, 1995. (Cited on page 17.)

[21] Vladimir N. Uversky, Joel R. Gillespie, and Anthony L. Fink. Why are "natively unfolded" proteins unstructured under physiologic conditions? *Proteins: structure, function, and bioinformatics*, 41(3):415–427, 2000. (Cited on page 17.)

[22] Marc Niebuhr and Michel H.J. Koch. Effects of urea and trimethylamine-N-oxide (TMAO) on the interactions of lysozyme in solution. *Biophysical journal*, 89(3):1978–1983, 2005. (Cited on page 17.)

[23] Dmitri I. Svergun, Stephen Richard, Michel H. J. Koch, Z. Sayers, Sergei Kuprin, and Giuseppe Zaccai. Protein hydration in solution: experimental observation by X-ray and neutron scattering. *Proceedings of the National Academy of Sciences*, 95(5):2267–2272, 1998. (Cited on pages 17 and 85.)

[24] Lauren Boldon, Fallon Laliberte, and Li Liu. Review of the fundamental theories behind small angle X-ray scattering, molecular dynamics simulations, and relevant integrated application. *Nano Reviews*, 6(0), 2015. (Cited on page 17.)

[25] Masaki Kojima, Alexander A. Timchenko, Junichi Higo, Kazuki Ito, Hiroshi Kihara, and Kenji Takahashi. Structural refinement by restrained molecular-dynamics algorithm with Small Angle X-ray Scattering constraints for a biomolecule. *Journal of Applied Crystallography*, 37(1):103–109, Feb 2004. (Cited on pages 17 and 141.)

[26] Tobias Madl, Frank Gabel, and Michael Sattler. NMR and small-angle scattering-based structural analysis of protein complexes in solution. *Journal of Structural Biology*, 173(3):472 – 482, 2011. (Cited on page 17.)

[27] Vladimir N. Uversky, Jie Li, and Anthony L. Fink. Evidence for a partially folded intermediate in α-synuclein fibril formation. *Journal of Biological Chemistry*, 276(14):10737–10744, 2001. (Cited on page 17.)

[28] Mitsuru Tashiro, Masaki Kojima, Hiroshi Kihara, Kouki Kasai, Tomoaki Kamiyoshihara, Kenji Uéda, and Sakurako Shimotakahara. Characterization of fibrillation process of α-synuclein at the initial stage. *Biochemical and biophysical research communications*, 369(3):910–914, 2008. (Cited on page 17.)

[29] Kun Lu, Liang Guo, Anil K. Mehta, Seth W. Childers, Steven N. Dublin, S. Skanthakumar, Vincent P. Conticello, P. Thiyagarajan, Robert P. Apkarian, and David G. Lynn. Macroscale assembly of peptide nanotubes. *Chemical Communications*, pages 2729–2731, 2007. (Cited on page 17.)

[30] Mitushiro Hirai, Ryota Kimura, Kazuki Takeuchi, Masaaki Sugiyama, Kouji Kasahara, Noboru Ohta, Bela Farago, Andreas Stadler, and Giuseppe Zaccai. Change of dynamics of raft-model membrane induced by amyloid-β protein binding. *The European Physical Journal E*, 36(7):74, 2013. (Cited on pages 17 and 137.)

[31] Christopher M. Dobson. Protein folding and misfolding. *Nature*, 426(6968):884, 2003. (Cited on pages 19 and 26.)

[32] Jim Schnabel. Protein folding: The dark side of proteins. *Nature News*, 464(7290):828–829, 2010. (Cited on page 19.)

[33] Vladimir N. Uversky. Intrinsically disordered proteins from A to Z. *The international journal of biochemistry & cell biology*, 43(8):1090–1103, 2011. (Cited on pages 19 and 20.)

[34] Kathy L. Newell, Bradley T. Hyman, John H. Growdon, and E. Tessa Hedley-Whyte. Application of the National Institute on Aging (NIA)-reagan institute criteria for the neuropathological diagnosis of Alzheimer disease. *Journal of neuropathology and experimental neurology*, 58(11):1147–1155, 1999. (Cited on pages 19 and 21.)

[35] Samuel I.A. Cohen, Sara Linse, Leila M. Luheshi, Erik Hellstrand, Duncan A. White, Luke Rajah, Daniel E. Otzen, Michele Vendruscolo, Christopher M. Dobson, and Tuomas P.J. Knowles. Proliferation of amyloid-β42 aggregates occurs through a secondary nucleation mechanism. *Proceedings of the National Academy of Sciences*, 110(24):9758–9763, 2013. (Cited on pages 20, 23 and 29.)

[36] Paul H. Weinreb, Weiguo Zhen, Anna W. Poon, Kelly A. Conway, and Peter T. Lansbury. NACP, a protein implicated in Alzheimer's disease and learning, is natively unfolded. *Biochemistry*, 35(43):13709–13715, 1996. (Cited on pages 20 and 25.)

[37] Rakez Kayed and Cristian A Lasagna-Reeves. Molecular mechanisms of amyloid oligomers toxicity. *Journal of Alzheimer's Disease*, 33(s1):S67–S78, 2013. (Cited on pages 20 and 127.)

[38] Vladimir N. Uversky and Anthony L. Fink. Conformational constraints for amyloid fibrillation: the importance of being unfolded. *Biochimica et Biophysica Acta (BBA)-Proteins and Proteomics*, 1698(2):131–153, 2004. (Cited on pages 20 and 30.)

[39] Serene W. Chen, Srdja Drakulic, Emma Deas, Myriam Ouberai, Francesco A. Aprile, Rocío Arranz, Samuel Ness, Cintia Roodveldt, Tim Guilliams, Erwin J. De-Genst, David Klenerman, Nicholas W. Wood, Tuomas P.J. Knowles, Carlo Alfonso, German Rivas, Andrey Y. Abramov, JosÃ¨ Maria Valpuesta, Christopher M. Dobson, and Nunilo Cremades. Structural characterization of toxic oligomers that are kinetically trapped during α-synuclein fibril formation. *Proceedings of the National Academy of Sciences*, 112(16):E1994–E2003, 2015. (Cited on pages 20 and 41.)

[40] Maria Grazia Ortore, Francesco Spinozzi, Paolo Mariani, Alessandro Paciaroni, Leandro RS Barbosa, Heinz Amenitsch, Milos Steinhart, Jacques Ollivier, and Daniela Russo. Combining structure and dynamics: non-denaturing

high-pressure effect on lysozyme in solution. *Journal of The Royal Society Interface*, page rsif20090163, 2009. (Cited on page 20.)

[41] Bo Zhang-Haagen, Ralf Biehl, Luitgard Nagel-Steger, Aurel Radulescu, Dieter Richter, and Dieter Willbold. Monomeric amyloid beta peptide in hexafluoroisopropanol detected by small angle neutron scattering. *PloS one*, 11(2):e0150267, 2016. (Cited on page 20.)

[42] Vladimir N. Uversky. Introduction to intrinsically disordered proteins (idps), 2014. (Cited on page 20.)

[43] Madan M. Babu, Vladimir Vacic, and Lilia M. Iakoucheva. Themed collection: Intrinsically disordered proteins. *Molecular Biosystems*, 8:427–428, 2012. (Cited on page 20.)

[44] Keith A. Dunker, Israel Silman, Vladimir N. Uversky, and Joel L. Sussman. Function and structure of inherently disordered proteins. *Current opinion in structural biology*, 18(6):756–764, 2008. (Cited on page 20.)

[45] Bálint Mészáros, István Simon, and Zsuzsanna Dosztányi. Prediction of protein binding regions in disordered proteins. *PLoS computational biology*, 5(5):e1000376, 2009. (Cited on page 20.)

[46] Alaji Bah and Julie D. Forman-Kay. Modulation of intrinsically disordered protein function by post-translational modifications. *Journal of Biological Chemistry*, 291(13):6696–6705, 2016. (Cited on page 21.)

[47] Megan Sickmeier, Justin A. Hamilton, Tanguy LeGall, Vladimir Vacic, Marc S. Cortese, Agnes Tantos, Beata Szabo, Peter Tompa, Jake Chen, Vladimir N. Uversky, et al. DisProt: the database of disordered proteins. *Nucleic acids research*, 35(suppl_1):D786–D793, 2006. (Cited on page 21.)

[48] Alzheimer's association Website. Alz.org, cited June 2018. (Cited on page 21.)

[49] Dennis J. Selkoe. Alzheimer's disease: genes, proteins, and therapy. *Physiological reviews*, 81(2):741–766, 2001. (Cited on page 21.)

[50] John Hardy. Alzheimer's disease: the amyloid cascade hypothesis: an update and reappraisal. *Journal of Alzheimer's disease*, 9(s3):151–153, 2006. (Cited on page 21.)

[51] John A. Hardy and Gerald A. Higgins. Alzheimer's disease: the amyloid cascade hypothesis. *Science*, 256(5054):184, 1992. (Cited on page 22.)

[52] Arun K. Ghosh and Heather L. Osswald. BACE1 (β-secretase) inhibitors for the treatment of Alzheimer's disease. *Chemical Society Reviews*, 43(19):6765–6813, 2014. (Cited on page 22.)

[53] Wikipedia. Folding@home — wikipedia, l'enciclopedia libera, 2011. [Online; July 2018]. (Cited on page 23.)

[54] Mordhwaj S. Parihar and Gregory J. Brewer. Amyloid-β as a modulator of synaptic plasticity. *Journal of Alzheimer's Disease*, 22(3):741–763, 2010. (Cited on page 23.)

[55] Collaborative research center SFB/TRR 102 Martin Luther University Halle Wittenberg. Group of Daniel Huster at University of Leipzig, cited June 2018. (Cited on page 24.)

[56] Rebecca Nelson and David Eisenberg. Recent atomic models of amyloid fibril structure. *Current opinion in structural biology*, 16(2):260–265, 2006. (Cited on page 23.)

[57] Dominic M. Walsh and Dennis J. Selkoe. Aβ oligomers–a decade of discovery. *Journal of neurochemistry*, 101(5):1172–1184, 2007. (Cited on page 23.)

[58] Lukasz Goldschmidt, Poh K. Teng, Roland Riek, and David Eisenberg. Identifying the amylome, proteins capable of forming amyloid-like fibrils. *Proceedings of the National Academy of Sciences*, 107(8):3487–3492, 2010. (Cited on page 23.)

[59] Alexzander A.A. Asea, Naif N. Almasoud, Sunil Krishnan, Punit Kaur, et al. *Heat Shock Protein-based Therapies*. Springer, 2015. (Cited on page 23.)

[60] Atul Deshpande, Erene Mina, Charles Glabe, and Jorge Busciglio. Different conformations of amyloid β induce neurotoxicity by distinct mechanisms in human cortical neurons. *Journal of Neuroscience*, 26(22):6011–6018, 2006. (Cited on page 23.)

[61] Takeshi Kawarabayashi, Mikio Shoji, Linda H. Younkin, Lin Wen-Lang, Dennis W. Dickson, Tetsuro Murakami, Etsuro Matsubara, Koji Abe, Karen Hsiao Ashe, and Steven G. Younkin. Dimeric amyloid β protein rapidly accumulates in lipid rafts followed by apolipoprotein E and phosphorylated τ accumulation in the Tg2576 mouse model of Alzheimer's disease. *Journal of Neuroscience*, 24(15):3801–3809, 2004. (Cited on page 23.)

[62] Marco Diociaiuti, Cristiano Giordani, Gihan S. Kamel, Francesco Brasili, Simona Sennato, Cecilia Bombelli, Karen Y. Meneses, Marco A. Giraldo, and Federico Bordi. Monosialoganglioside-GM1 triggers binding of the amyloid-protein salmon calcitonin to a langmuir membrane model mimicking the occurrence of lipid-rafts. *Biochemistry and biophysics reports*, 8:365–375, 2016. (Cited on page 23.)

[63] Takeshi Iwatsubo, Asano Odaka, Nobuhiro Suzuki, Hidehiro Mizusawa, Nobuyuki Nukina, and Yasuo Ihara. Visualization of Aβ42 (43) and Aβ40

in senile plaques with end-specific Aβ monoclonals: evidence that an initially deposited species is Aβ42 (43). *Neuron*, 13(1):45–53, 1994. (Cited on page 24.)

[64] Karie N. Dahlgren, Arlene M. Manelli, W. Blaine Stine, Lorinda K. Baker, Grant A. Krafft, and Mary Jo LaDu. Oligomeric and fibrillar species of amyloid-β peptides differentially affect neuronal viability. *Journal of Biological Chemistry*, 277(35):32046–32053, 2002. (Cited on page 24.)

[65] David Frost, Paul M. Gorman, Christopher M. Yip, and Avijit Chakrabartty. Co-incorporation of Aβ40 and Aβ42 to form mixed pre-fibrillar aggregates. *The FEBS Journal*, 270(4):654–663, 2003. (Cited on page 24.)

[66] Lei Gu and Zhefeng Guo. Alzheimer's Aβ42 and Aβ40 peptides form interlaced amyloid fibrils. *Journal of neurochemistry*, 126(3):305–311, 2013. (Cited on page 24.)

[67] Gal Bitan, Marina D. Kirkitadze, Aleksey Lomakin, Sabrina S. Vollers, George B. Benedek, and David B. Teplow. Amyloid β-protein (Aβ) assembly: Aβ40 and Aβ42 oligomerize through distinct pathways. *Proceedings of the National Academy of Sciences*, 100(1):330–335, 2003. (Cited on page 24.)

[68] Brigita Urbanc, Luis Cruz, Sijung Yun, Sergey V. Buldyrev, Gal Bitan, David B. Teplow, and H. Eugene Stanley. In silico study of amyloid β-protein folding and oligomerization. *Proceedings of the National Academy of Sciences of the United States of America*, 101(50):17345–17350, 2004. (Cited on page 24.)

[69] Lonneke M.L. De Lau and Monique M.B. Breteler. Epidemiology of Parkinson's disease. *The Lancet Neurology*, 5(6):525–535, 2006. (Cited on page 24.)

[70] Dennis W. Dickson, Hiroshige Fujishiro, Carolyn Orr, Anthony DelleDonne, Keith A. Josephs, Roberta Frigerio, Melinda Burnett, Joseph E. Parisi, Kevin J. Klos, and J. Eric Ahlskog. Neuropathology of non-motor features of Parkinson disease. *Parkinsonism & related disorders*, 15:S1–S5, 2009. (Cited on page 24.)

[71] Vladimir N. Uversky and David Eliezer. Biophysics of Parkinson's disease: structure and aggregation of α-synuclein. *Current Protein and Peptide Science*, 10(5):483–499, 2009. (Cited on page 25.)

[72] Maria Grazia Spillantini, R Anthony Crowther, Ross Jakes, Masato Hasegawa, and Michel Goedert. α-synuclein in filamentous inclusions of Lewy bodies from Parkinson's disease and dementia with Lewy bodies. *Proceedings of the National Academy of Sciences*, 95(11):6469–6473, 1998. (Cited on page 25.)

[73] Louise C. Serpell, John Berriman, Ross Jakes, Michel Goedert, and Anthony R. Crowther. Fiber diffraction of synthetic α-synuclein filaments shows

amyloid-like cross-β conformation. *Proceedings of the National Academy of Sciences*, 97(9):4897–4902, 2000. (Cited on page 25.)

[74] David F. Clayton and Julia M. George. The synucleins: a family of proteins involved in synaptic function, plasticity, neurodegeneration and disease. *Trends in neurosciences*, 21(6):249–254, 1998. (Cited on page 25.)

[75] Julia M. George. The synucleins. *Genome biology*, 3(1):reviews3002.1–review3002.6, 2001. (Cited on page 25.)

[76] Juan Zhao, Qingnan Liang, Qing Sun, Congheng Chen, Lihui Xu, Yu Ding, and Ping Zhou. (-)-epigallocatechin-3-gallate (EGCG) inhibits fibrillation, disaggregates amyloid fibrils of α-synuclein, and protects PC12 cells against α-synuclein-induced toxicity. *RSC Advances*, 7(52):32508–32517, 2017. (Cited on page 25.)

[77] Tim Bartels, Logan S. Ahlstrom, Avigdor Leftin, Frits Kamp, Christian Haass, Michael F. Brown, and Klaus Beyer. The N-terminus of the intrinsically disordered protein α-synuclein triggers membrane binding and helix folding. *Biophysical journal*, 99(7):2116–2124, 2010. (Cited on page 25.)

[78] Reid T. Alderson and John L. Markley. Biophysical characterization of α-synuclein and its controversial structure. *Intrinsically disordered proteins*, 1(1):e26255, 2013. (Cited on page 26.)

[79] Tim Bartels, Joanna G. Choi, and Dennis J. Selkoe. α-synuclein occurs physiologically as a helically folded tetramer that resists aggregation. *Nature*, 477(7362):107, 2011. (Cited on page 26.)

[80] Alexander K. Buell, Céline Galvagnion, Ricardo Gaspar, Emma Sparr, Michele Vendruscolo, Tuomas P.J. Knowles, Sara Linse, and Christopher M. Dobson. Solution conditions determine the relative importance of nucleation and growth processes in α-synuclein aggregation. *Proceedings of the National Academy of Sciences*, 111(21):7671–7676, 2014. (Cited on page 26.)

[81] Ali Makky, Luc Bousset, Jérôme Polesel-Maris, and Ronald Melki. Nanomechanical properties of distinct fibrillar polymorphs of the protein α-synuclein. *Scientific reports*, 6:37970, 2016. (Cited on page 26.)

[82] Katsuya Araki, Naoto Yagi, Rie Nakatani, Hiroshi Sekiguchi, Masatomo So, Hisashi Yagi, Noboru Ohta, Yoshitaka Nagai, Yuji Goto, and Hideki Mochizuki. A small-angle X-ray scattering study of alpha-synuclein from human red blood cells. *Scientific reports*, 6:30473, 2016. (Cited on pages 26 and 38.)

[83] Fabrizio Chiti and Christopher M. Dobson. Protein misfolding, functional amyloid, and human disease. *Annu. Rev. Biochem.*, 75:333–366, 2006. (Cited on page 26.)

[84] Cyrus Levinthal. How to fold graciously. *Mossbauer spectroscopy in biological systems*, 67:22–24, 1969. (Cited on page 26.)

[85] Leandro Martinez. Introducing the Levinthal's protein folding paradox and its solution. *Journal of Chemical Education*, 91(11):1918–1923, 2014. (Cited on page 26.)

[86] Massimo Stefani. Protein folding and misfolding on surfaces. *International journal of molecular sciences*, 9(12):2515–2542, 2008. (Cited on page 27.)

[87] Christian B. Anfinsen. Principles that govern the folding of protein chains. *Science*, 181(4096):223–230, 1973. (Cited on page 26.)

[88] Mark R. Wilson, Justin J. Yerbury, and Stephen Poon. Potential roles of abundant extracellular chaperones in the control of amyloid formation and toxicity. *Molecular Biosystems*, 4(1):42–52, 2008. (Cited on page 28.)

[89] Louise Serpell. Amyloid structure. *Essays in biochemistry*, 56:1–10, 2014. (Cited on page 29.)

[90] Margaret Sunde, Louise C. Serpell, Mark Bartlam, Paul E. Fraser, Mark B. Pepys, and Colin C.F. Blake. Common core structure of amyloid fibrils by synchrotron X-ray diffraction. *Journal of molecular biology*, 273(3):729–739, 1997. (Cited on page 29.)

[91] Georg Meisl, Thomas C.T. Michaels, Sara Linse, and Tuomas P.J. Knowles. Kinetic analysis of amyloid formation. In *Amyloid Proteins*, pages 181–196. Springer, 2018. (Cited on page 29.)

[92] Serge N. Timasheff et al. Control of protein stability and reactions by weakly interacting cosolvents: the simplicity of the complicated. *Advances in Protein Chemistry*, 51(51):355–432, 1998. (Cited on page 30.)

[93] Slavomíra Poniková, Andrea Antošová, Erna Demjén, Dagmar Sedláková, Jozef Marek, Rastislav Varhač, Zuzana Gažová, and Erik Sedlák. Lysozyme stability and amyloid fibrillization dependence on Hofmeister anions in acidic pH. *JBIC Journal of Biological Inorganic Chemistry*, 20(6):921–933, 2015. (Cited on pages 30 and 35.)

[94] Kerensa Broersen, Frederic Rousseau, and Joost Schymkowitz. The culprit behind amyloid β peptide related neurotoxicity in Alzheimer's disease: oligomer size or conformation? *Alzheimer's research & therapy*, 2(4):12, 2010. (Cited on page 30.)

[95] Agustina Taglialegna, Iñigo Lasa, and Jaione Valle. Amyloid structures as biofilm matrix scaffolds. *Journal of bacteriology*, 198(19):2579–2588, 2016. (Cited on page 30.)

[96] Douglas M. Fowler, Atanas V. Koulov, William E. Balch, and Jeffery W. Kelly. Functional amyloid–from bacteria to humans. *Trends in biochemical sciences*, 32(5):217–224, 2007. (Cited on page 30.)

[97] Bumjoon Choi, Gwonchan Yoon, Sang Woo Lee, and Kilho Eom. Mechanical deformation mechanisms and properties of amyloid fibrils. *Physical Chemistry Chemical Physics*, 17(2):1379–1389, 2015. (Cited on page 30.)

[98] Chaoxu Li and Raffaele Mezzenga. The interplay between carbon nanomaterials and amyloid fibrils in bio-nanotechnology. *Nanoscale*, 5(14):6207–6218, 2013. (Cited on page 30.)

[99] Shruti Mankar, Anoop Arunagiri, Shamik Sen, and Samir K. Maji. Nanomaterials: amyloids reflect their brighter side. *Nano reviews*, 2(1):6032, 2011. (Cited on page 30.)

[100] Ludmilla A. Morozova-Roche, Jesús Zurdo, Andrew Spencer, Wim Noppe, Veronique Receveur, David B. Archer, Marcel Joniau, and Christopher M. Dobson. Amyloid fibril formation and seeding by wild-type human lysozyme and its disease-related mutational variants. *Journal of structural biology*, 130(2-3):339–351, 2000. (Cited on page 30.)

[101] Mark B. Pepys, Philip N. Hawkins, David R. Booth, David M. Vigushin, Glenys A. Tennent, Anne K. Soutar, Nicholas Totty, Oanh Nguyen, Colin C.F. Blake, Carla J. Terry, Anthony M. Zalin, and Justin J. Hsuan. Human lysozyme gene mutations cause hereditary systemic amyloidosis. *Nature*, 362(6420):553, 1993. (Cited on page 30.)

[102] Shinpei Tanaka, Yutaka Oda, Mitsuo Ataka, Kazuo Onuma, Satoru Fujiwara, and Yasushige Yonezawa. Denaturation and aggregation of hen egg lysozyme in aqueous ethanol solution studied by dynamic light scattering. *Biopolymers*, 59(5):370–379, 2001. (Cited on page 30.)

[103] Luben N. Arnaudov and Renko de Vries. Thermally induced fibrillar aggregation of hen egg white lysozyme. *Biophysical Journal*, 88(1):515–526, 2005. (Cited on page 30.)

[104] Peter B. Stathopulos, Guenter A. Scholz, Young-Mi Hwang, Jessica A.O. Rumfeldt, James R. Lepock, and Elizabeth M. Meiering. Sonication of proteins causes formation of aggregates that resemble amyloid. *Protein Science*, 13(11):3017–3027, 2004. (Cited on page 30.)

[105] Jens Brange, Lennart Andersen, Erik D. Laursen, Giorgio Meyn, and Eigil Rasmussen. Toward understanding insulin fibrillation. *Journal of pharmaceutical sciences*, 86(5):517–525, 1997. (Cited on page 30.)

[106] Eri Chatani, Rintaro Inoue, Hiroshi Imamura, Masaaki Sugiyama, Minoru Kato, Masahide Yamamoto, Koji Nishida, and Toshiji Kanaya. Early aggregation preceding the nucleation of insulin amyloid fibrils as monitored by small angle X-ray scattering. *Scientific reports*, 5:15485, 2015. (Cited on page 30.)

[107] Nikolaj K. Holm, Stine K. Jespersen, Lise V. Thomassen, Tine Y. Wolff, Pankaj Sehgal, Line A. Thomsen, Gunna Christiansen, Christian Beyschau Andersen, Anders D. Knudsen, and Daniel E. Otzen. Aggregation and fibrillation of bovine serum albumin. *Biochimica et Biophysica Acta (BBA)-Proteins and Proteomics*, 1774(9):1128–1138, 2007. (Cited on page 30.)

[108] Sara M. Vaiana, Antonio Emanuele, Maria Beatrice Palma-Vittorelli, and Massimo Ugo Palma. Irreversible formation of intermediate BSA oligomers requires and induces conformational changes. *Proteins: Structure, Function, and Bioinformatics*, 55(4):1053–1062, 2004. (Cited on page 30.)

[109] Cynthia Akkermans. *Protein fibrillization: preparation, mechanism and application*. 2008. (Cited on page 30.)

[110] Wolfgang Hoyer, Thomas Antony, Dmitry Cherny, Gudrun Heim, Thomas M. Jovin, and Vinod Subramaniam. Dependence of α-synuclein aggregate morphology on solution conditions. *Journal of molecular biology*, 322(2):383–393, 2002. (Cited on pages 31 and 97.)

[111] Youcef Fezoui, Dean M. Hartley, James D. Harper, Ritu Khurana, Dominic M. Walsh, Margaret M. Condron, Dennis J. Selkoe, Peter T. Lansbury, Anthony L. Fink, and David B. Teplow. An improved method of preparing the amyloid β-protein for fibrillogenesis and neurotoxicity experiments. *Amyloid*, 7(3):166–178, 2000. (Cited on pages 31 and 113.)

[112] Andy P. Hammersley. FIT2D. 2004. (Cited on page 32.)

[113] David Necas and Petr Klapetek. Gwyddion: an open-source software for SPM data analysis. *Central European Journal of Physics*, 10:181–188, 2012. (Cited on pages 33 and 98.)

[114] Christine Xue, Tiffany Yuwen Lin, Dennis Chang, and Zhefeng Guo. Thioflavin T as an amyloid dye: fibril quantification, optimal concentration and effect on aggregation. *Royal Society open science*, 4(1):160696, 2017. (Cited on pages 34 and 118.)

[115] LeVine H. 3rd. Thioflavine t interaction with synthetic Alzheimerś disease β-amyloid peptides: detection of amyloid aggregation in solution. *Protein Science*, 2(3):404–410, 1993. (Cited on pages 34 and 118.)

[116] Hironobu Naiki, Keiichi Higuchi, Masanori Hosokawa, and Toshio Takeda. Fluorometric determination of amyloid fibrils in vitro using the fluorescent

dye, thioflavine T. *Analytical biochemistry*, 177(2):244–249, 1989. (Cited on pages 34 and 118.)

[117] Michele D'Amico, Maria Giovanna Di Carlo, Minna Groenning, Valeria Militello, Valeria Vetri, and Maurizio Leone. Thioflavin T promotes Aβ amyloid fibrils formation. *The Journal of Physical Chemistry Letters*, 3(12):1596–1601, 2012. PMID: 26285714. (Cited on page 35.)

[118] Josephine W. Wu, Kuan-Nan Liu, Su-Chun How, Wei-An Chen, Chia-Min Lai, Hwai-Shen Liu, Chaur-Jong Hu, and Steven S-S Wang. Carnosine's effect on amyloid fibril formation and induced cytotoxicity of lysozyme. *PloS one*, 8(12):e81982, 2013. (Cited on page 35.)

[119] Ritu Khurana, Vladimir N. Uversky, Liza Nielsen, and Anthony L. Fink. Is Congo Red an Amyloid-specific Dye? *Journal of Biological Chemistry*, 276(25):22715–22721, 2001. (Cited on page 36.)

[120] William R. Krigbaum and F.R. Kügler. Molecular conformation of egg-white lysozyme and bovine α-lactalbumin in solution. *Biochemistry*, 9(5):1216–1223, 1970. (Cited on page 36.)

[121] Maria Grazia Ortore, Francesco Spinozzi, Silvia Vilasi, Ivana Sirangelo, Gaetano Irace, Anuj Shukla, Theyencheri Narayanan, Raffaele Sinibaldi, and Paolo Mariani. Time-resolved small-angle X-ray scattering study of the early stage of amyloid formation of an apomyoglobin mutant. *Physical Review E*, 84(6):061904, 2011. (Cited on pages 38 and 85.)

[122] Pierre-Emmanuel Milhiet, Daisuke Yamamoto, Olivia Berthoumieu, Patrice Dosset, Christian Le Grimellec, Jean-Michel Verdier, Stéphane Marchal, and Toshio Ando. Deciphering the structure, growth and assembly of amyloid-like fibrils using high-speed atomic force microscopy. *PLoS One*, 5(10):e13240, 2010. (Cited on page 43.)

[123] Ya-Ling Chiang, Yuan-Chih Chang, I-Chen Chiang, Huey-Ming Mak, Shouh Hwang, and Yu-Ling Shih. Atomic force microscopy characterization of protein fibrils formed by the amyloidogenic region of the bacterial protein mine on mica and a supported lipid bilayer. *PloS one*, 10(11):e0142506, 2015. (Cited on page 43.)

[124] Antonella Sgarbossa, Susanna Monti, Francesco Lenci, Emilia Bramanti, Ranieri Bizzarri, and Vincenzo Barone. The effects of ferulic acid on β-amyloid fibrillar structures investigated through experimental and computational techniques. *Biochimica et Biophysica Acta (BBA)-General Subjects*, 1830(4):2924–2937, 2013. (Cited on page 45.)

[125] Loretta Laureana Del Mercato, Pier Paolo Pompa, Giuseppe Maruccio, Antonio Della Torre, Stefania Sabella, Antonio Mario Tamburro, Roberto

Cingolani, and Ross Rinaldi. Charge transport and intrinsic fluorescence in amyloid-like fibrils. *Proceedings of the National Academy of Sciences*, 104(46):18019–18024, 2007. (Cited on page 45.)

[126] Mariya Yu Suvorina, Olga M. Selivanova, Elizaveta I. Grigorashvili, Alexey D. Nikulin, Victor V. Marchenkov, Alexey K. Surin, and Oxana V. Galzitskaya. Studies of polymorphism of amyloid-β42 peptide from different suppliers. *Journal of Alzheimer's Disease*, 47(3):583–593, 2015. (Cited on page 49.)

[127] Thomas Hohn, Barbara Hohn, Andreas Engel, Michel Wurtz, and Phillip R. Smith. Isolation and characterization of the host protein groE involved in bacteriophage lambda assembly. *Journal of Molecular Biology*, 129(3):359 – 373, 1979. (Cited on pages 51 and 52.)

[128] Ulrich F. Hartl, Andreas Bracher, and Manajit Hayer-Hartl. Molecular chaperones in protein folding and proteostasis. *Nature*, 475(7356):324, 2011. (Cited on pages 52 and 56.)

[129] John R. Ellis. Proteins as molecular chaperones. *Nature*, 328(328):378–379, 1987. (Cited on page 51.)

[130] Zhaohui Xu, Arthur L. Horwich, and Paul B. Sigler. The crystal structure of the asymmetric GroEL–GroES–(ADP) 7 chaperonin complex. *Nature*, 388(6644):741, 1997. (Cited on pages 52 and 71.)

[131] George H. Lorimer, Xue Fei, and Xiang Ye. The GroEL chaperonin: a protein machine with pistons driven by ATP binding and hydrolysis. *Philosophical Transactions of the Royal Society B: Biological Sciences*, 373(1749):20170179, 2018. (Cited on pages 52 and 56.)

[132] Shahar Nisemblat, Oren Yaniv, Avital Parnas, Felix Frolow, and Abdussalam Azem. Crystal structure of the human mitochondrial chaperonin symmetrical football complex. *Proceedings of the National Academy of Sciences*, 2015. (Cited on pages 52, 80 and 81.)

[133] Caterina Ricci, Maria Grazia Ortore, Silvia Vilasi, Rita Carrotta, Maria Rosalia Mangione, Donatella Bulone, Fabio Librizzi, Francesco Spinozzi, Giosalba Burgio, Heinz Amenitsch, and Pier Luigi San Biagio. Stability and disassembly properties of human naive Hsp60 and bacterial GroEL chaperonins. *Biophysical Chemistry*, 208:68 – 75, 2016. (Cited on pages 53, 81, 84, 86, 87, 88 and 141.)

[134] Caterina Ricci, Rita Carrotta, Giacoma Cinzia Rappa, Maria Rosalia Mangione, Fabio Librizzi, Pier Luigi San Biagio, Heinz Amenitsch, Maria Grazia Ortore, and Silvia Vilasi. Investigation on different chemical stability of mitochondrial Hsp60 and its precursor. *Biophysical chemistry*, 229:31–38, 2017. (Cited on pages 53, 81, 84, 86 and 141.)

[135] Micha M.M. Wilhelmus, Robert M.W. De Waal, and Marcel M. Verbeek. Heat shock proteins and amateur chaperones in amyloid-beta accumulation and clearance in alzheimer's disease. *Molecular neurobiology*, 35(3):203–216, 2007. (Cited on pages 53 and 142.)

[136] Maria Rosalia Mangione, Silvia Vilasi, Claudia Marino, Fabio Librizzi, Claudio Canale, Dario Spigolon, Fabio Bucchieri, Alberto Fucarino, Rosa Passantino, Francesco Cappello, et al. Hsp60, amateur chaperone in amyloid-β fibrillogenesis. *Biochimica et Biophysica Acta (BBA)-General Subjects*, 1860(11):2474–2483, 2016. (Cited on pages 53, 91, 92 and 142.)

[137] Arthur L. Horwich, George W. Farr, and Wayne A. Fenton. GroEL- GroES-mediated protein folding. *Chemical reviews*, 106(5):1917–1930, 2006. (Cited on page 54.)

[138] Francesco Cappello, Antonella Marino Gammazza, Antonio Palumbo Piccionello, Claudia Campanella, Andrea Pace, Everly Conway de Macario, and Alberto JL Macario. Hsp60 chaperonopathies and chaperonotherapy: targets and agents. *Expert opinion on therapeutic targets*, 18(2):185–208, 2014. (Cited on page 54.)

[139] Manajit Hayer-Hartl, Andreas Bracher, and Ulrich F. Hartl. The GroEL–GroES chaperonin machine: a nano-cage for protein folding. *Trends in biochemical sciences*, 41(1):62–76, 2016. (Cited on page 54.)

[140] PyMOL Molecular Graphics System, ver 1.5.0.4, Schrödinger, LLC. `www.pymol.org`. 2016. (Cited on page 55.)

[141] Luciano Brocchieri and Samuel Karlin. Conservation among Hsp60 sequences in relation to structure, function, and evolution. *Protein Science*, 9(3):476–486, 2000. (Cited on page 54.)

[142] Bhag Singh and Radhey S. Gupta. Conserved inserts in the Hsp60 (GroEL) and Hsp70 (DnaK) proteins are essential for cellular growth. *Molecular genetics and genomics*, 281(4):361–373, 2009. (Cited on page 54.)

[143] Celeste Weiss, Fady Jebara, Shahar Nisemblat, and Abdussalam Azem. Dynamic complexes in the chaperonin-mediated protein folding cycle. *Frontiers in molecular biosciences*, 3:80, 2016. (Cited on page 54.)

[144] Arthur L. Horwich, Adrian C. Apetri, and Wayne A. Fenton. The GroEL/GroES cis cavity as a passive anti-aggregation device. *FEBS letters*, 583(16):2654–2662, 2009. (Cited on page 54.)

[145] Tomoya Sameshima, Ryo Iizuka, Taro Ueno, and Takashi Funatsu. Denatured proteins facilitate the formation of the football-shaped GroEL–(GroES) 2 complex. *Biochemical Journal*, 427(2):247–254, 2010. (Cited on page 56.)

[146] Silvia Vilasi, Rita Carrotta, Maria Rosalia Mangione, Claudia Campanella, Fabio Librizzi, Loredana Randazzo, Vincenzo Martorana, Antonella Marino Gammazza, Maria Grazia Ortore, Annalisa Vilasi, Gabriella Pocsfalvi, Giosalba Burgio, Davide Corona, Antonio Palumbo Piccionello, Giovanni Zummo, Donatella Bulone, Everly Conway de Macario, Alberto J. L. Macario, Pier Luigi San Biagio, and Francesco Cappello. Human Hsp60 with its mitochondrial import signal occurs in solution as heptamers and tetradecamers remarkably stable over a wide range of concentrations. *PLoS ONE*, 9(5):e97657, 05 2014. (Cited on pages 56, 57, 58 and 70.)

[147] Galit Levy-Rimler, Paul Viitanen, Celeste Weiss, Rajach Sharkia, Anat Greenberg, Adina Niv, Ariel Lustig, Yacov Delarea, and Abdussalam Azem. The effect of nucleotides and mitochondrial chaperonin 10 on the structure and chaperone activity of mitochondrial chaperonin 60. *The FEBS Journal*, 268(12):3465–3472, 2001. (Cited on page 57.)

[148] Paul V. Viitanen, George Lorimer, Wolfgang Bergmeier, Celeste Weiss, Martin Kessel, and Pierre Goloubinoff. Purification of mammalian mitochondrial chaperonin 60 through in vitro reconstitution of active oligomers. In *Methods in enzymology*, volume 290, pages 203–217. Elsevier, 1998. (Cited on page 57.)

[149] Kei Amada, Masafumi Yohda, Masafumi Odaka, Isao Endo, Noriyuki Ishii, Hideki Taguchi, and Masasuke Yoshida. Molecular cloning, expression, and characterization of chaperonin-60 and chaperonin-10 from a thermophilic bacterium, thermus thermophilus HB8. *The Journal of Biochemistry*, 118(2):347–354, 1995. (Cited on page 57.)

[150] Jung Nyeo Chun, Boae Choi, Kyung Wha Lee, Doo Jae Lee, Dong Hoon Kang, Joo Young Lee, In Sung Song, Hye In Kim, Sang-Hee Lee, Hyeon Soo Kim, et al. Cytosolic Hsp60 is involved in the nf-κb-dependent survival of cancer cells via ikk regulation. *PLoS One*, 5(3):e9422, 2010. (Cited on page 57.)

[151] Celeste Caruso Bavisotto, Dragana Nikolic, Antonella Marino Gammazza, Rosario Barone, Filippa Lo Cascio, Emanuele Mocciaro, Giovanni Zummo, Everly Conway de Macario, Alberto JL Macario, Francesco Cappello, Valentina Giacalone, Andrea Pace, Giampaolo Barone, Antonio Palumbo Piccionello, and Claudia Campanella. The dissociation of the Hsp60/pro-caspase-3 complex by bis(pyridyl)oxadiazole copper complex (cubipyoxa) leads to cell death in nci-h292 cancer cells. *Journal of Inorganic Biochemistry*, 170:8 – 16, 2017. (Cited on page 57.)

[152] Francesco Cappello, Antonella Marino Gammazza, Silvia Vilasi, Maria Grazia Ortore, Pier Luigi San Biagio, Claudia Campanella, Andrea Pace, Antonio Palumbo Piccionello, Giulio Taglialatela, Everly Conway De Macario, et al. Chaperonotherapy for Alzheimer's disease: Focusing on Hsp60. In *Heat Shock Protein-Based Therapies*, pages 51–76. Springer, 2015. (Cited on pages 57 and 93.)

[153] Francesco Cappello, Everly Conway de Macario, Lorenzo Marasi, Giovanni Zummo, and Alberto J. L. Macario. Hsp60 expression, new locations, functions, and perspectives for cancer diagnosis and therapy. *Cancer Biology & Therapy*, 7(6):801–809, 2008. (Cited on page 57.)

[154] Caroline Desmetz, Frederic Bibeau, Florence Boissiere, V Bellet, Philippe Rouanet, Thierry Maudelonde, Alain Mange, and Jerome Solassol. Proteomics-based identification of Hsp60 as a tumor-associated antigen in early stage breast cancer and ductal carcinoma in situ. *Journal of Proteome Research*, 7(9):3830–3837, 2008. (Cited on page 57.)

[155] Dhyan Chandra, Grace Choy, and Dean G. Tang. Cytosolic accumulation of Hsp60 during apoptosis with or without apparent mitochondrial release: Evidence that its pro-apoptotic or pro-survival functions involve differential interactions with caspase-3. *Journal of Biological Chemistry*, 282(43):31289–31301, 2007. (Cited on page 57.)

[156] Heba O. Barazi, Longen Zhou, Nancy Smyth Templeton, Henry C. Krutzsch, and David D. Roberts. Identification of heat shock protein 60 as a molecular mediator of $\alpha 3\beta 1$ integrin activation. *Cancer research*, 62(5):1541–1548, 2002. (Cited on page 57.)

[157] Eric F. Pettersen, Thomas D. Goddard, Conrad C. Huang, Gregory S. Couch, Daniel M. Greenblatt, Elaine C. Meng, and Thomas E. Ferrin. UCSF Chimera - A visualization system for exploratory research and analysis. *Journal of Computational Chemistry*, 25(13):1605–1612, 2004. (Cited on pages 58, 95 and 117.)

[158] Heinz Amenitsch, Michael Rappolt, Manfred Kriechbaum, H. Mio, Peter Laggner, and Sigrid Bernstorff. First performance assessment of the small-angle X-ray scattering beamline at ELETTRA. *Journal of Synchrotron Radiation*, 5(3):506–508, May 1998. (Cited on page 60.)

[159] Francesco Spinozzi and Mariano Beltramini. Quafit: A novel method for the quaternary structure determination from small-angle scattering data. *Biophysical journal*, 103(3):511–521, 2012. (Cited on pages 61 and 71.)

[160] Munehito Arai, Tomonao Inobe, Kosuke Maki, Teikichi Ikura, Hiroshi Kihara, Yoshiyuki Amemiya, and Kunihiro Kuwajima. Denaturation and reassembly of chaperonin GroEL studied by solution X-ray scattering. *Protein science*, 12(4):672–680, 2003. (Cited on pages 68 and 81.)

[161] Changbong Hyeon, George H. Lorimer, and Devarajan Thirumalai. Dynamics of allosteric transitions in GroEL. *Proceedings of the National Academy of Sciences*, 103(50):18939–18944, 2006. (Cited on page 71.)

[162] Shahar Nisemblat, Avital Parnas, Oren Yaniv, Abdussalam Azem, and Felix Frolow. Crystallization and structure determination of a symmetrical football

complex of the mammalian mitochondrial Hsp60–Hsp10 chaperonins. *Acta Crystallographica Section F: Structural Biology Communications*, 70(1):116–119, 2014. (Cited on page 80.)

[163] Brian K. Shoichet, Walter A. Baase, Ryota Kuroki, and Brian W. Matthews. A relationship between protein stability and protein function. *Proceedings of the National Academy of Sciences*, 92(2):452–456, 1995. (Cited on pages 81 and 87.)

[164] Jiwen Chen and David L. Smith. Unfolding and disassembly of the chaperonin GroEL occurs via a tetradecameric intermediate with a folded equatorial domain. *Biochemistry*, 39(15):4250–4258, 2000. (Cited on page 81.)

[165] Rakez Kayed, Elizabeth Head, Jennifer L. Thompson, Theresa M. McIntire, Saskia C. Milton, Carl W. Cotman, and Charles G. Glabe. Common structure of soluble amyloid oligomers implies common mechanism of pathogenesis. *Science*, 300:486–489, 2003. (Cited on page 81.)

[166] Nicholas C. Price, Sharon M. Kelly, Graeme J. Thomson, John R. Coggins, Stephan Wood, and Arlene auf der Mauer. The unfolding and attempted refolding of the bacterial chaperone protein GroEL (cpn60). *Biochimica at Biophysica acta*, 1161:52–58, 1993. (Cited on page 81.)

[167] Raymond F. Greene and Nick C. Pace. Urea and guanidine hydrochloride denaturation of ribonuclease, lysozyme, α-chymotrypsin, and β-lactoglobulin. *Journal of Biological Chemistry*, 249(17):5388–5393, 1974. (Cited on page 81.)

[168] Alan Fersht. *Structure and mechanism in protein science. A guide to enzyme catalysis and protein folding.* New York: Freeman, 1999. (Cited on page 83.)

[169] Félix Sauvage, Samir Messaoudi, Elias Fattal, Gillian Barratt, and Juliette Vergnaud-Gauduchon. Heat shock proteins and cancer: How can nanomedicine be harnessed? *Journal of Controlled Release*, 248:133–143, 2017. (Cited on page 87.)

[170] Daniela Russo, Maria Grazia Ortore, Francesco Spinozzi, Paolo Mariani, Camille Loupiac, Burkhard Annighofer, and Alessandro Paciaroni. The impact of high hydrostatic pressure on structure and dynamics of β-lactoglobulin. *Biochimica et Biophysica Acta (BBA)-General Subjects*, 1830(10):4974–4980, 2013. (Cited on page 87.)

[171] Maho Yagi-Utsumi, Tomoko Kunihara, Takashi Nakamura, Yoshinori Uekusa, Koki Makabe, Kunihiro Kuwajima, and Koichi Kato. NMR characterization of the interaction of GroEL with amyloid β as a model ligand. *FEBS letters*, 587(11):1605–1609, 2013. (Cited on page 89.)

[172] Amere Subbarao Sreedhar and Peter Csermely. Heat shock proteins in the regulation of apoptosis: new strategies in tumor therapy: a comprehensive review. *Pharmacology & therapeutics*, 101(3):227–257, 2004. (Cited on page 93.)

[173] Isabel Rivera, Ricardo Capone, David M Cauvi, Nelson Arispe, and Antonio De Maio. Modulation of Alzheimer's amyloid β peptide oligomerization and toxicity by extracellular Hsp70. *Cell Stress and Chaperones*, 23(2):269–279, 2018. (Cited on page 93.)

[174] Jochen Klucken, Youngah Shin, Eliezer Masliah, Bradley T Hyman, and Pamela J McLean. Hsp70 reduces α-synuclein aggregation and toxicity. *Journal of Biological Chemistry*, 279(24):25497–25502, 2004. (Cited on pages 93 and 142.)

[175] Stephan N Witt. Hsp70 molecular chaperones and Parkinson's disease. *Biopolymers*, 93(3):218–228, 2010. (Cited on page 93.)

[176] Francesco A. Aprile, Pietro Sormanni, and Michele Vendruscolo. A rational design strategy for the selective activity enhancement of a molecular chaperone toward a target substrate. *Biochemistry*, 54(32):5103–5112, 2015. (Cited on pages 93, 94, 95, 96, 97, 105, 107 and 142.)

[177] Itzhaq Azoulay, Nataly Kucherenko, Esther Nachliel, Menachem Gutman, Abdussalam Azem, and Yossi Tsfadia. Tracking the interplay between bound peptide and the lid domain of DnaK, using molecular dynamics. *International journal of molecular sciences*, 14(6):12675–12695, 2013. (Cited on page 94.)

[178] Anna Rodina, Pallav D. Patel, Yanlong Kang, Yogita Patel, Imad Baaklini, Michael J.H. Wong, Tony Taldone, Pengrong Yan, Chenghua Yang, Ronnie Maharaj, et al. Identification of an allosteric pocket on human Hsp70 reveals a mode of inhibition of this therapeutically important protein. *Chemistry & biology*, 20(12):1469–1480, 2013. (Cited on page 94.)

[179] Deepak Sharma and Daniel C. Masison. Hsp70 structure, function, regulation and influence on yeast prions. *Protein and peptide letters*, 16(6):571–581, 2009. (Cited on page 94.)

[180] Markus Vogel, Matthias P. Mayer, and Bernd Bukau. Allosteric regulation of Hsp70 chaperones involves a conserved interdomain linker. *Journal of biological chemistry*, 281(50):38705–38711, 2006. (Cited on page 94.)

[181] Christopher G. Evans, Susanne Wisén, and Jason E. Gestwicki. Heat shock proteins 70 and 90 inhibit early stages of amyloid β(1–42) aggregation in vitro. *Journal of Biological Chemistry*, 281(44):33182–33191, 2006. (Cited on page 94.)

[182] Chunjuan Huang, Han Cheng, Shufeng Hao, Hui Zhou, Xujia Zhang, Jianen Gao, Qi-Hong Sun, Hongyu Hu, and Chih-chen Wang. Heat shock protein 70

inhibits α-synuclein fibril formation via interactions with diverse intermediates. *Journal of molecular biology*, 364(3):323–336, 2006. (Cited on pages 94 and 105.)

[183] Paul J. Carter. Introduction to current and future protein therapeutics: a protein engineering perspective. *Experimental cell research*, 317(9):1261–1269, 2011. (Cited on page 95.)

[184] Sebastian Krause, Hans-Ulrich Schmoldt, Alexander Wentzel, Matthias Ballmaier, Karlheinz Friedrich, and Harald Kolmar. Grafting of thrombopoietin-mimetic peptides into cystine knot miniproteins yields high-affinity thrombopoietin antagonists and agonists. *The FEBS journal*, 274(1):86–95, 2007. (Cited on page 95.)

[185] Marie Nicole Bongiovanni, Francesco Antonio Aprile, Pietro Sormanni, and Michele Vendruscolo. A rationally designed Hsp70 variant rescues the aggregation-associated toxicity of human IAPP in cultured pancreatic islet β-cells. *International journal of molecular sciences*, 19(5):1443, 2018. (Cited on page 95.)

[186] Francesco A. Aprile, Anne Dhulesia, Florian Stengel, Cintia Roodveldt, Justin L.P. Benesch, Paolo Tortora, Carol V. Robinson, Xavier Salvatella, Christopher M. Dobson, and Nunilo Cremades. Hsp70 oligomerization is mediated by an interaction between the interdomain linker and the substrate-binding domain. *PLoS One*, 8(6):e67961, 2013. (Cited on pages 95, 101 and 102.)

[187] Ali Reza A. Ladiwala, Moumita Bhattacharya, Joseph M. Perchiacca, Ping Cao, Daniel P. Raleigh, Andisheh Abedini, Ann Marie Schmidt, Jobin Varkey, Ralf Langen, and Peter M. Tessier. Rational design of potent domain antibody inhibitors of amyloid fibril assembly. *Proceedings of the National Academy of Sciences*, 109(49):19965–19970, 2012. (Cited on page 95.)

[188] Jonathan R. Heal, Gareth W. Roberts, Gary Christie, and Andrew D. Miller. Inhibition of β-amyloid aggregation and neurotoxicity by complementary (antisense) peptides. *ChemBioChem*, 3(1):86–92, 2002. (Cited on page 95.)

[189] Pietro Sormanni, Francesco A Aprile, and Michele Vendruscolo. Rational design of antibodies targeting specific epitopes within intrinsically disordered proteins. *Proceedings of the National Academy of Sciences*, 112(32):9902–9907, 2015. (Cited on pages 95 and 97.)

[190] SIB Swiss Institute of Bioinformatics. ExPASy-ProtParam tool, 2011. [Online; July 2018]. (Cited on page 97.)

[191] Roman Kityk, Jürgen Kopp, Irmgard Sinning, and Matthias P Mayer. Structure and dynamics of the ATP-bound open conformation of Hsp70 chaperones. *Molecular cell*, 48(6):863–874, 2012. (Cited on pages 99 and 100.)

[192] Dmitri I. Svergun. Determination of the regularization parameter in indirect-transform methods using perceptual criteria. *Journal of applied crystallography*, 25(4):495–503, 1992. (Cited on page 102.)

[193] Li Shi, Mikio Kataoka, and Anthony L. Fink. Conformational characterization of DnaK and its complexes by Small-Angle X-ray Scattering. *Biochemistry*, 35(10):3297–3308, 1996. (Cited on page 102.)

[194] Sean A. Hudson, Heath Ecroyd, Tak W. Kee, and John A. Carver. The Thioflavin T fluorescence assay for amyloid fibril detection can be biased by the presence of exogenous compounds. *The FEBS journal*, 276(20):5960–5972, 2009. (Cited on page 105.)

[195] Francesco A. Aprile, Paolo Arosio, Giuliana Fusco, Serene W. Chen, Janet R. Kumita, Anne Dhulesia, Paolo Tortora, Tuomas P.J. Knowles, Michele Vendruscolo, Christopher M. Dobson, and Nunilo Cremades. Inhibition of α-synuclein fibril elongation by Hsp70 is governed by a kinetic binding competition between α-synuclein species. *Biochemistry*, 56(9):1177–1180, 2017. (Cited on page 106.)

[196] Xuechao Gao, Marta Carroni, Carmen Nussbaum-Krammer, Axel Mogk, Nadinath B. Nillegoda, Anna Szlachcic, D. Lys Guilbride, Helen R. Saibil, Matthias P. Mayer, and Bernd Bukau. Human Hsp70 disaggregase reverses Parkinson's-linked α-synuclein amyloid fibrils. *Molecular cell*, 59(5):781–793, 2015. (Cited on page 106.)

[197] Matthew M. Dedmon, John Christodoulou, Mark R. Wilson, and Christopher M. Dobson. Heat shock protein 70 inhibits α-synuclein fibril formation via preferential binding to prefibrillar species. *Journal of Biological Chemistry*, 280(15):14733–14740, 2005. (Cited on pages 106 and 108.)

[198] Venugopal P. Menon and Adluri Ram Sudheer. Antioxidant and anti-inflammatory properties of curcumin. In *The molecular targets and therapeutic uses of curcumin in health and disease*, pages 105–125. Springer, 2007. (Cited on page 111.)

[199] Ina Caesar, Maria Jonson, K. Peter R. Nilsson, Stefan Thor, and Per Hammarström. Curcumin promotes A-β fibrillation and reduces neurotoxicity in transgenic Drosophila. *PloS one*, 7(2):e31424, 2012. (Cited on page 111.)

[200] John M. Ringman, Sally A. Frautschy, Gregory M. Cole, Donna L. Masterman, and Jeffrey L. Cummings. A potential role of the curry spice curcumin in Alzheimer's disease. *Current Alzheimer Research*, 2(2):131–136, 2005. (Cited on page 111.)

[201] Praveen P.N. Rao, Tarek Mohamed, Karan Teckwani, and Gary Tin. Curcumin binding to β amyloid: a computational study. *Chemical biology & drug design*, 86(4):813–820, 2015. (Cited on page 111.)

[202] Shatadal Ghosh, Sharmistha Banerjee, and Parames C. Sil. The beneficial role of curcumin on inflammation, diabetes and neurodegenerative disease: A recent update. *Food and Chemical Toxicology*, 83:111–124, 2015. (Cited on pages 111 and 142.)

[203] Rajeshwar Narlawar, Marcus Pickhardt, Stefanie Leuchtenberger, Karlheinz Baumann, Sabine Krause, Thomas Dyrks, Sascha Weggen, Eckhard Mandelkow, and Boris Schmidt. Curcumin-derived pyrazoles and isoxazoles: Swiss army knives or blunt tools for Alzheimer's disease? *ChemMedChem*, 3(1):165–172, 2008. (Cited on page 111.)

[204] Antonella Battisti, Antonio Palumbo Piccionello, Antonella Sgarbossa, Silvia Vilasi, Caterina Ricci, Francesco Ghetti, Francesco Spinozzi, Antonella Marino Gammazza, Valentina Giacalone, Annamaria Martorana, et al. Curcumin-like compounds designed to modify amyloid β peptide aggregation patterns. *RSC Advances*, 7(50):31714–31724, 2017. (Cited on pages 111 and 112.)

[205] Antonella Sgarbossa, Dario Buselli, and Francesco Lenci. In vitro perturbation of aggregation processes in β-amyloid peptides: A spectroscopic study. *FEBS Letters*, 582(23-24):3288 – 3292, 2008. (Cited on page 113.)

[206] Emilia Bramanti, Lorenzo Fulgentini, Ranieri Bizzarri, Francesco Lenci, and Antonella Sgarbossa. β-amyloid amorphous aggregates induced by the small natural molecule ferulic acid. *The Journal of Physical Chemistry B*, 117(44):13816–13821, 2013. (Cited on page 113.)

[207] Thorsten Lührs, Christiane Ritter, Marc Adrian, Dominique Riek-Loher, Bernd Bohrmann, Heinz Döbeli, David Schubert, and Roland Riek. 3D structure of Alzheimer's amyloid-β (1–42) fibrils. *Proceedings of the National Academy of Sciences of the United States of America*, 102(48):17342–17347, 2005. (Cited on pages 116 and 117.)

[208] Yuichi Masuda, Masashi Fukuchi, Tatsuya Yatagawa, Masato Tada, Kazuyuki Takeda, Kazuhiro Irie, Ken ichi Akagi, Youko Monobe, Takayoshi Imazawa, and K. Takegoshi. Solid-state NMR analysis of interaction sites of curcumin and 42-residue amyloid β-protein fibrils. *Bioorganic & Medicinal Chemistry*, 19(20):5967 – 5974, 2011. (Cited on page 116.)

[209] Jessica Nasica-Labouze, Phuong H. Nguyen, Fabio Sterpone, Olivia Berthoumieu, Nicolae-Viorel Buchete, and *et al.* Amyloid β protein and Alzheimer's disease: When computer simulations complement experimental studies. *Chemical Reviews*, 115(9):3518–3563, 2015. PMID: 25789869. (Cited on page 116.)

[210] Julio Alvarez-Builla, Juan Jose Vaquero, and José Barluenga. *Modern Heterocyclic Chemistry: Vol. 4*. John Wiley & Sons, 2011. (Cited on page 117.)

[211] Sean A. Hudson, Heath Ecroyd, Tak W. Kee, and John A. Carver. The Thioflavin T fluorescence assay for amyloid fibril detection can be biased by the presence of exogenous compounds. *FEBS Journal*, 276(20):5960–5972, 2009. (Cited on page 118.)

[212] Eduardo Coelho-Cerqueira, Anderson S. Pinheiro, and Cristian Follmer. Pitfalls associated with the use of Thioflavin-T to monitor anti-fibrillogenic activity. *Bioorganic & Medicinal Chemistry Letters*, 24(14):3194 – 3198, 2014. (Cited on page 118.)

[213] Doris Orthaber, Alexander Bergmann, and Otto Glatter. SAXS experiments on absolute scale with Kratky systems using water as a secondary standard. *Journal of Applied Crystallography*, 33(2):218–225, Apr 2000. (Cited on page 120.)

[214] Claudio Canale, Silvia Seghezza, Silvia Vilasi, Rita Carrotta, Donatella Bulone, Alberto Diaspro, Pier Luigi San Biagio, and Silvia Dante. Different effects of Alzheimer's peptide Aβ oligomers and fibrils on supported lipid membranes. *Biophysical Chemistry*, 182:23 – 29, 2013. XXI SIBPA Meeting. (Cited on page 124.)

[215] Katsuhiko Yanagisawa and Yasuo Ihara. GM1 ganglioside-bound amyloid β-protein in Alzheimer's disease brain. *Neurobiology of aging*, 19(1):S65–S67, 1998. (Cited on page 127.)

[216] Katsuhiko Yanagisawa, Asano Odaka, Nobuhiro Suzuki, and Yasuo Ihara. GM1 ganglioside–bound amyloid β–protein (Aβ): A possible form of preamyloid in Alzheimer's disease. *Nature medicine*, 1(10):1062, 1995. (Cited on page 127.)

[217] Rakez Kayed, Anna Pensalfini, Larry Margol, Yuri Sokolov, Floyd Sarsoza, Elizabeth Head, James Hall, and Charles Glabe. Annular protofibrils are a structurally and functionally distinct type of amyloid oligomer. *Journal of Biological Chemistry*, 2008. (Cited on page 127.)

[218] Urmi Sengupta, Ashley N Nilson, and Rakez Kayed. The role of amyloid-β oligomers in toxicity, propagation, and immunotherapy. *EBioMedicine*, 6:42–49, 2016. (Cited on page 127.)

[219] Bruno A. Costa, Leonardo Sanches, Andreza Barbosa Gomide, Fernando Bizerra, Caroline Dal Mas, Eduardo B. Oliveira, Katia Regina Perez, Rosangela Itri, Nancy Oguiura, and Mirian A.F. Hayashi. Interaction of the rattlesnake toxin crotamine with model membranes. *The Journal of Physical Chemistry B*, 118(20):5471–5479, 2014. (Cited on pages 127 and 129.)

[220] Andrea C Woodka, Paul D Butler, Lionel Porcar, Bela Farago, and Michihiro Nagao. Lipid bilayers and membrane dynamics: insight into thickness fluctuations. *Physical review letters*, 109(5):058102, 2012. (Cited on page 128.)

[221] Maikel C Rheinstädter, Wolfgang Häußler, and Tim Salditt. Dispersion relation of lipid membrane shape fluctuations by neutron spin-echo spectrometry. *Physical review letters*, 97(4):048103, 2006. (Cited on page 128.)

[222] Drew Marquardt, Frederick A Heberle, Jonathan D Nickels, Georg Pabst, and John Katsaras. On scattered waves and lipid domains: detecting membrane rafts with x-rays and neutrons. *Soft Matter*, 11(47):9055–9072, 2015. (Cited on page 128.)

[223] Tatiane P. Sudbrack, Nathaly L. Archilha, Rosangela Itri, and Karin A. Riske. Observing the solubilization of lipid bilayers by detergents with optical microscopy of guvs. *The Journal of Physical Chemistry B*, 115(2):269–277, 2010. (Cited on pages 129 and 132.)

[224] Peter Lindner, Roland P. May, and Peter A. Timmins. Upgrading of the SANS instrument D11 at the ILL. *Physica B: Condensed Matter*, 180-181(Part 2):967 – 972, 1992. (Cited on page 131.)

[225] Lawrence D. Mayer, Michael J. Hope, Pieter R. Cullis, and Andrew S. Janoff. Solute distributions and trapping efficiencies observed in freeze-thawed multilamellar vesicles. *Biochimica et Biophysica Acta (BBA)-Biomembranes*, 817(1):193–196, 1985. (Cited on page 132.)

[226] Jianjun Pan, Xiaolin Cheng, Melissa Sharp, Chian-Sing Ho, Nawal Khadka, and John Katsaras. Structural and mechanical properties of cardiolipin lipid bilayers determined using neutron spin echo, small angle neutron and x-ray scattering, and molecular dynamics simulations. *Soft matter*, 11(1):130–138, 2015. (Cited on page 135.)

[227] Zheng Yi, Michihiro Nagao, and Dobrin P. Bossev. Bending elasticity of saturated and monounsaturated phospholipid membranes studied by the neutron spin echo technique. *Journal of Physics: Condensed Matter*, 21(15):155104, 2009. (Cited on pages 135 and 143.)

[228] Laura R. Arriaga, Iván López-Montero, Francisco Monroy, Guillermo Orts-Gil, Bela Farago, and Thomas Hellweg. Stiffening effect of cholesterol on disordered lipid phases: a combined neutron spin echo+ dynamic light scattering analysis of the bending elasticity of large unilamellar vesicles. *Biophysical journal*, 96(9):3629–3637, 2009. (Cited on page 135.)

[229] M Kummrow and Wolfgang Helfrich. Deformation of giant lipid vesicles by electric fields. *Physical Review A*, 44(12):8356, 1991. (Cited on page 135.)

[230] Scott T Milner and SA Safran. Dynamical fluctuations of droplet microemulsions and vesicles. *Physical Review A*, 36(9):4371, 1987. (Cited on page 135.)

[231] Anton G. Zilman and Rony Granek. Undulations and dynamic structure factor of membranes. *Physical Review Letter*, 77:4788–4791, Dec 1996. (Cited on page 136.)

[232] Frank J. Millero, Roger Dexter, and Edward Hoff. Density and viscosity of deuterium oxide solutions from 5-70 °C. *Journal of Chemical & Engineering Data*, 16(1):85–87, 1971. (Cited on page 136.)

[233] Paul Hamilton-Brown, Innocent Bekard, William A. Ducker, and Dave E. Dunstan. How does shear affect Aβ fibrillogenesis? *The Journal of Physical Chemistry B*, 112(51):16249–16252, 2008. (Cited on page 136.)

[234] Milka Doktorova, Frederick A Heberle, Richard L Kingston, George Khelashvili, Michel A Cuendet, Yi Wen, John Katsaras, Gerald W Feigenson, Volker M Vogt, and Robert A Dick. Cholesterol promotes protein binding by affecting membrane electrostatics and solvation properties. *Biophysical journal*, 113(9):2004–2015, 2017. (Cited on pages 137 and 143.)

[235] Valeria Rondelli, Paola Brocca, Simona Motta, Massimo Messa, Laura Colombo, Mario Salmona, Giovanna Fragneto, Laura Cantù, and Elena Del Favero. Amyloidβ peptides in interaction with raft-mime model membranes: a neutron reflectivity insight. *Scientific reports*, 6:20997, 2016. (Cited on page 137.)

[236] Zheng Yi, Michihiro Nagao, and Dobrin P Bossev. Bending elasticity of saturated and monounsaturated phospholipid membranes studied by the neutron spin echo technique. *Journal of Physics: Condensed Matter*, 21(15):155104, 2009. (Cited on page 138.)

[237] Thomas R Jahn and Sheena E Radford. The yin and yang of protein folding. *The FEBS journal*, 272(23):5962–5970, 2005. (Cited on page 141.)

[238] Christopher M Dobson. Experimental investigation of protein folding and misfolding. *Methods*, 34(1):4–14, 2004. (Cited on page 141.)

[239] Christopher M Dobson and Martin Karplus. The fundamentals of protein folding: bringing together theory and experiment. *Current opinion in structural biology*, 9(1):92–101, 1999. (Cited on page 141.)

[240] Sebastian Wärmländer, Ann Tiiman, Axel Abelein, Jinghui Luo, Jyri Jarvet, Kajsa L Söderberg, Jens Danielsson, and Astrid Gräslund. Biophysical studies of the amyloid β-peptide: Interactions with metal ions and small molecules. *ChemBioChem*, 14(14):1692–1704, 2013. (Cited on page 141.)

[241] John Hardy and Dennis J Selkoe. The amyloid hypothesis of Alzheimer's disease: progress and problems on the road to therapeutics. *science*, 297(5580):353–356, 2002. (Cited on page 141.)

[242] Mireille Dumoulin, Alexander M Last, Aline Desmyter, Klaas Decanniere, Denis Canet, Göran Larsson, Andrew Spencer, David B Archer, Jurgen Sasse, Serge Muyldermans, et al. A camelid antibody fragment inhibits the formation of amyloid fibrils by human lysozyme. *Nature*, 424(6950):783, 2003. (Cited on page 141.)

[243] Sebastian Pechmann and Judith Frydman. Interplay between chaperones and protein disorder promotes the evolution of protein networks. *PLoS computational biology*, 10(6):e1003674, 2014. (Cited on page 141.)

[244] Markus Kunze and Johannes Berger. The similarity between n-terminal targeting signals for protein import into different organelles and its evolutionary relevance. *Frontiers in Physiology*, 6:259, 2015. (Cited on page 141.)

[245] Kuang Lin, Victor A Simossis, Willam R Taylor, and Jaap Heringa. A simple and fast secondary structure prediction method using hidden neural networks. *Bioinformatics*, 21(2):152–159, 2004. (Cited on page 141.)

[246] Douglas B Kitchen, Hélène Decornez, John R Furr, and Jürgen Bajorath. Docking and scoring in virtual screening for drug discovery: methods and applications. *Nature reviews Drug discovery*, 3(11):935, 2004. (Cited on page 142.)

[247] Clorinda Malmo, Silvia Vilasi, Clara Iannuzzi, Silvia Tacchi, Cesare Cametti, Gaetano Irace, and Ivana Sirangelo. Tetracycline inhibits w7fw14f apomyoglobin fibril extension and keeps the amyloid protein in a pre-fibrillar, highly cytotoxic state. *The FASEB journal*, 20(2):346–347, 2006. (Cited on page 143.)

[248] Ji-Hwan Lee, Sung-Min Choi, Changwoo Doe, Antonio Faraone, Philip A Pincus, and Steven R Kline. Thermal fluctuation and elasticity of lipid vesicles interacting with pore-forming peptides. *Physical review letters*, 105(3):038101, 2010. (Cited on page 143.)

[249] B Scott Perrin, Alexander J Sodt, Myriam L Cotten, and Richard W Pastor. The curvature induction of surface-bound antimicrobial peptides piscidin 1 and piscidin 3 varies with lipid chain length. *The Journal of membrane biology*, 248(3):455–467, 2015. (Cited on page 143.)

[250] Li Lin, Se-Chan Kim, Yin Wang, Sanjiv Gupta, Ben Davis, Scott I Simon, Guillermo Torre-Amione, and Anne A Knowlton. Hsp60 in heart failure: abnormal distribution and role in cardiac myocyte apoptosis. *American Journal of Physiology-Heart and Circulatory Physiology*, 2007. (Cited on page 143.)

[251] John J Kremer, Monica M Pallitto, Daniel J Sklansky, and Regina M Murphy. Correlation of β-amyloid aggregate size and hydrophobicity with decreased bilayer fluidity of model membranes. *Biochemistry*, 39(33):10309–10318, 2000. (Cited on page 143.)

[252] Rishi Sharma, Issan Zhang, Tze Chieh Shiao, Giovanni M Pavan, Dusica Maysinger, and René Roy. Low generation polyamine dendrimers bearing flexible tetraethylene glycol as nanocarriers for plasmids and sirna. *Nanoscale*, 8(9):5106–5119, 2016. (Cited on page 145.)

[253] Thomas C.B. Klauber, Rikke V. Søndergaard, Rupa R. Sawant, Vladimir P. Torchilin, and Thomas L. Andresen. Elucidating the role of free polycations in gene knockdown by siRNA polyplexes. *Acta biomaterialia*, 35:248–259, 2016. (Cited on page 145.)

[254] Patrizia Andreozzi, Eleftheria Diamanti, Karen Rapp Py-Daniel, Paolin Rocio Cáceres-Vélez, Chiara Martinelli, Nikolaos Politakos, Ane Escobar, Marco Muzi-Falconi, Ricardo Azevedo, and Sergio E Moya. Exploring the ph sensitivity of poly (allylamine) phosphate supramolecular nanocarriers for intracellular sirna delivery. *ACS applied materials & interfaces*, 9(44):38242–38254, 2017. (Cited on page 145.)

[255] Andrey V. Dobrynin and Michael Rubinstein. Theory of polyelectrolytes in solutions and at surfaces. *Progress in Polymer Science*, 30(11):1049–1118, 2005. (Cited on page 145.)

[256] Barbara Jachimska, Tomasz Jasiński, Piotr Warszyński, and Zbńgniew Adamczyk. Conformations of poly (allylamine hydrochloride) in electrolyte solutions: Experimental measurements and theoretical modeling. *Colloids and Surfaces A: Physicochemical and Engineering Aspects*, 355(1-3):7–15, 2010. (Cited on page 145.)

[257] Jean-Pierre Hansen and Ian R McDonald. *Theory of simple liquids*. Elsevier, 1990. (Cited on pages 149 and 150.)

[258] Heinrigh B. Stuhrmann and Rudolf G. Kirste. Elimination der intrapartikulären untergrundstreuung bei der röntgenkleinwinkelstreuung an kompakten teilchen (proteinen). *Zeitschrift für Physikalische Chemie*, 46(3-4):247–250, 1965. (Cited on page 151.)

[259] Igor pro, (WaveMetrics, Lake Oswego, OR, USA). `http://www.wavemetrics.com/`. 2016. (Cited on page 154.)